6-29-2020

Designing silk protein-based composite materials with tunable heat transfer and magnetic properties

Ye Xue
Rowan University

DESIGNING SILK PROTEIN-BASED COMPOSITE MATERIALS WITH TUNABLE HEAT TRANSFER AND MAGNETIC PROPERTIES

by

Ye Xue

A Dissertation

Submitted to the
Department of Biomedical Engineering
College of Engineering
In partial fulfillment of the requirement
For the degree of
Doctor of Philosophy
at
Rowan University
May 13, 2020

Dissertation Chair: Xiao Hu, Ph.D.

Acknowledgement

I would like to thank my advisor, Prof. Xiao Hu, the Chairman of my Advisory Committee, for his patient guidance and constant support. He is not only an amazing mentor but also a good friend. He inspired me and shared his wisdom with me in pursuing a successful career and the meaning of life. I would like to thank my committee member, Prof. Samuel Lofland, for his always patient guidance and help in designing and conducting experiments and analyzing data. His scientific and rigorous academic attitude inspired me. I would like to thank my committee members, Prof. Vince Beachley, Prof. Jiwook Shim, and Prof. Erik Brewer for spending time on being part of this. Each of you has motivated me in the professional development of my career as a scientist or teacher and I really appreciate your guidance.

Thanks to Prof. Jeffrey Hettinger and Mr. Carl Lunk for their help in operating SEM, X-ray, EDS and PPMS in Physics department. Thanks to my master advisor and collaborator Prof Wengbing Hu. I would like to acknowledge the financial support from US National Science Foundation, New Jersey Health Foundation, and Sekisui Chemical Research Grant.

I would like to thank my friends Bingyao Huang, Chunjie Gan, Dave Jao, Guoshan Jiang, Paul Hu, Shuting Zhangzhang, Xiaotian Chen, Guoxiang Jiang, Jianhua Cai and the Cerquoni family. They brought me so much fun and have been so helpful to me in the past five years. I wish you the best in the future!

Finally, I would like to thank my girlfriend, Huiwen Tao, for her company, sacrifice and encouragement. I am grateful for my parents, Yinsheng Xue and Yixia Sha, for their forever support and love.

Abstract

Ye Xue
DESIGNING SILK PROTEIN-BASED COMPOSITE MATERIALS WITH TUNABLE HEAT TRANSFER AND MAGNETIC PROPERTIES
2019 - 2020
Xiao Hu, Ph.D.
Doctor of Philosophy

Renewable and biocompatible silk protein materials with desired physical properties show promising applications in biomedical field. In this work, a set of protein-based composites with desired thermal and magnetic properties, enhanced by the appropriate distribution of nanofillers in the protein matrix in both 2D-film and 1D-fiber forms was investigated. Results indicate that secondary structures of silk protein materials regenerated by a formic acid-calcium chloride method are different from those of their respective natural silk fibers. Intramolecular β-sheet structures were found to dominate these silk films, causing these regenerated samples to be water-insoluble but more flexible than traditional silk films with intermolecular β-sheet crystals. New renewable thermal management materials based on a stable composite system of biocompatible silk fibroin protein materials and AlN /BN were developed. The self-assembly of nanofillers and SF was promoted by water annealing to enhance the interaction between the phases to reduce the phonon scattering. Thermal conductivity of the composites was significantly improved. Silk protein with three types of magnetic nanoparticles were combined and investigated. Results indicate that magnetite (Fe_3O_4) and barium hexaferrite ($BaFe_{12}O_{19}$) can inhibit β-sheet formation due to strong coordination bonding between Fe^{3+} ions and carboxylate ions and on silk fibroin chains where cobalt particles showed minimal effect. All three types of magnetic composites films maintained high magnetization. This work is significant in that it represents a novel and systematic study on expanding the potential biomedical applications of a set of protein-based composites.

Table of Contents

Table of Contents (Continued)

Table of Contents (Continued)

Table of Contents (Continued)

Table of Contents (Continued)

List of Figures

Figure Page

List of Figures (Continued)

Figure Page

List of Figures (Continued)

Figure Page

List of Figures (Continued)

Figure Page

List of Figures (Continued)

Figure Page

List of Figures (Continued)

Figure Page

List of Figures (Continued)

Figure Page

List of Figures (Continued)

Figure Page

List of Figures (Continued)

Figure Page

List of Tables

Chapter 1

Introduction

1.1 Overview of Protein-Based Polymers

Protein-based polymers are green polymers due to their biological nature and recyclability [1, 2]. This covers a broad range of biopolymers such as silks, elastin, keratin, resilin and collagen. They have been used in biomedical fields for many applications because of their biocompatibility, biodegradability, extraordinary mechanical properties and economic benefits. Tunable properties of natural proteins can be achieved through modifying their structure at micro- or nano- scale. It has been a hot topic recently to modify the protein structure to achieve high thermal conductivity.

1.1.1 Silk

Silk is a well-known natural fiber produced by silkworms or spiders. Silk has been well studied in the past decades due to its outstanding mechanical durability, stable chemical properties and good biocompatibility [3]. It can be classified into wild silk and domestic silk according to the growth environment of the insects. Domestic silkworm's silk fiber mainly consists of fibroin and sericin. Silk fibroins accounts for 60-80%, and sericin account for 20-30%. Sericin functions as natural glue that binds fibroin fibers together, forming silk fibers [4]. For Bombyx mori silk fibroin, it is characterized with an unique amino acid sequences of GAGAGS, which contributes to the formation of beta sheets in the fibroin structure, a hydrophobic block[5]. The high tensile strength of silk fiber is attributed to the beta sheets, while the hydrophobic block contributes to its elasticity[6]. Studies have shown that properties of silk-based materials can be effectively

manipulated through controlling the content and alignment of the beta sheets [6]. Silk fibroin has been manufactured into nanofibers, particles, scaffold and film that can be widely used in biomedical field and healthcare industry [7-9]. Regenerated water-based silk fibroin suspension have been coated onto fruits, and this method can effectively modulate the gas diffusion through the silk fibroin thin membrane [10]. It can help manage fruit freshness during the transportation and in the poor areas where they lack refrigerators. Also, silk fibroin has been manufactured into particles as a carrier for controllable drug release [8]. Spider silk fiber [36] has been reported with high thermal conductivity, up to 416 W/mK, although this claim is not universally accepted[11-13].

1.1.2 Collagen

Collagen is a structural protein that mainly exist in the extracellular matrix. Collagen is mostly found in the connective tissues and fibrous of animals, such as tendons, bones, ligaments and skin [14]. Arranged collagens provide mechanical support in the connective tissues, while fractional collagen provides toughness and maintain the anisotropy for the biomineralized material [15, 16]. Most of the collagens found in body are classified into type I, II or III [16]. All the collagens share the right-handed triple helix structure feature [17]. Up to 29 types of collagens have been identified according to its structure diversity, function and splice variants. Collagen is called as the “steel of biological materials”, and thousands of papers about collagens have been published [18].

Collagens have been widely used in the tissue engineering. It is reported that oriented collagen tubes (OCT) combined with fibroblast growth factor can accelerate the repair of sciatic nerve defects in rats [19]. Large and complex 3D scaffold with uniform

and homogeneous porous structure can also been obtained through the freeze-drying method using collagens as raw materials [20].

1.1.3 Keratin

Keratin is a fibrous structural protein that mainly exist in hair, fingernails, scales, feathers and wools [21]. Keratin is known for its excellent chemical stability, and it is insoluble in both water and organic solvents [22]. Keratins can be further classified into type I and type II according to their sequences [23]. They are long and unbranched filaments containing a central alpha helical domain that separated by three beta-turn segments[24]. Around thirty types of keratins are divided into acidic and basic groups. Due to its high molecular diversity, keratin is an important type of intermediate filament. In epithelia cells, keratin filaments are bundled as tonofilaments, which act as bones of the cellular scaffold and contribute rigidity to the cell. They can maintain the structural integrity and sustain mechanical stress [24, 25].

Good biocompatibility and biodegradability has made keratin one of the most promising biomaterials. Regenerated wool keratin films manufactured from ionic liquid have been well studied. Beta-sheet and alpha-helix structures can be manipulated through changing the process parameters [26]. Keratin-PCL nanofibers have been obtained through electrospinning, and cellular compatibility of the composite nanofibers have also been proved [27].

1.2 Overview of Applications of Thermal Conductive Biopolymers

Biopolymers are polymers that have components found in nature. They can be synthesized naturally or man-made. Similar to synthetic polymers, biopolymers are long

chain molecules with many repeating units. Based on their main components, biopolymers can be specified into three main categories: proteins (*e.g.* silks, elastin, resilin, keratin, collagen, and variable plant proteins), polysaccharides (*e.g.* cellulose, starch and chitin), and nucleic acids (*e.g.* deoxyribonucleic acid and ribonucleic acid). In addition to biomedical applications, biopolymers, especially protein polymers, are also widely used in green applications, which significantly reduce or eliminate the use or production of substances hazardous to humans, animals, plants, and the environment [28]. Figure 1.1 shows the general pathway that raw protein materials can be processed into flexible 2D materials with enhanced thermal conductivity.

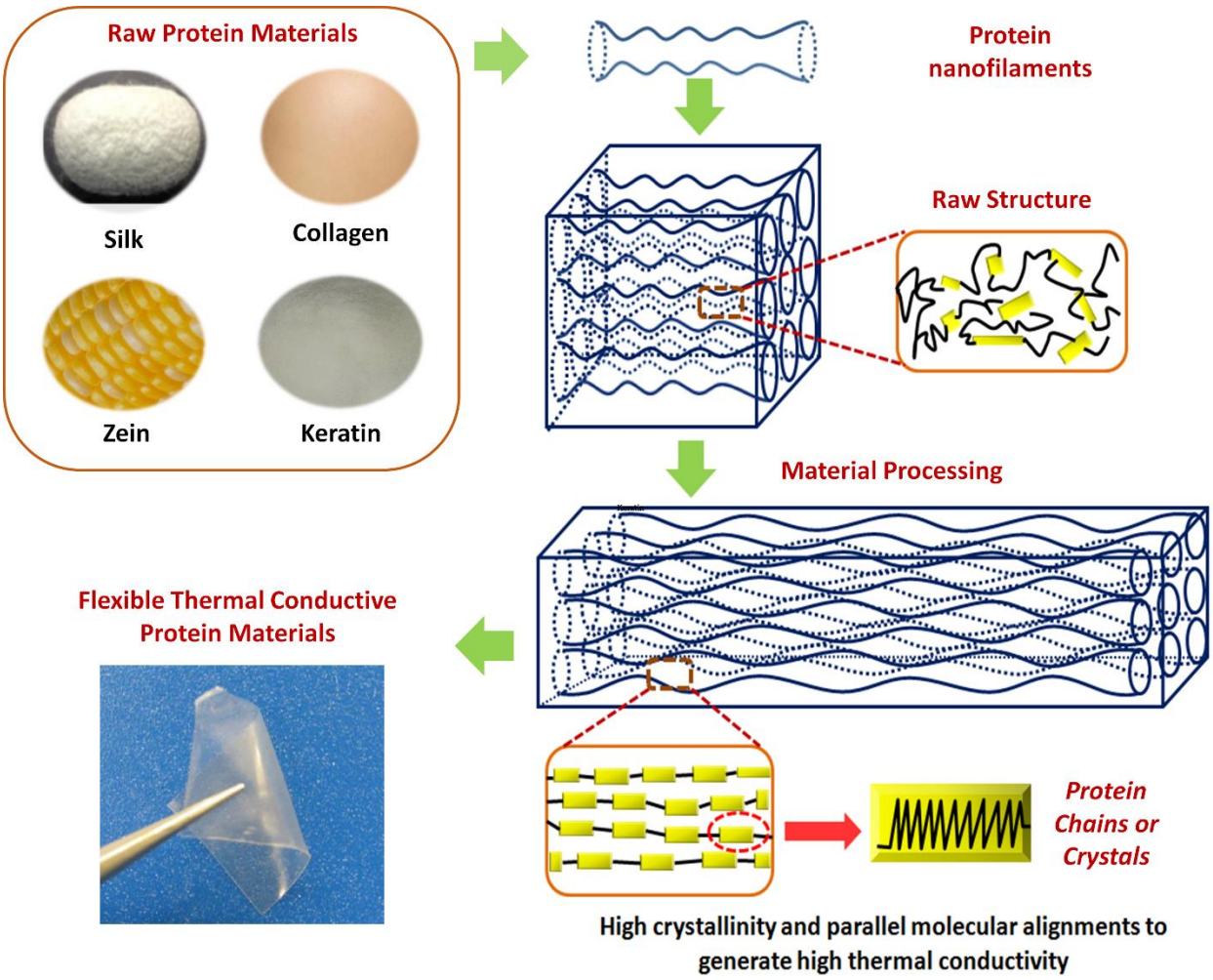

Figure 1.1 Illustration of the relations between raw protein materials, material processing and flexible thermal conductive protein materials. Tunable thermal conductivity can be achieved through modifying the structure of protein structures.

Thermal conductivity describes the transport of heat through a material body, driven by a temperature gradient. With the rapid development of delicate high-tech instruments, such as ultra large scale integration (ULSI) in digital device and communication equipment, special materials with tunable thermal conductivity or heat transfer direction are in tremendous demand [29, 30]. A better understanding of the thermal conductivity of materials will enhance current material design techniques and applications

in various fields. Typically, most polymers are classified as poor conductors, while metals are generally very good conductors. As shown in Table 1, the thermal conductivity of Nylon 6 is 0.25 W/m·K, compared to 400 W/m·K for copper [31]. The contrasting thermal conductivity values of these two materials in specific, or polymers and metals in general, are caused by their different principles of heat transport [32, 33]. In metals, their thermal conductivities can be attributed to free electrons, which transfer energy. However, for polymers, heat conduction takes place through lattice vibrations (phonons). In general, the amorphous structure in polymers results in a decrease in the mean free path of phonons, which lowers the material's thermal conductivity. Moreover, defects in bulk polymers, voids, chain ends, interfaces and impurities also affect a material's thermal conductivity.

Table 1.1
Thermal conductivity values of common polymers and metals at room temperature [34-40]

Material	**Thermal conductivity(W/m·K)**
Low density polyethylene (LDPE)	0.3
High density polyethylene (HDPE)	0.44
Polycarbonate	0.22
Polyvinyl chloride (PVC)	0.19
Nylon-6 (PA6)	0.25
Polythiophene nanofibers (amorphous)	~4.4
Polyethylene nanofibers	~104
Silkworm silk (axial direction)	~6.53

Table 1 (continued)

Material	Thermal conductivity(W/m·K)
Flax fiber	0.1187
Squid protein	0.3-1.3
Silk/wool hybrid	0.000397-0.000663
Human skin	0.23-0.488
Aluminum	235
Copper	400
Nickel	158
Gold	345
Aluminum	235
Diamond	1000

The thermal conductivity of polymers is normally on the order of 0.1 W/m·K, which makes most polymers good thermal insulators. Their insulating properties can be enhanced by foaming them and controlling the pore size in the foams. Today, polymer-based thermal insulation materials have been used in space technology [41], for example, to prevent the temperature increase of the spaceship motors to maintain their structural integrity. Polymer-based thermal insulation materials are also an important part of buildings, electrical power lines, and clothing for firefighters [42-44]. Due to their low density, low thermal expansion and low maintenance, these materials could be utilized in microelectronics, automobiles, and satellite devices as well.

On the other hand, with appropriate nanostructure, polymers can also possess very high thermal conductivity. For example, polymer nanofibers grow in a limited nanotube

space have been found to have a thermal conductivity of up to 100 W/m·K [34], and it can maintain the ultrahigh thermal conductivity over a wide range of temperature without degradation.

Compared with biopolymers, however, most synthetic polymer materials or metals with high conducting or insulating properties have obvious drawbacks for certain applications. For instance, thermal transfer films made of polyurethane and polystyrene have a limited temperature usage range because of flammability. Besides, synthetic polymers are often non-biocompatible, which may produce toxic residues when they are used as biomedical materials or food packaging materials. Although metals have high thermal conductivities, they are also electrically conductive and are not mechanically flexible. Nevertheless, thermal transfer biopolymer materials, such as silk, collagen and keratin, are mechanically flexible, naturally fire retardant, transparent and biocompatible. The relationship between hardness and thermal conductivity in current market is shown in Figure 1.2. Protein polymers, such as silk, can be manufactured into diverse applications, such as sensor parts, aerospace recycling components, electrical products, medical materials, and textile materials [45-49]. Due to their light weight, flexibility, easy processing and corrosion resistance, biopolymer insulators or biopolymer materials with high thermal conductivity have attracted much attention recently [34, 50-52]. With numerous ongoing studies to increase their thermal conductivity and a tremendous potenial market in the future, protein-based thermal conductive materials may have vast application in green and sustainable material industry in the future.

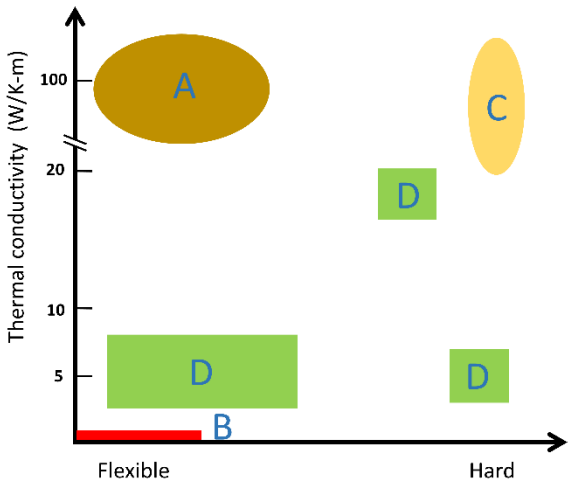

Figure 1.2 A and B are the ideal areas of thermal conductive and thermal insulating materials using protein-based polymers, respectively; C areas represent metal-based or ceramic-based materials that have both high thermal conductivity and high elastic modulus; D areas represents the typical synthetic polymer-based heat transfer materials that currently exist in the market.

1.2.1 Parameters to Influence the Thermal Conductivity of Protein Polymers

In general, the Debye equation (**Equation 1.1**) [53] is used to model the thermal conductivity κ of isotropic 3-D materials due to the phonon transport [54]:

$$\kappa = \frac{1}{3} Cvl \qquad (1.1)$$

where C is the volumetric heat capacity, v the speed of sound, and l the mean free path of the phonons, which is limited by point defects, scattering from sample boundaries, and phonon-phonon interactions [55]. The thermal conductivity of protein polymer materials can be governed by many factors, such as crystallinity, molecular chain alignment, temperature, moisture, impurities, interfaces, and chemical bonds. Therefore, many recent studies have focused on manipulating thermal conductivity of polymer materials at micro- and nano-scales [56-68].

1.2.1.1 Crystallinity. Many experiments have proved that polymers with high crystallinity have much higher thermal conductivity values compared to that of amorphous counterparts [32, 34, 69-73]. Amorphous structure decreases the mean free path of phonons, and disordered alignment will scatter phonons and decrease the speed of sound *v*, which can be seen in Figure 1.3. Xu *et al*. reported that less crystalline structure and more random coils would contribute to the relatively lower thermal conductivity of hexafluoroisopropanol (HFIP) film of *L. hesperus* [69]. On the other hand, Shen *et al*. found that thermal conductivity of polyethylene nanofibers fabricated by a ultra-drawn method can reach as high as 104 W/m·K [34]. After crystallization, the crystallinity of the polymer materials can be improved, with nanofibrous structures formed with an almost perfect orientation following the crystalline direction. A mechanism was proposed in Figure 1.4 to help understand this idea. It was also believed that the density defect of polymers would decrease after a crystallization process.

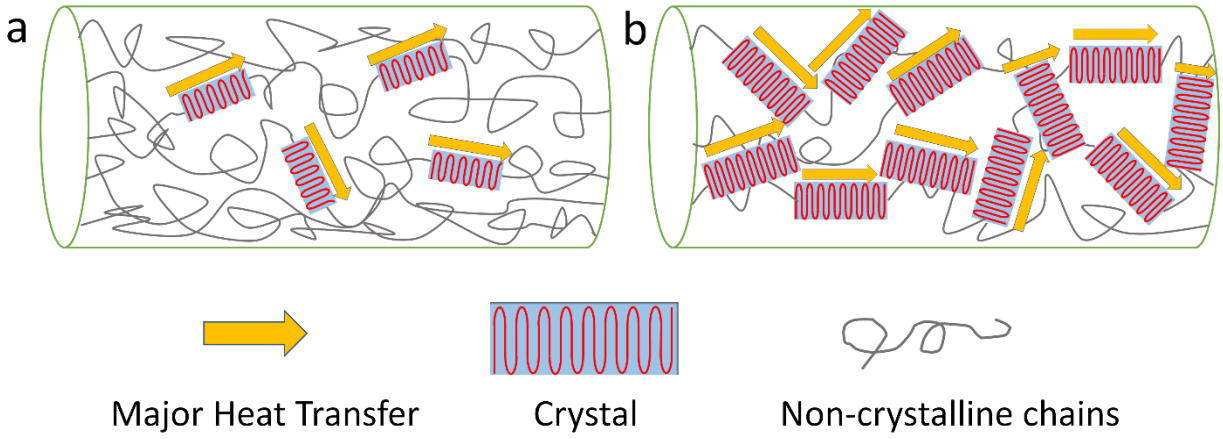

Figure 1.3 Effect of crystallinity on heat transfer: (a) structure of bulk polymer material with low crystallinity; (b) structures of polymer material with higher crystallinity.

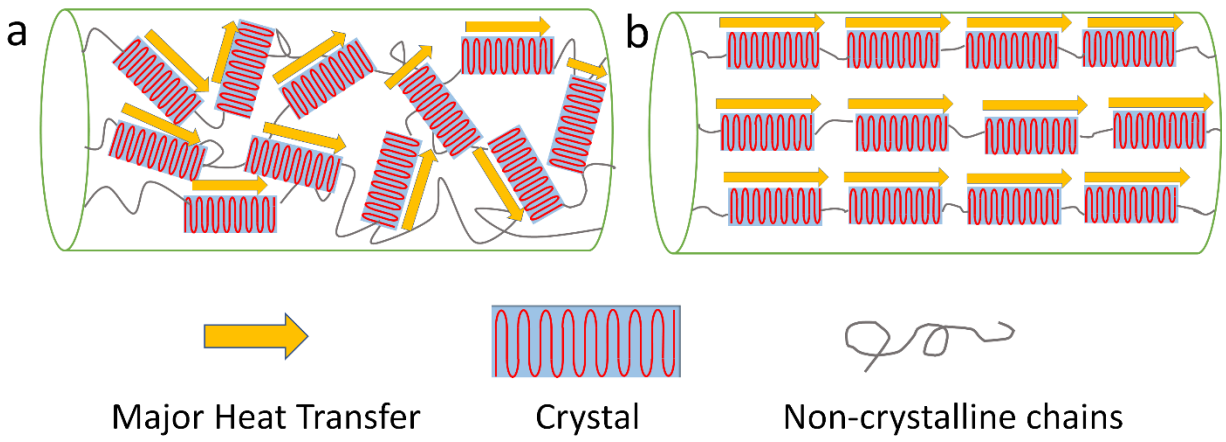

Figure 1.4 Effect of crystal alignment on heat transfer:(a) structure of bulk crystalized polymer with less crystal alignment; (b) structure of stretched crystalized polymer with good crystal orientation.

1.2.1.2 Chain Orientation. High degree of chain orientation can help increase the thermal conductivity of polymers even with an amorphous conformation [74-77]. For example, progress has been made recently by Singh *et al.* [78] to improve the thermal conductivity of amorphous polythiophene using a nano-scale design method. The molecular chain orientation in the cross-plane direction of polythiophene was significantly improved during electropolymerization through a nanoscale template (Figure 1.5b). The thermal conductivity of formed amorphous polythiophene reached up to 4.4 W/m·K, compared to 0.2 W/m·K of the bulk polymer. The smaller the diameter of the nanofiber, the higher its degree of orientation and likewise thermal conductivity were. It was hypothesized that the enhancement of chain orientation in polythiophene

nanofibers increased the speed of sound in materials while decreasing the phonon scattering. This was subsequently confirmed by molecular simulation studies [79].

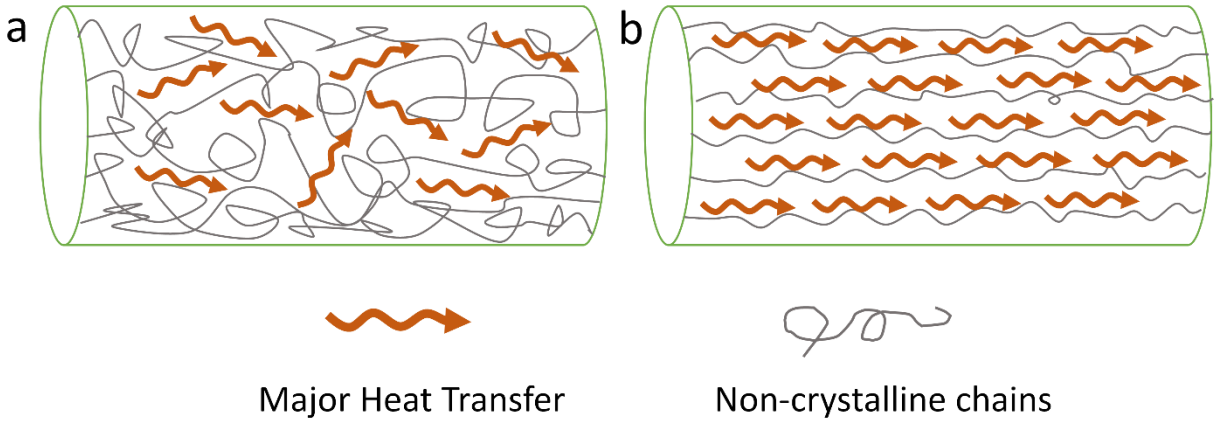

Figure 1.5 Effect of molecular chain alignment on heat transfer:(a) structure of bulk non-crystalized polymer with less chain alignment; (b) structure of stretched non-crystalized polymer with good chain orientation.

1.2.1.3 Composites. Another effective way to improve the thermal conductivity of polymers is to mix them with nano-structural materials that have high thermal conductivity, such as carbon nanotubes, graphene, boron nitride nanosheets, nano-scale aluminum nitride, and copper nanoparticles [55, 80-90]. Nanostructure fillers are not only used in elevating thermal conductivity but also in controlling electrical and mechanical properties of polymer composites [77, 80]. The thermal conductivity of a polymer composite can be directly controlled by the filler's size, shape, volume fraction and distribution in the polymer matrix.

For example, it was demonstrated that polyvinyl alcohol (PVA) incorporated with boron nitride nanotubes can be electrospun into composite mats with a much higher thermal

conductivity than that of pure PVA mats [77]. The thermal conductivity of the film increased as the volume fraction and alignment degree of nano-filler increased. It is noted that nano-structural materials can provide a better thermal transport path which limits phonon scattering.

Due to the different phases in the polymer composites, which are phonon-based conductors, it is unavoidable that phonons would scatter at the interfaces. Therefore, the size and shape of the filler is important. A recent study reported that thermal conductivity of polymer composite decreased as the filler particle size increased when the filler volume fraction was above 5%, as shown in Figure 1.6 [91].

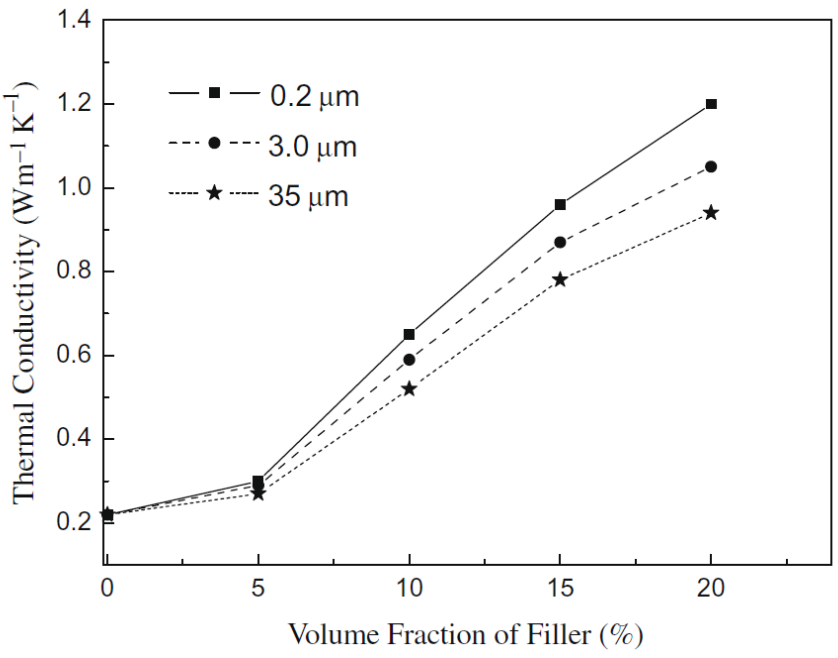

Figure 1.6 Different impacts of filler diameter and volume fraction on thermal conductivity of composites. [91].

1.2.1.4 Other Parameters. Researchers have shown that the κ values of polymer nanocomposites can increase with the temperature [92, 93]. Besides, it is also believed that the chemical process can help improve the interfacial bonding between the graphite nanoplatelets (GNPs) and polymer matrix, which also increased the κ values of the nanocomposites [92]. As reported by C. Cassignol *et al*., the κ values of polypyrrole increased with the moisture content, especially from 8.5% to 13.5% [94]. Therefore, in addition to parameters such as crystallinity, chain orientation and fillers, thermal conductivity of polymer also varies with the change of temperature, moisture and other factors [55, 94, 95]. Due to the anisotropic property of polymer, thermal conductivity of polymer in the cross-plane direction or the in-plane direction is also different [96].

1.2.2 Experimental Setups to Measure the Thermal Conductivity of Protein-Based Materials

Owing to the biodegradable and biocompatible properties of silks, silk-based composite materials have been used as artificial tissue scaffolds and medical products. Because of their low electrical conductivity and outstanding mechanical properties, silk fibers have also been made into various forms, which have huge potential applications for digital devices [97, 98]. Because of their broad applications in biomedical field, the thermal conductivity values of collagens and keratins were also measured previously [99, 100].

κ is defined by the heat flow due to a temperature gradient. More precisely,

$$\kappa = \frac{QL}{A\Delta T} \tag{1.2}$$

where L is the length, A the cross-sectional area and ΔT is the temperature difference across the ends of the sample. Fourier's Law states that

$$\frac{1}{A}\frac{dQ}{dt} = -\kappa\frac{dT}{dz} \tag{1.3}$$

where dQ/dt is the rate of heat flow along the z direction, and dT/dz the resulting thermal gradient. Many techniques have been developed in the last decades to measure the thermal conductivity of solids, nanoparticles and nanofluids [101-105]. Thus, different kinds of experimental setups, as described below, have been made to measure the thermal conductivity of protein-based biopolymers [30, 61-63, 69, 100, 106, 107].

1.2.2.1 Temperature-Modulated Differential Scanning Calorimetry Method.

Differential scanning calorimetry (DSC) is a thermal analysis technology that can be used to measure various thermal and chemical properties of materials, such as glass transition temperature, decomposition temperature, melting point, crystallinity and oxidative stability, based on measuring the heat flow into or out of the specimen as a function of temperature or time [108-110]. Temperature-modulated differential scanning calorimetry (TMDSC) [111] divides the total heat flow into reversing part (heat capacity) and non-reversing part (kinetic). As a result, specific transition information, direct measurement of heat capacity and higher sensitivity can be obtained. TMDSC method was used to measure the thermal conductivity of silkworm cocoon in the cocoon sheets (thickness) direction [63, 70, 111].

As reported by Zhang *et al*., the measurement was under the protection of nitrogen gas, and the TMDSC had a temperature amplitude of ± 1℃ and 60 s period. For a circular cylinder sample, the principle of measurement is based on Equation 1.4 listed below:

$$\kappa_0 = \frac{8LC^2}{C_p m d^2 P} \tag{1.4}$$

where κ_0 is the measured thermal conductivity, d the diameter, P an experimental parameter, m the mass of the circular cylinder sample, C the apparent heat capacity, and C_p the specific heat capacity of the sample, which can be measured directly by the TMDSC. Because of the heat loss through side areas of the circular cylinder sample, which resulted in the measurement discrepancy, κ is ultimately determined by:

$$\kappa = \frac{1}{2}\left[\kappa_0 - 2D + (\kappa_0^2 - 4D\kappa_0)^{\frac{1}{2}}\right] \tag{1.5}$$

where D is the thermal conductivity calibration constant, determined by κ_0 and the thermal conductivity of the reference sample.

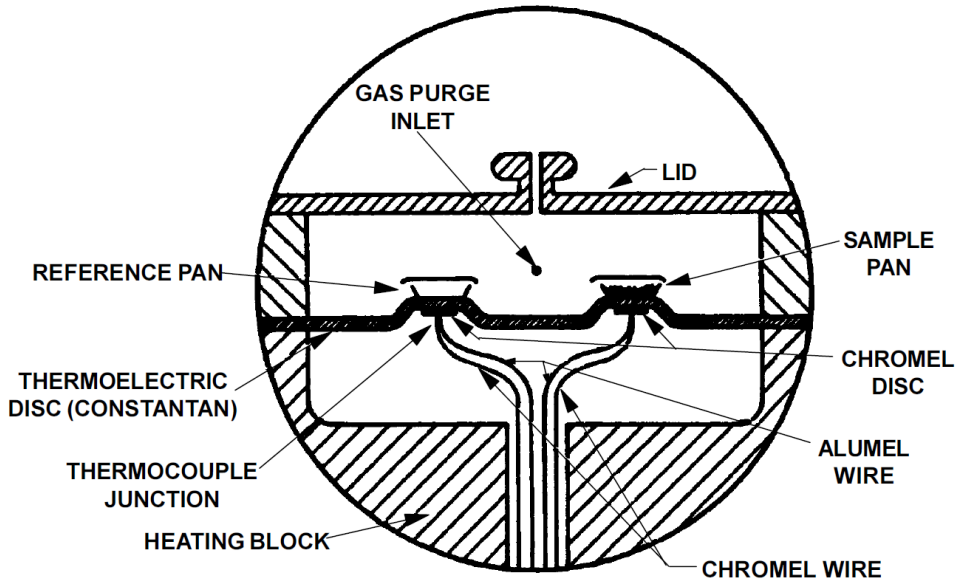

Figure 1.7 Schematic of the differential scanning calorimetry method. [112].

Figure 1.7 shows the schematic of TM-DSC method. In principle, the discrepancy from the purge gas may be reduced effectively with a low thermal conductivity purge gas, such as argon. Based on various assumptions [111], the accuracy of this method is around 3-4% from the values measured from other techniques. Besides, this method is also limited to measure the thermal conductivity in the range from 0.1 to 1.5 W/m·K. In addition, there are also studies conducted with the conventional DSC recently [70, 112-115]. Therefore, the DSC methods are simple accessible techniques to measure the thermal conductivity of biopolymer insulators in the future.

1.2.2.2 3-ω Method (Transient Hot Wire Method). 3-ω method is a contact measurement system that has been widely used to measure the thermal conductivity of thin films for several decades [105, 116]. Compared to non-contact measurements, it does not require expensive devices with a complicated setup. A typical experimental setup for the 3-ω method is shown in Figure 1.8. As reported by Delan *et al*. [106], this method was used to test the thermal conductivity of porous silk film in thickness direction. For this method, a narrow metal line is patterned on the surface of the film sample directly. Alternating current at angular frequency ω is applied to the metallic strip, and Joule heating is caused at a frequency of 2ω. In addition, the temperature-dependent resistance of the metal results in a voltage of third harmonic 3ω. Thus, thermal conductivity of the silk film in thickness direction can be obtained from the correlation curves of the temperature vs. the voltage frequency [116].

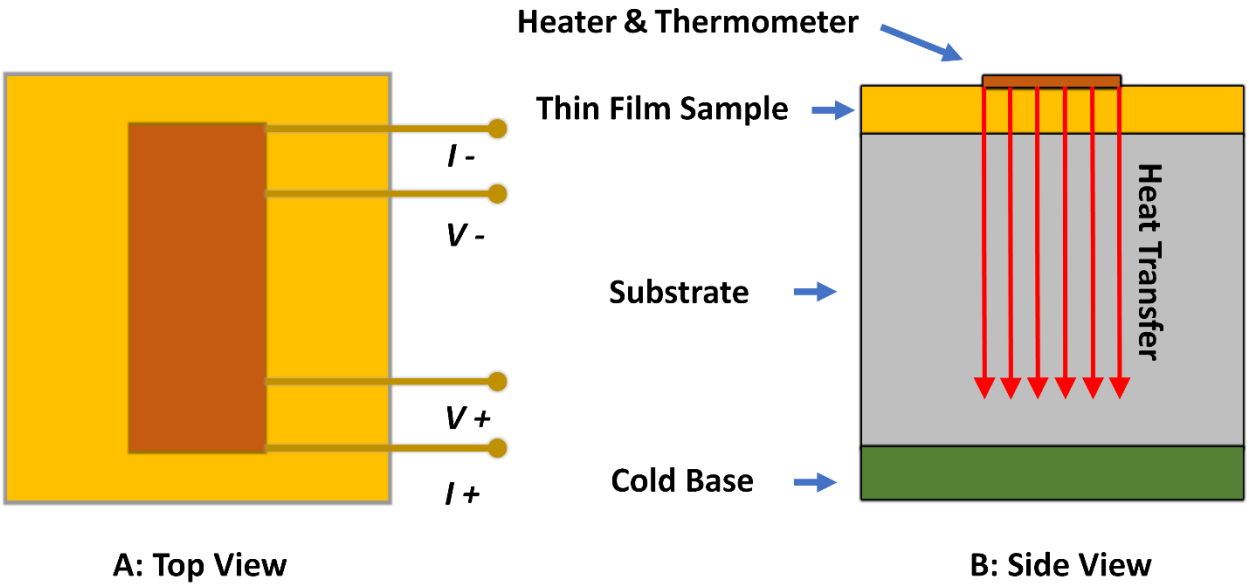

Figure 1.8 Experimental setup of the 3-w method. A is the top view of the measurement setup, and B is the side view of the setup.

Even though the 3-ω method is a simple, fast, low-cost method with high accuracy, this technique is limited to nonconductive materials previously [117]. Therefore, many extended/modified techniques have been developed recently to solve this problem, which also simplified the technique and increased the measurement accuracy [62, 117].

1.2.2.3 Transient Electrothermal Technique (TET) method. Based on the original 3-ω method, the transient electrothermal technique (TET) [118] was developed by Liu *et al*. [62] to test the thermal conductivity of silk fiber in the axial direction. Figure 1.9 is a schematic of the TET method[62]. In order to keep the heat flow in one dimension, length *L* of the silk fiber is ensured to be much longer than its diameter. A thin gold film is coated on the silk to make it electrically conductivity. The two ends of the silk fiber are fixed on the copper base by silver paste with direct current (DC) fed

through it. An oscilloscope is used to record the current and the induced voltage as a function of time. The measured thermal conductivity κ_0 is then calculated from Equation 1.6:

$$\kappa_0 = I^2RL/(12A\Delta T) \tag{1.6}$$

where I is the current, R the total resistance of silk fiber and gold film, L is the length of the silk fiber, A is the total cross-sectional area of the silk fiber and gold film and ΔT the temperature difference. ΔT can be determined from the resistance change ΔR and the measured temperature coefficient of resistance η. Because of the gold film radiation, as well as the heat convection between the gold film and the surrounding gas, the value of κ of the silk fiber can be determined:

$$\kappa = \kappa_0 - \frac{L_{Lorenz}TL}{RA} \tag{1.7}$$

where L_{Lorenz} is the Lorenz number.

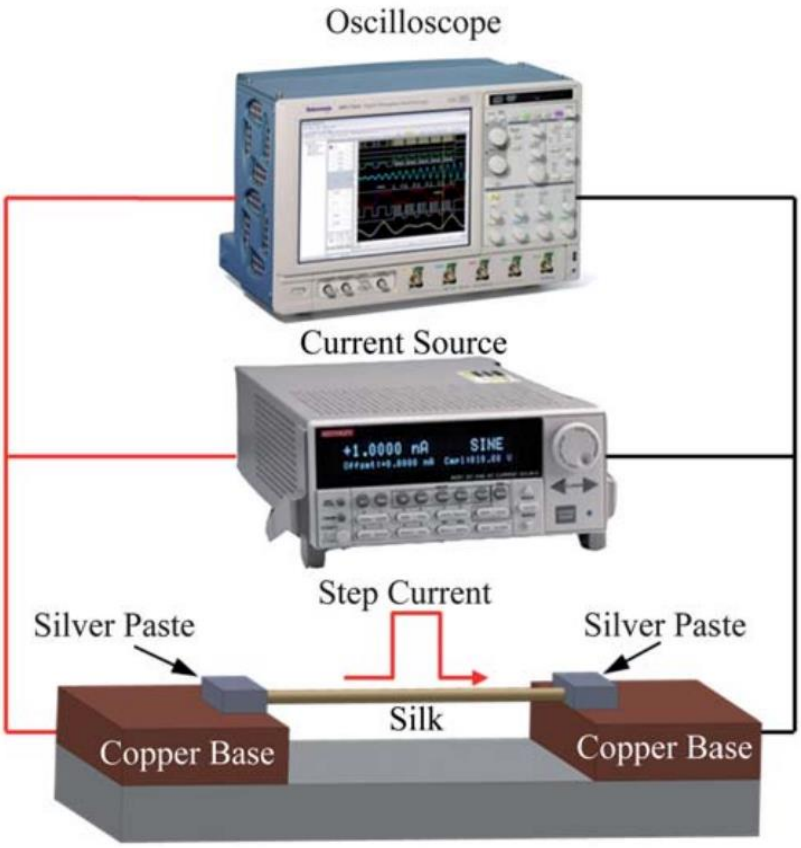

Figure 1.9 Schematic of the transient electrothermal technique (TET). [62].

1.2.2.4 Photothermal Technique. Photothermal technique (PT) method is an efficient way to measure thermal conductivity of carbon nanotubes, composite films and thin metal layers [119-122]. As reported by Xu *et al*., PT was used to measure the thermal conductivity of spider silk films [69]. The schematic and principle of PT method are shown in Figure 1.10. Due to high thermal conductivity of gold, a thin gold film is coated onto the surface of the silk films. In this technique, the gold film is irradiated and heated by a modulated-intensity laser. Due to the thermal excitation, the temperature of the silk film changes periodically with a phase shift. Based on the relation between the phase shift and thermal property of the silk film, thermal conductivity of the silk film is

measured by fitting the phase shift as the function of the modulation frequency of the laser. Besides, the thermal conductivity can also be calculated from fitting the amplitude of thermal radiation from the gold film. Compared to the previous method, the second one has a larger discrepancy. Therefore, it is useful to have a comparison and check the results of phase shift.

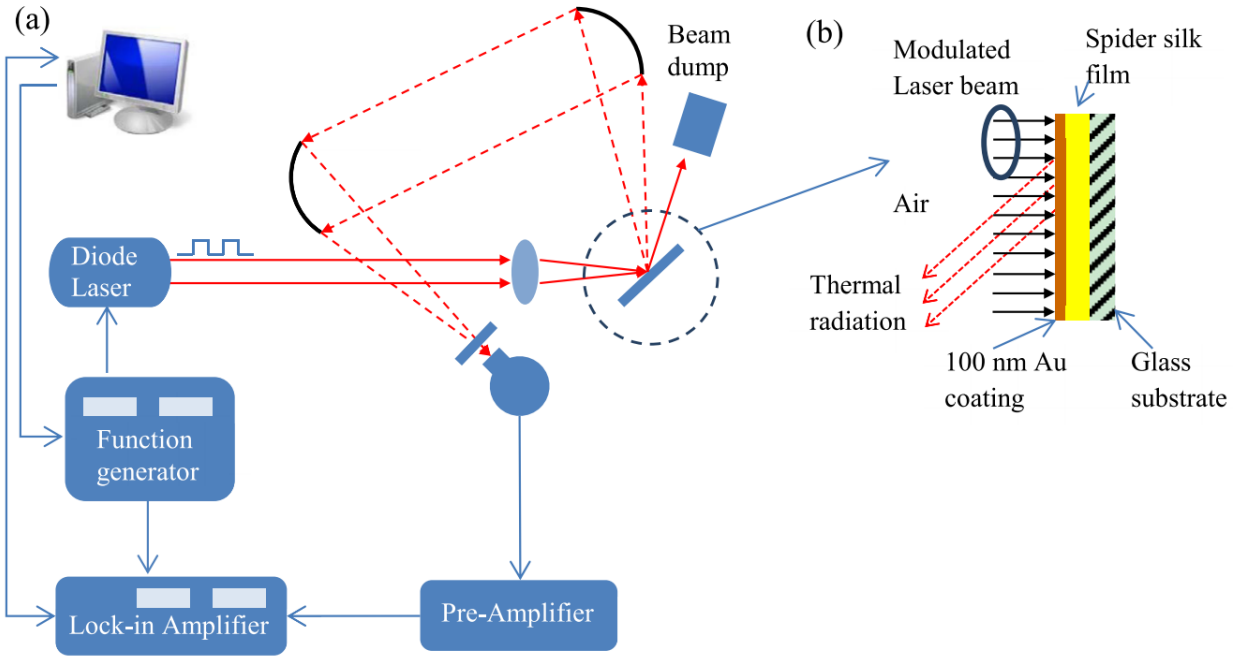

Figure 1.10 A schematic for photothermal technique (PT) b. principle of photothermal technique (PT). [69].

1.2.3 Thermal Conductivity of Different Types of Protein-Based Materials

There are many studies discussing the thermal conductivity of silkworm silk. At relaxed condition, the thermal conductivity of silkworm silk in the axial direction is 0.042 W/m·K[62]. Under tension, the thermal conductivity increases. At 68% elongation, silkworm silk achieves its highest thermal conductivity of 13.1 W/m·K[62]. Beyond that elongation point, its thermal conductivity and diffusivity decrease rapidly with strain.

In a study reported by Huang *et al.*, spider silk had the thermal conductivity increased from 348.7 to 415.9 W/m·K under a strain of 3.9% and 19.7% respectively. Spider silk highest thermal conductivity value is approximately 1000 times higher than that from *B. Mori* silk at the normal condition (416 W/m·K in comparison to 0.37W/m·K). However, this claim is not universally accepted. The measured thermal conductivity and thermal diffusivity of *Nephila (N.) clavipes* spider silk reported by Xing et al was 1.2 W/m K and 6×10^{-7} m^2 s^{-1}, respectively[11]. Xing and coworkers explained the thermal conductivity difference may be attributed to the vacuum level and heat transfer analysis method. Results published by Fuente et al[13] show that the thermal diffusivity of spider silk is around 0.20 mm^2 s^{-1}, which is 400 times lower than the value reported by Huang et al[61]. Due to the extremely thin diameter of spider fibers, it's a challenge to get the accurate thermal conductivity and thermal diffusivity, and more research should be conducted in this field.

Thermal conductivity values of collagens and keratins were reported before. It showed that the thermal conductivity of sheep collagens to be a linear function of temperature (25 °C< T < 50 °C), and the values are around 0.53 W/m·K [99]. The thermal

conductivity of keratins (wool fibres) was measured in as earlier as 1945. The thermal conductivity of wool fibers in the diameter direction is around 4.62×10^{-4} W/m·K, which suggested that the wool fibers could be near perfect thermal insulation materials[100].

1.2.4 Thermal Conductivity Differences between 1-D Fibers and 2-D Films

Compared to silk films, the structure of silk fiber is much simpler. The structure of single silk fiber can be easily characterized and manipulated. By comparing the thermal conductivity of the silk fiber and of the modified silk fiber in the axial direction, Liu *et al*. reported that the thermal conductivity of silkworm silk fiber in axial direction ranges from 0.54-6.53 W/m·K. When the silk fiber was stretched to different elongation by a spring-control device. The thermal conductivity of the stretched silk fiber increased. When the elongation was 63.8%, thermal conductivity of the stretched fiber was up to 13.1 W/m·K. However, thermal conductivity of both silkworm silk films and spider silk films in the thickness direction is only in a range from 0.15-1 W/m·K [30, 63, 69, 106].

In these studies, Raman spectra, scanning electron microscopy [123], differential scanning calorimetry (DSC) and infrared spectroscopy (FTIR) are used to characterize the structure of the films and the single fibers. It is revealed that higher crystallinity and molecular chain alignment will result in a higher thermal conductivity. For example, when a single fiber is strained at, the crystallinity increases, which means the amorphous structure transforms into β-pleated sheets. As for silk films, due to its uncontrolled process of synthesis, lower degree of alignment, less crystallinty, porosity and structural defects result in relatively low thermal conductivity in the cross-plane direction.

1.3 Overview of Magnetic Applications of Biopolymers

Magnetic materials have been widely used in biomedical fields, such as targeted drug delivery and tumor hyperthermia. Physical and chemical properties of the materials can be adjusted through modifying the shape, size, composition and surface chemical properties of magnetic particles. Magnetic materials are usually composed of iron, cobalt and nickel and their compounds. The size of magnetic nanoparticles varies between a few nanometers and 100 nanometers. The nano-scale size of the magnetic nanomaterial structure makes it have significant small size effect and interface effect. This also makes magnetic nanomaterials have many excellent properties that large-size magnetic materials do not have. Taking advantage of its nano-scale size, magnetic nanoparticles and biomacromolecule materials with good biocompatibility can be combined to prepare new biomaterials that can be used in a variety of applications. Study on applications of magnetic nanoparticles as drug delivery systems has caught a lot attention in recent years. By modifying the surface of the magnetic nanoparticles and then self-assembling with the polymer, the magnetic nanoparticles can be used to deliver drugs. One advantage is that the size of the magnetic nanoparticles will not block blood vessels, thereby avoiding clogging of blood vessels. Under the magnetic guidance of the applied magnetic field, magnetic nanoparticles loaded with drugs can be accurately moved to the diseased tissue, thereby improving the effect of the drug and reducing its side effects. Magneto-thermotherapy is a promising approach to treat cancer. The principle is to inject magnetic nanoparticles into the tumor tissue, and an alternating magnetic field was applied to heat the magnetic nanoparticles and its surrounding tissues, thereby killing the cancer cells. By controlling the saturation magnetization, size and shape of the nanoparticles, the heating

efficiency and curative effect of the magnetic nanoparticles can be improved. Natural green polymer materials such as silk proteins, keratins and polysaccharides have excellent biocompatibility and mechanical properties. If magnetic nanoparticles are combined with these natural green polymers, the application of magnetic nanoparticles in the field of biomedicine will be greatly expanded.

The magnetization (M) describes the degree to which the magnetic material is magnetized in the applied magnetic field (H).

$$M = xH \tag{1.8}$$

Where M is the magnetization, H is the applied magnetic field strength, χ is the magnetic susceptibility.

According to the magnetic strength of magnetic substances, magnetic materials can be divided into paramagnetic, diamagnetic, ferromagnetic and antiferromagnetic material. Paramagnetic, diamagnetic and antiferromagnetic materials have weak magnetic properties, and their magnetic susceptibility is about 10^{-5}. Ferromagnetic materials have strong magnetism, and their magnetic susceptibility can be up to 10^{6}. Ferromagnetic materials can exhibit strong magnetization even in a weak magnetic field. When the external magnetic field is removed, the ferromagnetic substance can still maintain the magnetization in the direction of the applied magnetic field. The saturation magnetization (*Ms*) refers to the maximum magnetization that a magnetic material can achieve when it is magnetized in an external magnetic field (*H*). It depends on the atomic composition of the magnetic material, the influence of the magnetic moment and the ambient temperature. For ferromagnetic materials, with the gradual increase of the strength of the external magnetic

field, the magnetic particles spin in the ferromagnetic material was magnetized, and the direction is consistent with the external magnetic field direction. When the *H* value is sufficiently high, the magnetization of the ferromagnetic material reaches the maximum (*Ms*). At this time, the spin orientation of all magnetic particles in the ferromagnetic material is consistent with the external magnetic field (*H*). When the magnetic field strength decreases, the residual magnetization will continue to exist without applied magnetic field, and the coercive field *M* will only change sign when the magnetic field is opposite to the magnetization of *Hc*. The equations of magnetization of magnetic materials and applied magnetic field strength (*H*) are shown as *M*-*H* hysteresis curves (Figure 1.11).

The shape of the magnetic material affects the magnetization direction of the magnetic material. When the shape of the material is ellipsoid, the magnetic material is more likely to be magnetized along the long axis of the ellipsoid. The magnetic field lines are always closed loop, and the demagnetizing field (Hd) is opposite to the magnetization direction of the ferromagnetic material (Figure 1.11). Therefore, the actual magnetic field

$$H = H_{app} + H_d \tag{1.9}$$

where $H_d = -NM$. H_{app} is the applied magnetic field strength, and N is the demagnetization factor. For spherical particles, $N = 1/3$. For long rods, $N = 0$ along the axis and $N = 1/2$ in the lateral direction. In addition, spherical particles and long rod-shaped particles are subjected to different forces in the magnetic field. The magnetic torque density is given by

$$\tau = \mu_0 M \times H \tag{1.10}$$

where μ_0 is the permeability of vacuum. When the axis of the particle and the direction of the applied magnetic field H_{app} are not parallel, then *H* and *M* are not parallel. Therefore, the magnetic field will generate magnetic torque on the magnetic particles (Figure 1.11). Magnetic torque tends to align the axis of the object with the smallest *N* value with the magnetic field. This means that the spherical particles have no torque, and the main axis of the needle tends to be oriented along *H*.

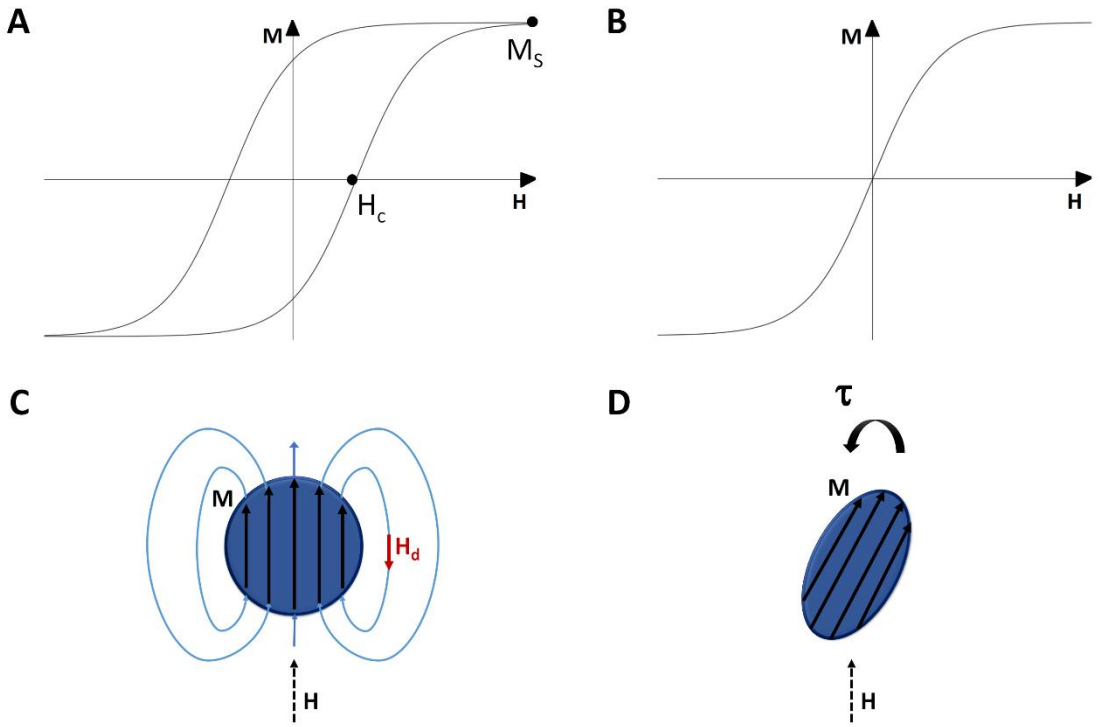

Figure 1.11 Schematic M-H curves of a) a ferromagnet and b) a superparamagnet; c) A schematic showing the demagnetization field in a spherical magnetic particle; d) A schematic showing a non-spherical magnetic particle can experience a magnetic torque even in a uniform field[124].

1.4 Research Background and Motivation

In the past few decades, synthetic polymers have been well studied. However, biopolymers such as proteins have received more attention due to their good biocompatibility, non-toxicity and controllable biodegradation[125]. Many types of natural proteins are available in large quantities, such as silks, wool keratins, and corn zeins. However, the lack of manufacturing and processing technologies still hinders the full potential of biopolymer materials - especially the application of protein materials with enhanced functional properties on an industrial scale.

Three main application barriers are as follows: (1) Pure protein materials generally do not have high thermal conductivity, strong magnetic properties or large dielectric constants. (2) Synthetic polymers do not have the same biocompatibility as natural proteins, which are more non-toxic and biodegradable. (3) It is difficult to uniformly distribute and align the nanoparticles in the synthetic polymer matrix to prepare a polymer-based composite material with enhanced functional properties. Synthetic polymer solutions generally have a higher viscosity, which is favorable to the formation of non-uniform large aggregates. Compared to synthetic polymers, natural proteins may be more promising in the biomedical field due to their good biocompatibility and non-toxicity. Natural proteins are a good substitute for polymeric materials. Studies have shown that silk protein can be easily dissolved with aqueous and acid methods. In this proposal, I will also use external physical field to fabricate biopolymer-based composites with good molecular chain alignment and optimized nanoparticle distribution. This opens the door to mass production

of biopolymer composites with enhanced physical properties and can be used for large-scale industrial production in the future.

1.5 Project Overview and Objectives

The overall objective of this dissertation is to investigate a set of protein-based composites with desired physical properties, enhanced by the appropriate distribution of designed nanofillers in the protein matrix. It is expected to achieve tunable thermal, magnetic, and dielectric properties for these biomaterials with desired mechanical properties. The mechanism of interaction between protein molecules and nanofillers will systematically examined. Due to their good biocompatibility, natural proteins, such as silk, keratin, elastin and collagen, have been manufactured into scaffolds, fibers, films, and particles, and researches have proposed to use them for drug delivery, joint replacement, bone plates, contact lenses and surgical mesh [125-129]. A composite material is a material that consists of two or more components with significantly enhanced physical or chemical properties that outperform that of the individual components. However, most of the previous and current studies have focused on manipulating the properties of pure biomaterials, which limits the maximum performance of the physical properties as well as their applications. At the same time, there are many limitations in the manufacture of synthetic polymer matrix composites such as their poor biodegradability and biocompatibility while the relatively slow progression in developing pure polymer-based biomaterial from promising research in the laboratory to practical industry manufacture technology has demonstrated the need to develop protein-based composites. Therefore, there is a reasonable expectation that novel composites with enhanced physical properties

may be achieved through study on the protein-based composites to be used for biomedical and bioelectronics applications.

This thesis aims to apply a simple method to fabricate a set of protein-based composites with enhanced physical properties, such as thermal conductivity, magnetic response, dielectric constant and thermal stability, through advanced processing to manipulate the nanofillers/particles distribution, orientation and size in the matrix. Specifically, I propose to fabricate protein-based composites with optimal distribution of nanofillers and ordered protein chain alignment with the aid of physical field (stress and/or magnetic). Study has shown that composites can achieve better properties with the addition of nanoparticles, which is attributed to the physical presence of nanoparticles and by the interaction between nanoparticles and polymer matrix [130]. However, polymer nanocomposites have not always shown expected improvement in the relevant performance. For example, the mechanical property of polymer-matrix nanocomposites is supposed to be reinforced with the addition of graphene, which has extremely high strength up to 130 GPa and Young's modulus up to 1 TPa [131]. Graphene-reinforced polymer-matrix composites have not always demonstrated better mechanical properties[132]. It has been hypothesized that this is due to the poor distribution and random alignment of graphene in the polymer-matrix. The degree of agglomeration of graphene nanosheets might negatively influence the mechanical property of the composite [131]. Efforts have also been made to improve the distribution of nanoparticles in the synthetical polymer solution. However, due to the high viscosity of synthetic polymer solution, it is very difficult to achieve expected results [133, 134]. Study has shown that both aqueous silk solution and acid silk solution has relatively low viscosity, which might be beneficial to

improve the distribution of nanoparticles in protein matrix [135, 136]. Multiple studies have also demonstrated good biocompatibility of protein biomaterials [137-139]. Therefore, I will investigate the processing methods that allow us to finely control the distribution of nanofillers in the biopolymer matrix using force field, magnetic field or electrical field. Our preliminary work and expertise in biomaterial fabrication and characterization demonstrate our ability to successfully carry out the two main objectives of this project.

Objective 1: Optimize the method to fabricate protein composite solutions with different types and contents of nanoparticles. I hypothesize that the optimized method can be fast and easy. The molecular weight and microstructure of the natural protein fibrils can be well maintained.

Objective 2: Investigate the relationship between the processing parameters and the physical properties of biopolymer-based composites such as heat transfer, magnetic, and dielectric properties.

Sub-objective 2a: I hypothesize that the applied physical field (stress and/or magnetic,) can finely control the protein chain alignment and the distribution of nanoparticles in the biopolymer matrix. I will investigate the relationship of nanoparticles distribution with the applied physical fields in one or two dimensions.

Sub-objective 2b: I hypothesize that applied physical field will result in biopolymer composites with enhanced functional properties. I will investigate the relationship of these final functional properties to the manufacturing conditions.

Chapter 2

Mechanism of Self-assembly: Silk Materials Fabricated from Formic Acid and Their Properties

2.1 Introduction

Silk fibroin (SF) is one of the most promising biomaterials studied in recent years because of the performance of its mechanical properties and also that it is environmentally friendly and biocompatible[140]. Through controlling the secondary structure of proteins, various morphologies of silk-based biomedical materials have been made, including tubes, sponges, hydrogels, fibers, and thin films[141-146]. Silk-based composite materials have also been fabricated with novel physical, chemical, and optical properties, which have been utilized in electrical and chemical fields[147-150]. However, many studies[141-143, 151] have demonstrated that the water-based regenerated SF materials in the dry state are very brittle and rigid after crystallization and thus not suitable for many applications. The traditional water-based synthesis method is also very time-consuming, and the samples made by the process are initially water-soluble, requiring further treatments such as methanol annealing, water annealing, thermal treatment, and mechanical pressing[143, 151-153] to induce insolubility through the formation of intermolecular β-sheet crystals. Therefore, a novel regeneration method to quickly induce both insolubility while retaining flexibility of SF materials is desired.

One potential option recently brought to attention is a formic acid (FA)-based fabrication method that has proven to be successful on Bombyx mori silk materials[154-161]. However, the utility of this method on the silk from other species has not been studied. In nature, Mori and Thai Bombyx silks, both produced by cultivated mulberry silkworms,

have been used as luxurious textile commodities for centuries[1, 4, 8, 125, 162]. The white Mori silk comes from China, and the yellow Thai silk is from Thailand. Other silks from wild silkworms are often mechanically stiffer than that from the domesticated species. Dark tan Tussah silk is produced by Antheraea mylitta, light tan Muga silk comes from Antheraea assamensis, and Eri silk is from Philosamia ricini[163]. In the present research, I comparatively studied these five different types of regenerated silk protein films (Mori (China), Thai, Eri, Muga, and Tussah) produced by the formic acid-calcium chloride method, with a focus on the insolubility and flexibility. The function of calcium ions in these silk materials is also discussed, which can act as plasticizers to interact with the silk structure and prevent the molecules from forming stacked β-sheet crystals.

The FA regenerated films are water-insoluble and mechanically flexible in the dry state after direct solution casting, and no further physical or chemical treatments were needed for cross-linking. Using different methods, I comparatively demonstrate that the structural and physical properties of the original silk fibers (predominantly intermolecular β-sheet crystals or silk II), water-based regenerated films (predominantly random coils or α-helix), and these FA-based regenerated films (predominantly intramolecular β-sheets or silk I) are completely different. Furthermore, the material properties, such as morphology, content of protein secondary structures, thermal and enzymatic stability, as well as mechanical properties of samples, are also investigated. A model is developed to explain the insolubility and flexibility mechanism of the regenerated films fabricated from this FA-based method, which can expand the potential applications of silk materials.

2.2 Experimental Section

2.2.1 Materials and Preparation

Silk cocoons of P. ricini (Eri), A. assamensis (Muga), and A. mylitta (Tussah) were obtained from India, while B. mori silkworm cocoons were obtained from China (denoted as Mori) and Thailand (denoted as Thai), separately. To remove the sericin coating on the silk fibers, the silkworm cocoons were first boiled in a 0.02 M $NaHCO_3$ (Sigma-Aldrich, U.S.) solution for 2 h and then rinsed thoroughly with deionized water three times. The details of the degumming procedure have been reported previously[3, 163].

After the SF fibers were obtained, two methods were used to generate silk films. One method was to gradually put the fibers into a mixture solution of formic acid (98%, MilliporeSigma) with 4 wt % calcium chloride ($CaCl_2$), and then continuously shake the solution until it dissolved at room temperature. The maximum concentration of silk samples in the FA-$CaCl_2$ solution is about 0.15 g/mL. The solution then was filtered with a syringe filter with 0.45 μm pore size (VWR International) to remove the impurities in the silk solution, after which the solution was centrifuged at 8000 rpm for 10 min to remove bubbles. Finally, the homogeneous solution was cast onto polydimethylsiloxane (PDMS) substrates at room temperature to form regenerated silk films. No gel formation was observed during the drying process. After 2 days of vacuum drying at room temperature, the formic acid was removed from the silk samples (verified by FTIR), and the regenerated silk films based on this FA-$CaCl_2$ method were produced. Films made this way are denoted by a suffix of FA. Figure 2.1 displays the appearances and shapes of five silks manufactured through the FA method at different processing stages.

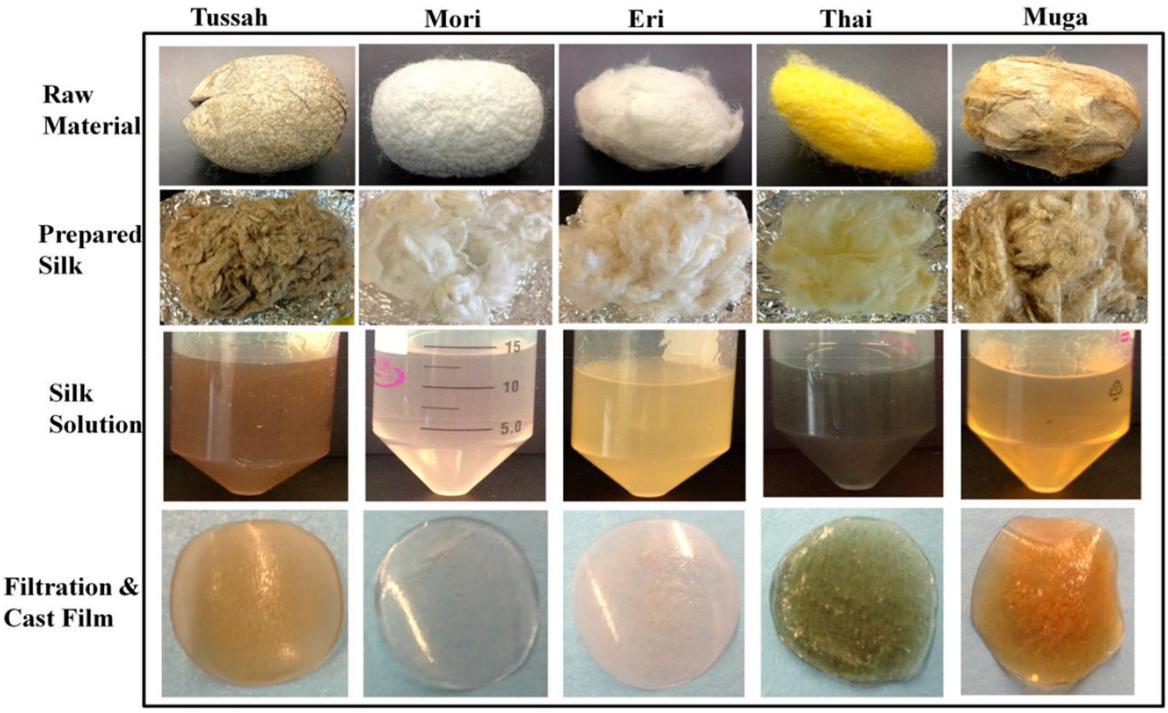

Figure 2. 1 Processing of five different silkworm cocoons (top row) into silk fibroin films by the FA method. After the glue-like sericin proteins were removed (second row), silk fibroin fibers were dissolved into solution (third row), and then filtered and cast into regenerated films (bottom row).

The second method to obtain regenerated silk films was based on the traditional water-based procedure[3]. In general, the dried fibers were dissolved in a melted $Ca(NO_3)_2 \cdot 2H_2O$ (Sigma-Aldrich, U.S.) solution at 90 °C at a concentration of 10 wt %. The silk solution then was dialyzed by dialysis cassettes (Pierce Snake Skin MWCO 3500; Thermo Fisher Scientific Waltham, MA) against pH = 8-9 Milli-Q water for at least 2 days. Centrifugation was used to further remove small insoluble residues, and then SF aqueous solution with 6 wt % silk was obtained. Finally, the silk aqueous solutions were cast onto PDMS substrates and dried in a vacuum for 2 days to form the water-based silk fibroin films. Films synthesized in this fashion are denoted by a suffix of W.

2.2.2 Fourier Transform Infrared Spectroscopy

FTIR analysis of silk samples was performed with a FTIR spectrometer (Tensor 27, Bruker, U.S.) with a deuterated triglycine sulfate detector and a multiple reflection, horizontal MIRacle ATR attachment with a Ge crystal (Pike Tech, Madison, WI). For each measurement, 128 scans were coded at a resolution of 4 cm^{-1} over the range 400–4000 cm^{-1}. Fourier self-deconvolution (FSD) of the IR spectra covering the amide I region (1595–1705 cm^{-1}) was performed with the Opus 5.0 software. Deconvolution was performed with Lorentzian line shapes with a half-width of 25 cm^{-1} and a noise reduction factor of 0.3, and the self-deconvoluted spectra were then subsequently fitted with Gaussian peaks, which were normalized by area to determine the fraction of the secondary structures in the silk films[164].

2.2.3 X-Ray

Wide-angle X-ray scattering (WAXS) was performed with a Panalytical Empyrean X-ray diffractometer. Silk fibers and films were mounted on an aluminum sample holder. The setup includes a fixed anode X-ray source for Cu Kα radiation (wavelength $\lambda = 0.154$ nm), operating at 45 kV and 40 mA. The scattering angle 2θ ranged from 5° to 40°, and data were taken in steps of 0.013° with a hold time of 30 s/step. The baseline was determined by subtracting the air background and fitted with a quadratic baseline as described previously[165]. The q vector was obtained from $q = 4\pi \times (\sin \theta)/\lambda$.

2.2.4 Scanning Electron Microscope

Surface morphology was characterized with a LEO ZEISS 1530 VP scanning electron microscope (Oberkochen, Germany). Silk film samples with a thickness of 1.0-

1.2 mm were mounted onto a standard specimen holder with conductive carbon double-sided tape with the fracture surfaces toward the electron beam. The acceleration voltage was varied between 5 and 10 kV depending on the different imaging sizes and sample characteristics. To analyze the cross-sectional area of the silks, the samples were first quickly freeze-dried with liquid nitrogen to avoid deformation. They then were fractured in liquid nitrogen with a pair of tweezers and analyzed along the new surface.

2.2.5 Differential Scanning Calorimetry

Samples with masses about 6 mg were encapsulated in Al pans and heated in a differential scanning calorimeter (Q100, TA Instruments Co. Ltd., U.S.) with dry nitrogen gas flow of 50 mL min^{-1} and equipped with a refrigerated cooling system. Aluminum and sapphire reference standards were used for calibration of the heat capacity through a three-run method described previously,[166] and the heat flow and temperature were calibrated with an indium standard. Standard mode DSC measurements were performed from −25 to 400 °C at a heating rate of 2 °C min^{-1}, while temperature-modulated differential scanning calorimetry (TM-DSC) measurements were performed at a heating rate of 2 °C min^{-1} with a modulation period of 60 s and temperature amplitude of 0.318 °C.

2.2.6 Thermal Gravimetric

Thermal gravimetric analysis (TGA) (Pyris 1, PerkinElmer Co. Ltd., U.S.) of regenerated silk-FA film samples was done with increasing temperature. Measurements were made under nitrogen atmosphere with a gas flow rate of 50 mL min^{-1} for temperatures ranging from ambient temperature to 450 °C at a heating rate of 5 °C min^{-1}.

2.2.7 Enzymatic Degradation

First, different silk films were cut into samples of mass 40 ± 5 mg. The films then were incubated at 37 °C in 40 mL of phosphate-buffered saline (PBS) solution containing 3.1 U mL^{-1} protease XIV, an enzyme used to analyze the biodegradation of the five silk samples. The buffer/enzyme solution was replaced daily so that the enzyme activity remained at a desired level throughout the entire experiment. The specimens were taken out and rinsed gently with distilled water three times and then weighed at room temperature until reaching constant mass[167]. For each type of silk film, at least seven samples were used to obtain a statistically significant result. Samples incubated in PBS solution without enzyme served as controls.

2.2.8 Mechanical Analysis

Static tensile experiments were performed with a dynamic mechanical analyzer (Diamond DMA, Perkins-Elmer Instruments Co., U.S.) apparatus under SS pattern for silk-FA films. The shape of the film samples was rectangular, with a size of 5.0 mm × 6.0 mm and a thickness of 1.0-1.2 mm. The force was loaded from 5 to 4000 mN at 50 mN min^{-1} with the temperature maintained at ambient, and stress-strain curves were thus obtained.

2.3 Results and Discussion

2.3.1 FTIR Analysis

FTIR analysis was performed to understand the structural differences of the five regenerated silk films. Figure 2.2 a-e shows the FTIR absorbance spectra of different silk-FA films. For comparison, the spectra of the original SF fibers, as well as of silk-W films,

are also shown in Figure 2.2 Generally, the IR spectral region between 1700 and 1600 cm^{-1} is assigned to the peptide backbone absorptions of the amide I (1700-1600 cm^{-1}) and amide II (1600-1500 cm^{-1}) regions[63, 98]. The amide I region mainly comes from the C═O stretching vibrations (80%) of the protein backbones[98], with minor contributions from the N–H in-plane bending, the out-of-phase C≡N stretching vibrations, and the C–C≡N deformation. Therefore, this region is the most commonly used for the quantitative analysis of protein secondary structures[163]. The amide II region is caused mainly by the out-of-phase combination of vibrations from the C–N stretching and the N–H in-plane bending. The microenvironment of protein side chain groups can easily affect this region[163].

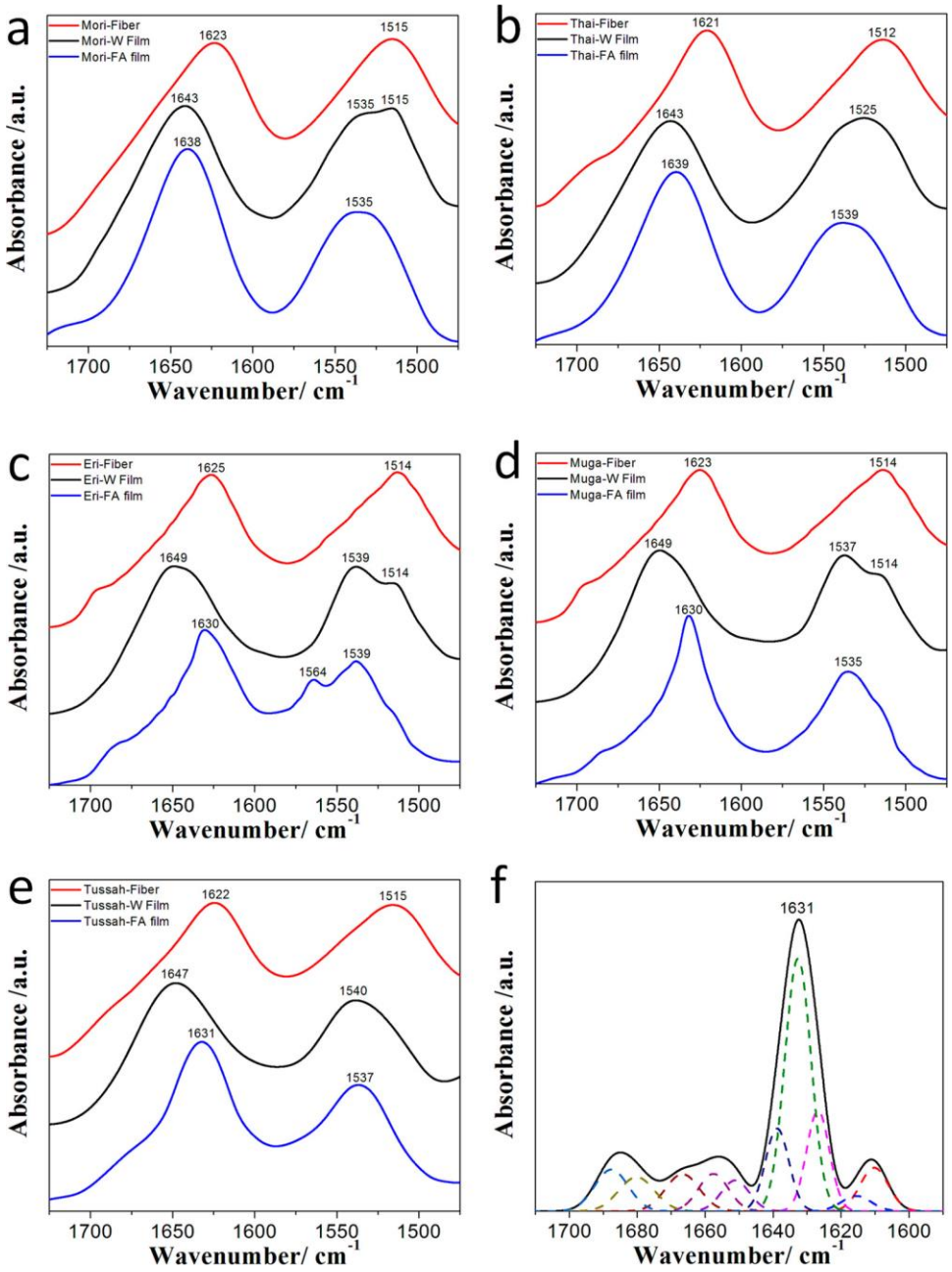

Figure 2. 2 (a-e) FTIR absorbance spectra of different silk fibroin fibers and silk films regenerated from the formic acid method (FA) and the water method (W). (f) A curve-fitting example for FSD amide I spectra of a Tussah silk-FA film (centered at 1631 cm^{-1}). The fitted peaks are shown by dashed lines.

All silk samples showed two strong peaks in the amide I and amide II regions (Figure 2.2), indicating the presence of primary protein structures. The amide I (1600–1700 cm^{-1}) region was then utilized to identify the secondary structures of silk materials. For the domestic Mori silk samples (Figure 2.2a), the peak of Mori fiber was centered at 1623 cm^{-1}, indicating mainly intermolecular β-sheet crystal structure. The peak of the Mori-FA film shifted to 1638 cm^{-1}, suggesting the presence of intramolecular β-sheet and random coil structures,[164, 168-172] while the peak of Mori-W film was centered at 1643 cm^{-1}, indicating a large portion of random coils structure formed in the sample.

Similar results were also found for the Thai silk samples (Figure 2.2b). For Thai fiber, the peak was centered at 1621 cm^{-1} (intermolecular β-sheet structure). For Thai-FA film, it shifted to 1639 cm^{-1} (intramolecular β-sheet and random coil structures), and for Thai-W film it was centered at 1643 cm^{-1} (random coil structure).

The wild silk (Eri, Muga, and Tussah) samples shared similar features. The peak of Eri fiber was centered at 1625 cm^{-1} (intermolecular β-sheet structure), the peak of Eri-FA film shifted to 1630 cm^{-1} (intramolecular β-sheet structure), and the peak of Eri-W film was centered at 1649 cm^{-1} (α-helix/random coils). For Muga fiber, the amide I peak was centered at 1623 cm^{-1} (intermolecular β-sheet structure), while that of the Muga-FA film shifted to 1630 cm^{-1} (intramolecular β-sheet structure), and the peak of Muga-W was centered at 1649 cm^{-1} (α-helix/random coil structures). Last, the peak of Tussah fiber was centered at 1622 cm^{-1} (intermolecular β-sheet crystal structure), the peak of Tussah-FA film shifted to 1631 cm^{-1} (intramolecular β-sheet structure), and the peak of Tussah-W film was centered at 1647 cm^{-1} (α-helix/random coils). The structures of these wild silks are

similar to each other where their intermolecular β-sheet content decreased during the FA-$CaCl_2$ dissolution process, while their intramolecular β-sheet content increased significantly. For all five types of silks, their peak positions in amide II region also shifted from being centered around 1512 cm^{-1} for silk fibers to higher wavenumber (centered around 1535 cm^{-1}, for silk-FA films).

Numerous studies have shown that secondary structures can significantly affect protein material properties. Schneider et al. reported that responsive hydrogels can be obtained through linking the intramolecular β-hairpin peptides[173, 174]. Chen et al. proposed that the intramolecular β-sheets formed during the nucleation stage play a key role in the formation of silk nanofibers[175]. Du et al. reported that the less stable intramolecular β-sheet crystals, rather than the highly oriented rigid intermolecular β-sheet crystals, contribute to the high extensibility of spider silk[176].

To quantify the percentage of the secondary structures in the regenerated silk samples, Fourier self-deconvolution was done for spectra in the amide I region (1595-1705 cm^{-1})[164]. Figure 2.2f shows an example of this FSD method on the amide I spectra of a Tussah silk-FA film. Table2.1 lists the percentages of secondary structures in different silk fiber and FA film samples calculated by this deconvolution method. In general, the intermolecular β-sheet content of the silks decreased from that in the fiber form to that in the regenerated FA film, while the converse is true for the intramolecular β-sheet content. For example, intermolecular β-sheets of Mori silk decreased significantly from 30.3% (fiber) to 16.9% (FA film), and the intramolecular β-sheets largely increased from 8.9% (fiber) to 20% (FA film). Domestic Thai silk showed a similar trend, where intermolecular

β-sheets decreased, and the intramolecular β-sheets increased from fiber to FA film. Meanwhile, the random coils content of Mori and Thai silk also increased more than 15% during the FA film regeneration process. For wild silk (Eri, Muga, and Tussah), likewise, the intermolecular β-sheet content was also reduced from fiber to FA film, while the intramolecular β-sheet content was greatly increased during the film formation. Interestingly, however, the relative amount of the random coil structure did not change significantly during regeneration.

Table 2.1

Percentages of secondary structures in silk protein fibers and FA regenerated films, calculated by a FTIR deconvolution method

	Intermolecular β-sheet	Intramolecular β-sheet	Random coils	α-helix	β-turn	Side Chain
Mori-FA Film	16.9	20	34.7	8.4	14.9	5
Mori Fiber	30.3	8.9	17.9	6.4	20.1	16.5
Thai-FA Film	15.1	23	33.8	7.1	17.6	3.3
Thai Fiber	30.1	9.9	16.3	5.8	17.4	20.5
Eri-FA Film	23.1	29.4	13.1	5.6	19.0	9.8
Eri Fiber	30.3	13.1	18.2	5.9	18.7	13.9
Muga-FA Film	13.4	44.3	12.7	6.4	18.9	4.4
Muga Fiber	31.4	14.8	18	5.7	22.2	8.9
Tussah-FA Film	13.6	38.9	13.7	5.4	19.5	8.9
Tussah Fiber	28	12.6	16.7	5.9	20.1	16.8

All calculated secondary structure fractions have the same unit (wt %) with a ±2 wt % error bar.

These results indicate that the structures of silk fibers, silk-FA films, and silk-W films are significantly different from each other. As for the silk fibers, they are dominated by intermolecular β-sheets crystal structures, while silk-W films are dominated by random coils structures, resulting in the water solubility of the film samples. In contrast, silk-FA films show completely different behavior: during the dissolving process, the hydrogen bonds between the intermolecular β-sheet layers of silk fibers were destroyed by the $CaCl_2$-FA solution, while the content of intramolecular β-sheet increased, indicating that more intramolecular hydrogen bonds may be formed. Meanwhile, protein chains that did not form new hydrogen bonds would transfer to random coil structures under the influence of the FA-$CaCl_2$ solvents. Therefore, the intramolecular β-sheets and random coils were connected by remaining intermolecular β-sheets or calcium ions and formed a network, resulting in the insolubility of the cast silk-FA films. A model based on these results will be further described in the Assembly Mechanism section.

2.3.2 WAXS Analysis

To further understand the results, WAXS was used to investigate the crystal structures of silk fibers and films regenerated from different methods (Figure 2.3). The predominant WAXS peak positions of silk-FA films, silk-W films, and natural silk fibroin fibers are summarized in Table 2.2. The WAXS data indicate that both domestic silk fibers (Mori and Thai) and wild silk fibers (Eri, Muga, and Tussah) have similar internal crystal structures. In Figure 2.3a, Mori fiber shows a peak at 20.3° (lattice spacing d = 0.437 nm), suggesting a typical β-sheet crystal dominated silk II structure[154, 177-179]. In Figure 2.3b, Thai fiber also shows a peak at 20.4° (d = 0.435 nm, silk II), which correlates well

with the FTIR data that silk fibers were dominated by intermolecular β-sheet crystal structures. In contrast, Mori-FA film and Thai-FA film both show a broad peak centered at 24.3° (d = 0.365 nm) and 24.8° (d = 0.358 nm), respectively, which is typically correlated with the silk I structure[179].

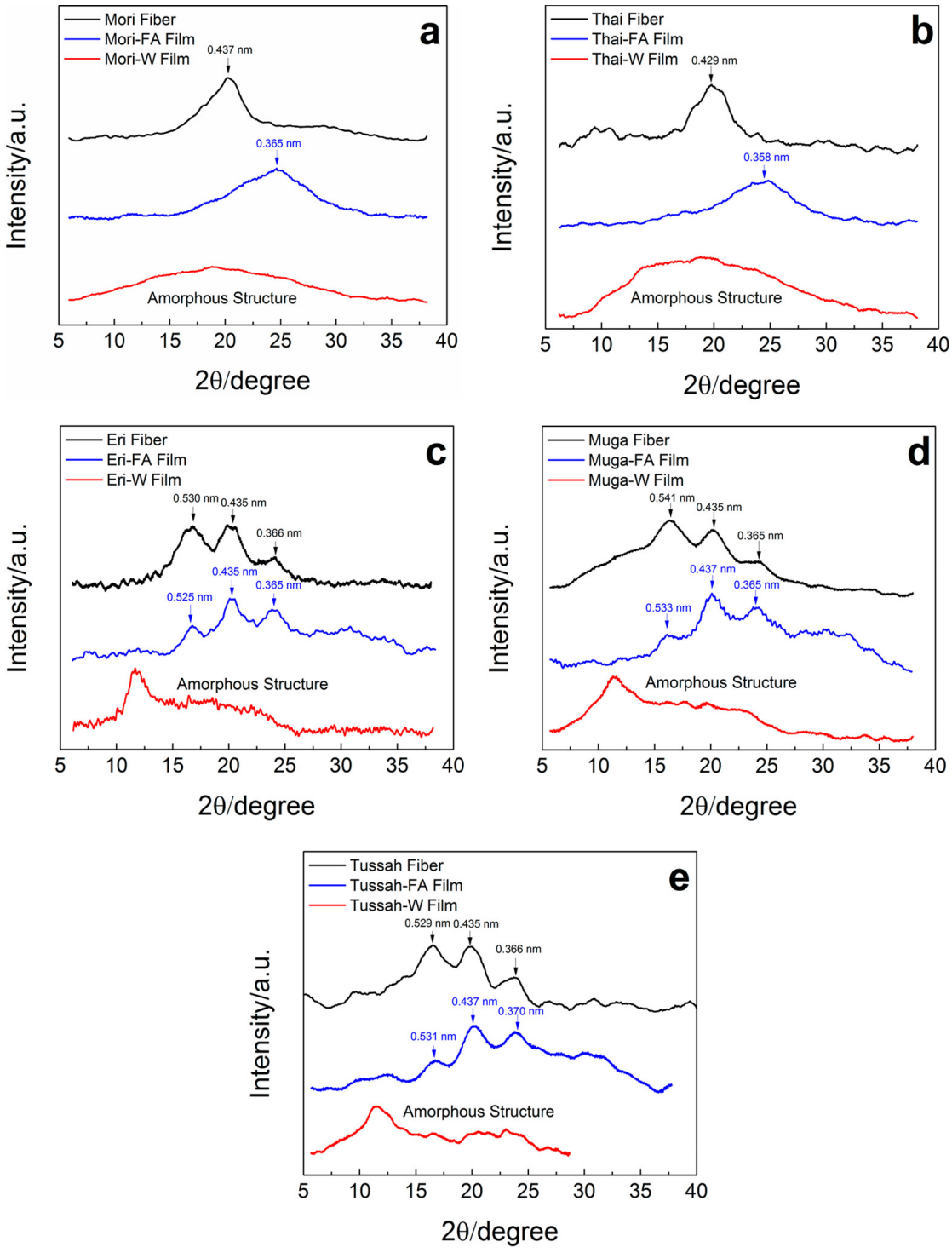

Figure 2. 3 Wide-angle X-ray diffraction patterns of silk fibers, silk-FA films, and silk-W films: (a) Mori silk, (b) Thai silk, (c) Eri silk, (d) Muga silk, and (e) Tussah silk.

Table 2.2

WAXS peak positions of silk-FA films, silk-W films and native fibroin fibers (wavelength λ = 0.154 nm) [180-187].

Sample	**Major peak position / 2θ**
Mori Fiber	20.3° (Silk II)
Mori-FA Film	24.3° (Silk I)
Mori-W Film	Amorphous halo
Thai Fiber	20.4° (Silk II),
Thai-FA Film	24.8° (Silk I)
Thai-W Film	Amorphous halo
Eri Fiber	16.6° (Silk II), 20.4° (Silk II), 24.3° (Silk I)
Eri-FA Film	16.6° (Silk II), 20.4° (Silk II), 24.0° (Silk I)
Eri -W Film	11.7° (α-helix), Amorphous halo
Muga Fiber	16.4° (Silk II), 20.4° (Silk II), 24.4° (Silk I)
Muga-FA Film	16.9° (Silk II), 20.3° (Silk II), 24.0° (Silk I)
Muga-W Film	11.7° (α-helix), Amorphous halo
Tussah Fiber	16.7° (Silk II), 20.4° (Silk II) and 24.3° (Silk I)
Tussah-FA Film	16.8° (Silk II), 20.4° (Silk II), 24.0° (Silk I)
Tussah-W Film	11.7° (α-helix), Amorphous halo

The silk I structure is the precursor structure of silk II crystals, found in silkworm glands just before the fiber spinning[188]. Previously, several studies have reported the fabrication of silk I materials, which can provide significantly improved flexibility to the samples[143, 154, 189]. According to the FTIR results, it is suggested that Mori and Thai films manufactured by the FA method are dominated by intramolecular β-sheets. Because intramolecular β-sheet structure may be an intermediate stage from ordered α-helix structure to stacked compact intermolecular β-sheet crystal structures[188], the WAXS data indicate that Mori and Thai FA films are in a late-stage silk I or early-stage silk II

structure, where most of the α-helix structures have transformed to the denser intramolecular β-sheet structures but are still not close enough to form β-sheet crystals. The high content of intramolecular β-sheets in FA films resulted in better flexibility, similar to that of the ordered α-helix structures.

As compared to the Mori-FA and Thai-FA films, Mori-W and Thai-W films both demonstrated apparent broad amorphous halo peaks centered around 16–20°, indicating that random coil structures dominate in the water regenerated films. The amorphous structure also accounts for the solubility of the silk-W films[190].

The three types of wild silk fibers show similar results. For the fiber samples, Eri fiber has three peaks at 16.6° (d = 0.530 nm, silk II), 20.4° (d = 0.435 nm, silk II), and 24.3° (d = 0.366 nm, silk I)[191-193]. Muga fiber also has three peaks at 16.4° (d = 0.541 nm, silk II), 20.4° (d = 0.435 nm, silk II), and 24.4° (d = 0.365 nm, silk I)[191-193]. For Tussah fiber, the three peaks are centered at 16.7° (d = 0.529 nm, silk II), 20.4° (d = 0.435 nm, silk II), and 24.3° (d = 0.366 nm, silk I)[191, 192]. It confirms that these three types of wild silk fibers have more ordered structures than the two domestic silk fibers, as suggested previously[166]. Those three types of wild silk fiber possess better mechanical properties than the domesticated ones likely due to their higher content of intermolecular and intramolecular β-sheets (Table2.1).

For the regenerated Eri-FA, Muga-FA, and Tussah-FA films, there were also three prominent X-ray peaks. However, their relative intensities and positions are different from those of their respective fibers. For Eri-FA film, the three peaks are centered at 16.6° (d = 0.533 nm, silk II), 20.4° (d = 0.435 nm, silk II), and 24.0° (d = 0.370 nm, silk I)[191-193].

As compared to the Eri fiber, the relative intensity of the silk II peak centered at 16.8° decreased significantly, while that of the silk I peak centered at 24.3° (Eri fiber) increased and slightly shifted slightly, indicating the formation of additional silk I structure[191-193]. Because it has been confirmed by FTIR that the content of intermolecular β-sheets drops while the amount of intramolecular β-sheets increases during this FA-based regeneration process, it is believed that $CaCl_2$-FA system first destroyed the hydrogen bonds within the intermolecular β-sheet crystals in silk fibers, and then the released silk chains self-assembled through intramolecular hydrogen bonds forming intramolecular β-sheets. The mechanism of assembly in Eri-silk films is the same as that in the domestic silk-FA films, that is, the formation of late-stage silk I or early-stage silk II structures.

There are similar results for the Muga-FA and Tussah-FA films. WAXS shows three peaks, which are located at 16.9° (d = 0.531 nm, silk II), 20.3° (d = 0.437 nm, silk II), and 24.0° (d = 0.370 nm, silk I) for the Muga-FA film, and likewise three peaks located at 16.8° (d = 0.531 nm, silk II), 20.4° (d = 0.435 nm, silk II), and 24.0° (d = 0.370 nm, silk I) for the Tussah-FA film. In contrast, all three types of wild silk-W films show similar amorphous and α-helix (2θ = 11.7°) peaks[193].

2.3.3 SEM Analysis

The cross-sectional morphologies of five different silk-FA films, silk-W films, and their native fibroin fibers were obtained by SEM (Figure 2.4). Alignment of the nanofibril structures can be seen clearly on the 2 μm and 200 nm scales for all silk-FA films[194]. Also, the nanofibril structures vary in length and shape (rod, “S”, circular, etc.) for different silk-FA films. For the Mori silk-FA films, the cross-section appears uniform on the 10 μm

scale, apart from random nanofibril structures. On the 2 μm scale, the areas become rougher, but no significant structural components can be identified from this scale. On the 200 nm scale, globular structures appeared, which are typical morphological components of Mori silk molecular aggregates found in previous studies[163]. On the 10 μm scale, the cross-section area of Thai silk-FA film appears smooth with patches of roughness, which becomes more prevalent at the 2 μm scale. On the 200 nm scale, the silk structure is clearly seen as globular shaped, similar to that of Mori silk-FA film. The Tussah silk-FA film shown on the 10 and 2 μm scales is random in shape but appears to be more aligned than the randomly dispersed Thai silk-FA in the 200 nm scale. For the Muga silk-FA sample, at the 10 μm scale, the cross-section appears solid with scattered cracks. Pellets appear scattered as well. Upon a 2 μm scale examination, the cross-section is composed of numerous globular structures. These globules appear in size and shape similar to smaller pellets present between globules. At the 200 nm scale, globule sizes are less similar, and smaller particles are more visible. As for the Eri silk-FA sample, the cross-section is flaky in appearance in the 10 μm scale, and there are obvious layers in the structure. Shown on the 2 μm scale, the flaky appearance is less sharp and defined. At the 200 nm scale, globular components are prevalent, and the laminar structure can no longer be seen. As compared to silk-FA films, the nanostructure features of silk-W films and silk fibroin fibers at 200 nm (Figure 2.4) are not obvious except for the Tussah and Muga fibers.

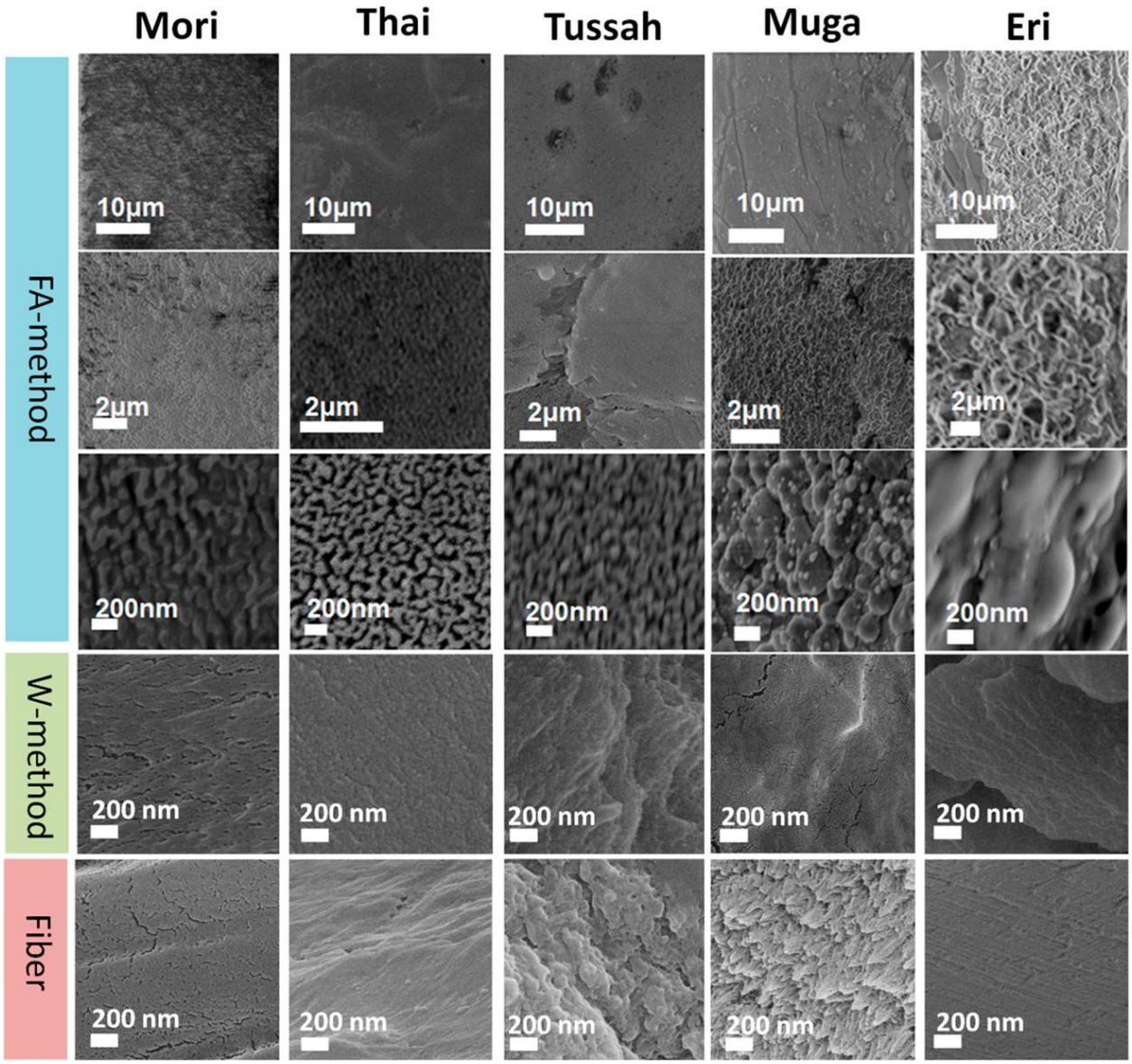

Figure 2. 4 SEM images of different types of silk-FA films, silk-W films, and native fibroin fibers at cross-section area.

2.3.4 DSC Analysis

Figure 2.5a shows the standard DSC scans of various silk-FA film samples. During heating scans, all samples first showed a low-boiling bound solvent evaporation peak T_{d1}[166] around 60–100 °C (333–373 K). Table 2.3 shows that the trend of the temperature of this peak is Mori-FA < Thai-FA < Eri-FA < Muga-FA < Tussah-FA, where the T_{d1} of Tussah-FA film was the highest temperature found in all silk samples. Similar to the silk-W films reported previously[163], the T_{d1} values of the three wild silk samples were higher than those of the two domesticated ones, indicating that wild silks are better at maintaining bound molecules in their structures. For the wild (Muga, Eri, and Tussah) silkworms, this silk structure could be more favorable for their surviving in the wild environment. However, the T_{d1} values of all silk-FA samples were generally lower than those of silk-W films. This implied that the FA-$CaCl_2$ solution may have affected their water inhibition or reservation ability during the dissolving process.

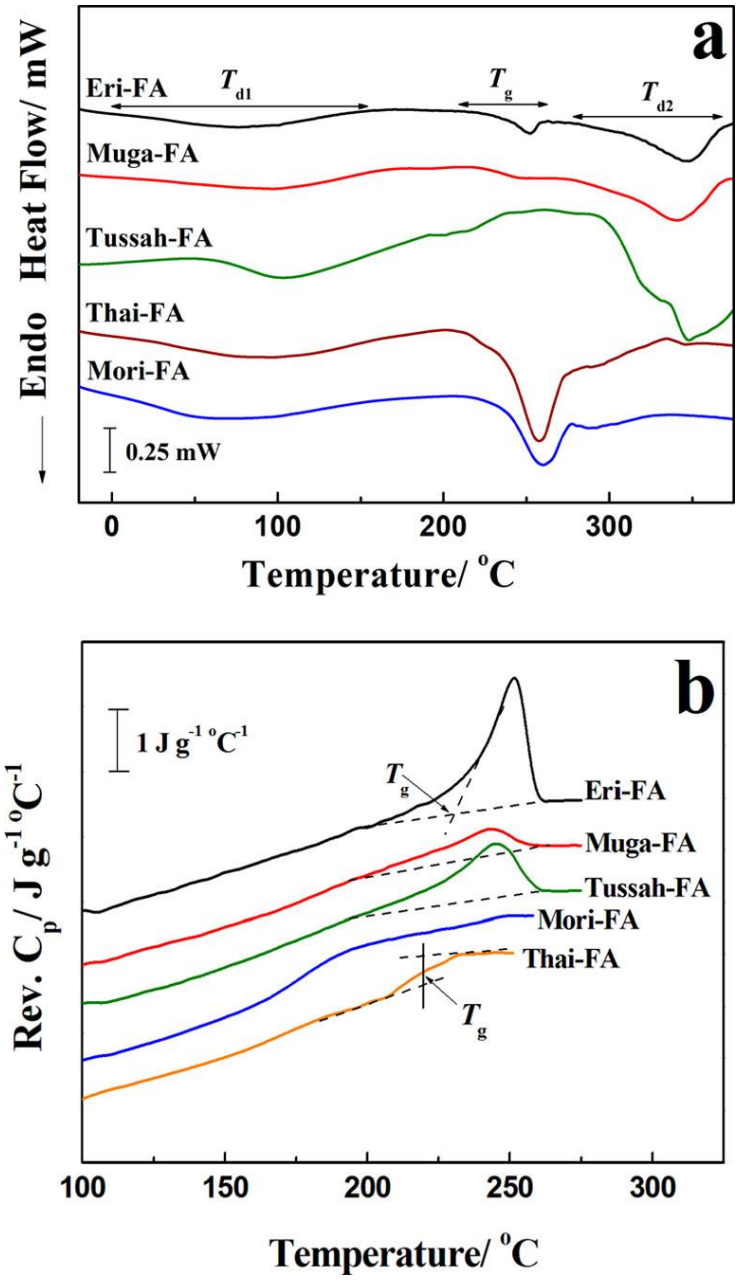

Figure 2. 5 (a) Standard DSC scans of five silk films (Tussah-FA, Mori-FA, Eri-FA, Thai-FA, and Muga-FA) prepared by the FA method, with temperature regions related to bound solvent evaporations (T_{d1}), glass transitions (T_g), and sample degradations (T_{d2}). (b) The reversing heat capacities of the five silk film samples prepared by the FA method, measured by TMDSC from 100 to 275 °C (glass transition region), with a 2 °C min^{-1} heating rate, a modulation period of 60 s, and a temperature amplitude of 0.318 °C.

Table 2.3

Thermal analysis data of different silk protein films produced by the FA method

Silk Sample	T_g (°C)	ΔC_p at T_g (J g^{-1} K^{-1})	Solvent release T_{d1} (°C)	Degradation T_{d2} (°C)	Onset temperature of decomposition (°C)	Solvent Content (%)	Degradation Middle Temperature T_{dm} (°C)	Remaining mass at 400 °C (%)
Eri	238.8^F /176.0 ^{W}	0.041^F/0.509^W	84.5^F/ 119.0^W	346.2^F/ 329.0^W	327.0	6.84^F	372.7	47.42
Muga	232.4^F /168.0 ^{W}	0.135^F/0.370 ^{W}	95.3^F/ 120.3^W	341.8^F/ 330.3^W	384.8	5.99^F	396.6	49.24
Tussah	233.9^F /188.0 ^{W}	0.019^F/0.282 ^{W}	103.2^F/ 131.6^W	348.2^F/ 336.6^W	319.1	6.43^F	375.3	49.26
Thai	217.8^F /149.0 ^{W}	0.388^F/0.564 ^{W}	78.2^F/ 96.2^W	258.1^F/ 245.4^W	306.0	12.33^F	328.3	54.06
Mori	176.3^F /175.0 ^{W}	0.483^F/0.475 ^{W}	74.5^F/ 112.7^W	260.3^F/ 244.3^W	300.3	10.09^F	313.8	26.32

All numbers have an error bar within ±5%. The first four columns (T_g, ΔC_p at T_g, T_{d1}, and degradation T_d) were determined by DSC and TMDSC analysis, while the rest were determined by TG analysis (silk-FA films only). T_g, T_{d1}, and T_{d2} represent the glass transition temperature, bound solvent release peak temperature, and degradation peak temperatures of different silk-FA films, where the superscript "F" indicates results from the samples manufactured by the formic acid-$CaCl_2$ method and "W" represents samples manufactured by the water-based method[163].

For temperatures above the T_{d1} region, the glass transition temperature T_g and the degradation temperature T_{d2} region of various silk films can be seen in Figure 2.5a. Near T_g regions, all silk-FA films showed clear heat capacity increases ΔC_p as found in their TMDSC curves (Figure 2.5b), which are used to investigate the reversible thermal properties of silk film materials. All samples showed clear heat capacity increases ΔC_p in

their T_g regions. Interestingly, for wild silk films synthesized by the FA method, there was an endothermal peak occurring with the ΔC_p step change in the T_g region, while domesticated silk films (Mori and Thai) only show a simple ΔC_p step occurring in the T_g region. The endothermal peak found in the wild silk T_g region may be associated with the physical relaxation process of wild silk molecular chains during the heating progress[195]. Thus, the midpoint temperature of this transition for domesticated silk films (Thai, Mori) was chosen as T_g, while the onset temperature was used for the T_g values of wild silk samples (Muga, Tussah, and Eri) in this study[196, 197]. Table 2.3 lists the T_g of various silk samples and their ΔC_p values during the glass transition. For silk films manufactured by the FA method, it showed a T_g trend of Mori < Thai < Muga < Tussah < Eri. It should be noted that the T_g values of the domestic silks are lower than those of the wild ones.

In contrast, the heat capacity increments ΔC_p at T_g of Mori and Thai films are higher than those of wild silk samples, with a ΔC_p trend of Tussah < Eri < Muga < Thai < Mori. For the Mori film sample, the ΔC_p increment at T_g was 0.483 J kg^{-1} $°C^{-1}$, which is close to our previous result obtained from the Mori-W films[163]. The Thai-FA film showed a similar ΔC_p increment (0.388 J kg^{-1} $°C^{-1}$) at T_g because it also belongs to the domestic silkworm species. The ΔC_p of Tussah sample was 0.019 J kg^{-1} $°C^{-1}$, which was the lowest among all silk samples. The ΔC_p is directly proportional to the average chain mobility of proteins, reflecting the number of freely rotating bonds capable of changing the chain conformation. In addition, T_g values of all silk-FA samples are higher than those of silk-W films (Table 2.3),[163] while their ΔC_p values are lower[163]. These results again prove that the FA method could make the protein chains arrange in a more ordered structure such as intramolecular β-sheet structure as compared to the silk-W samples.

Above T_g, all samples start to thermally degrade (Figure 2.5a)[197]. Table 2.3 lists the T_{d2} values of all silk-FA films, with an order of Thai < Mori < Muga < Eri < Tussah. It is clearly shown that the T_{d2} values of domestic silk-FA films (282.2 and 284.7 °C, respectively) were significantly lower than those of wild silk-FA films (Figure 2.5a), indicating that wild silk protein films are more thermally stable than domesticated silk protein films, which is consistent with our previous conclusions[163].

2.3.5 Thermal Stability

Figure 2.6a shows the mass percentage change of Thai, Mori, Eri, Tussah, and Muga silk-FA films during a heating scan from room temperature to 450 °C, while Figure 2.6b shows the temperature derivative of their respective mass percentage curves. The bound solvent/water content (T_w), onset temperature of decomposition (T_d), middle degradation temperatures (T_{dm}), and the remaining mass at 400 °C of different silk-FA films are summarized in Table 2.3.

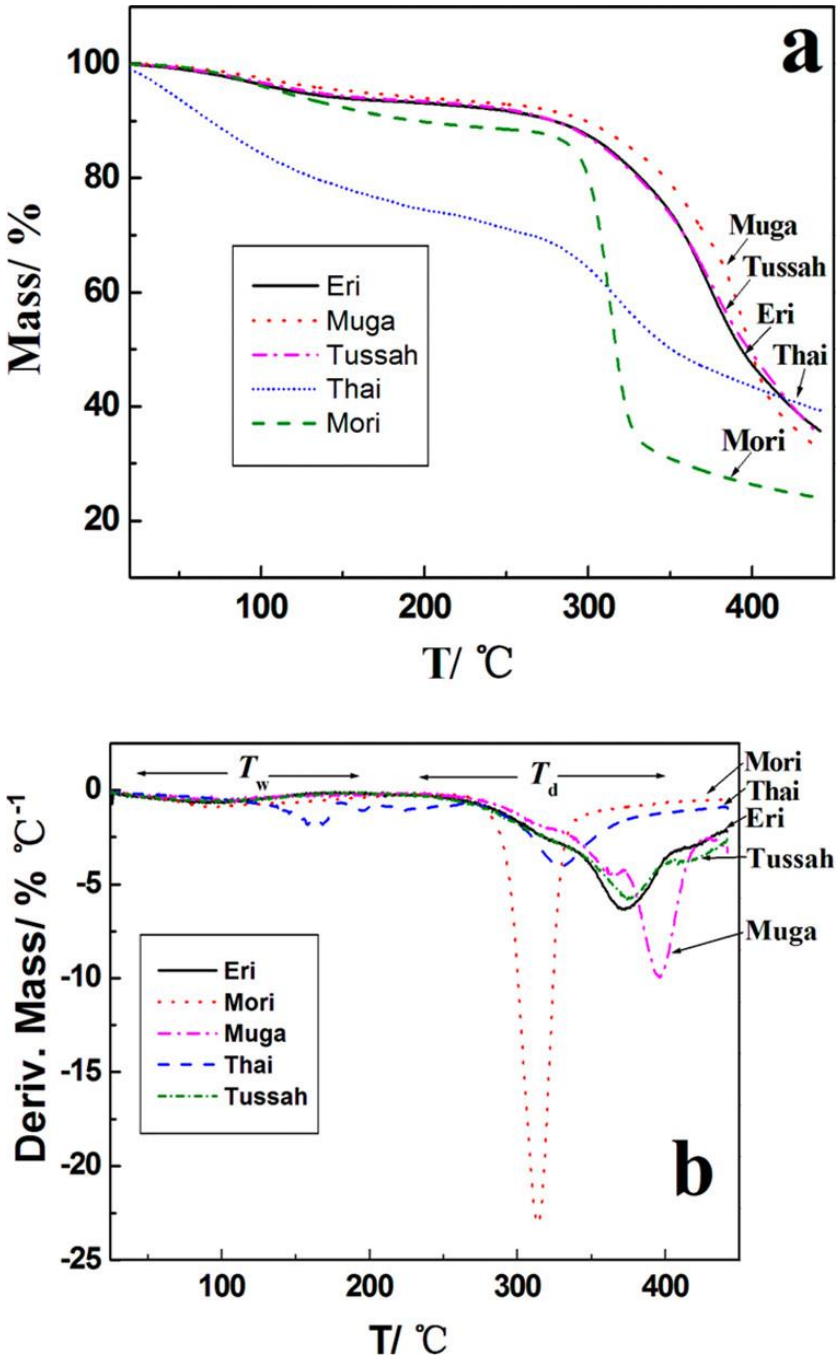

Figure 2. 6 (a) Percent mass remaining of different FA-based silk fibroin film samples measured by thermogravimetric analysis during heating from room temperature to 450 °C at 5 °C min^{-1}. (b) The first derivative of the percent mass remaining in (a), which reveals the degradation rates of silk films and demonstrates temperature regions related to bound solvent/water evaporations (T_w) and the sample degradations (T_d).

During the initial heating from room temperature to 150 °C, bound solvent/water molecules were first removed from all silk-FA samples, as demonstrated in the DSC study (T_{d1}). Table 2.3 lists the solvent content (%) of various silk-FA films measured by TGA. It shows that all samples contained bound solvent/water around 5.9-12.4%, with a trend of Muga < Tussah < Eri < Mori < Thai, with domesticated silk films showing larger values than those of the wild silks. Dehydration of bound solvent/water in domestic silks is much easier than it is in the wild silks, as was seen in the DSC study. The dehydration step in the TGA curve (Figure 2.6a) corresponds to a small peak in the differential thermogravimetric curve (Figure 2.6b), while the initial decomposition of the silk proteins started around 300 °C (Figure 2.6a). Figure 2.6b also shows that some wild silk samples (Muga and Eri) had a very quick mass loss during their major degradation stages, while the T_{dm} values of the two domesticated silks were lower than those of all wild silks, with a T_{dm} trend of Mori < Thai < Eri < Tussah < Muga (Table 2.3). The trend of middle degradation temperatures confirmed that wild silk-FA films are more robust than the domesticated films, as suggested by the DSC study. The remaining mass (%) of all samples at 400 °C was also listed in Table 2.3. For the Mori silk samples, the remaining mass was 26.32% at 400 °C, which is the lowest content among all film samples, suggesting that the thermal stability of Mori film in high temperature regions is weaker than that of others. The Eri, Tussah, and Muga silks showed very similar decomposition curves with about 50% of the mass lost by 400 °C.

Previously, I have investigated the thermal properties of all silk-W samples by DSC[163]. As compared to those of the silk-W samples, the solvent release temperature and the thermal degradation temperature of silk-FA samples were much higher, especially

for the wild silk types. This implies that the FA method increases the thermal stability of silk materials, perhaps through enhancing intramolecular β-sheet content in the structure.

2.3.6 Enzymatic Degradation

Enzymatic degradation of silk-FA films was studied in vitro. Figure 2.7 shows the weight losses of five silk-FA films in PBS solutions (Figure 2.7a) and protease XIV enzyme solutions (Figure 2.7b). For comparison, Figure 2.7c also shows the weight losses of five silk-W films in the protease XIV enzyme solutions (precrystallized by 30 min pure methanol treatment). During the first 5 h, the degradation rate appeared to be quicker, with a trend of Tussah < Thai < Eri < Muga < Mori, due to the degradation of nanocrystalline components in the films. As compared to other silk samples, the Thai silk sample continue to degrade quickly up to 20 h (similar to its TGA thermal degradation trend at low temperature region in Figure 2.6a), whereas the degradation rate of other silk samples tended to significantly slow after 5 h. The Tussah sample degraded only ~10% after 20 h of protease XIV enzymatic treatment. After 30 h, the degradation of silk films reached a quasi-equilibrium state, suggesting that β-sheet structures (intra- and intermolecular) can prohibit the enzymatic degradation of silk materials very well[143, 167, 190, 198, 199]. Their degradation profiles followed a clear trend of Tussah < Eri < Muga < Mori < Thai. It also demonstrated that the wild silk samples were more stable in the protease as compared to the domestic silk samples, probably due to the larger amount of β-sheet structures in the wild silk-FA samples as seen from FTIR.

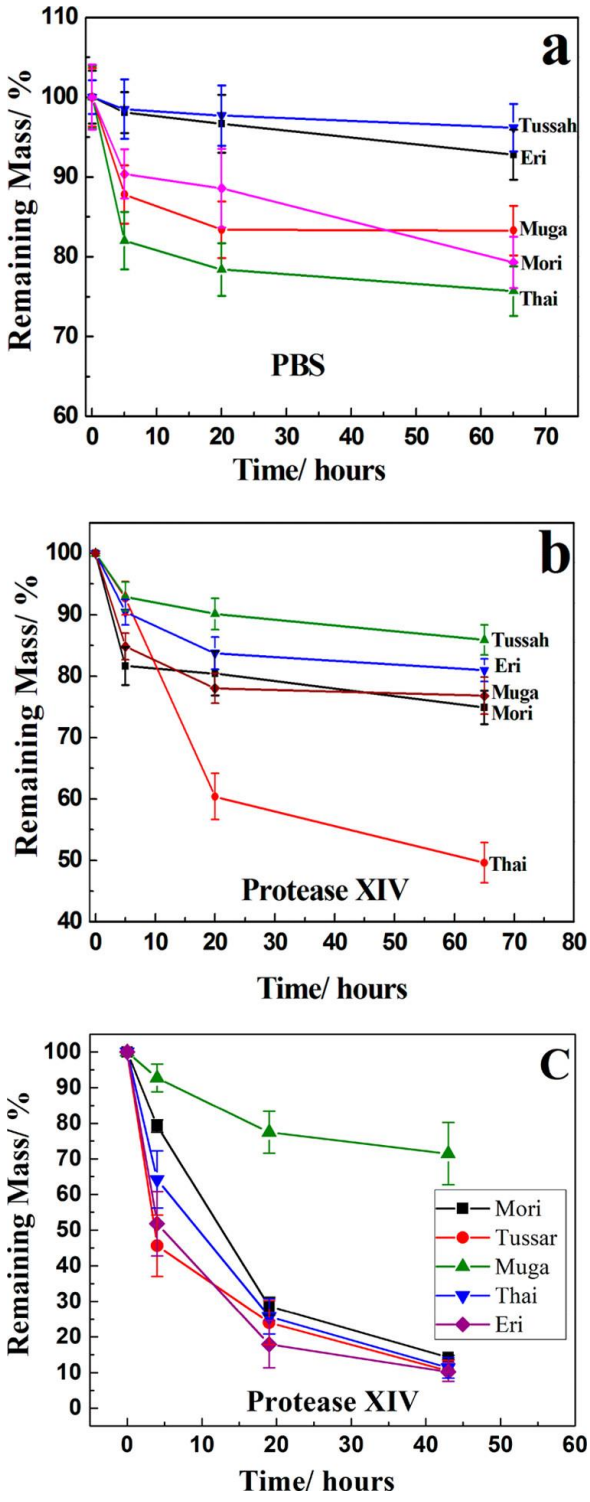

Figure 2. 7 (a) PBS solution degradation and (b) protease XIV enzymatic degradation study of silk-FA films, and (c) protease XIV enzymatic degradation of silk-W films precrystallized by methanol.

However, for the pure methanol cross-linked silk-W films (Figure 2.7c), after 45 h, the degradation of Thai, Mori, Tussah, and Eri was significant with only about 10–15% of the original mass left. The MeOH cross-linked Muga-W was an exception, showing the lowest degradation rate (85% mass remaining) in all silk samples. In general, it is shown that the enzymatic degradation rate of methanol cross-linked silk-W films is much quicker than that of silk-FA samples. Because it has been widely proved that methanol can induce ~50% β-sheet structures (intra- and intermolecular β-sheets in total) in the regenerated water-based silk materials[143, 189, 200], which is similar to the silk-FA samples, this result also indicates that not only the amount of β-sheet structures contributes to the stability of silk materials in enzymes, but also the size, pattern, or distribution of β-sheet structures in silk materials could be critical to help the protein molecules against enzyme digestions for a long time.

2.3.7 Mechanical Properties

Figure 2.8 shows the stress–strain curves of different silk-FA films, and Table 2.4 lists their elastic modulus, strength of extension, and elongation ratio calculated from the strain–stress curves. For the five silk-FA films, the trend of elastic modulus is Eri > Tussah > Muga > Mori > Thai, and their strength of extension trend is Muga > Mori > Tussah > Eri > Thai, while the elongation ratio trend is Mori > Muga > Thai > Tussah > Eri. It shows that the Eri sample has the largest modulus and a high tensile strength but the lowest elongation. The Mori sample was soft and tough, with a lower modulus and the highest elongation, while the Thai film sample had a low strength of extension, although it had the lowest modulus among them. Both Muga and Tussah silk films fabricated from the FA method

have relatively high strengths of extension and elongation ratios. As compared to data on crystallized insoluble water-based silk films[97, 201], the silk FA films are softer with higher elastic modulus and larger elongation ratio, which can be used for large deformation of materials in the future.

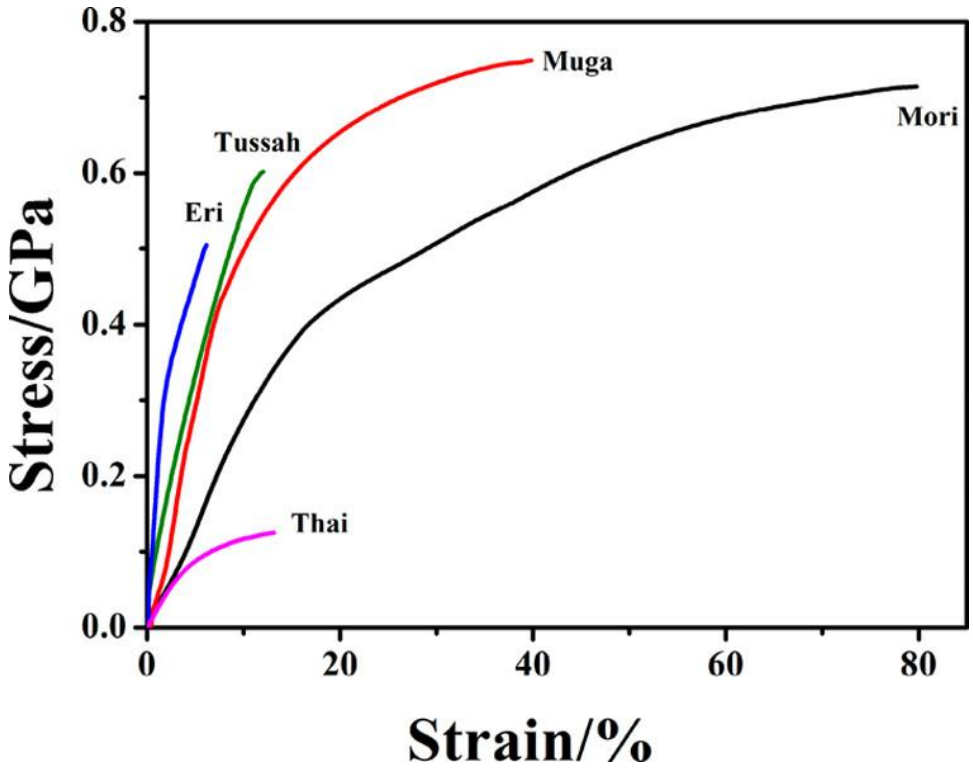

Figure 2. 8 Stress–strain curves of different silk-FA samples (Tussah-FA, Muga-FA, Eri-FA, Mori-FA, and Thai-FA) measured by the static tensile test using DMA.

Table 2.4

Mechanical properties of silk-FA films by DMA (Sample size n = 5)

Sample	Elastic Modulus (GPa)	Strength of extension (×GPa)	Elongation (%)
Tussah	5.797 ± 0.406	0.602 ± 0.042	12.12 ± 0.82
Muga	5.658 ± 0.458	0.749 ± 0.060	39.83 ± 2.79
Eri	18.712 ± 1.16	0.502 ± 0.031	6.11 ± 0.35
Mori	2.573 ± 0.129	0.716 ± 0.034	79.72 ± 3.83
Thai	2.236 ± 0.094	0.125 ± 0.005	13.11 ± 0.60

2.3.8 Assembly Mechanism

To elucidate the mechanism of assembly and water insolubility of silk-FA films, a schematic model is proposed in Figure 2.9. As shown in Figure 2.9, silk-W films regenerated from silk fibers (Figure 2.9a) are random coils dominated with only a little amount of α-helix and intramolecular β-sheets (Figure 2.9c)[163]. It has been well-studied that these noncrystalline amorphous structures resulted in the water solubility of silk-W films (Figure 2.9c)[143, 190]. Two methods are generally used to induce insolubility of the silk-W films: (i) an annealing or preaggregation procedure (low temperature water annealing[143, 189], a repeated concentrating–dissolving procedure in solution[202], self-assembly in silkworm glands[203, 204], etc.) can cause the noncrystalline structure to transfer to an early stage of silk I structure, with a high content of α-helix and intramolecular β-sheet[143, 190]; (ii) the use of organic solvents (MeOH, EtOH, etc.), salts,

mechanical pressing, or thermal treatments can make the silk noncrystalline structure transform back into the silk II structure (Figure 2.9a) with a large amount of intermolecular β-sheet crystals[189, 203-205].

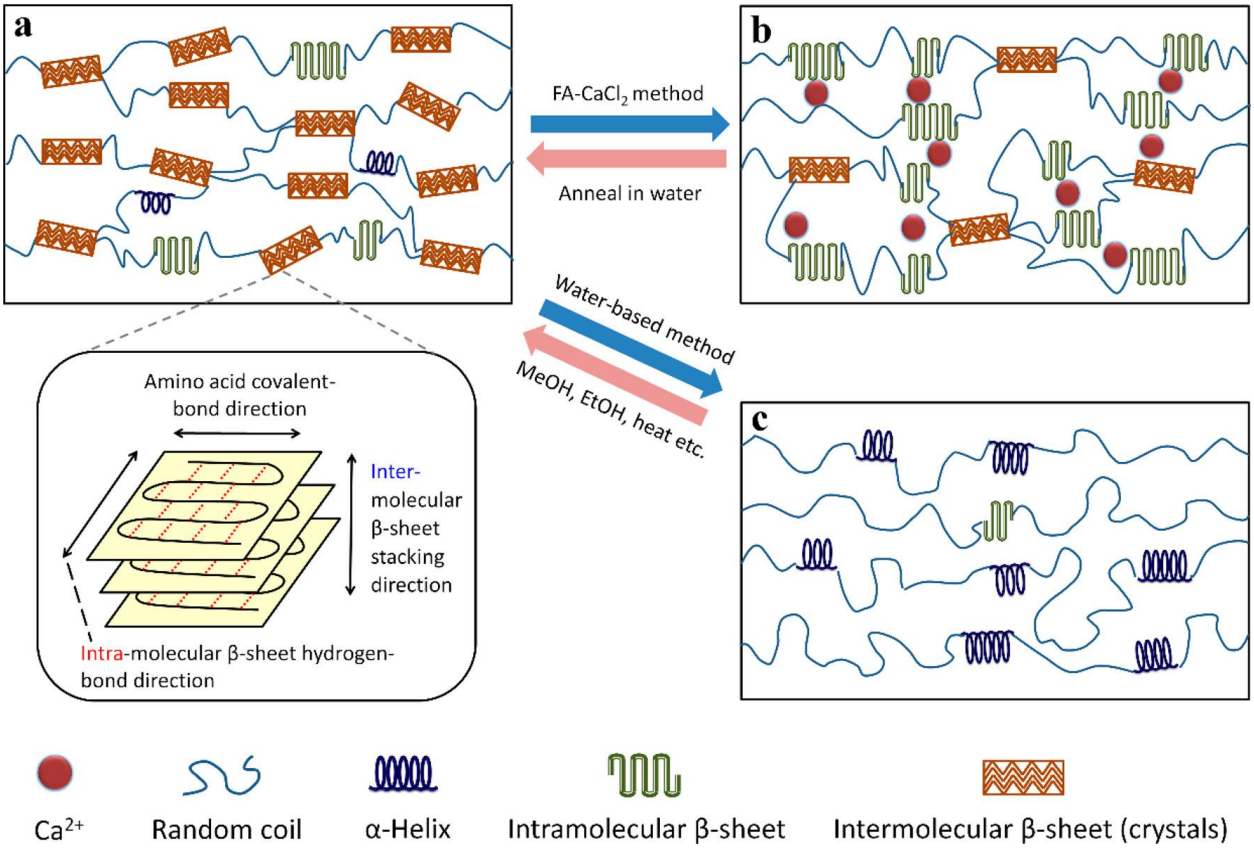

Figure 2. 9 Structure models of silk fibers and films: (a) large amount of intermolecular β-sheets (crystals) and less amount of intramolecular are connected by random coils, silk II structure, forming the stable property of silk fibers; (b) large amount of intramolecular β-sheets and less amount of intermolecular β-sheets are connected by random coils forming a stable network, causing the insolubility of silk-FA films; and (c) a little amount of α-helix and tiny amount of intramolecular β-sheets are connected by the random coils, forming the amorphous structure of silk-W films.

On the basis of our previous results, it is believed that the $CaCl_2$-FA solvent system can directly disrupt the intermolecular cohesive force within the intermolecular β-sheet crystals in the SF fibers. Formic acid and $CaCl_2$ molecules functioned as plasticizers in this system, and the stacked intermolecular multilayer β-sheet crystals (silk II) within the highly crystallized natural silk fibers were quickly exfoliated into single layer intramolecular β-sheets or even random coils. Thus, the silk fibers were totally dissolved into the $CaCl_2$-FA system forming a homogeneous fibroin solution. During the drying process, with the evaporation of the formic acid, the fibroin fibers assembled together into nanofibrils with dominated intramolecular β-sheet structures (Figure 2.9b). The function of calcium ions (Ca^{2+}) in silk materials has been studied previously[154, 205]. Furthermore, it has been demonstrated that Ca^{2+} ions can strongly interact with the silk structure in solution and prevent the molecules from forming intermolecular β-sheet crystals (Figure 2.9b)[154, 205]. Therefore, with the help of calcium ions as plasticizers, the cast silk-FA films show a structure dominated with intramolecular β-sheets instead of a large amount of intermolecular β-sheet crystals. Our results suggest that the intramolecular β-sheets not only provide additional flexibility to the system (as compared to intermolecular β-sheet crystals), but also result in the water insolubility of the silk-FA films. Because this structure is very close to the silk I structure found in WAXS patterns, I believe it is a late-stage silk I structure or the silk II precursor structure in the silk materials. In fact, upon long-time annealing in aqueous solution, the structure does transfer to silk II β-sheet crystal structure in the films.

2.4 Conclusion

This study presents a mechanism study on the structure and insolubility of the silk materials from five different species regenerated from a formic acid-$CaCl_2$ method. It reveals that the secondary structures of silk-FA films are different from those of their natural silk fibroin fibers, which are typically dominated by stacked intermolecular β-sheet crystals. In addition, the intramolecular β-sheet content of the silk-FA films is much higher than that regenerated from the traditional water-based method, causing silk-FA films to become insoluble in water. These results show that the intermolecular hydrogen bonds within β-sheets crystals in the silk fibers can be quickly disrupted during the dissolving process and allow a film network structure dominated by intramolecular β-sheets to form. From these observations, a model was proposed to explain the mechanism of assembly for the silk-FA films. This comparative study offers important insight into how to manipulate the secondary structures of silk-based biomaterials to tune its properties.

Chapter 3

Thermal Conductive Biofilms from Silk/AlN-Particle Composites

3.1 Introduction

Since the development of integrated circuit technology, the electronic device dimensions have continued to shrink while the power density is gradually increasing. Consequently, there has been increased effort to develop renewable or biocompatible materials with high thermal conductivity to serve as substrates to mitigate heating.[206-211] The ideal material should have good thermal conductivity, but it must also be electrically insulating and possess a low coefficient of thermal expansion. Because of their strong bonding, novel 1D and 2D materials such as BN, carbon nanotube and graphene, show promising applications in thermal management.[208, 212-214] The thermal conductivity of the single-layer graphene at room temperature can reach 1800 W/m·K[215, 216] while the thermal conductivity of multi-walled nanotubes can be as high as 3000 W/m·K.[217] However, the electrical conductivity of these carbon phases limits their use as thermal management materials for electronic devices. [206, 212, 218]

Aluminum nitride is an electrical insulator with high thermal conductivity (320 $Wm^{-1}K^{-1}$) but also has a low dielectric constant, a very wide bandgap of about 6.2 eV, a low thermal expansion coefficient (4.4 ppm K^{-1}) and stable chemical properties.[219-221] However, unlike polymers, ceramic AlN does not have enough strength or flexibility for practical applications. On the other hand, the properties of silk include high tensile strength, elasticity, toughness, environmental friendliness, biocompatibility and insolubility (in most solvents),[222] which make it attractive to applications over a range of fields, from dietary

applications to biomedical devices. Many of its properties can be attributed to the fact that silk is a protein polymer, yet most polymers typically have a thermal conductivity of about 0.1 $Wm^{-1}K^{-1}$,[216, 223-225] rendering them impractical for thermal management.

One alternative is the synthesis of composite materials which can display the salient properties of its component materials. The properties of composites can be modulated by the size, distribution, and orientation of particles within a matrix, often a polymer. In insulators, heat is transported by phonons, and studies have shown that the filler content and the interface between the filler and the matrix are the main factors affecting the thermal conductivity in composites with interfacial scattering of phonons often dominating the thermal resistance.[223, 226]

Silk fibroin (SF) has a large number of hydroxyl groups on the protein chains, and these hydroxyl groups can form stable hydrogen bonds with the N atoms of the AlN. This may reduce the direct thermal resistance of the interface between SF and AlN particles.[227-229] In addition, the SF chain consists of both negatively (aspartic acid and glutamic acid) and positively (arginine and lysine) charged amino acid groups which may also reduce the interfacial phonon scattering.[230] At the same time, the secondary structure of the silk material can be more easily modified to achieve desired mechanical and structural properties than many polymer materials,[222] which makes it advantageous to serve as a matrix.

Here I report on the structural and physical properties of SF and AlN composites. This composite material has the advantages of its constituent materials: excellent mechanical properties, biocompatibility and green environmental properties of SF protein,

as well as the excellent high-temperature thermal stability, improved thermal conductivity and fire resistance of AlN. Based on the thermal and structural analysis, AlN particles are able to form continuous networks that confine the crystalline and amorphous parts of silk proteins, which contribute to the good thermal stability and high thermal conductivity of AlN/SF films. Due to these advantages, SF and AlN composites have sizable potential for applications in high performance microelectronic devices and implantable biomedical electronic devices.

3.2 Experimental Section

3.2.1 Synthesis

Bombyx mori mulberry (Mori) silks were purchased from Treenway Silks (Colorado, USA). Silkworm cocoons were first boiled in a 0.02 M NaHCO3 (Sigma-Aldrich, USA) solution for 30 mins and then rinsed thoroughly with deionized water three times to completely remove sericin. The degummed silks were dried overnight in a fume hood and further dried in vacuum at room temperature for 1 day to remove the remaining moisture. The obtained pure SF fibers were dissolved in a formic acid solution with 4wt.% $CaCl_2$ at room temperature. The density of dry state SF films and AlN (Sigma-Aldrich, USA) were measured to be 1.4 and 3.26 g/cm^3, respectively. AlN was added into the SF solution at different ratios so that the resulting composites had a volume fraction of AlN of up to 25%. Henceforth, samples are designated as x% AlN/SF where x represents the percent volume fraction of AlN. The mixture solution was shaken by a vortex mixer for 10 minutes and then slowly cast onto polydimethylsiloxane (PDMS) substrates to form films. After drying in a hood for 2 days, the AlN/SF films were annealed in deionized water

for 1 hour to remove formic acid and $CaCl_2$ residues, and promote the hydrogen bond formation of silk fibroin and AlN particles. The water-annealed samples were left in a 30 °C vacuum oven to dry for 2 days before the tests.

3.2.2 Characterization

Fourier transform infrared (FTIR) spectroscopy (Bruker Tensor 27, USA) was used to characterize the secondary structures of SF within the composite material.[231] The spectrometer was equipped with a deuterated triglycine sulfate detector and a multiple-reflection horizontal MIRacle ATR attachment (Ge crystal) from Pike Tech (Madison, WI). The instrument was continuously purged with N_2 gas to eliminate the spectral contributions of atmospheric water vapor. For each measurement, 128 scans were co-added with a resolution of 4 cm^{-1}. Wide-angle X-ray scattering (WAXS) was performed with a Panalytical Empyrean X-ray diffractometer. The setup included a fixed anode X-ray source for Cu Kα radiation (wavelength λ = 0.154 nm), operating at 45 kV and 40 mA. The scattering angle 2θ ranged from 5° to 70°, and data were taken in steps of 0.013º with a hold time of 30 s/step. Measurements were taken as a function of the film orientation with the sample plane being rotated from 0° to 90° with respect to the incident beam (see Fig. 4.5d). X-ray diffraction (XRD) was also done with the same instrument in Bragg-Bretano geometry with similar operating parameters. The cross-section morphology of the AlN/SF films was characterized with a LEO ZEISS 1530 VP scanning electron microscope (Oberkochen, Germany). The acceleration voltage was varied between 5 and 20 kV depending on the magnification. The elemental distribution of AlN was characterized by energy dispersive X-ray spectroscopy (EDS, Oxford Instruments).

Differential scanning calorimetry (DSC) was performed with a Q100 calorimeter (TA Instruments) equipped with a refrigerated cooling system. The N_2 flow rate was set to 50ml/min, and measurements started at -30 °C and ended at 400 °C. The temperature increased at a rate of 2 °C/min and was modulated every 60 seconds at an amplitude of 0.318 °C to measure the reversing heat capacity. The decomposition behavior was analyzed by thermogravimetric analysis (TGA) on a TA Instruments SDT Q600 at a heating rate of 10 °C min^{-1} from 25 to 800 °C under 100 ml/min N_2 air flow. Linear thermal expansion was measured by a Q400 (TA Instruments) thermal mechanical analyzer (TMA) from 25 to 120 °C at a scan rate 10 °C/min. The sample was pre-loaded with 50 mN of force. The infrared thermal images were taken with a Seek Reveal thermal imaging camera (California, USA). The in-plane thermal conductivity was measured with a Physical Property Measurement System (Quantum Design, USA) with the thermal transport option (TTO) under steady-state conditions. Leads were attached with silver epoxy to a film sample with an area of 5 × 20 mm, and measurements were taken at vacuum below 9×10^{-5} Torr. The dielectric constant and loss were measured with an Agilent 4285A Precision LCR Meter (Agilent, USA).

Parallel flame testing was performed on pure SF and 25% AlN/SF films. The size of the sample was 20 mm in length and 6 mm in width. A propane torch was used, and the samples were heated by flame until completely burned.

3.3 Results and Discussion

3.3.1 Morphology and Structure

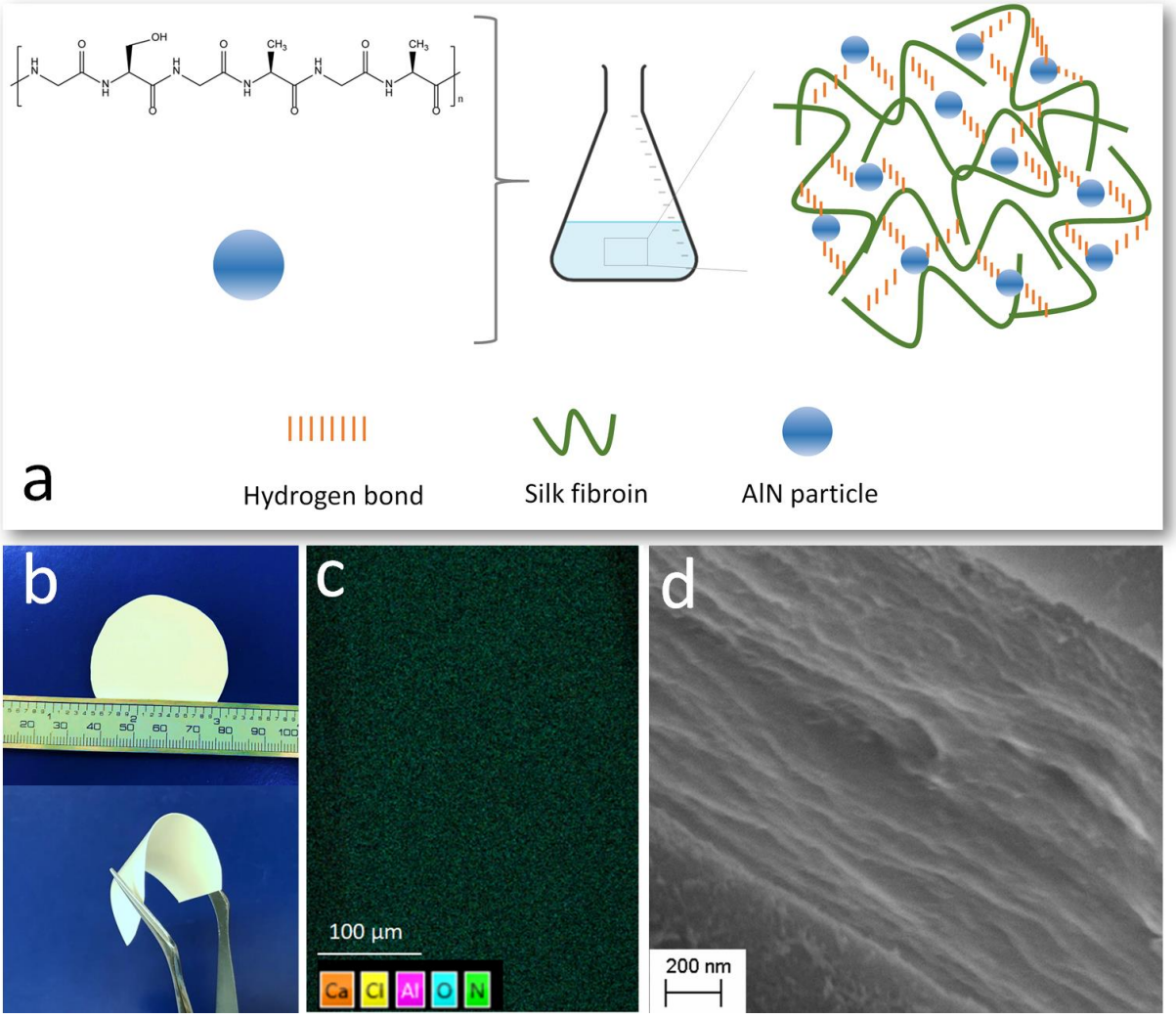

Figure 3.1 (a) Schematic of preparation of AlN/SF solution, and the interaction between AlN particles and silk fibroin chains. (b) Photos of flexible 15% AlN/SF film. (c) Ca, Cl, Al, O and N EDS mapping of pure SF film shows the only measurable signal was from O and N. (d) Scanning electron micrograph of the cross section of the 2% AlN/SF sample.

Silk fibroin solutions were prepared according to our previously reported method.[232] Fig. 3.1b shows the 15% AlN/SF film, which is uniform in thickness and very flexible and shows no signs of mechanical fatigue even after being bent 90° over 50 times. The excellent mechanical properties is attributed to the strong hydrogen bonding interaction and electrostatic interaction between AlN and SF chains[233] (Fig. 3.1a, 1b). EDS was used to check the spatial distribution of various elements in the composites. It shows that there is no $CaCl_2$ left in any of the samples after water annealing (Fig. 3.1c and Fig. 3.2). In addition, the AlN is nearly homogeneous after annealing although there is some indication the particles are interconnected (Fig. 3.1c and Fig. 3.2).

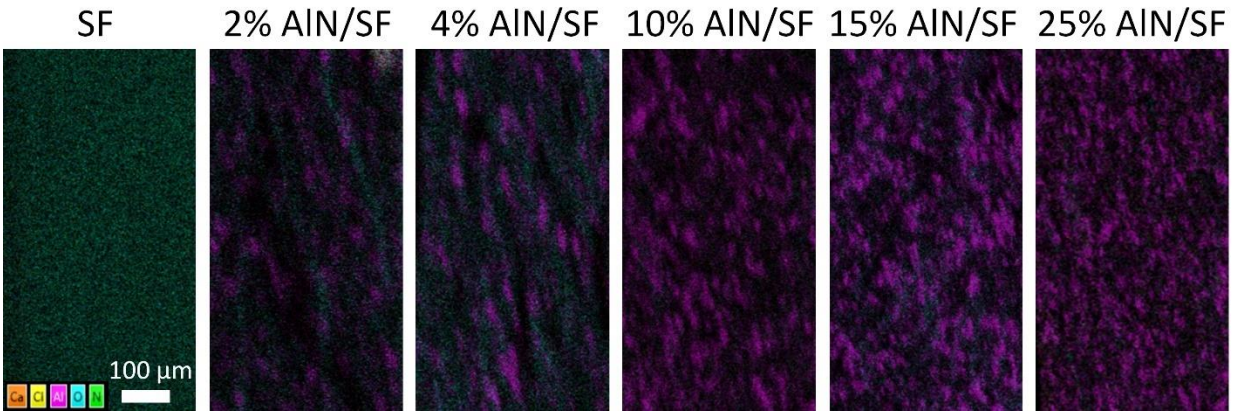

Figure 3.2 EDS element mapping of the cross section of AlN/SF films. All examples with non-zero AlN show some evidence of networking since one notes that the size of the inclusions is only 1 µm.

SEM was used to study the internal structure and morphology of the matrix. It was found layer-by-layer structures in all of the samples, which was induced by water annealing processing and silk-AlN molecular interactions (Fig. 3.1d and Fig. 3.4).[234-237] As the

concentration of AlN increased, more AlN particles were found in the cross section of the sample (Fig. 3.3a and 3.3b) and they formed larger networks (Fig. 3.3e-f).

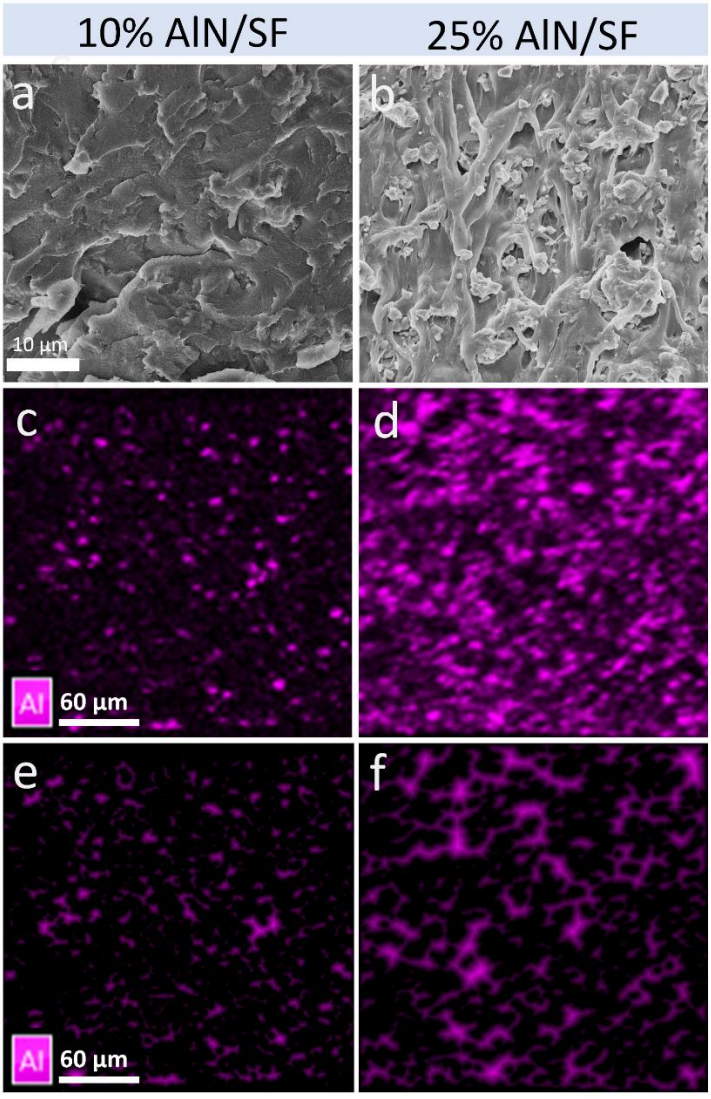

Figure 3.3 Cross-sectional SEM images of (a) 10% AlN/SF, (b) 25% AlN/SF. EDS Al element mapping in (c) 10% AlN/SF, and (d) 25% AlN/SF. (e) and (f) show the morphological distance maps of the Al composition for 10% AlN/SF and 25% AlN/SF, respectively.

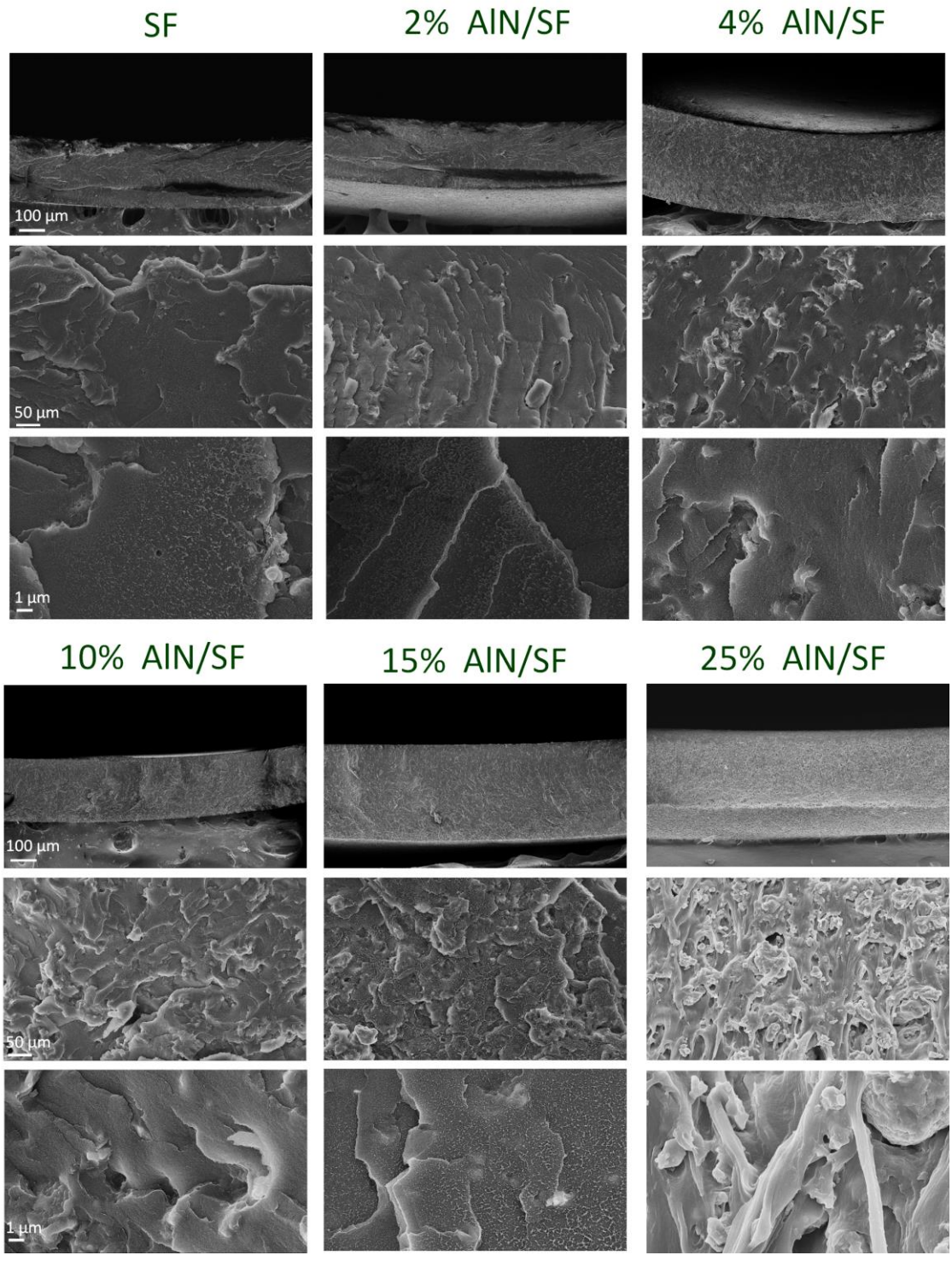

Figure 3.4 Cross-sectional SEM images AlN/SF films.

Previous studies have shown that water annealing can induce the crystallization of SF materials,[238] so the orientation of β-sheet crystals and AlN particles was studied by WAXS. Those results demonstrate that both β-sheet and AlN crystallites are randomly oriented (Fig. 3.5a & 5b, Fig. 3.6) which suggests that the layered structure observed in SEM did not affect the crystal orientation and distribution in the material. The main x-ray diffraction peaks for AlN are consistent with literature (Joint Committee for Powder Diffraction Standards (JCPDS) card No. 25-1133),[239] with 2θ values of 33.2°, 35.9°, 37.9°, 49.8°, 59.3°, and 65.9° assigned to the (010), (002), (011), (012), (110), and (013) reflections, respectively (Fig. 3.5c). Pure SF (Fig. 3.5c) showed a broad peak centered at 20.6° (silk II structure, β-sheet crystals) with a shoulder at 24.5° (silk I structure).[240-243] As the concentration of AlN increased, the intensity of those two peaks gradually weakened.

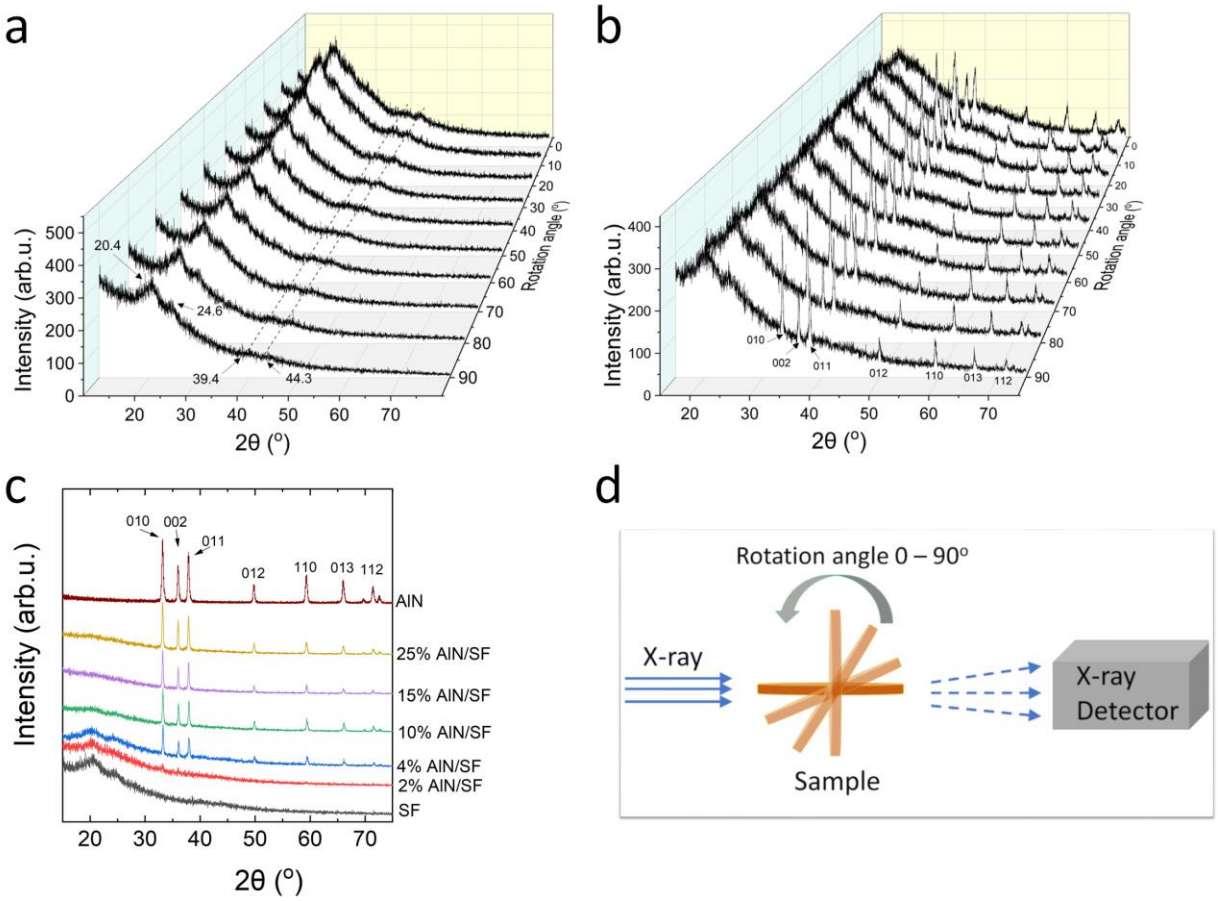

Figure 3.5 WAXS patterns of (a) SF and (b) 4% AlN/SF films at different orientations. (c) The XRD patterns of the SF, AlN/SF and AlN samples. (d) Scattering geometry.

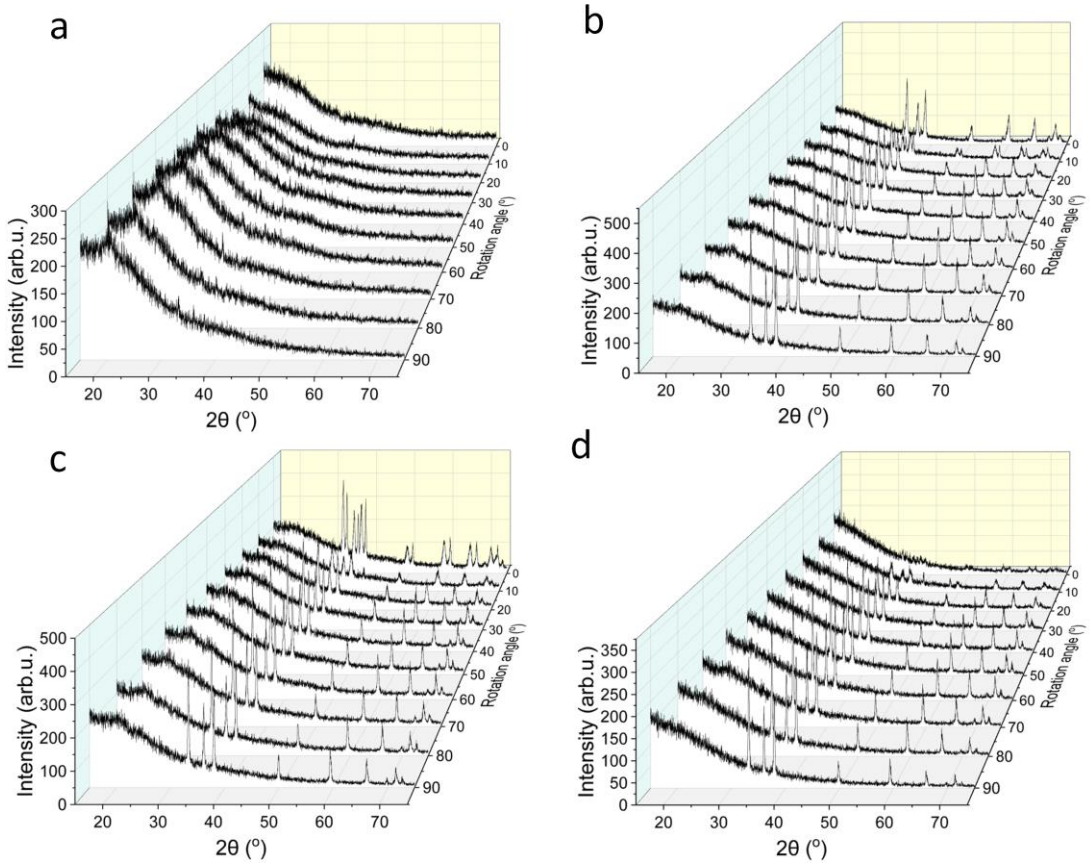

Figure 3.6 WAXS patterns of (a) 2% AlN/SF, (b) 10% AlN/SF, (c) 15% AlN/SF and (d) 25% AlN/SF films at different orientations.

FTIR was used to study the secondary structure of silk fibroin (Fig. 3.7a). Whereas the spectrum of pure AlN was featureless above 900 cm^{-1}, that of pure SF (Fig. 3.7a) displayed a peak at 3250 cm^{-1} caused by the O-H stretching vibration[231, 243] in addition to multiple peaks from 900 to 1700 cm^{-1}. The amide I region of silk fibroin proteins corresponds to 1610-1700 cm^{-1} (inset Fig. 3.7a),[244] and pure SF spectrum had a pronounced peak at 1619 cm^{-1}, indicating a high β-sheet crystalline content after the water annealing. It needs to be noted that the spectra of the SF and silk-AlN films exhibited a predominately random coil structure prior to the water annealing procedure, with a

pronounced peak at 1639 cm^{-1} (inset Fig. 3.8a). Through water annealing, the characteristic peaks of AlN (from 500 to 900 cm^{-1}) also shifted slightly and changed in intensity (Fig. 3.7a and 3.8a). Therefore, water annealing may not only promote the formation of strong hydrogen bonds between silk protein molecules, but also enhance the formation of hydrogen bonds between silk and AlN molecules.

Fourier self-deconvolution (FSD) method is an effective tool to calculate the secondary structure content in SF,[231, 240] and a curve fitting example for FSD amide I spectra of the SF sample is shown in Fig. 3.8b. Results show that pure SF (after water annealing) contains 38% β-sheet crystals and 20% random coil structure. As the AlN content increased, the shoulder at 1649 cm^{-1} grew, and the peak at 1619 cm^{-1} gradually shifted to a higher value at 1625 cm^{-1} (Fig. 3.7a, inserted figure), indicating that the addition of AlN particles inhibited the formation of β-sheet crystals (probably through forming more hydrogen bonds with the protein chains) and promoted the random silk structure (Fig. 3.7b), the latter of which helps maintain the flexibility of the composite.[231, 244]

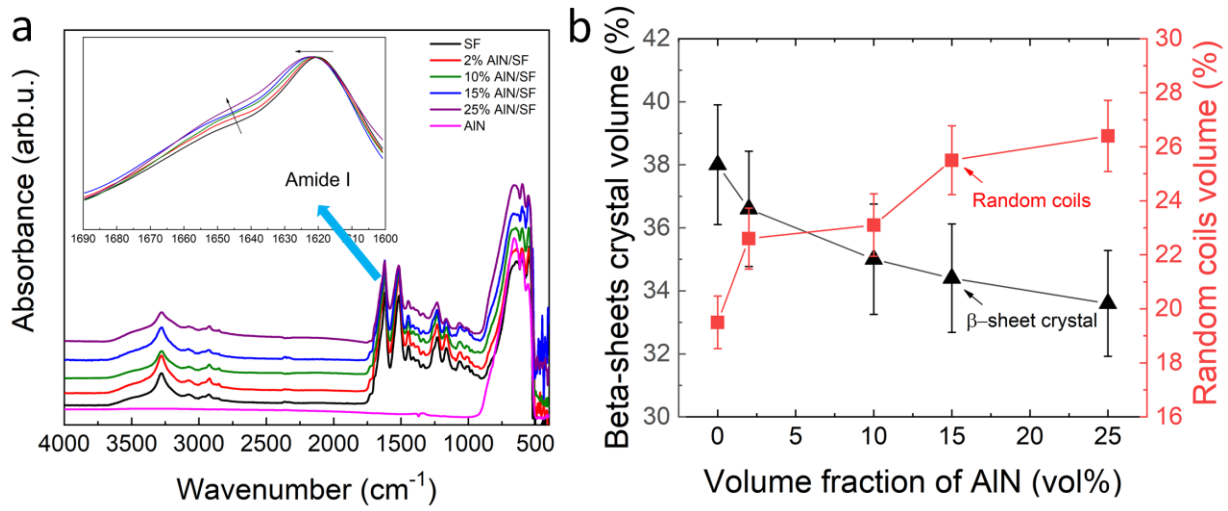

Figure 3.7 (a) FTIR curves of water-annealed SF, AlN/SF films and AlN, the inset picture is the zoom in image of amide I region of silk fibroin. (b) Volume fraction of β-sheet crystals and random coils of the silk fibroin component.

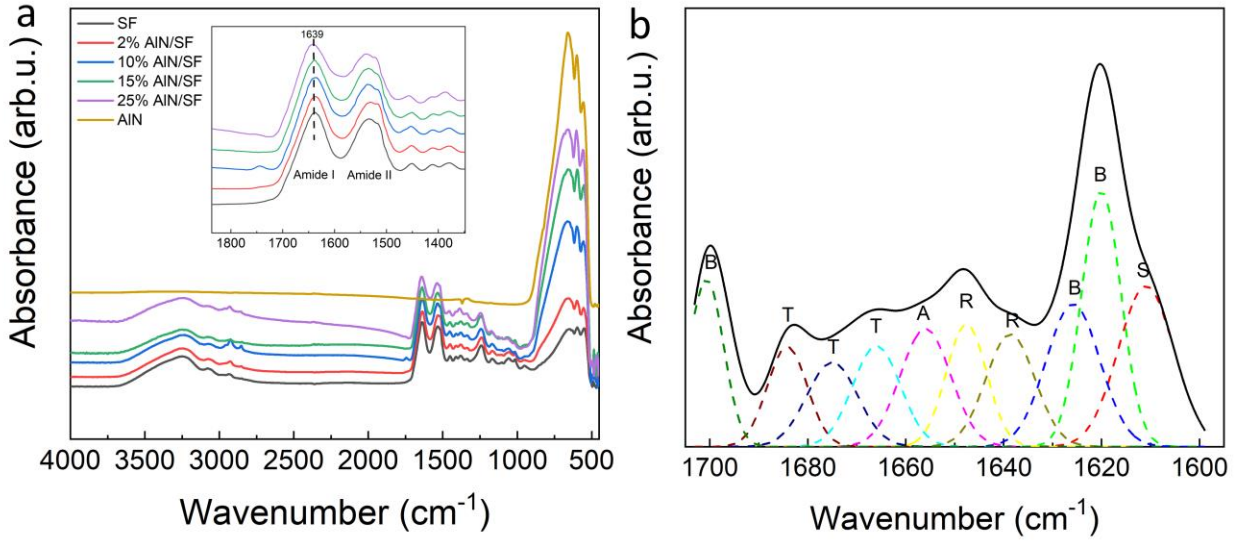

Figure 3.8 (a) FTIR curves of SF, AlN/SF films and AlN before the water annealing procedure, the inset picture is a zoom in image of amide I and II regions of silk fibroin. (b) A curve fitting example for FSD amide I spectra of the F sample. The fitted peaks are shown by dashed lines in different colors. B is β-sheet crystal, T is β-turns, A is α-helix, R is random coil, and S is side chain [231].

3.3.2 Physical Properties

To model the elongation at break, I assume that a is the average distance between the centers of AlN spherical inclusions of radius r in the SF matrix. For a hexagonal close packed arrangement,

$$f = \frac{8\pi r^3}{3\sqrt{2}a^3} \tag{3.1}$$

The average separation between particle surfaces is therefore a - 2r, and the relative separation between spheres we define as

$$\gamma = \frac{(a-2r)}{a} = 1 - 2\sqrt[3]{\frac{3\sqrt{2}f}{8\pi}} \tag{3.2}$$

If we assume that the composite fails when the average shortest length of SF fails, (i.e. when the distance between the surfaces of adjoining particles exceeds the elongation at break of the matrix) then the elongation at break of the composite A is given by

$$A = \gamma A_{SF} \tag{3.3}$$

where A_{SF} is the elongation at break of the SF matrix alone. Fig.3.9a shows the elongation decreased with the AlN content and the experimental data fits well with the modelling data.

Fig.3.9a shows the stress-strain curves of the composite; Young's modulus steadily increased with the AlN content (Fig. 3.9b). Berryman[245-247] has developed a self-consistent model of the effective bulk (K_{eff}) and shear (μ_{eff}) moduli of composites based

upon the geometric means of the Hashin-Shtrikman bounds[248, 249]: i.e. $K_{\text{eff}} = \sqrt{K_{HS}^{+}K_{HS}^{-}}$, $\mu_{\text{eff}} = \sqrt{\mu_{HS}^{+}\mu_{HS}^{-}}$ where

$$K_{HS}^{\pm} = K_m + \frac{f}{(K_i - K_m)^{-1} + (1-f)(K_m + \frac{4}{3}\mu_m)^{-1}} \tag{3.4}$$

and

$$\mu_{HS}^{\pm} = \mu_m + \frac{f}{(\mu_i - \mu_m)^{-1} + \frac{2(1-f)(K_m + 2\mu_m)}{5\mu_m(K_m + \frac{4}{3}\mu_m)}} \tag{3.5}$$

with K_{HS} (μ_{HS}) being the upper and lower bounds of the bulk (shear) modulus for the composite, K_{m} (μ_{m}) the bulk (shear) modulus of the matrix, K_{i} (μ_{i}) the bulk (shear) modulus of the inclusions, and f the volume fraction of the inclusions. Consequently, the effective Young's modulus E_{eff} is given by

$$E_{eff} = \frac{9K_{eff}\mu_{eff}}{(3K_{eff} + \mu_{eff})} \tag{3.6}$$

The bulk modulus of silk and AlN are 4.5 and 200 GPa,[250-252] respectively, while the shear modulus of silk and AlN are 1 and 120 GPa,[250-252] respectively. Previous measurements have shown that the modulus of silk is the same for crystallized and amorphous phases.[253-255] This yields the dashed line in Fig. 3.9b which is in good agreement with the experimental results.

I model the ultimate strain by assuming that it is controlled by the SF. That is the ultimate strain of each composite should be proportional to the average distance between two single AlN particles if the failure is due to SF and not due to failure of the bond between the SF and the AlN. The experimental data fit well with the model (Fig. 3.9a and 3.9b). In particular, given that the strains on the order of 1%, there is no slippage of the bond between the SF matrix and the AlN particles, confirming that the SF and AlN are tightly bound. Note that the 10% AlN/SF sample is strong enough to support 100-g weight, which is over thousand times of its own weight (Fig. 3.9c).

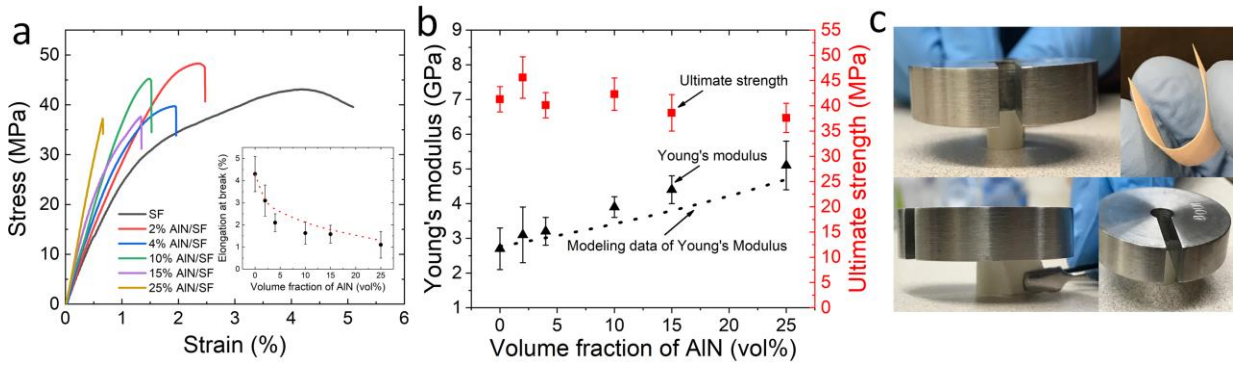

Figure 3.9 (a) Representative stress-strain curves of SF and AlN/SF composites. The inset shows the elongation at break and the dotted line represents modeling results from Eqs. (S2) and (S3). (b) Dependence of the of Young's modulus and ultimate strength on the volume fraction of AlN. The dotted line represents modeling results from Eq. (3). (c) A demo picture shows a flexible single layer 10% AlN/SF is strong enough to support a 100 g weight.

The temperature dependence of the DSC heat flow and reversing heat capacity are shown in Fig. 3.10a and Fig. 3.11a, respectively. All samples have a similar bound water evaporation peak (T_w) in Fig. 3.11a near 31 °C (summarized in Table 3.1) due to the water

annealing procedure, followed by a major degradation peak around 260 °C. The glass transition steps showed in Fig. 3.10a are attributed to the reversible transitions of amorphous component in the materials, from the frozen state to rubbery state as the temperature goes up. Previous studies have shown that silk fibers have a glass transition temperature T_g near 176 °C.[229, 256, 257] The value of T_g increased with the AlN concentration (Fig. 3.10a & Table 3.1) due to the increase of β-sheet crystallinity. By 25% AlN, there was no clear indication of a glass transition even though the volume fraction of random coils in the composite remained constant at about 20%.

To further understand the thermal stability of the composites, TGA (Fig. 3.10b and Fig. 3.11b) was used to determine the mass loss during heating as a function of temperature. Fig. 3.10b shows that the thermal stability of samples increased with the AlN concentration. Thus, the weight remaining percentage at 800 °C increased with the increase of AlN content in SF matrix (Table 3.1). For all samples, a multi-step mass loss mechanism can be observed through the first derivative of the mass curves (Fig. 3.11b), with two major degradation peaks (T_{d1} and T_{d2}). T_{d1} increased with increasing AlN content, while T_{d2} decreased with increasing AlN content in SF matrix (Table 3.1). Although it is difficult to determine which component is degrading in the two peaks of the AlN/SF samples, the shift of the degradation peaks clearly suggests that the strong interaction between silk and AlN has changed the thermal stability of the composites.

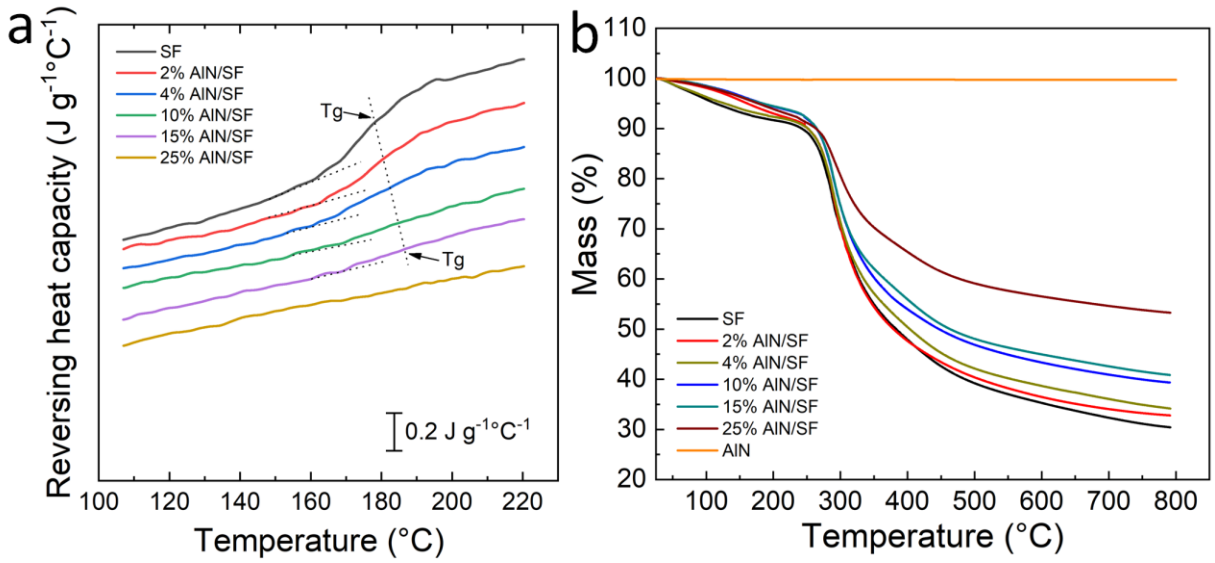

Figure 3.10 (a) Reversing heat capacity of SF and AlN/SF films. (b) Mass remaining of SF SF, 2% AlN/SF, 4% AlN/SF, 10% AlN/SF, 15% AlN/SF, 25% AlN/SF and AlN from room temperature to 800 °C.

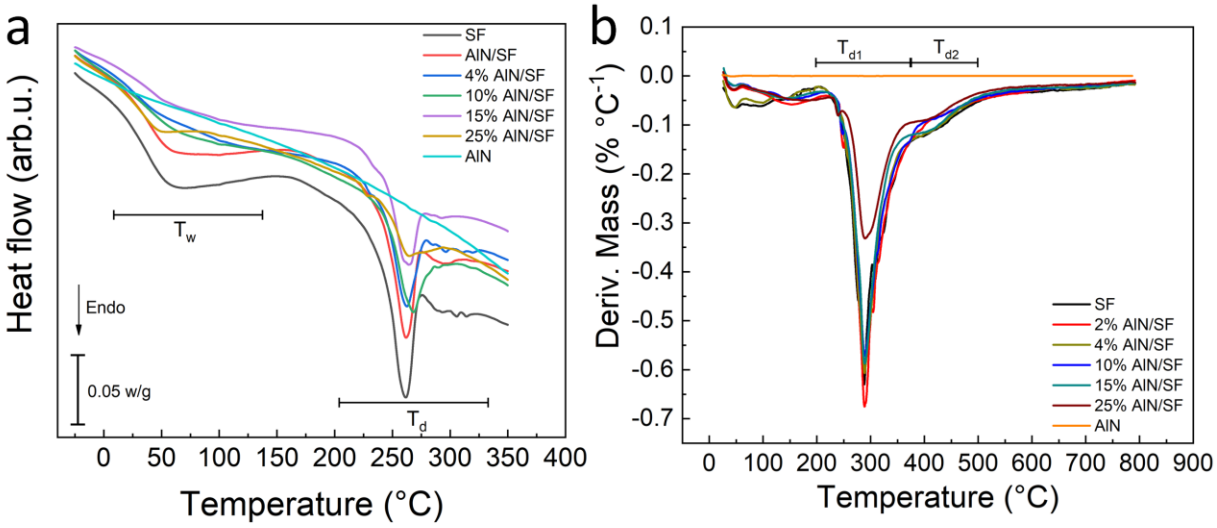

Figure 3.11 (a) Heat flow curves and (b) the temperature derivative of the mass remaining of AlN/SF films.

Table 3.1

Thermal analysis data from DSC and TGA.

Sample	T_g (°C)	T_w (°C)	T_{d1} (°C)	T_{d2} (°C)	*Mass fraction at 800 °C* (%)
SF	177.3	31.2	207.6	390.1	30.4
2% AlN/SF	180.4	31.0	223.8	387.2	32.8
4% AlN/SF	183.5	30.6	214.2	388.9	34.2
10% AlN/SF	184.3	31.8	226.3	385.6	39.3
15% AlN/SF	186.4	31.4	224.1	373.3	40.9
25% AlN/SF	N/A	31.0	230.1	366.6	53.3

N/A indicate the value was undetermined; All numbers have an error of less than ±1 °C.

The thermal expansion is shown in Fig. 3.12a & b. The pure SF sample showed a negative linear expansion of -37 ppm K^{-1}. With increasing AlN concentration, the magnitude of the coefficient of thermal expansion decreased, with 25% AlN having a value of -15.7 ppm K^{-1}, which is much lower than that of traditional polymers[212, 258] The dashed line is a linear fit to the data which is compared with the model of Gibiansky and Torquato for the effective coefficient of thermal expansion α_{eff} given by

$$\alpha_{eff} = \frac{\alpha_m K_m (K_{eff} - K_i) + \alpha_i K_i (K_m - K_{eff})}{K_{eff}(K_m - K_i)} \tag{3.7}$$

with K_{eff} being the effective bulk (shear) modulus of composites, K_i and K_m the bulk (shear) modulus of the AlN inclusions and matrix, respectively; α_i and α_m the coefficients

of thermal expansion of the AlN inclusions and pure SF matrix, respectively.[259-261] It is notable that the deviation from the model is not sizable but it is significant. The fact that the elastic modulus follows the theory while the magnitude of the thermal expansion is less than expected may be an indication that there is enhanced bonding between the AlN particles[262] which prevents the thermal expansion of the SF matrix. Since the model uses the value for α_m for pure SF, which has the highest crystalline content and therefore a lower magnitude for α_m than the actual SF content in the composites, the model perhaps underestimates the magnitude of α_{eff}.

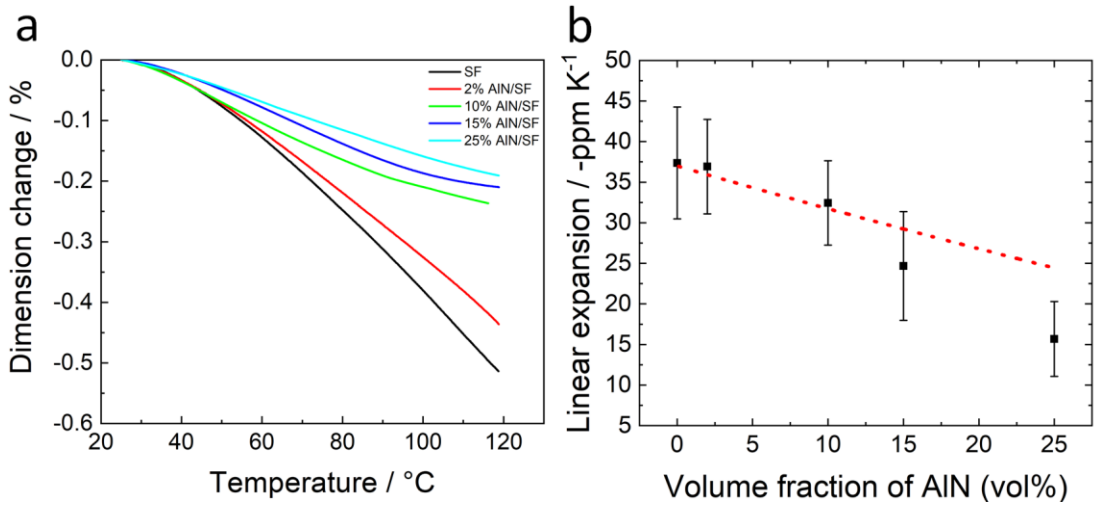

Figure 3.12 (a) Dimension change of SF and AlN/SF composites with a function of temperature. (b) Linear thermal expansion of AlN/SF films. The dotted line represents modeling results from Eq. (3.7).

The thermal conductivity κ of the pure SF film in the in-plane direction was 0.28 $Wm^{-1}K^{-1}$.[223, 263-266] AlN has a high thermal conductivity of ~320 $Wm^{-1}K^{-1}$ [219-221] and thus the composites have larger κ values than SF does (Fig. 3.13). Assuming that one can ignore interfacial thermal resistance, one can model the thermal conductivity via the Maxwell Garnett equation[267]

$$\kappa_{eff} = \kappa_m \frac{2f(\kappa_i - \kappa_m) + \kappa_i + 2\kappa_m}{2\kappa_m + \kappa_i - f(\kappa_i - \kappa_m)} \tag{3.8}$$

where κ_{eff} is the effective thermal conductivity of the AlN/SF film, κ_m the thermal conductivity of the matrix, and κ_i the thermal conductivity of the inclusions. The predicted values are low because the SF matrix is thermally insulating and there is no significant contribution to κ by the AlN until percolation, which occurs at $f = 1/3$ for the present model. Note that the deviation of the data from the model is particularly sizable. There are numerous reasons why the model may overestimate the value of κ, including interfacial scattering and size effects. The observed underestimate is most likely due to percolating networks of AlN particles in the SF as seen in Fig. 3.3.

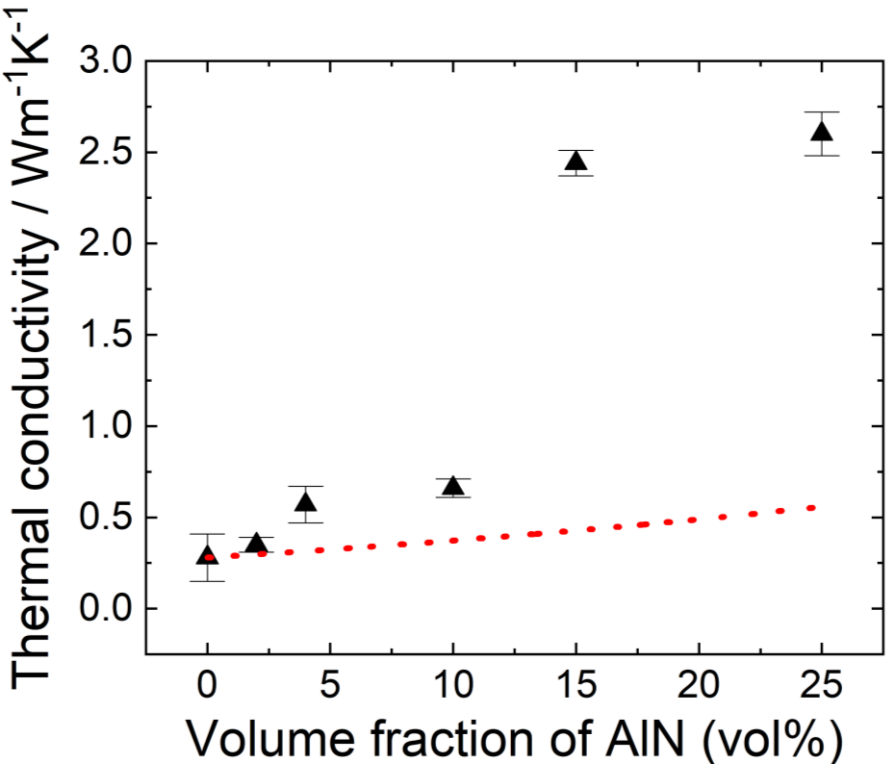

Figure 3.13 Thermal conductivity of SF and AlN/SF films. The dotted line represents modeling values from the Maxwell-Garnet theory, Eq. (3.8).

To investigate this in more detail, pure SF and 25% AlN/SF samples were coated by magnetron sputtering with a layer of patterned copper of 1 μm thick. Leads were attached to the copper and both samples were subjected 0.1 W of ohmic heating. When the heat distribution on both samples reached the steady state, the temperature at the center of pure SF was nearly 70 °C, which is much higher than the 35 °C found for the 25% AlN/SF sample and in accord with the tenfold increase in κ as the thermal gradient is proportional to the in-plane conductivity for a thin film.[268, 269]

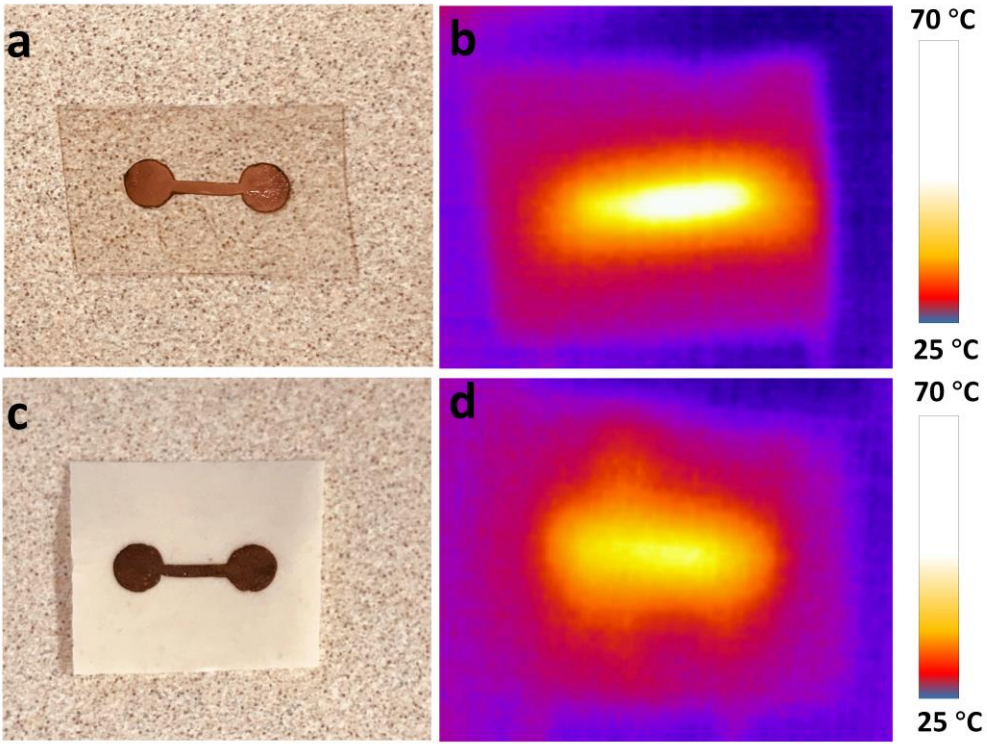

Figure 3.14 Both the SF and 25% AlN/SF were coated with a copper film of about 1 μm in thickness. Leads were attached to the contact pads and 0.1 W of power was supplied for 5 minutes. (a) and (c) are images of SF and 25% AlN/SF samples coated with the patterned copper thin films. (b) and (d) are the thermal images of SF and 25% AlN/SF sample, respectively.

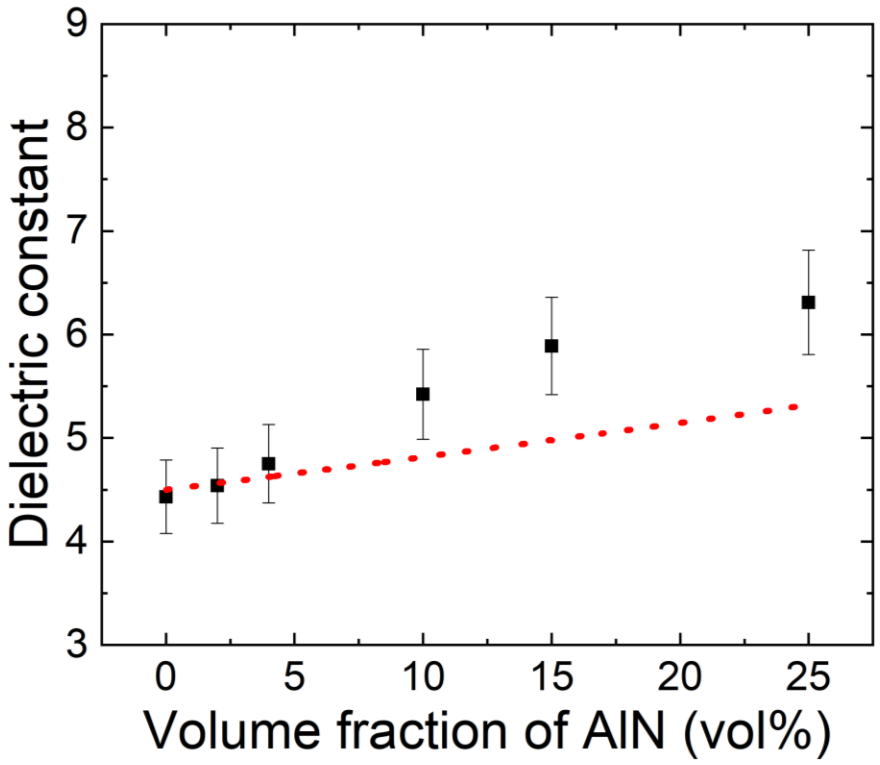

Figure 3.15 Dielectric constant of SF and AlN/SF composites at 75 kHz. The dotted line represents the expected values from Maxwell-Garnet theory, Eq. (3.9).

The dielectric properties of SF and AlN/SF composites were also investigated to further investigate the particle structure. Fig.3.16 shows the frequency dependence of the dielectric constant and loss tangent at room temperature. The real part of the dielectric constant ε as a function of AlN content is shown in Fig. 3.15 and Fig. 3.16, which increased with the increase of AlN content. It also was modeled with the Maxwell Garnett equation:

$$\varepsilon_{eff} = \varepsilon_m \frac{2f(\varepsilon_i - \varepsilon_m) + \varepsilon_i + 2\varepsilon_m}{2\varepsilon_m + \varepsilon_i - f(\varepsilon_i - \varepsilon_m)} \tag{3.9}$$

where ε_{eff} is the effective dielectric constant of the composite, ε_m the dielectric constant of the SF matrix, ε_i the dielectric constant of the AlN inclusions, and f the volume fraction of those inclusions.

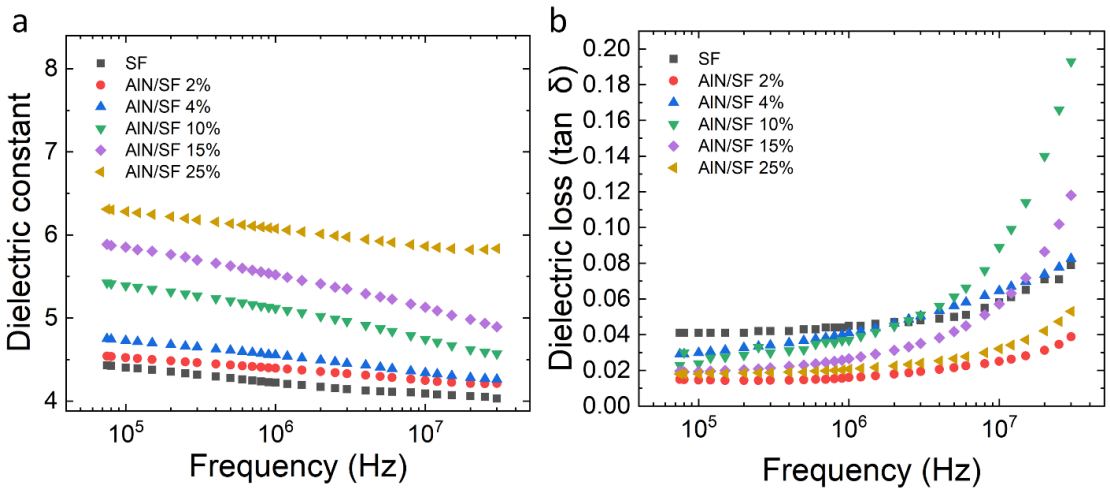

Figure 3.16 Frequency dependence of (a) the dielectric constant and (b) the loss tangent of AlN/SF films at room temperature.

The agreement is reasonable except for the highest AlN content, where the measured value is somewhat larger than the predicted one. That difference might be related to enhancement due to a decrease in the effective depolarization factor of the AlN particles which arises when the particles form networks. Alternatively, one must also recall that the amorphous component of SF has a larger dielectric than the crystalline form.[253, 260] That may also contribute to larger value of ε of the composite, although it is unlikely to be the predominant factor.

3.3.3 Fire-Retardance

Materials with good flame retardancy have a wider range of application. Fig. 3.17a shows that the pure SF sample ignited after 1s and burned throughout the duration and eventually bent. The 25% AlN/SF composite showed significantly better fire resistance. The film retained its original shape after burning for more than 20 minutes. The AlN particles distributed in the SF substrate make it more flame retardant. Accordingly, the TGA results also show that at 800 °C, AlN/SF has more residue as the concentration of AlN increases (Table 3.1).

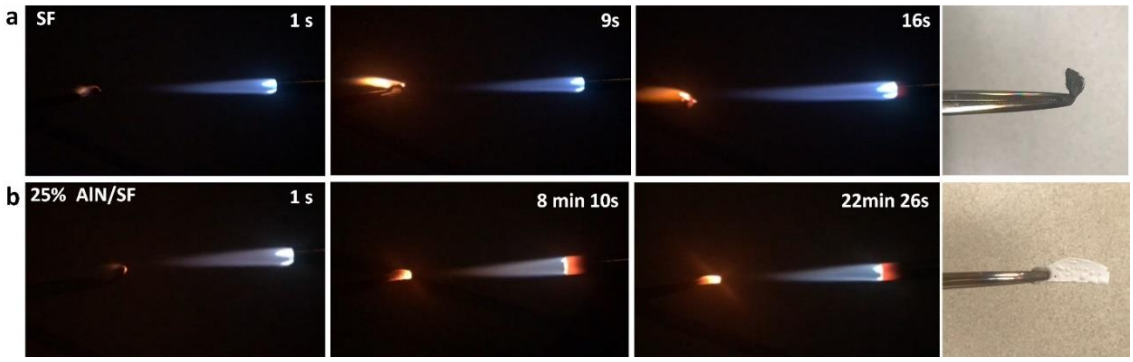

Figure 3.17 Fire-retardant properties of AlN/SFfilms. Photographs of (a) SF and (b) AlN/SF 25% films heated by a flame torch at different times.

3.3.4 Mechanism

There is clear interaction between the SF and the AlN, probably due to the formation of hydrogen bonds between the N atoms in AlN and SF proteins. According to the SEM and EDS data, it is believed that the AlN particles distribute homogeneously at lower concentration. However, at higher concentration, the AlN particles formed a

continuous network. Fig 3.18 shows a schematic of the proposed secondary structure of the composite. X-ray studies show that the SF and AlN particles are randomly oriented, but the particles are tightly bound to SF fiber by hydrogen bonding as evidenced by the trend in the glass transition temperature and the coefficient of thermal expansion. In particular, the behavior of the glass transition behavior is consistent with AlN forming a network which encapsulates the amorphous component. This network structure and hydrogen bonding are central to the significantly enhanced thermal conductivity[227] of the composites, making them viable candidates for thermal management.

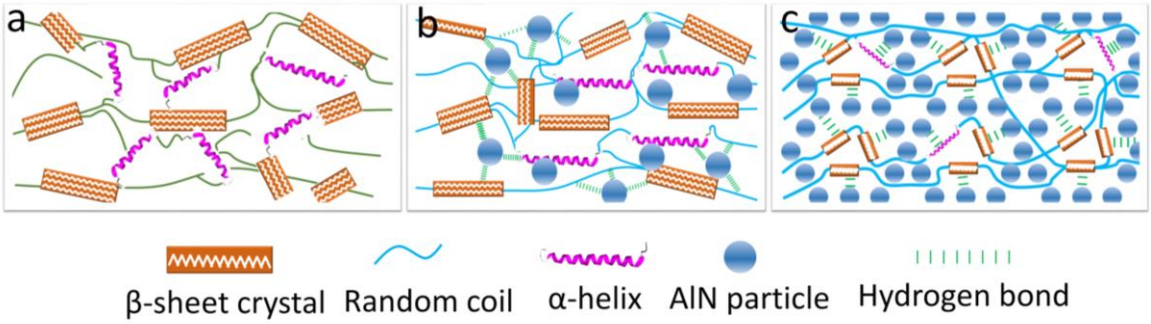

Figure 3.18 Schematic diagram of secondary structure of (a) silk fibroin, and distribution of AlN in (b) 10% AlN/SF and (c) 25% AlN/SF, respectively.

3.4 Conclusion

In summary, this study investigated the physical and structural properties of AlN/SF composites. I found layered structures in the cross section of the AlN/SF films. In the SF component, the content of the β-sheet crystal decreases as the AlN content increases. AlN/SF has good thermal stability, low linear thermal expansion, and higher stiffness while

maintaining flexibility. The 25% AlN/SF has a negative linear thermal expansion of at -15.7 ppm K^{-1}. The thermal conductivity of AlN/SF is also significantly improved, which result from AlN forming networks to provide paths of low thermal resistance. This is aided by the strong hydrogen bonding between the AlN and SF which reduced the interfacial phonon scattering. This work demonstrates that there can be significant interaction between organic and inorganic phases in composite materials, and the effects can be synergistic to create greatly enhanced materials which can be tailored for a variety of applications.

Chapter 4

Thermal Conductive Biofilms from Silk/BN-Sheet Composites

4.1 Introduction

Heat dissipation is a critical issue for the good performance and reliability of electronics. Removing the large amount of heat made by the fast processing system in time can build a high-performance system for digital devices. Because of its good electrical insulation, ease of processing, low density and tunable mechanical properties, polymer-based high thermal conductivity composites seem promising. Silk fibroin fibers are natural and renewable polymers which feature strong mechanical strength and toughness due to its hierarchical structure[270], and they have been widely used in biomedical devices because of their good biocompatibility and biodegradability. As the FDA-approved materials for *in vitro* and *in vivo* use, silk fibroin material has been engineered into various types of biomedical materials, such as nanoparticles, scaffolds, and films, and their water solubility and other properties can be manipulated through modifying the secondary structure, most of the cases are β-sheet nanocrystals, of the silk protein. It's well known that high crystallinity contributes to high thermal conductivity because it minimized phonon scattering. Studies done on silk materials demonstrate that the disordered portion of the silk protein can play a dominant role in the heat transfer[271] for that reason. Even though the bulk silk materials show much low thermal conductivity κ (~0.2 W m^{-1} K^{-1}), its exceptional strength and renewability make it a good matrix for thermal management materials.

Many common materials with high thermal conductivity are metals, such as silver and copper where the heat is conducted by free electrons. However, their electric

conductivity limits their applications for electronics, and so considerable effort has been applied to develop electrically insulating phases with high thermal conductivity. Among them, boron nitride (BN) has found practical applications in thermal transportation. There are four types of BN (a-BN, h-BN, c-BN and w-BN) according to its crystalline forms. Both h-BN and c-BN show excellent thermal conductivity, thermal and chemical stability. h-BN shows a highly anisotropic thermal conductivity with ~ 420 and ~30 W m^{-1} K^{-1} for in-plane and cross-plane direction, respectively[272-278]. The relatively lower cross-plane value of κ of h-BN is attributed to the acoustic phonons scattering at the interlayer of BN nanosheets [279-281]. However, BN is often used a ceramic and the resulting brittleness restricts it utility.

The ideal case is a composite material with higher κ values and desired mechanical properties. Thr large anisotropy in thermal transportation and good electrical insulation of h-BN make it ideal reinforcing filler for thin-film thermal management materials. Given the low thermal conductivity of bulk silk protein, simply mixing silk and BN does not increase the thermal conductivity of the composite largely. The κ values of composite materials is also limited by many other factors, such as interface, defects and voids in the matrix, chain alignment of the matrix, and filler alignment[282-285] [286]. On the other hand, one study showed that the weakest chemical bonds of nanoconfined β-sheet nanocrystals, hydrogen bonds, give silk fiber its exceptional strength [287]. Inspired by this, I considered hydrogen bonds formed between amino acid groups on silk fibroin chains and BN would reduce the thermal resistance between the silk protein and BN.

Here I demonstrate that SF/BN composites have enhanced κ values which I have achieved through water annealing to induce more β-sheet nanocrystals and strengthen the interactions between SF and BN. In addition, by processing I can align both h-BN nanosheets and β-sheet nanocrystals. The highly oriented structure has fewer defects which leads to this substantial effect. This environment friendly functional material provides an alternative for the electrical and electronics industry.

4.2 Experimental Section

4.2.1 Raw Materials

Bombyx mori cocoons were purchased from Treenway Silks (Lakewood, CO, USA). The silkworm cocoons were degummed to remove the sericin coatings and extract the pure silk protein fibers by boiling in a 0.02 M $NaHCO_3$ (Sigma-Aldrich, USA) solution for 30 min followed by thorough rinsing with deionized water. The degummed silk fibers were air dried overnight and put into a vacuum oven at room temperature for 24 h to remove the remaining moisture. Formic acid (ACS Grade 98%) was purchased from EMD Millipore Corporation (Burlington, MA, USA), calcium chloride (anhydrous, ACS Grade) was purchased from AMRESCO Inc. (Solon, OH, USA), and hexagonal-boron nitride (98%) was purchased from Aldrich chemistry. All the chemicals were used as purchased.

4.2.2 Material Synthesis

Pure mori protein fibers were firstly dissolve into formic acid solution with 4 w/v% calcium chloride at room temperature. The pure silk solution was firstly centrifuged to remove impurities. Afterwards, BN nanosheets were added into the SF solution at different ratios so that the resulting composites had a volume fraction of BN of up to 30%. The

density of dry state SF films and BN were measured to be 1.4 and 2.1 g/cm^3, respectively. The mixture solution was mixed by a vortex mixer for 15 minutes to distribute the BN nanosheets distribute evenly throughout the solution. The solution was then immediately cast onto polydimethylsiloxane (PDMS) substrates to form films. Films were left to dry 2 days in the fume hood at room temperature. Henceforth, these as cast samples are designated as x% ac-BNSF where x represents the volume fraction of BN. These samples were annealed in DI water for 1 h to remove the formic acid residue and $CaCl_2$, and promote the hydrogen bonding between SF and BN. A batch of these samples were left in a 30 °C vacuum oven to dry for 2 days before the tests. These unprocessed samples are designated as x% up-BNSF where x represents the volume fraction of BN. The weight of another batch of these samples were recorded first, and the samples were dried in a 30 °C vacuum until there was10 wt% water left. Afterwards, the film was pressed under 500 kPa for 10 minutes, and then the samples were fixed with our self-designed clips and left in a 30 °C vacuum oven to dry for 2 days before the tests. These water-annealed and soaked-pressed samples are designated as x% BNSF where x represents the volume fraction of BN.

Cross-section morphology of the composite films were characterized with a FEI Teneo LV SEM (Oregon, USA). The surface profiling portfolio of the composites is characterized by MicroXAM-100 (KLA Tencor, USA) optical interferometer. The elemental distribution of BN was characterized by energy dispersive X-ray spectroscopy (EDS, Oxford Instruments). Structure information of the composites were characterized using a Bruker Tensor 27 Fourier-Transform Infrared Spectrometer (Bruker Tensor 27, USA) equipped with a deuterated triglycine sulfate detector and a multiple reflection, horizontal MIRacle ATR attachment (Pike Tech, USA). For each measurement, 128 scans

were co-added with a resolution of 4 cm^{-1}. Wide-angle X-ray scattering (WAXS) was conducted with a Panalytical Empyrean X-ray diffractometer. The setup included a fixed anode X-ray source for Cu Kα radiation (wavelength λ = 0.154 nm), operating at 45 kV and 40 mA. The scattering angle 2θ ranged from 5° to 70°, and data were taken in steps of 0.013º with a hold time of 30 s/step. Measurements were taken as a function of the film orientation with the sample plane being rotated from 0° to 90° with respect to the incident beam (Fig. 4.1). Raman spectroscopy was done with A LabRAM HR Evolution Raman spectrometer (Horiba, Japan).

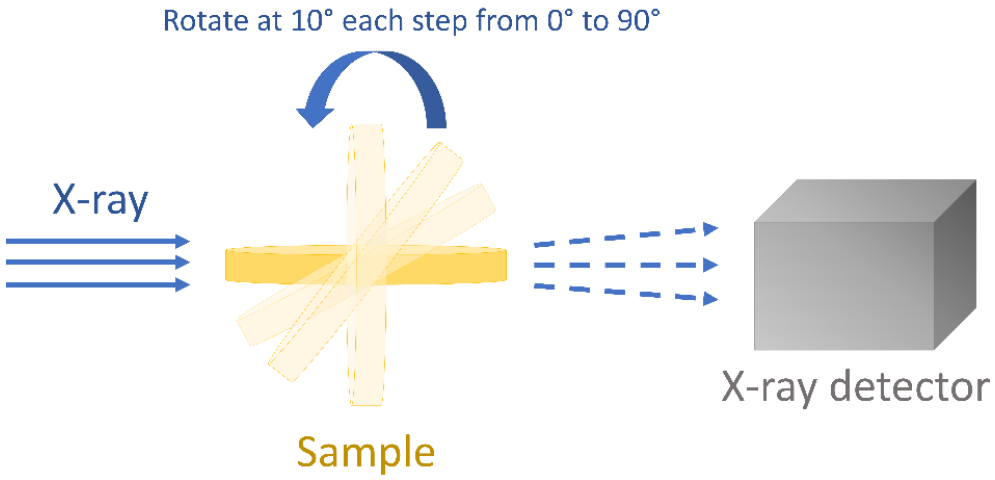

Figure 4.1 X-ray scattering geometry.

Glass transition temperature and heat capacity of the samples were measured by Q100 DSC (TA Instruments, USA), The measurements were taken at a heating rate of 2 °C/min with a temperature modulation amplitude of 0.318 °C per 60 seconds. Thermal stability of the samples was characterized by a TA Instruments SDT Q600. The mechanical test was conducted with a Universal Tensile Tester (SHIMAZDU, Japan) with 100 N force at 5 mm/min. The relative humidity of the day these samples were measured was around 40%. The coefficient of thermal expansion (CTE) was measured by a Q400 (TA Instruments) thermal mechanical analyzer (TMA) from 25 to 120 °C at a scan rate 10 °C/min. The sample was pre-loaded with 50 mN of force.

Thermal conductivity of all the samples were measured at 300 K. The in-plane and cross-plane TC of up-BNSF composites, and the in-plane TC of BNSF composites were measured with a Physical Property Measurement System (Quantum Design, USA) with the thermal transport option (TTO) under steady-state conditions. Leads were attached with silver epoxy to a film sample with an area of 5 × 20 mm, and measurements were taken at vacuum below 9×10^{-5} Torr. The cross-plane TC of BNSF composites were conducted with the Light Flash Apparatus (LFA 467 HyperFlash, NETZSCH, USA). The specimen was cut into a round shape with diameter of 25.4mm, with a thickness around 0.3 mm. The thermal diffusivity (D) was firstly measured at 300 K using the laser flash diffusivity method (Netzsch LFA-467), with laser voltage at 260V. The thermal conductivity was calculated from

$$\kappa = D^{*}C_p^{*}\rho$$

where the κ is thermal conductivity (W $m^{-1}K^{-1}$), C_p is the heat capacity of the material, and ρ is the density of the material.

The infrared thermal images were taken with a Seek Reveal thermal imaging camera (California, USA). Parallel flame testing was performed on pure SF and 25% BNSF film. The size of the sample was 25 mm in length and 6 mm in width. A propane torch was used, and the samples were heated by flame until they were completely burned. The dielectric constant and loss were measured with an Agilent 4285A Precision LCR Meter (Agilent, USA).

4.3 Result and Discussion

4.3.1 Fabrication and Morphology of the BNSF Films

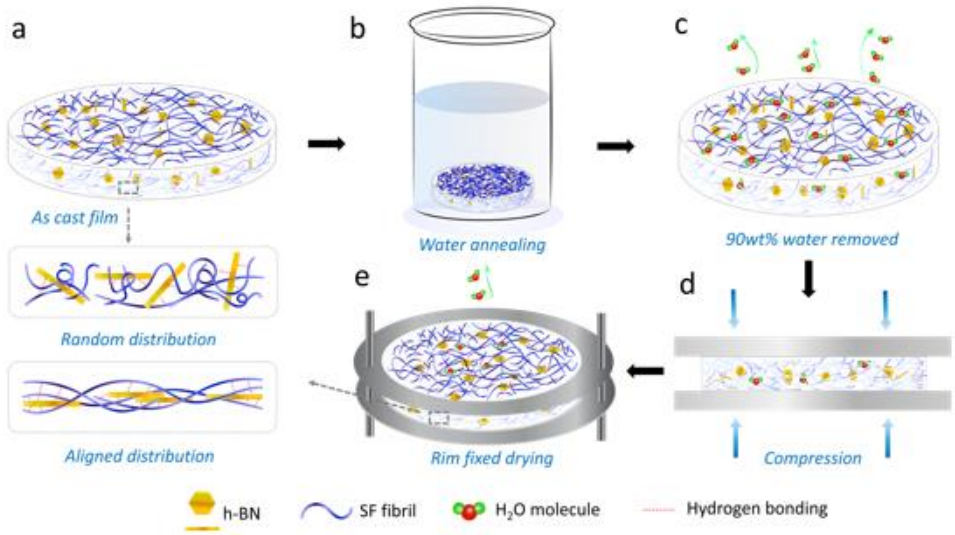

Figure 4.2 Schematic diagram for synthesizing BNSF composites. a) shows dry state as cast samples; b) shows the ac-SF and ac-BNSF samples are annealed in deionized water; c) The annealed samples are drying; d) the wet-state samples are pressed under 500 kPa for 10 minutes; e) Samples were fixed using self-designed clips and dry.

Key procedures for preparing the BNSF films with aligned BN nanosheets and higher crystallinity are shown in Figure 4.3. To promote thermal conduction, ac-BNSF films were annealed in DI water (Figure 4.3b). During this procedure, the SF fibrils gain more mobility and self-assembled in more ordered structure and the higher crystallinity can be achieved. In addition, the remaining FA and $CaCl_2$ can be completely removed, which reduced the impurity of the composite system and the matrix-filler interface. To get aligned BN nanosheets in the SF matrix, the annealed films were pressed under 500 kPa for 10 min (Figure 4.3d). However, to keep the mobility of both the BN nanosheets and silk fiber, 10 wt% of the total amount water absorbed in the annealing step was maintained (Figure 4.3c). I found that the composite film would curl while drying so the film was held under biaxial in-plane tension by a home-built fixture (Figure 4.3e). The tension is believed to induce more crystals and maintain the alignment of the BN nanosheets.

Photos of 15% ac-BNSF film (up) and 15% BNSF film (down) are shown in Figure 4.3a. Both samples show a uniform white color, while the 15% BNSF is uniform in thickness and shows a flat surface. The surface profiling portfolio of 30% BNSF film shows a rather smooth surface with Ra at 0.29 μm and Rq at 0.35 μm (Figure 4.3b, Figure 4.4 and Table 4.1). The alignment of both BN nanosheets and layer-by-layer SF can be clearly observed in the cross-section of 30% BNSF film (Figure 4.3c & 3d, Figure 4.5 and Figure 4.6). To make the alignment of BN nanosheet more clearly, FFT is applied to filter the SF matrix (black part in Figure 4.3f) and highlight the alignment of the BN nanosheets.

Table 4.1

Roughness parameters of SF and 30% BNSF films.

	SF	30% BNSF
Mean	7.0 μm	6.7 μm
Rp	375.8 nm	836.7 nm
Rv	825.5 nm	1.2 μm
Rt	1.2 μm	2.0 μm
Ra	111.4 nm	287.8 nm
Rq	154.3 nm	354.9 nm
Rsk	-1.620	-0.246
Rkr	3.238	-0.199

The spatial distribution of various elements in the composites was characterized by EDS. There is no $CaCl_2$ left in the film after water annealing (Figure 4.7), and this confirms the composite consists of only BN and SF. In addition, the BN spatial distribution is nearly homogeneous after annealing (Figure 4.3e and Figure 4.9).

The structural makeup of the constituents was studied with Raman spectroscopy. BN shows a sharp peak at 1368 cm^{-1} (Figure 4.3h and Figure 4.8), and it is attributed to the high frequency intralayer E2g vibration mode. Pure Mori silk sample shows a broad peak at 1669 cm^{-1}, which is the β-sheet/β-turn configuration of the polypeptide backbone[288]. However, the peak at 1669 cm^{-1} becomes sharper and slightly decreases to 1663 cm^{-1}, which suggest more random coils and alpha-helix structures are formed as the BN content increases.

Details of SF secondary structure were characterized by the FTIR by Fourier self-deconvolution (FSD). After the water-annealing and compression, a broad peak at 1638 cm^{-1} in amide I region shifts from to a sharp peak at 1623 cm^{-1} (Figure 4.3i and Figure

4.10), indicating these processes inhibit the formation of random coils/extended chains and promoted β-sheet crystals structure [164]. However, as the BN loading increased, the shoulder at 1649 cm^{-1} grew, and the peak at 1622 cm^{-1} gradually shifted to a higher value at 1624 cm^{-1}, indicating that the addition of BN nanosheets inhibited the formation of β-sheet crystals and promoted the random silk structure (Fig. 4.3j) in accord with the Raman results.

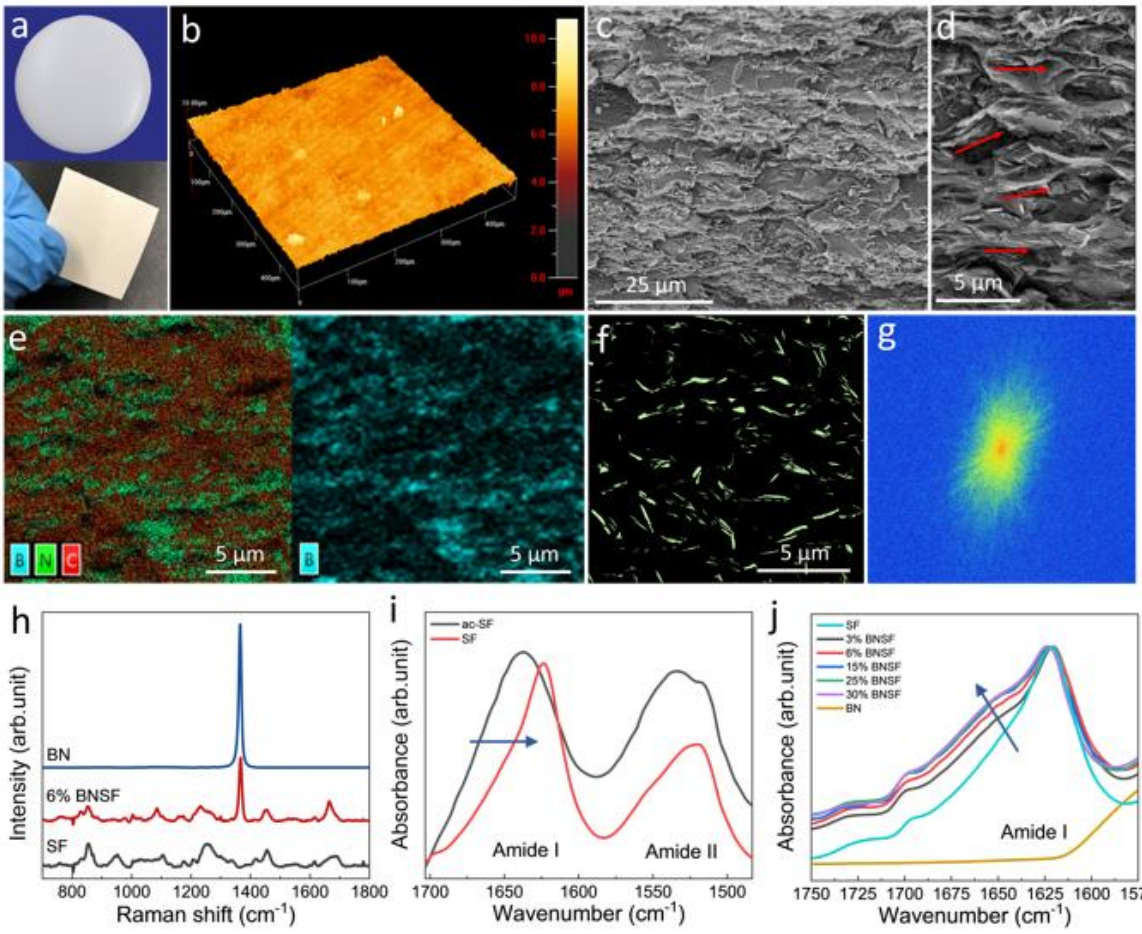

Figure 4.3 Morphology and structural characterizations of the BNSF composites. a) Photos of 15% ac-BNSF film (up) and 15% BNSF film (down); b) Surface roughness of 30% BNSF film; c) and d) are cross-section morphology of 30% BNSF film, which shows the well-aligned structure; e) Cross-section EDS B(boron), N(nitride) and C(carbon) element mapping of 15% BNSF film. f) FFT processed data of 25% BNSF film; g) FFT processed data of 25% BNSF film. h) Raman spectroscopy of h-BN nanosheets, 6% BNSF and SF films; i) FTIR spectrum results for ac-SF and SF films. j) FTIR spectrum results for BN, SF and BNSF films with different BN loading, which shows the impact of the added BN on the secondary structure of silk fibroin.

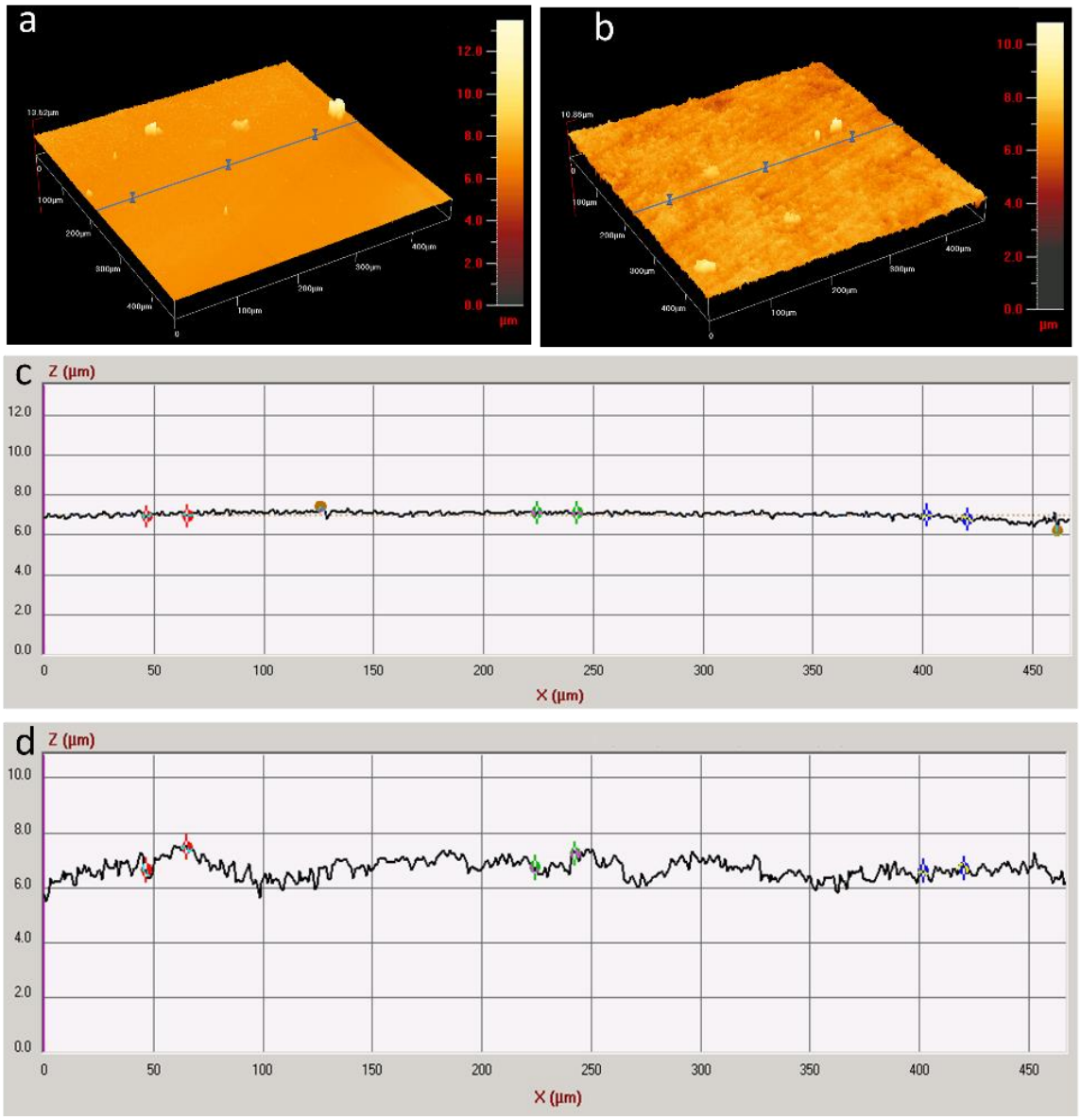

Figure 4.4 Surface roughness of (a) SF and (b) 30% BNSF film; (c) and (d) show roughness parameter of the two lines showed in (a) and (b), respectively.

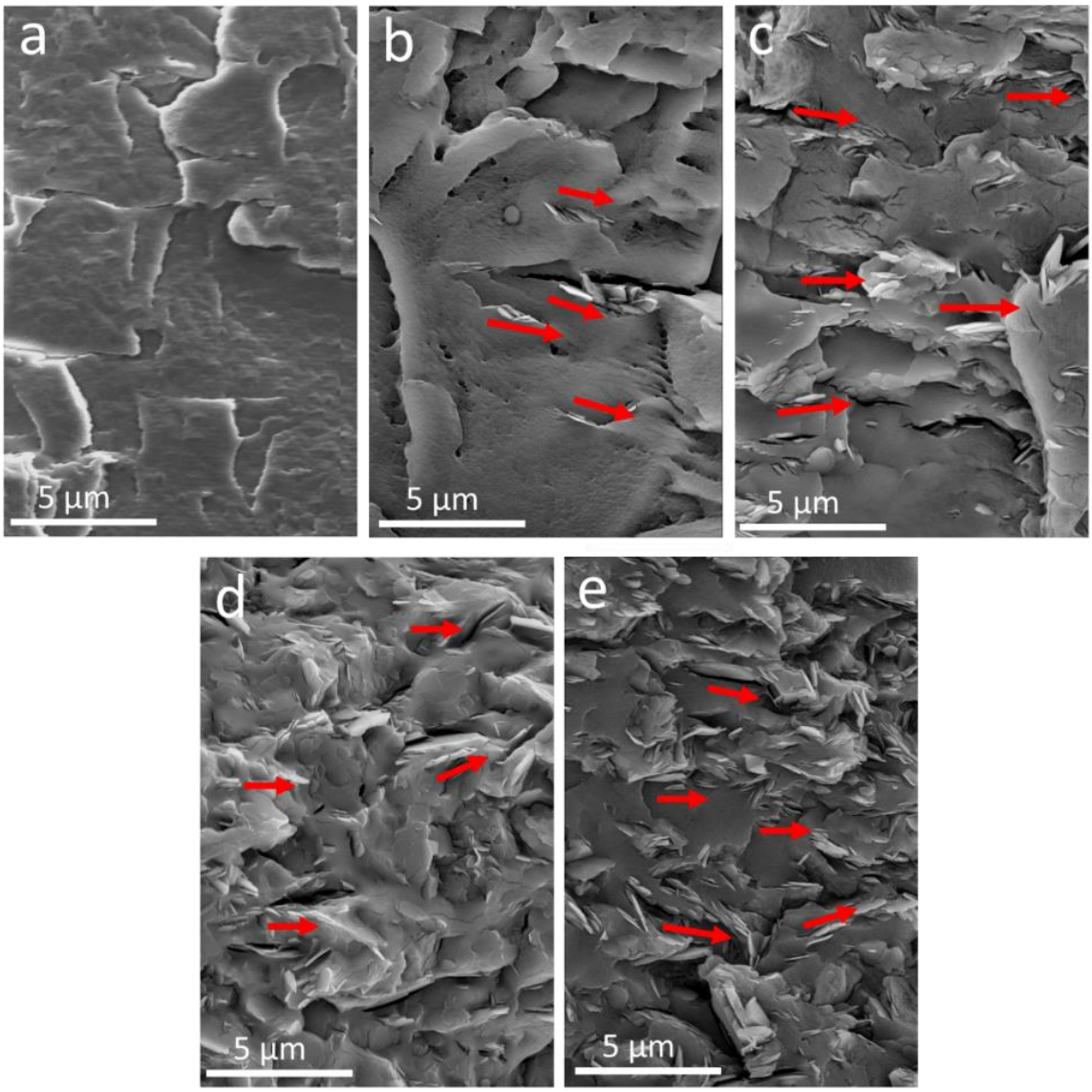

Figure 4.5 Cross-sectional SEM images of (a) SF, (b) 3% BNSF, (c) 6% BNSF, (d) 15% BNSF, (e) 25% BNSF films. Red arrows show the alignment of h-BN sheets parallel to the in-plane direction of the film.

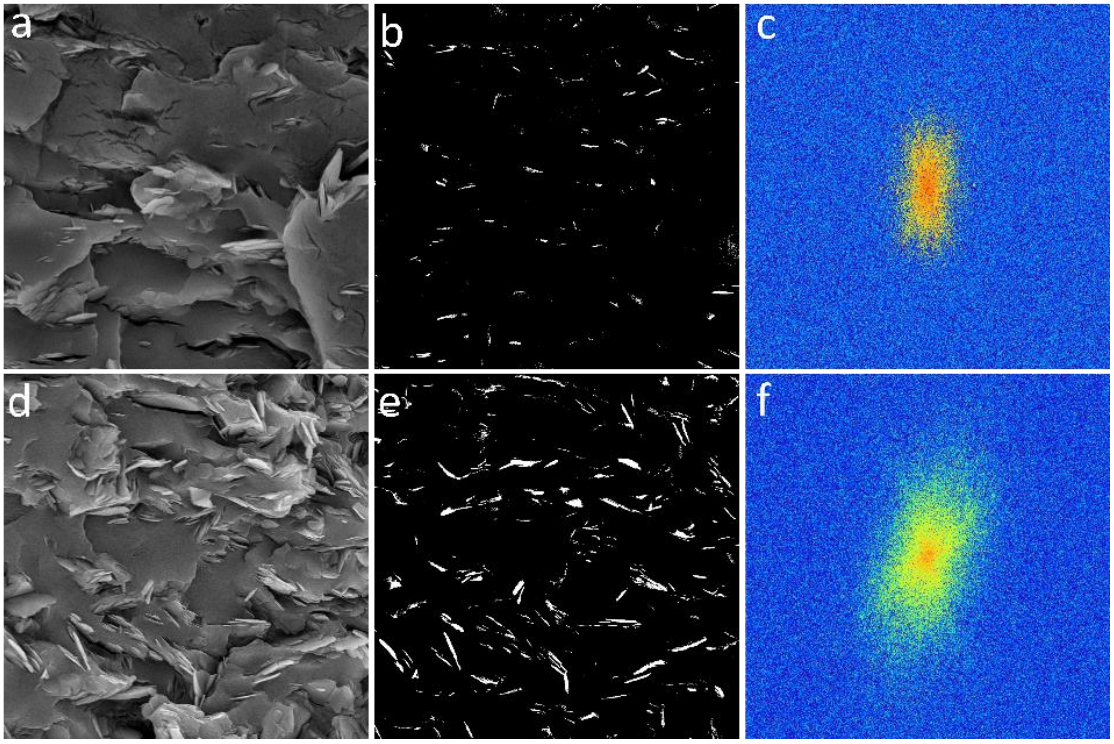

Figure 4.6 Cross-sectional SEM images of (a) 6% BNSF and (d) 25% BNSF, (b) and (e) are FFT processed SEM images of 6% BNSF and 25% BNSF, respectively;(c) and (f) are FFT processed alignment images of 6% BNSF and 25% BNSF films, respectively.

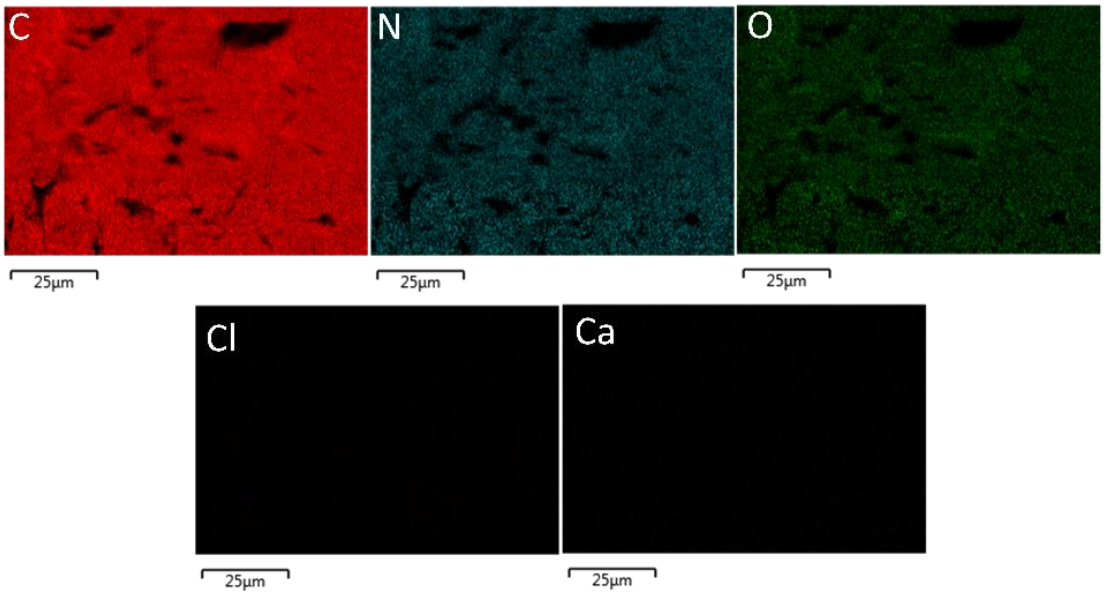

Figure 4.7 EDS element (C, N, O, Cl and Ca) mapping in SF.

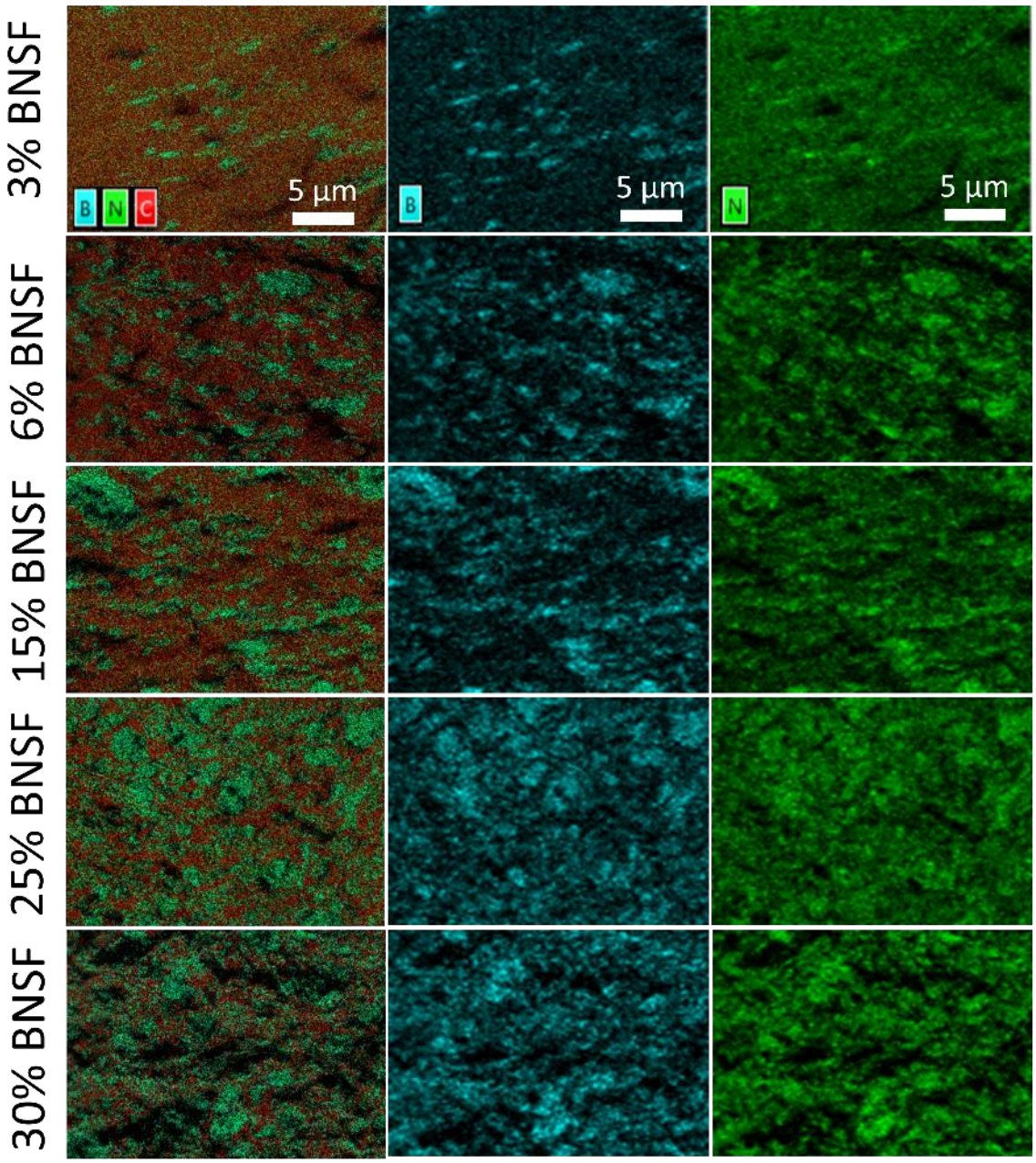

Figure 4.8 EDS element (C, N, B) mapping in BNSF films with different BN loading.

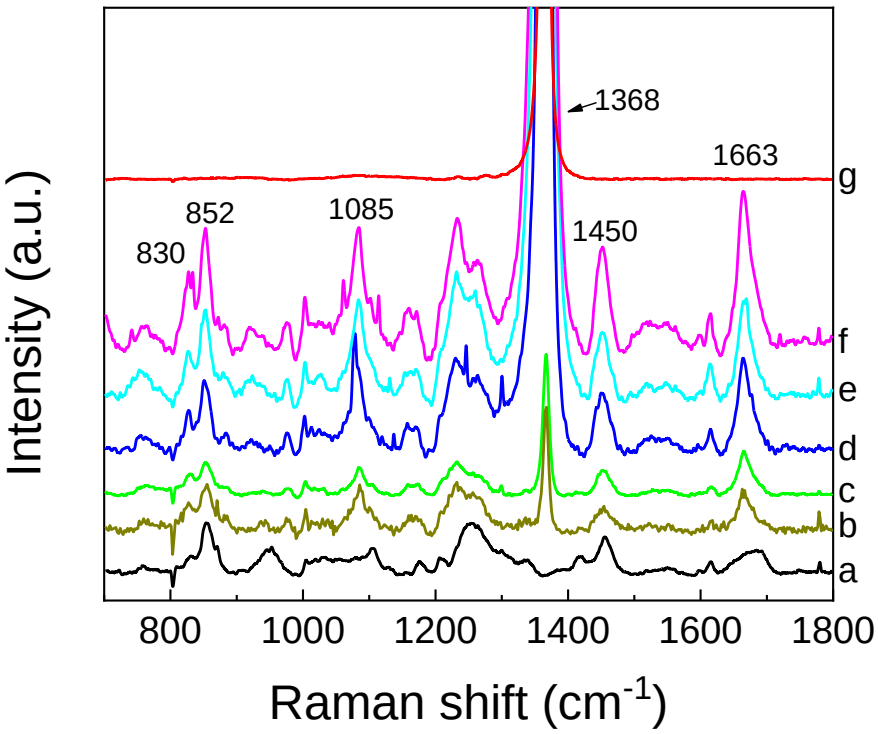

Figure 4.9 Raman spectra of (a) SF, (b) 3% BNSF, (c) 6% BNSF, (d) 15% BNSF, (e) 25% BNSF, (f) 30% BNSF, (g) h-BN samples.

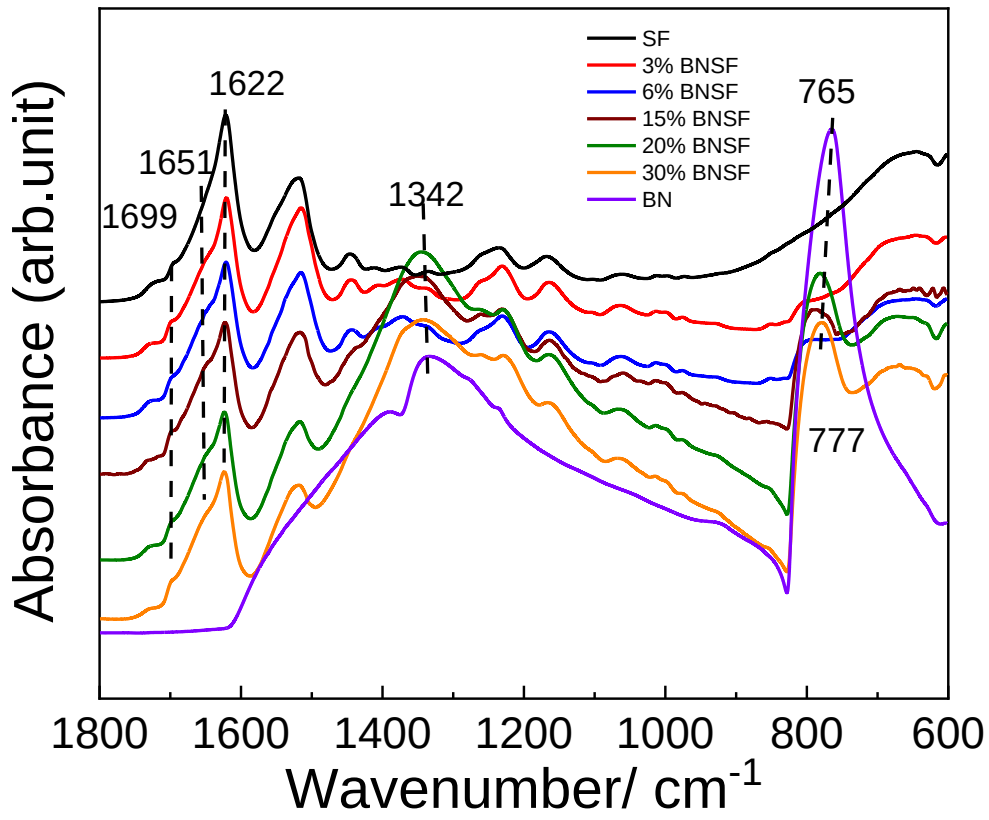

Figure 4.10 FTIR spectra of SF, h-BN and BNSF composites.

The orientation of β-sheet crystals and BN was studied by WAXS (Figure 4.11c & 4.11d). The BN sample shows a strong sharp peak (002) and six relatively weak peaks, corresponding to (100), (101), (102), (004), (110) and (112) h-BN planes (Figure 4.12, Figure 4.13). The up-SF (Figure. 4.12) showed a broad peak centered at 20.6° (silk II structure, β-sheet crystals) with a shoulder at 24.5° (silk I structure), while the SF film showed a much narrower peak at 20.6°. Those results demonstrate that β-sheet crystals are randomly oriented (Fig. 4.11c, Fig. 4.12) in the up-BNSF films, while well oriented in the

BNSF films. The BN nanosheets are randomly oriented in up-BNSF films while well aligned in the BNSF films (Figure 4.11c,11d and Figure 4.13). This confirms the FFT analysis in Figure 4.3g and Figure 4.6.

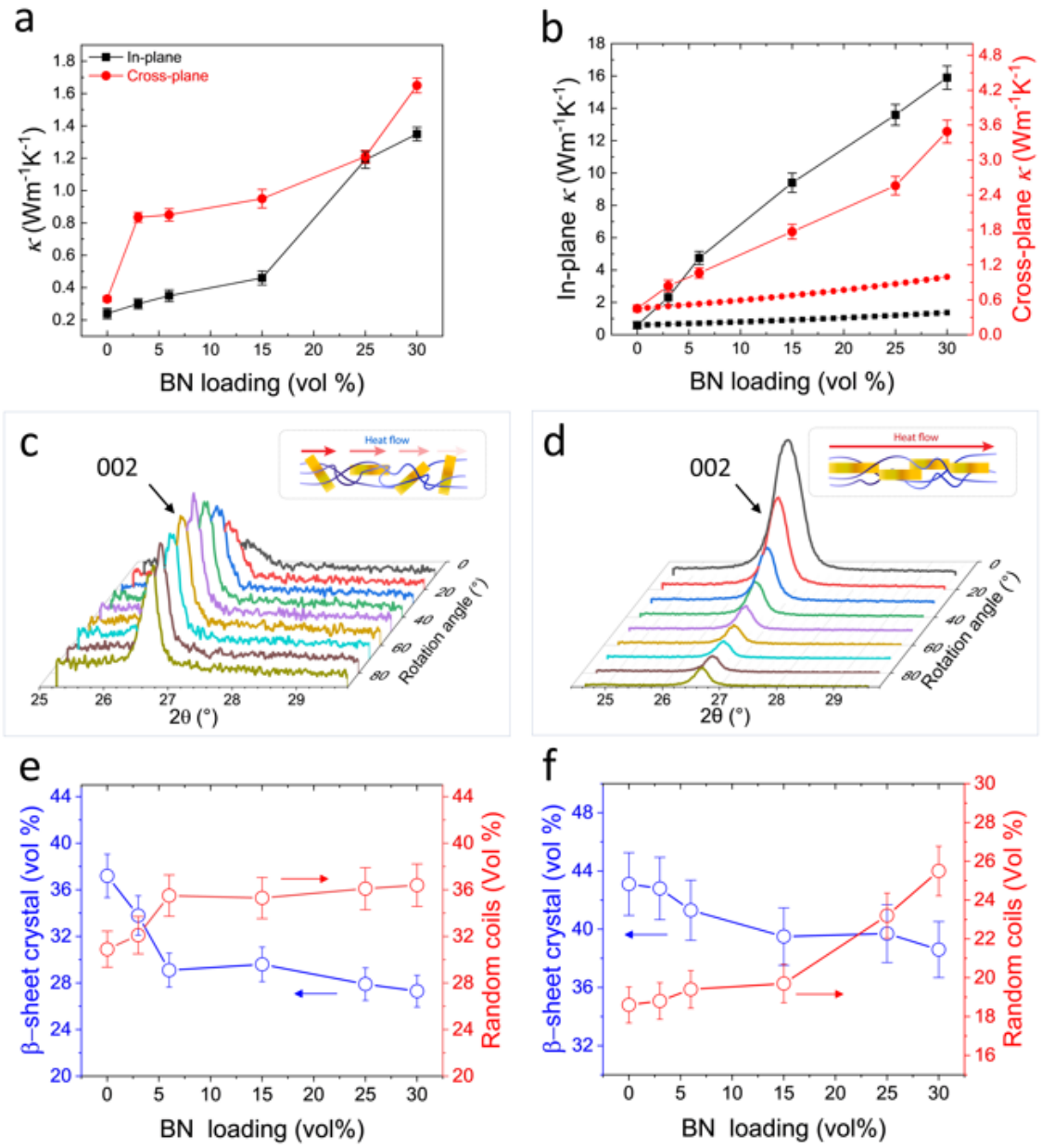

Figure 4.11 a) In-plane and cross-plane thermal conductivity of up-SF and up-BNSF samples; b) In-plane and cross-plane thermal conductivity of SF and BNSF samples; WAXS patterns of (c) 25% up-BNSF and (d) 25% BNSF films at different orientations, respectively. The inset images show the alignment of h-BN nanosheets in the silk fibroin matrix; e) Volume fraction of β-sheet crystals and random coils of the silk fibroin component for ac-SF and ac-BNSF samples; f) Volume fraction of β-sheet crystals and random coils of the silk fibroin component for SF and BNSF samples.

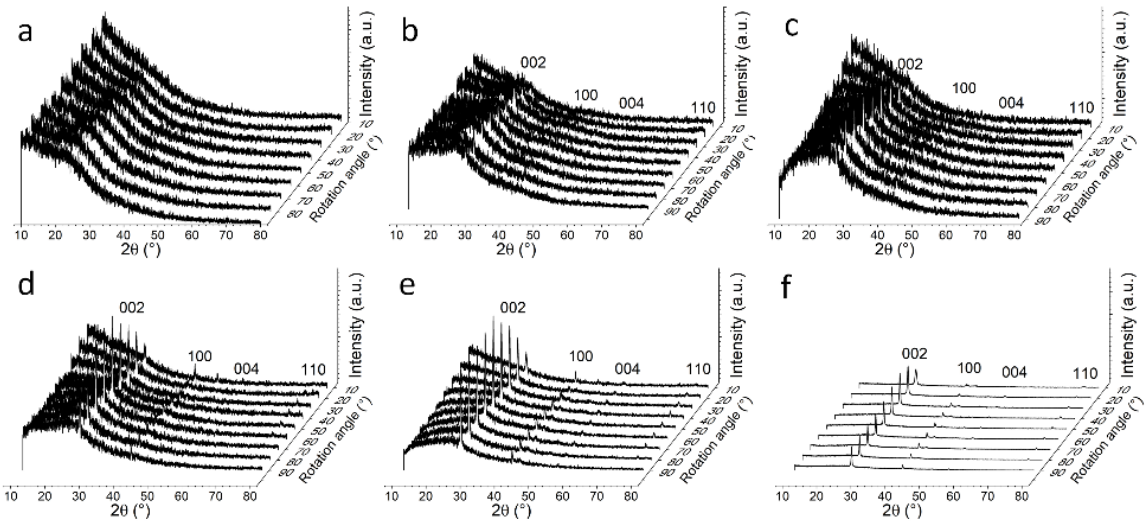

Figure 4.12 WAXS patterns of (a) UP-SF, (b) 3% UP-BNSF, (c) 6% UP-BNSF, (d) 15% UP-BNSF, (e) 25% UP-BNSF, (f) 30% UP-BNSF films at different orientations.

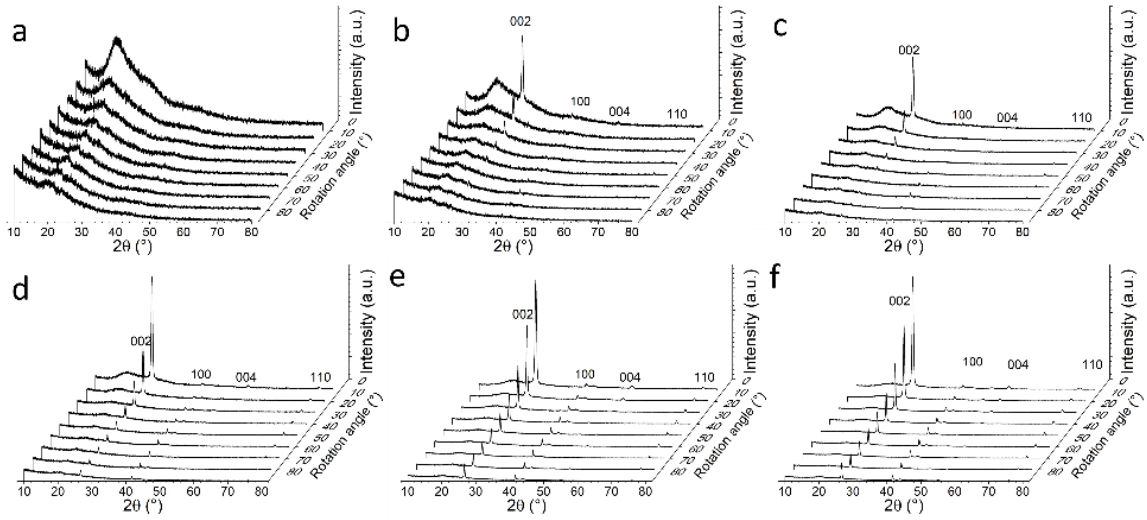

Figure 4.13 WAXS patterns of (a) SF, (b) 3% BNSF, (c) 6% BNSF, (d) 15% BNSF, (e) 25% BNSF, (f) 30% BNSF samples.

Thermal stability of the BNSF samples was studied by TGA and temperature modulated DSC. BN shows an excellent thermal stability as expected (Figure 4.14c). All samples except the BN showed a slow degradation temperature around 250 °C. The weight remaining percentage at 900 °C increased with the increase of BN loading. The first derivative of the mass loss curve (Figure 4.15a) shows a multi-step mass loss mechanism, and it is believed that the amorphous part of the SF degrades at lower temperature than the crystalline part does. Although it is difficult to determine the degradation order of each secondary structure component, the shift of the degradation peaks clearly suggests that the strong interaction between silk and BN has formed.

The temperature dependence of reversible heat capacity and heat flow of BNSF films are shown in Figure 4.14d and Figure 4.15b, respectively. SF and BNSF composites firstly show a broad endothermic peak between 25 and 100 °C, which is attributed to the evaporation of bound water in the composite (Figure 4.15b). SF shows an endothermic peak around 270 °C, which is caused by degradation. As the BN content increases, the degradation endothermic peak diminishes and the degradation temperature also slightly shifts to higher temperature, which is caused by the lower content of silk in the composites and the stronger bonding between BN and SF. A clear glass transition can be seen in the SF sample near 176 °C. As the BN content increases, the glass transition of the BNSF composite becomes weak and disappears by 15% BN.

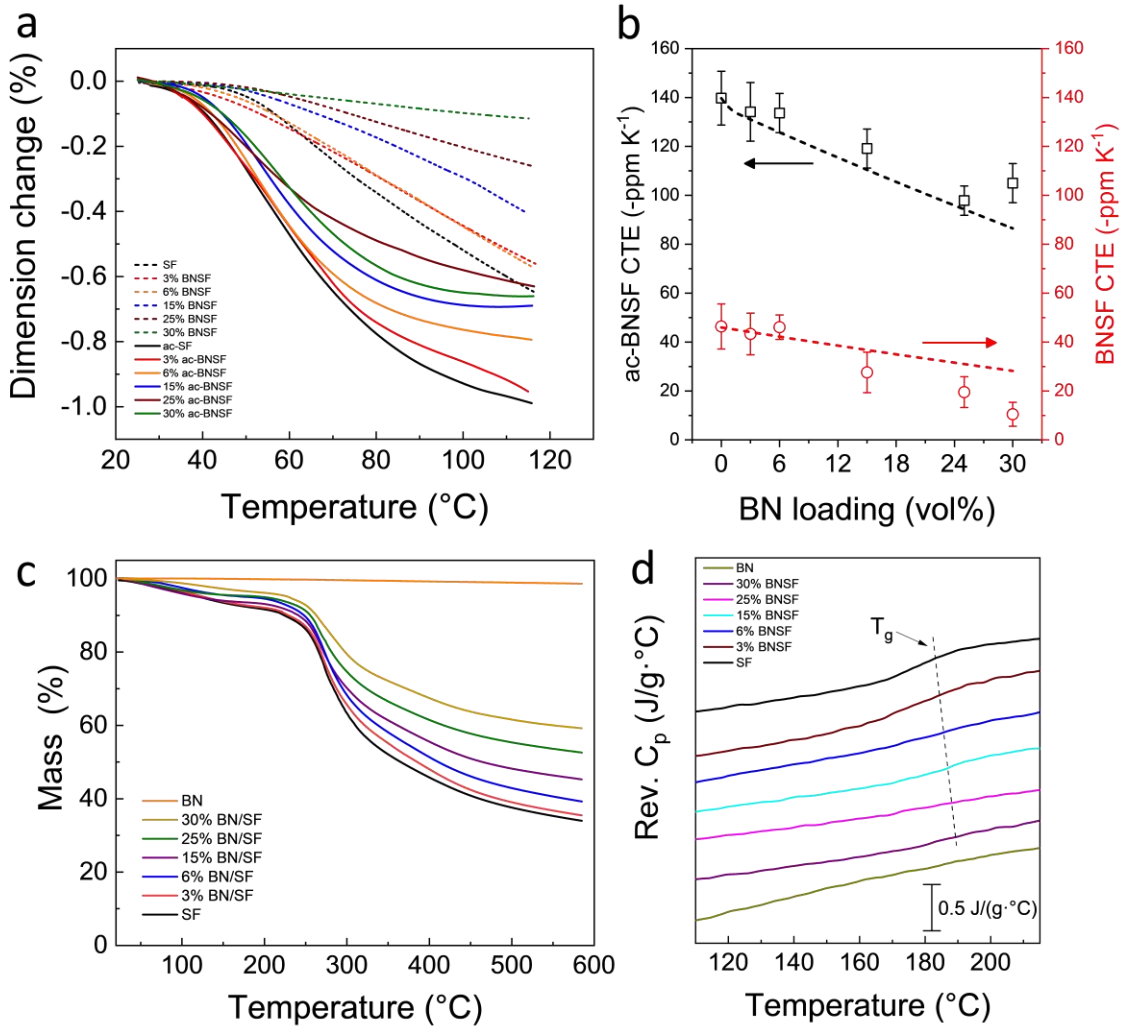

Figure 4.14 a) Relations of dimension change of ac-BNSF and BNSF films with temperature. b) Relations of CTE of ac-BNSF and BNSF films with BN loading. The dotted line represents modeling results from Eq. (2). c) Mass remaining of BN, SF and BNSF films; d) Reversing heat capacity of BN, SF and BNSF films.

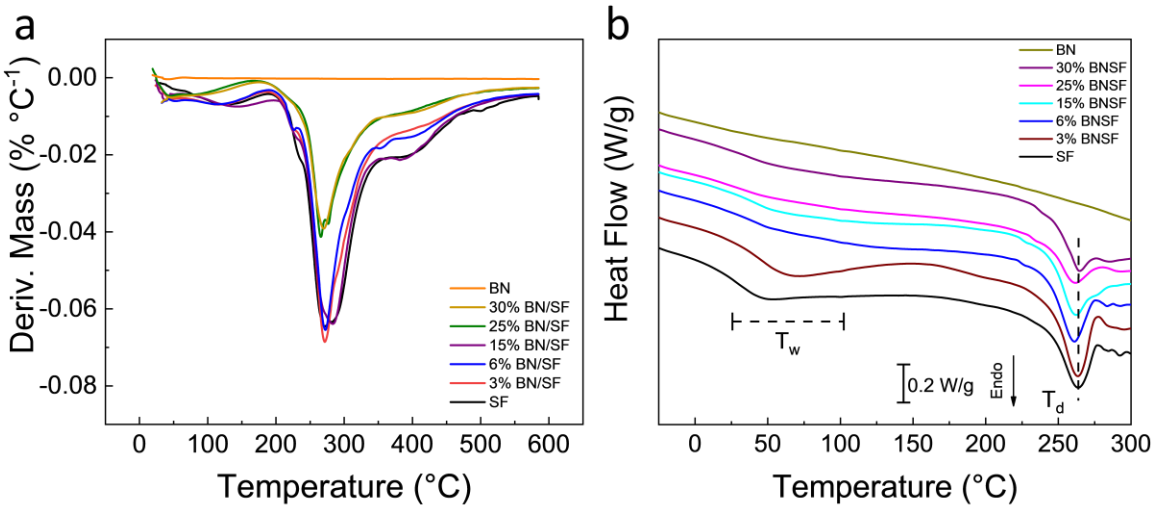

Figure 4.15 (a) The temperature derivative of the mass remaining of SF and BNSF samples from TGA; (b) DSC heat flow curves of SF and BNSF samples.

4.3.2 Anisotropic Thermal Conductivity and Thermal Stability of BNSF Films

Thermal conductivity of up-BNSF and BNSF film were both measured in in-plane ($\kappa_{\parallel}$) and cross-plane ($\kappa_{\perp}$) direction for comparison. For the up-SF film $\kappa_{\parallel}$ and $\kappa_{\perp}$ were 0.24 W m^{-1} K^{-1} and 0.33 W m^{-1} K^{-1}, respectively. Since BN has a much higher thermal conductivity than that of the SF matrix, the ac-BNSF films have larger κ values than ac-SF does (Figure.4.11a). However, ac-BNSF films do not show anisotropy in thermal conductivity which agrees with the random dispersion of the beta sheets and the BN nanosheets. SF film shows a slightly higher values for $\kappa_{\parallel}$ and $\kappa_{\perp}$ than those of ac-SF film at 0.59 W m^{-1} K^{-1} and 0.45 W m^{-1} K^{-1}, respectively. This might be attributed to the higher crystallinity and better alignment of the glycine-rich matrix [271]. As the BN loading increased, film $\kappa_{\parallel}$ and $\kappa_{\perp}$ of the BNSF films also increased, with $\kappa_{\parallel}$ 30% BNSF reaching 16 W m^{-1} K^{-1}. The anisotropy of the BNSF films increased from 1.3 for SF to ~5.3 for 6%

BNSF and above. Assuming the interfacial thermal resistance can be ignored, the thermal conductivity can be modelled via the Maxwell Garnett equation [267]

$$\kappa_{eff} = \kappa_m \frac{2f(\kappa_i - \kappa_m) + \kappa_i + 2\kappa_m}{2\kappa_m + \kappa_i - f(\kappa_i - \kappa_m)} \tag{4.1}$$

where κ_{eff} is the effective TC of the BNSF film, κ_m the TC of the SF matrix, and κ_i the TC of the BN inclusions. The predicted values are low because the TC of SF matrix is significantly lower than that of BN, and there is no significant contribution to κ by the BN until percolation. The deviation of the experimental data from the model is particularly obvious, and there are numerous reasons why the model may overestimate the value of κ, including interfacial scattering and size effects.

The thermal expansion of ac-BNSF and BNSF films is shown in Figure 4.11a & b. All the samples show a negative coefficient of thermal expansion (CTE), and the absolute value of the CTE decreased as BN loading increased. The BNSF films show a much smaller CTE than the ac-BNSF films, with 30% BNSF having a value of -10.48 ppm K^{-1}, indicating the water annealing, soaked-compression and fixed drying strategy strengthen the SF-BN interactions. The dashed line shows the fitted effective coefficient of thermal expansion α_{eff} using Gibiansky and Torquato model given by

$$\alpha_{eff} = \frac{\alpha_m K_m (K_{eff} - K_i) + \alpha_i K_i (K_m - K_{eff})}{K_{eff}(K_m - K_i)} \tag{4.2}$$

with K_{eff} being the effective bulk (shear) modulus of composites, K_i and K_m the bulk (shear) modulus of the BN inclusions and SF matrix, respectively; α_i and α_m are the CET of the BN inclusions and pure SF, respectively. For the ac-BNSF samples, the modeling

data is slightly lower than the experimental data. For the BNSF samples, the experimental data is slightly lower than the modelling data. It indicates the BNSF films have much more expansion stability upon heating than that of ac-BNSF samples, and this can be attributed to the enhanced bonding during the post treatment of the samples.

4.3.3 Flexible and Electrical Insulation Material

Figure 4.16 shows the mechanical properties of the composite. Silk fibers are known for outstanding mechanical properties, such as high elastic modulus and elongation values. Studies have shown that these exceptional mechanical properties are attributed to the highly ordered β-sheet nanocrystals and hydrogen bonding in the silk proteins[287]. BN is also known for its high mechanical strength and elasticity. The ac-BNSF films show a much larger maximum strain ratio than that of BNSF films. This can be attributed to the large amorphous component in the ac-BNSF sample. Young's modulus of BNSF film is much larger than that of ac-BNSF. There is no clear trend found in the Young's modulus of ac-BNSF films, but its value increased as the BN loading increased. It is known that water molecules functions as plasticizer in the silk protein, which make the silk film flexible. Therefore, this might be caused by the hydrophobicity of the BN, which make it less moisture in the composites when the BN loading is high. And the young's modulus of BNSF films generally decreased with the BN content (Fig. 4.16d), it suggests that the silk component plays a dominated part in controlling the mechanical property and the stronger interactions between silk protein and BN nanosheets in the BNSF film after the wet-pressing.

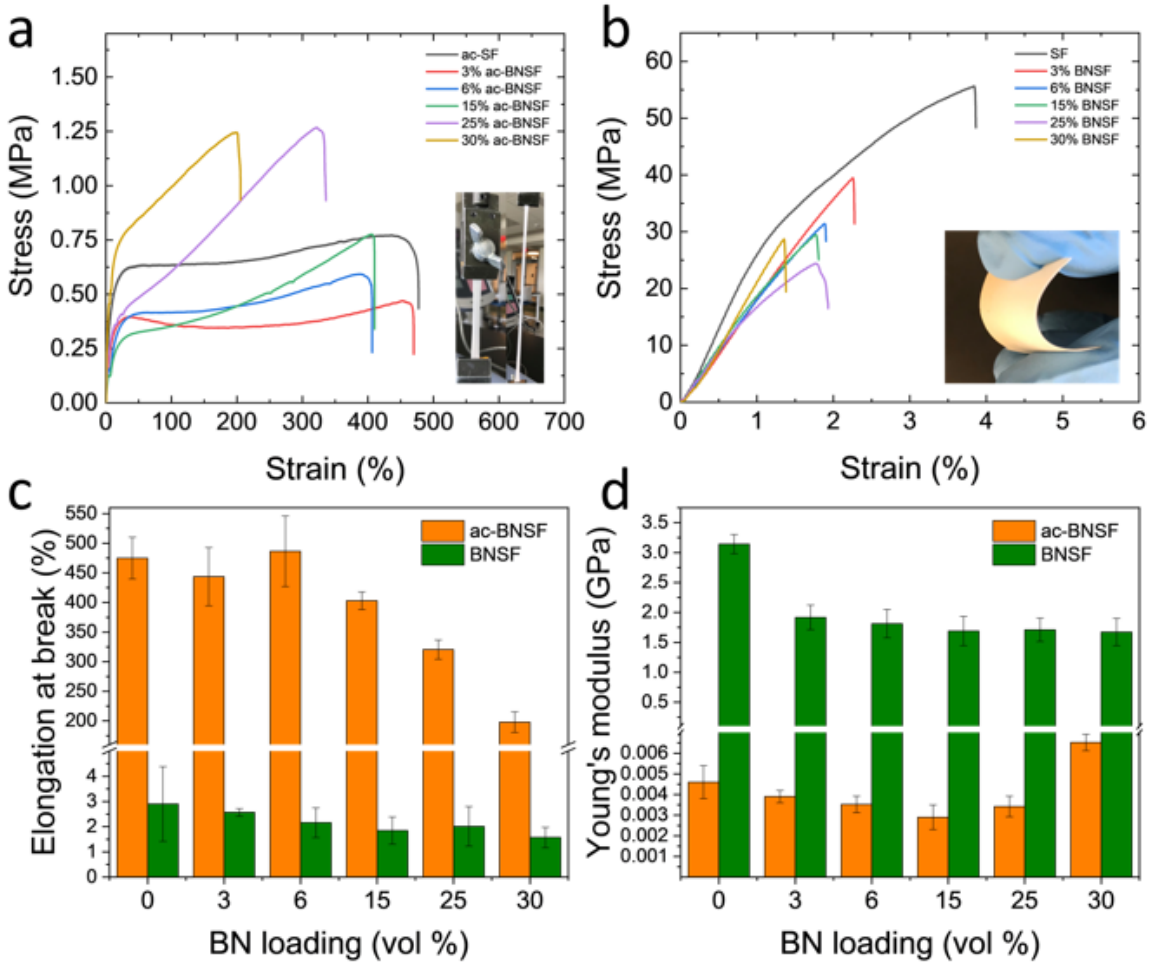

Figure 4.16 Representative stress-strain curves of (a) ac-SF and ac-BNSF films, (b) SF and BNSF films; c) Relations of elongation at break of ac-BNSF and BNSF films with BN loading; d) Relations of Young's modulus of ac-BNSF and BNSF films with BN loading.

The dielectric properties of SF and BNSF films were also investigated to further explore the composite applications. The frequency dependence of the dielectric constant and loss tangent at room temperature are shown in Figure 4.17a and Figure 4.18. The real part of the dielectric constant ε as a function of BN content is shown in Figure 4.17b, which

decreased with the increase of BN content. Its theoretical value was modeled with the Maxwell Garnett equation:

$$\varepsilon_{eff} = \varepsilon_m \frac{2f(\varepsilon_i - \varepsilon_m) + \varepsilon_i + 2\varepsilon_m}{2\varepsilon_m + \varepsilon_i - f(\varepsilon_i - \varepsilon_m)} \tag{4.3}$$

where ε_{eff} is the effective dielectric constant of the BNSF composite, ε_m and ε_i are the dielectric constant of the SF matrix and AlN inclusions, respectively. And f is the volume fraction of those inclusions.

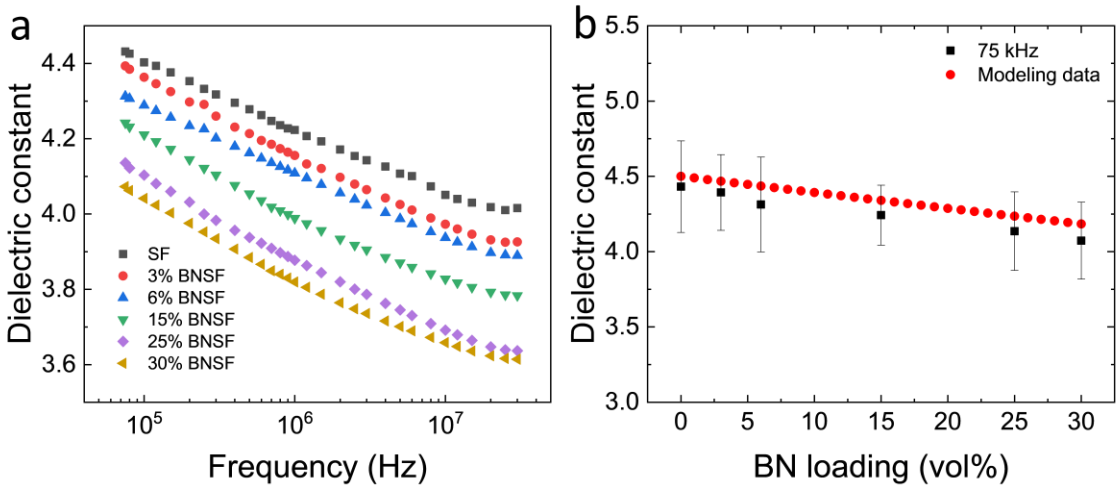

Figure 4.17 a) Dielectric constant of SF and BNSF films with frequency from 75 kHz to 300 MHz; b) Relations of dielectric constant of SF and BNSF films at 75 kHz with BN loading.

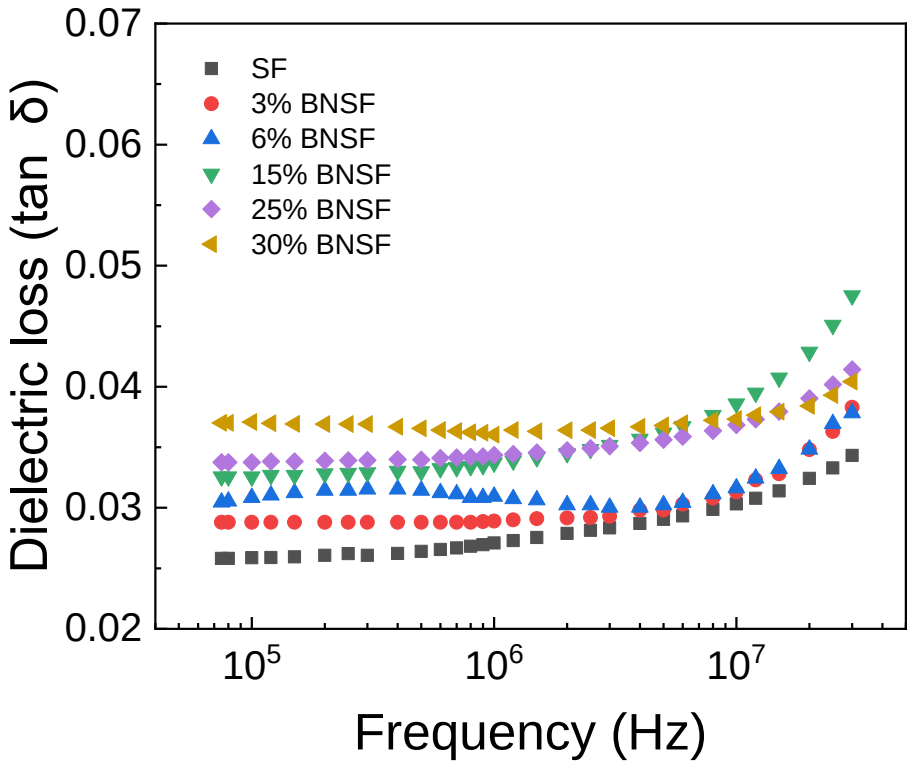

Figure 4.18 Frequency dependence of the loss tangent of SF and BNSF films at room temperature.

4.3.4 Thermal Management Capability and Fire-Retardance of the BNSF Composites

To investigate the thermal management capability of the BNSF, 15% up-BNSF and 15% BNSF were kept in a 65 °C over for long enough time (more than 5 hours), and then taken out and kept in the lab with the temperature at 20 °C. The heat distribution on both samples were recorded by infrared camera at different time. At 5 s, 15 BNSF film shows much smaller high temperature region (white color) than that of 15% up-BNSF film, and the 15% BNSF film also shows a much more pronounced temperature gradient than that of 15% up-BNSF. It took 110 and 35 seconds for 15% ac-BNSF and 15% BNSF films to reach the steady state (20 °C), which indicates the enhanced TC of the BNSF films.

The BNSF composite shows better flame retardancy than SF film (Figure 4.19c & d), which suggests a wider range of applications. Shown in Figure 4.19c, SF film was ignited and the burning lasted 10 s as it bent and eventually shrank. The 30% BNSF film showed a blue flame at 5 s and showed a bright green flame at 90 s due to the boron. That sample maintained its original shape. This result is consistent with the TGA results that 30% BNSF retains up to 59% of its original weight.

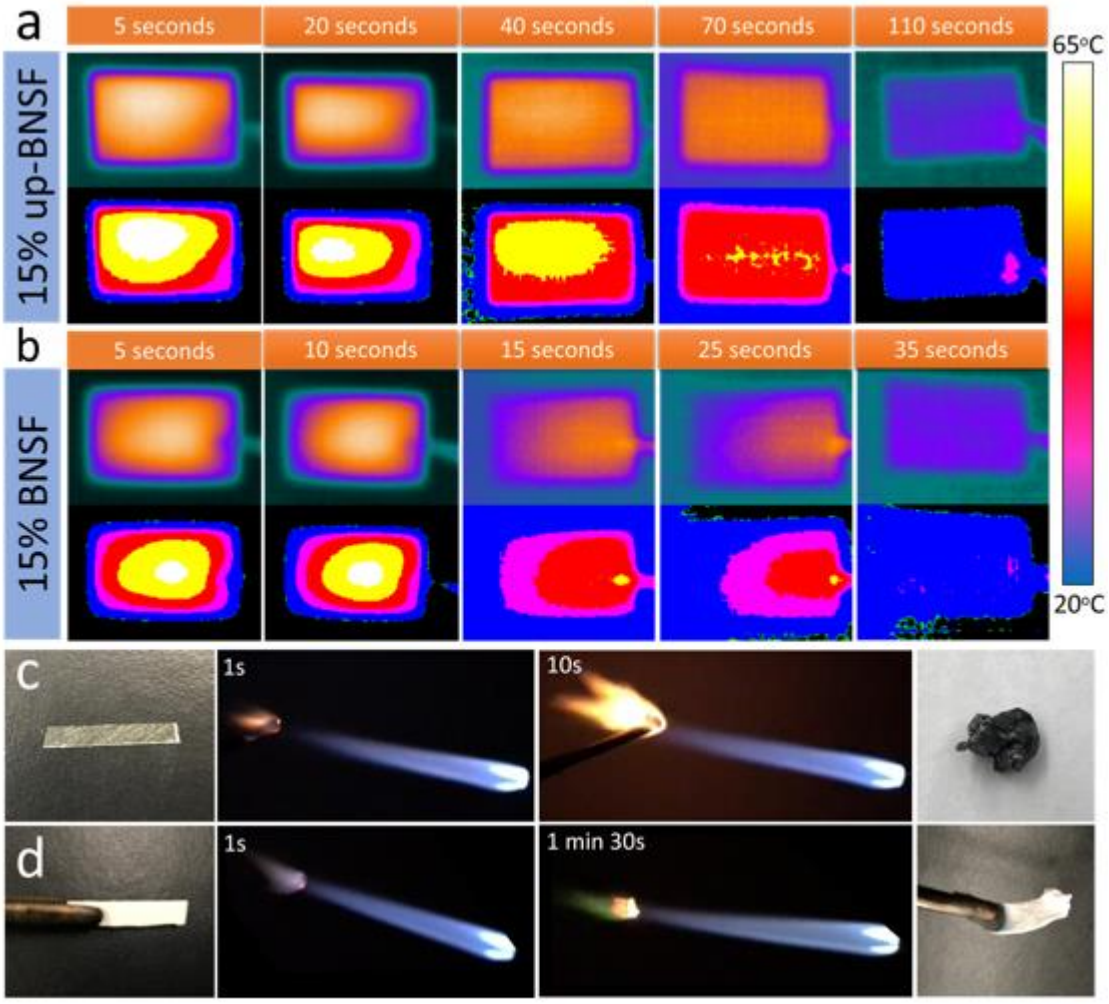

Figure 4.19 15% up-BNSF and 15% BNSF films were kept in a 65 °C oven for long enough time (more than 5 hours), (a) and (b) are the thermal images of 15% up-BNSF and 15 BNSF films, respectively, when they cool down in a lab at 20 °C; Photographs of (c) SF and (d) 30% BNSF films heated by a flame torch at different times.

4.4 Conclusion

In the present study, a facile and low-cost method was used to fabricate SF and BN composite. The BNSF film shows enhanced thermal conductivity of up to 15 W m^{-1} K^{-1} in the in-plane direction and has sizable anisotropy. Based on the cross-section morphology

and X-ray analysis, the enhanced thermal conductivity and accompanying anisotropy are attributed to the good alignment of the BN nanosheets and the strong interaction between the BN and SF matrix. The BNSF composites also have low coefficient of linear thermal expansion and are reasonably stiff yet maintain flexibility. These composites also have good electrical insulation and flame retardancy and shows promising potential as green and renewable materials for thermal management in electronic devices.

Chapter 5

Thermal Conductive Nanofibers from Silk/BN-Sheet Composites

5.1 Introduction

Electrospinning is an unique technique to stretch polymer droplets at high speed by the electrostatic field force and then phase-separate polymer chains and solidified them into fibers [289-291]. The physical properties of the fibers, such as diameter, morphology, mechanical strength, crystallinity, and specific surface area, can be controlled by adjusting the parameters of electrospinning [292]. Controlling the diameter of the fibers has great effect on their physical properties. When the fiber diameter is relatively large, the specific surface area of the fiber will be small, and more defects on the fiber surface could generally reduce the mechanical strength of the fiber [290, 293]. When the diameter of the fiber is less than 1 μm, the mechanical properties of the nanofiber will be greatly improved because the surface defects of the fiber are reduced [294]. Electrospinning is an effective technique to produce nanofibers with tunable properties that has been used in biomedical science, environmental research, clean energy in recent years.

Silk protein is a renewable natural material with good biocompatibility and degradability [143, 295, 296]. Natural silk fiber has excellent mechanical properties, it has extremely high tensile strength and excellent ductility. These excellent functions make it a good application prospect in the biomedicine fields. Silk protein usually comes from silkworm and spiders. Different silk protein sources lead to different physical and chemical properties. Genetic engineering techniques have been used to adjust gene sequences to manipulate amino acid composition to obtain silk protein materials with special functions [297-299]. The secondary structures of silk protein has also been well studied, and the

structure of silk protein can be manipulated to obtain specific functions through post-processing [164, 300]. Natural silk proteins and recombinant silk proteins have been widely used as scaffolds for tissue engineering, and microspheres for drug delivery. It was found that the thermal conductivity of silk can be greatly improved by increasing the crystallinity of silk protein [12, 61, 282]. Boron nitride (BN) nanomaterials have excellent thermal stability, thermal conductivity and stable chemical properties, and also have very good insulation properties [275, 276, 301, 302]. Cell and animal experiments also show that boron nitride has no cytotoxicity and does not have any negative effects on animal signs within a suitable dose, which indicates that boron nitride is also biocompatible [303-305]. In recent years, the application of boron nitride in the field of biomedicine has been gradually developed. Functionally modified boron nitride nanoparticles have made great progress as a delivery system for treating tumor drugs [306-308]. However, the hydrophobicity and extremely stable chemical properties of boron nitride also limit its drug release response in drug delivery [307, 309]. Therefore, by making hydrophobic boron nitride and hydrophilic silk protein into a composite material so that it has more controllable functions will significantly expand its application scope.

In this study, h-BN nanosheets and *Bombyx Mori* silk fibroin protein solution mixture was electrospun into nanofibers. I investigated the interaction between the h-BN and protein matrix. Imact of h-BN on the morphology and diameters of electrospun BN-silk fibroin (BNSF) fibers were studied by scanning electron microscopy (SEM). Effects of h-BN on the secondary structure of silk protein was investigated using Fourier-transform infrared spectroscopy (FTIR). Thermal stability and properties of the BNSF electrospun

nanofibers were studied using thermogravimetric analysis (TGA) and temperature-modulated differential scanning calorimetry (TM-DSC).

5.2 Experimental Section

5.2.1 Raw Materials

Bombyx mori silk cocoons were purchased from Treenway Silks (Lakewood, CO, USA). Silk cocoons were firstly degummed by boiling in a 0.02 M NaHCO3 (Sigma-Aldrich, St. Louis, MO, USA) solution for 30 min. Then the degummed fibers were rinsed three times in DI water to thoroughly remove the sericin coatings. The rinsed silk fibroin fibers were dried in a vacuum oven overnight [3, 310]. The following materials were used as purchased: formic acid (ACS Grade 98%) was purchased from EMD Millipore Corporation (Burlington, MA, USA), calcium chloride (anhydrous, ACS Grade) was purchased from AMRESCO Inc. (Solon, OH, USA), and h-BN powders (~1 μm, 98%) were purchased from Aldrich chemistry.

5.2.2 Material Synthesis

Dried silk fibroin (SF) fibers were dissolved in a formic acid solution with 4% w/v calcium chloride at a concentration of 0.15 g/ml. The SF solution was centrifuged to remove the undissolved residues at 5000 rpm for 10 minutes. h-BN was added into the solution at atvarious weight ratios to the SF (5%, 10%, 20%, 30%, 40%). For example, 5% suggests BNSF fibers consist of 95g silk protein and 5 g h-BN. The BNSF solution was shaken with a vortex mixer for 10 minutes. And the thoroughly mixed BNSF solution was electrospun into nanofibers with an 20 kV applied voltage at room temperature and relative humidity about 50%. The solution flow rate was controlled at 20 μml/min using a syringe

pump (Harvard Apparatus Model 22, Holliston, MA). Electrospun samples were collected between two parallel metal plates lined with aluminum foil, placed at 4 cm from the needle tip. The two parallel plates collecting design can help the solvent evaporate faster from the as-spun fibers and slightly improve the alignment of the fibers as compared to that of the pad collector. In addition, free standing fiber mesh samples can be collected directly. The fibers were then dried in a vacuum oven at 40 °C for 24 hours to remove the solvent residues (verified by FTIR).

5.2.3 Surface Morphology Analysis

The electrospun fibers were characterized with a Leo 1530 VP scanning electron microscope (SEM) (Oberkochen, Germany). All samples were sputter-coated with gold before SEM imaging. Experiments were done with an accelerating voltage ranging between 10 and 20 kV.

5.2.4 Structure Analysis

Structure information of the electrospun fibers was investigated using a Bruker Tensor 27 Fourier-transform infrared (FTIR) spectrometer (Billerica, MA, USA). The spectrometer is equipped with a deuterated triglycine sulfate detector and a multiple reflection, horizontal MIRacle ATR attachment with a Ge crystal (Pike Tech, Madison, WI, USA). A continuously purging nitrogen gas was provided while t he experiments were conducted. The spectra were taken at a range of 4000 to 400 cm^{-1} with 64 background scans and 64 sample scans at a resolution of 4 cm^{-1}. Each sample was characterized at three different spots to ensure homogeneity, and the obtained spectra were then all normalized.

Between each measurement, the ATR crystal was cleaned with a lint-free tissue. The Fourier self-deconvolution (FSD) was conducted as reported previously.

5.2.5 Thermal Analysis

Thermogravimetric analysis (TGA) of BNSF nanofibers was investigated with a TA Instruments Q600 SDT instrument (Wilmington, DE, USA). Each sample weighed between 5-10 mg. Measurements were made from 25 °C to 600 °C at a heating rate of 10 °C/min. All experiments were conducted with continuous nitrogen gas flow rate of 50 ml/min.

Temperature modulated differential scanning calorimetry (TM-DSC) was performed with a Q100 calorimeter (TA Instruments) equipped with a refrigerated cooling system. The N_2 flow rate was set to 50ml/min, and measurements started at -30 °C and ended at 400 °C. The temperature increased at a rate of 2 °C/min and was modulated every 60 seconds at an amplitude of 0.318 °C to measure the reversing heat capacity.

5.3 Results and Discussion

5.3.1 Morphology Study

SEM was performed to analyze the morpology and microstructure of the nanofibers. As seen in Figure 5.1a and b, pure SF nanofibers showed a smooth and uniform surface. For BNSF samples, h-BN nanosheets can be found either immersed into the fiber matrix or spread on the fiber surface. The 5% BNSF sample showed the best fiber alignment. When the concentration of h-BN is 10% or higher, it can be seen that the crosslinking density between the fibers is significantly increased (Fig. 5.1e, h, k and n), suggesting the

interactions between h-BN and the silk fibroin become stronger. The 30% and 40% BNSF samples have a much rougher surfaces due to the high content of h-BN nanosheets. The pure SF nanofibers had the largest fiber diameter with a size distribution centered around 800 nm, while all other samples showed smaller diameters with an average size of 400~750 nm.

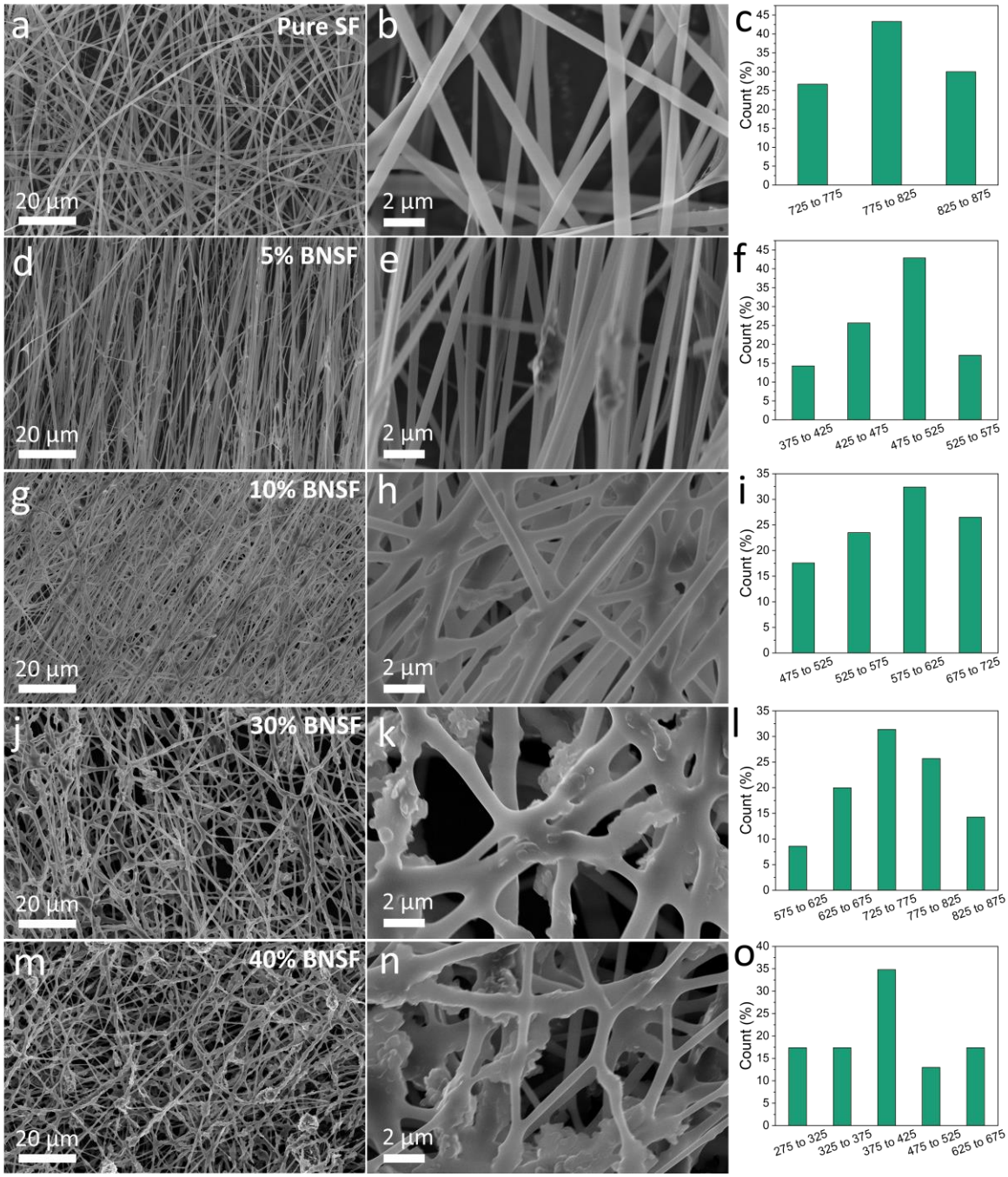

Figure 5. 1 SEM images of pure SF (a, b), 5% BNSF (d, e), 10% BNSF (g, h), 30% BNSF (j, k), and 40% BNSF (m, n) nanofibers; Quantitative analysis of diameter distribution of pure SF (c), 5% BNSF (f), 10% BNSF (i), 30% BNSF (l), and 40% BNSF (o) nanofibers.

5.3.2 Structural Study

FTIR spectroscopy was performed to characterize the interaction between h-BN and silk fibroin and the secondary structure of silk fibroin. All BNSF samples showed two peaks at 774 and 1364 cm-1, which were attributed to the h-BN sheets [311, 312]. As the BN content increases, the intensity of these two peaks gradually increases. The raw BN sheets did not show absorbance in the amide I region. Both the pure SF sample and BNSF samples show a broad amide I peak, while the peak position of the pure SF sample shifted from 1649 cm^{-1} (pure SF) to 1645 cm^{-1} (40% BNSF). This indicates that the pure SF nanofibers are mainly composed of α -helical structure (centered at 1650 cm^{-1}), and the high content of BN nanosheets in BNSF fibers can transform part of the secondary structures into random coils (centered around 1642 cm-1) [143, 164]. During the dissolution and fiber drying process, the α-helix structures in the pure SF protein matrix may be disrupted by the BN nanosheets, and stronger hydrogen bonds were formed between the nitrogen atoms of the BN and the protein chains, which resulted in a reduction in the number of α-helixes in BNSF nanofibers [164].

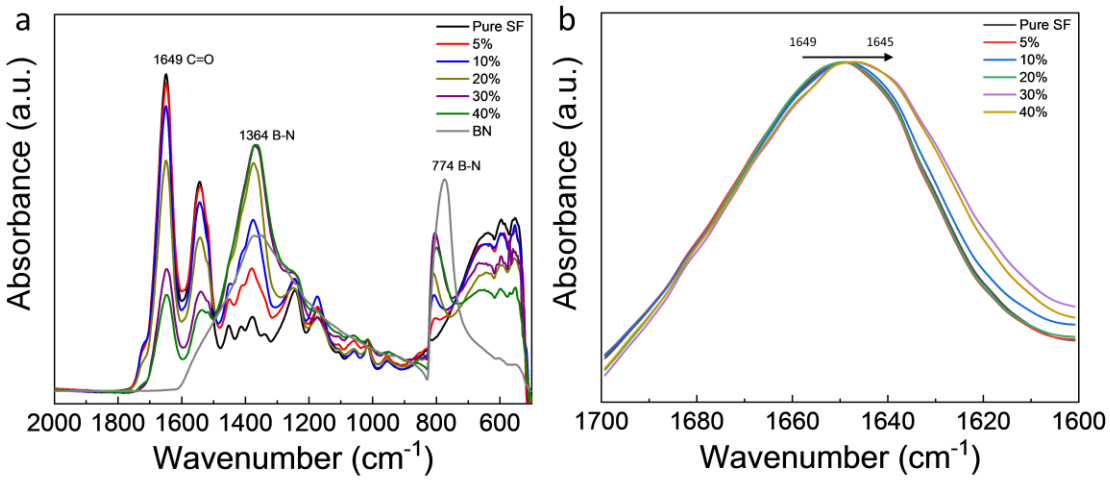

Figure 5. 2 FTIR spectra of a) electrospun pure SF and BNSF nanofibers and raw BN sheets; b) the amide I region of pure SF and BNSF nanofibers.

5.3.3 Thermal Stability and Properties Study

Thermal stability of BNSF nanofibers was first studied by TGA (Fig. 5.3), and their thermal properties are summarized in Table 5.2. Pure BN was highly thermally stable with only 1.4% weight loss until 600 °C. In Fig 5.3, pure SF and BNSF electrospun nanofibers all showed a first weight loss step around 55 °C (Fig. 5.3a), which is caused by the evaporation of bound water molecules. Silk protein can quickly absorb large amounts of water even in a low humidity environment. The pure SF showed the largest weight loss about 15% in this region, while the 40% BNSF sample showed the smallest weight loss about 7.4%. This difference can be attributed to the high hydrophobicity of BN sheets. All the pure SF and BNSF samples showed a major degradation temperature around 330 °C (Fig. 5.3b), which is attributed to the major decomposition of the silk proteins. There are two tiny weight loss steps shifting in the degradation region of 200~300 °C, which may be

caused by the interactions between the silk protein and the BN. The residual weight of pure SF and BNSF electrospun fibers at 800 °C is between 43.7-63.6%, and the residual weight of electrospun fibers generally increases with the increase of BN content, which suggest that interactions between BN and SF improves the thermal stability of the fibers.

Heat flow curves from TM-DSC scans (Fig. 5.4a) confirmed the bound water evaporation and protein decomposition temperatures from TGA. The peaks from bound water evaporation (Tw) are much broader than the protein decomposition peaks (Td), and the pure SF fibers showed the lowest Tw peak compared to all BNSF fibers, indicating the interaction between SF and BN molecules has significant impact on the bound water. Reversing heat capacity curves (Fig. 5.4b) showed that pure SF has the highest onset glass transition temperature at about 120 °C, while 40% BNSF has the lowest onset glass transition temperature at about 96 °C. This suggests that amorphous components such as random coils in silk fibroin gained more mobility when combined with BN nanosheets.

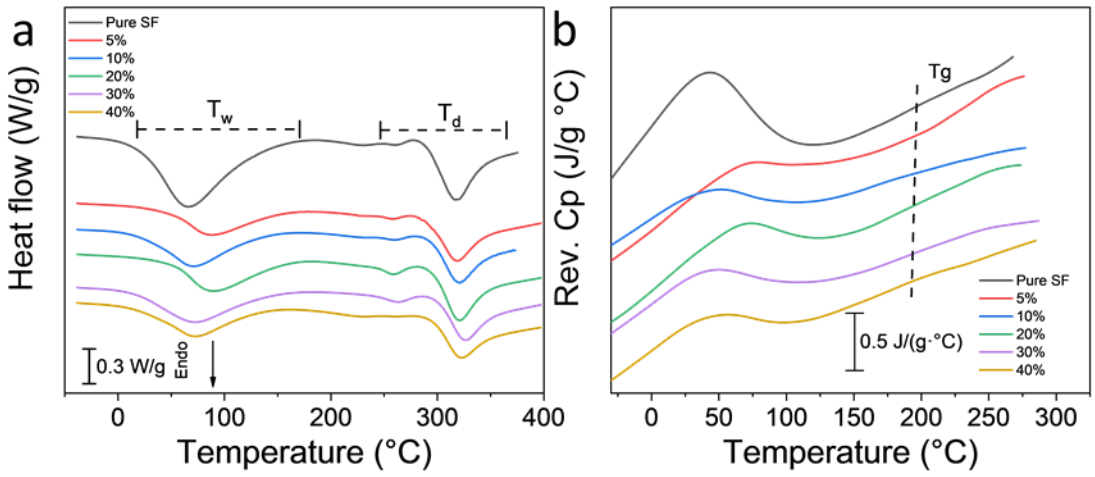

*Figure 5. 3*Thermogravimetric curves of a) BNSF electrospun fibers and raw BN sheets; b) display the 1st derivative TG (DTG) curves of the electrospun nanofibers.

Table 5. 1

Thermal properties of pure SF nanofibers, different BNSF nanofibers and raw BN sheets.

	T_w (°C)*	T_w (°C)**	T_g (°C)**	T_d (°C)*	T_d (°C)**	Mass remaining % at 600 °C*
Pure SF	50.8	66.2	204.9	332.2	319.0	43.7
5% BNSF	53.2	87.7	202.7	331.3	319.4	47.4
10% BNSF	57.9	71.3	177.9	331.6	321.3	50.5
20% BNSF	48.5	89.7	185.6	328.5	321.3	55.5
30% BNSF	54.2	74.4	189.5	339.1	327.2	58.2
40% BNSF	47.9	73.3	190.2	330.7	322.8	63.6
Pure BN	N/A	N/A	N/A	N/A	N/A	98.6

* data is obtained from TGA analysis; ** data is obtained from DSC analysis.

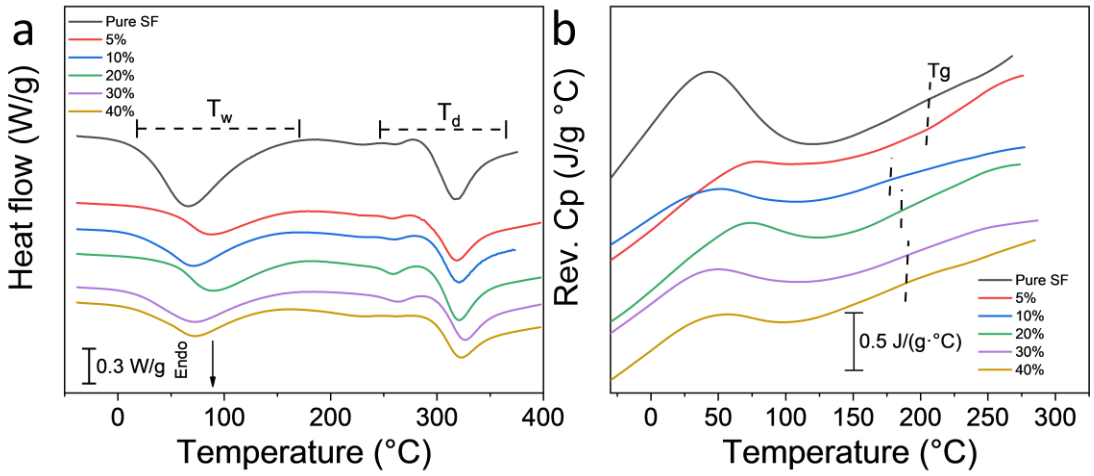

Figure 5. 4 a) Total heat flow curves of electrospun BNSF nanofibers; b) the reversing heat capacity curves of BNSF nanofibers. The scans were at a rate of 2 °C/min and temperature was modulated every 60 seconds at an amplitude of 0.318 °C.

5.3.4 Mechanism of Self-Assembly

Based on the results of secondary structure analysis from FTIR and the thermal analysis from TGA and DSC, a mechanism of self-assembly for the BNSF nanofiber materials is proposed in Figure 5.5. As discussed in Figure 5.2, pure SF and BNSF samples showed a peak shift between 1645 and 1649 cm^{-1}, which indicated that the electrospun pure silk fibers are dominated with α-helical structures. After adding the BN nanosheets, the peak shifted to a lower wavelength, which suggested that the α-helix structure in the protein matrix is reduced and the random coil structure is increased. The hydrogen bonds between BN molecules and the protein backbones can effectively disrupt the α-helix structures and transform them into random coil structures (Fig. 5.5b). Meanwhile, these hydrogen bonds/interactions between BN and SF proteins at different locations will also increase the numbers of crosslinks between the nanofibers, as shown in the SEM (Figure 5.1). The smaller and dispersed distribution of α-helices resulted in higher mobility of the amorphous components, which in turn resulted in broader and lower glass transition temperatures of the composite nanofibers (Figure 5.4).

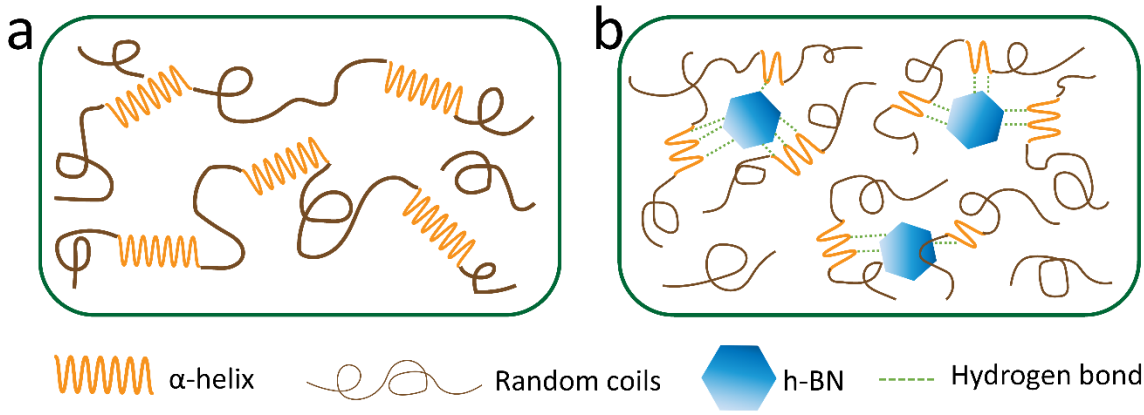

Figure 5. 5 Mechanism of self-assemble structures of a) pure SF electrospun nanofibers; b) displays the disrupted secondary structures of silk fibroin by BN nanosheets.

5.4 Conclusion

In this study, the interactions between h-BN nanosheets and silk fibroin proteins in their electrospun nanofibers were investigated. The morphology and microstructure of the electrospun fibers were observed using SEM. Pure SF sample showed a smooth fiber surface with uniform fiber diameter. Electrospun fibers with a high BN content (over 10%) showed rougher surface morphology and higher crosslink density. FTIR results showed that BN molecules can form hydrogen bonds with silk proteins and transform the α-helical structure of pure SF into random coils, which suggests that the composite material has better flexibility. Due to the high hydrophobicity of BN and the strong interaction of SF-BN, pure SF samples showed the highest bound water content and the lowest bound water evaporation temperature. The good thermal stability of BN can significantly improve the

thermal stability of electrospun BNSF fibers, and a self-assembly mechanism of electrospun BNSF nanofiber materials is proposed.

Chapter 6

Magnetic Biofilms from Silk/Cobalt, Silk/Fe_3O_4 and Silk/$BaFe_{12}O_{19}$ Composites

6.1 Introduction

Magnetic nanoparticles have been widely used in the biomedical fields such as targeted drug delivery, biosensors, cancer treatment and medical imaging, due to their small size, tunable surface chemistry and controllable magnetization [124, 313-315]. Their magnetic properties mainly depend on the size, shape and particle distribution, which may be significantly different from those of their bulk counterparts. Magnetic particles can be easily functionalized with other biopolymer materials such as proteins to improve their mechanical flexibility and biocompatibility. $BaFe_{12}O_{19}$ is a hexagonal magnetoplumbite-type ferrite material [316, 317], which has a remarkably high intrinsic coercivity, saturation magnetization and Curie temperature [318]. These unusual properties give it great potential for use in biological science applications. Cobalt is another broadly used magnetic material, which has stable chemical properties at room temperature, with a Curie temperature of up to 1121 °C[319]. Fe_3O_4 has been used in the biomedicine field recently, specifically with applications on magnetic resonance imaging, targeted drug delivery and tumor hyperthermia [320-324]. Magnetic Fe_3O_4 nanoparticles have high biocompatibility and low cytotoxicity [321, 323], while their production method is simple and low-cost. Due to the existence of various free radical groups in human body fluids, the direct use of magnetic particles in the body can be largely limited and even cause harm to the human body. Therefore, a functional composite material that combines magnetic particles and biocompatible protein materials can significantly enhance the advantages of the two components and expand their scope of application.

Silk fibroin protein materials have shown excellent tensile strength, flexibility and biocompatibility[140, 188, 295]. Natural silk fibers are composed of sericin coating and silk fibroin proteins. Sericin as a protective gel coat wraps the silk fibroin, which can be removed by a degumming process [325]. Silk fibroin protein contains 18 amino acids, of which simple glycine (Gly), alanine (Ala) and serine (Ser) account for above 70% [142, 326]. The secondary structure of silk fibroin includes β sheets, random coils and α helices [164, 327, 328], which greatly control the physical properties. For instance, the mechanical properties of silk fiber can be enhanced by a high content of β-sheet crystals [329, 330]. The highly crosslinked silk fibril network structure through β-sheet crystals is believed to also cause the insolubility of the regenerated silk materials in water and many mild organic solvents[295, 331]. Different types of silk materials, such as silk films, gels, particles and fibers, have shown great potential in biomedical applications [332-335], and by manipulating their secondary structure, one can control the release time and dose during targeted drug delivery[328, 336]. A high content of β-sheet crystals, which can be stimulated through alcohol solutions or water annealing, also helps to improve cell adhesion and tissue growth [189, 335, 337]. Also, the hydrophilic functional groups on the network composed of the protein chain and its crosslinked structure can make the material absorb water while still maintaining its shape and structure well, permitting its use for bone reconstruction, bioelectronics, and *in vivo* tumor models [338-340].

In this study, three magnetic nanoparticles, M-type hexaferrite $BaFe_{12}O_{19}$ (BaM), Fe_3O_4, and cobalt (Co) particles were blended with silk fibroin (SF) proteins to form robust composite films (denoted as BaM-SF, Fe_3O_4-SF and Co-SF, respectively) by a wet-pressing method. Performance of the obtained silk-magnetic functional films were

comparatively tested at various concentrations of different magnetic particles. The effect of particle concentration on the secondary structure of silk fibroins was studied by FTIR analysis. TGA and DSC were used to study the thermal stability and transitions of silk-magnetic composite films, and SEM with EDS was used to characterize the morphology of the silk films and distribution of the particles while the magnetization was studied by magnetometry. This comparative study helps us better understand the interactions between the organic matrix and the inorganic inclusions in composites, which have a variety of potential uses as sustainable or biomedical materials.

6.2 Experimental Section

6.2.1 Materials and Synthesis

Mori silk cocoons were purchased from Treenway Silks (Lakewood, CO, USA). To remove the sericin coatings, silk cocoons were first degummed as reported previously[295]. 10 g of silk cocoons were added to 3 L boiling DI water with 6.36 g of $NaHCO_3$ (Sigma-Aldrich, St. Louis, MO, USA). The mixture was kept boiling and stirred for 30 min. The degummed silk fibers were then removed and rinsed in DI water and the water was changed every 20 min for 3 times. The degummed silk fibroin fibers were dried in a vacuum oven overnight. Dried silk fibroin (SF) was dissolved in a formic acid solution with 4% w/v $CaCl_2$ (AMRESCO Inc, Solon, OH, USA).) at a concentration of 0.15 g/mL. Silk solution was firstly centrifuged to remove undissolved parts at 5000 rpm for 10 min. BaM, Fe_3O_4 and Co particles were added to silk solution at various weight ratios (5%, 10%, 15%, 20% and 30%). More specifically, 5% means that the weight of magnetic particles accounts for 5% of total weight of silk fibroin and magnetic particles. The mixture solution

was vortexed for 10 min to disperse the nanoparticles homogeneously throughout the silk solution. The thoroughly mixed solution was cast onto a self-designed polydimethylsiloxane substrate and left to dry in fume hood for 24 h (Figure 6.1). All samples were water annealed in DI water for 30 min. Through this procedure, silk protein chains in composite films gain additional mobility to self-assemble into a more ordered structure with high β-sheet crystallinity. In addition, the remaining formic acid and $CaCl_2$ were completely removed as verified by wavelength dispersive X-ray fluorescence analysis. To obtain aligned molecular chains with magnetic particle in the protein matrix, the just annealed wet films were also pressed under 500 kPa for 10 min (Figure 6.1), with a wet-pressing method [341]. Then, the wet-pressed samples were placed in a vacuum oven at 30 °C for 2 days before testing.

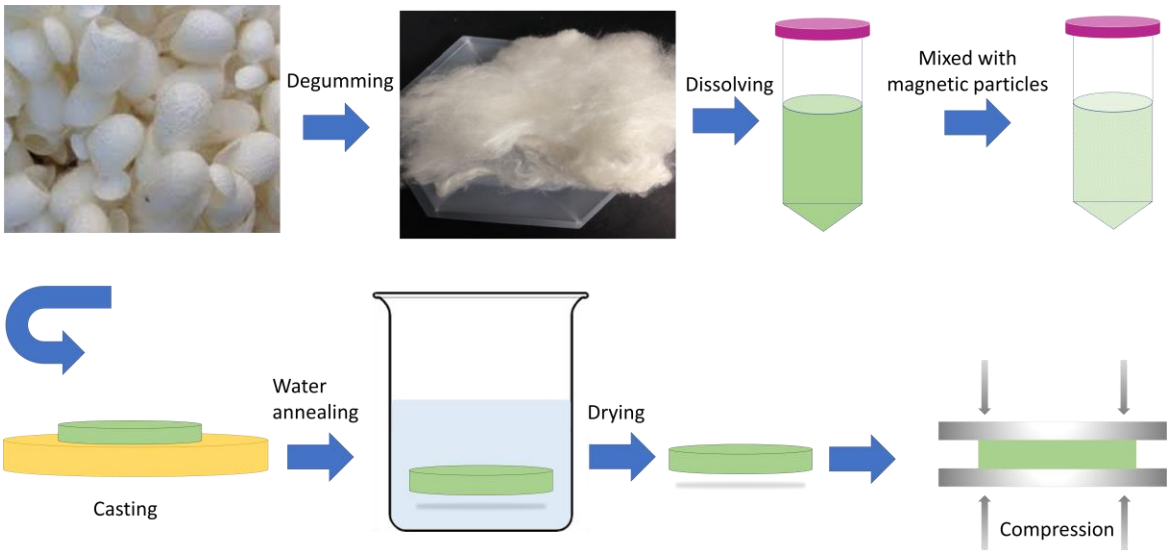

Figure 6.1 Procedures to prepare magnetic silk fibroin composite films.

6.2.2 FTIR Analysis

A Bruker Tensor Fourier-transform infrared spectrometer (FTIR) was used to characterize secondary structure and functional groups of the silk-magnetic composite films. The spectrometer is equipped with a deuterated triglycine sulfate detector and a multiple reflection, horizontal MIRacle ATR attachment (with a Ge crystal, from Pike Tech. (Madison, WI)). Experiments were conducted while continuously purging with nitrogen gas to eliminate unnecessary spectral contributions. The spectra were collected at a range of 4000 cm^{-1} to 400 cm^{-1}. Each run included 128 background scans and 128 sample scans at a resolution of 4 cm^{-1}. Each sample was measured three times, and each run was conducted a different area or side of the same film. The ATR diamond was cleaned between samples with methanol and distilled water to remove any residue from the previous sample. Fourier self-deconvolution (FSD) of the spectrum was conducted as reported previously [37].

6.2.3 SEM and EDS Analysis

The morphology was characterized with a Leo 1530 VP scanning electron microscope (SEM) (Oberkochen, Germany). To get the cross section of the composite films, samples were submerged in liquid nitrogen for 30 seconds each, and then were broken into small sections. All the samples were coated with gold before imaging. The characterization was conducted at various magnifications with an accelerating voltage ranging between 10 and 20 kV. The elemental distribution of magnetic particles in silk matrix was also characterized by energy dispersive X-ray spectroscopy (EDS, Oxford Instruments).

6.2.4 Thermal Property Characterization

Thermal analysis of magnetic silk composite films was conducted with simultaneous differential scanning calorimetry and thermogravimetric analysis (Q600 TA Instruments, Wilmington, DE, USA). The experiment was conducted with continuous nitrogen gas flow rate of 50 mL/min, and each specimen weighed between 5-10 mg. Measurements were made from 30 °C to 800 °C at a heating rate of 10 °C/min. Thermal transitions of all the samples were characterized by temperature-modulated differential scanning calorimetry (TMDSC). The system was purged with dry nitrogen gas at a rate of 50 mL/min and had an internal refrigerated cooling system. Indium was used to calibrate the heat flow and temperature of the DSC. Each piece of film sample weighed 5-7 mg. The measurement was conducted with Al pans at a heating rate of 2 ℃/min with a modulation period of 1 min and set temperature amplitude as 0.318 K, from -40 ℃ to 400 ℃.

6.2.5 Magnetic Characterization

Magnetic properties were characterized with a vibrating sample magnetometer (VSM) attachment to a Physical Property Measurement System (PPMS, Quantum Design, San Diego, CA, USA). Measurements were done at room temperature with magnetic fields up to 4 T. The procedure is summarized in Supplemental Figure 1.

6.3 Results and Discussion

6.3.1 Structural Analysis

FTIR is an effective tool to characterize the secondary structure and functional group of silk protein materials [164, 327] (Figure 6.2). For Fe_3O_4-SF samples, there is a

sharp peak at 1622 cm^{-1}, suggesting the β-sheet crystal structures are dominant. However, the peak shoulder at 1646 cm^{-1} (random coils structures) increased with Fe_3O_4 content, indicating that relative fraction of β-sheet crystals decreased. All BaM-SF samples also showed a sharp peak at 1620 cm^{-1}, indicating a predominant β-sheet secondary structure due to the wet-pressing method. The peak at 1650 cm^{-1} slightly increased when more nanoparticles were present, suggesting that the BaM particles in the silk matrix can also slightly enhance the formation of alpha helix or random coils structures. However, this structural change is not as significant for the Fe_3O_4-SF samples. Compared to the FTIR patterns of BaM-SF and Fe_3O_4-SF, Co-SF samples showed much sharper peaks at 1622 cm^{-1}, suggesting it has the highest β-sheet crystal content among the three types of magnetic inclusions. In addition, the shoulder at 1651 cm^{-1} decreased with the increase of Co particle content. In the amide II region, all three types of composite films showed peaks around 1615 cm^{-1}, which suggests Tyr side chains structure.

A quantitative analysis of the secondary structure contents was performed with FSD (Fig. 6.2b, d, and f) [164]. It shows that β-sheet content of SF sample is around 39% composed of mainly inter-molecular β sheets [295]. The β-sheet content of the Fe_3O_4-SF samples decreases with Fe_3O_4 content, reaching 33% at 30 wt%, while the random coils content increased 29-32% slightly. Similar behavior was found in BaM-SF samples, where the β-sheet content decreased slightly with increase in BaM weight fraction, while the random coils content nominally increased. In contrast, for the Co-SF samples, the secondary structure remained effectively unchanged.

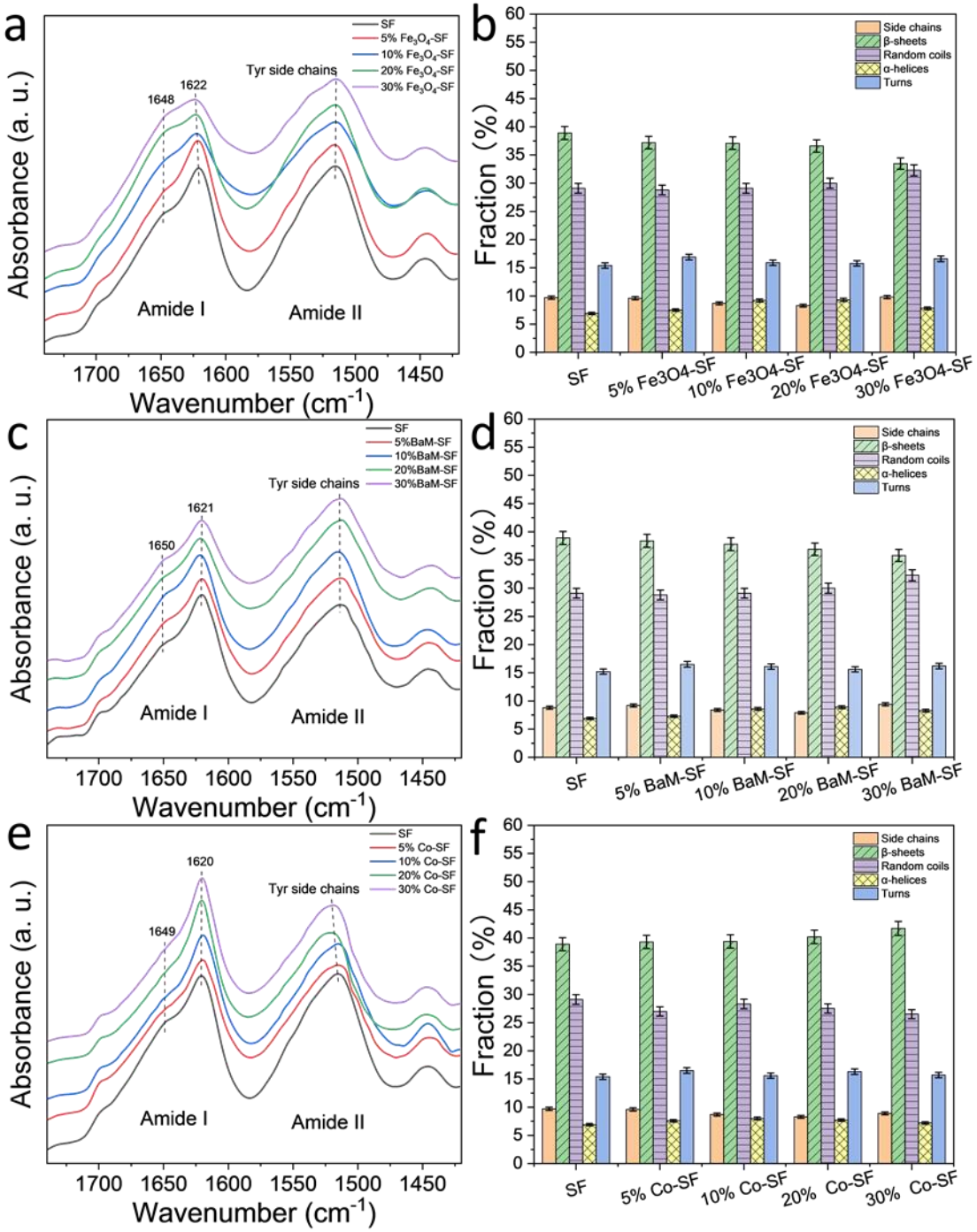

Figure 6.2 FTIR spectra of a) Fe3O4-SF, c) BaM-SF and e) Co-SF composite films. Secondary structure contents of b) Fe3O4-SF, d) BaM-SF and f) Co-SF calculated from a Fourier self-deconvolution curve fitting method.

6.3.2 Morphology Analysis

Surface and cross-section morphology of SF and magnetic silk composite films are shown in Figure 6.3. Squamous patterns evenly spread out across the cross section of SF and 20% BaM-SF films (Figure 6.3a and e). Cross section of 20% Fe_3O_4 (Figure 6.3c) showed a rougher morphology with wrinkles and densely distributed particles. Cross section of 20% Co-SF (Figure 6.3g) showed evenly distributed holes with connected wrinkles. When comparing the surface samples to the cross-sectional, the surface seems to be much more homogenous, containing fewer aggregates and wrinkles. SF film shows a smooth and uniform surface (Figure 6.3b). 20% BaM-SF sample (Figure 6.3f) showed a relatively rough surface, and BaM particles distribute homogenously instead of forming big aggregates. Compared to the surface morphology of 20% BaM-SF, 20% Fe_3O_4 (Figure 6.3d) and 20% Co-SF (Figure 6.3h) films showed smooth and uniform surface morphology with shallow pits.

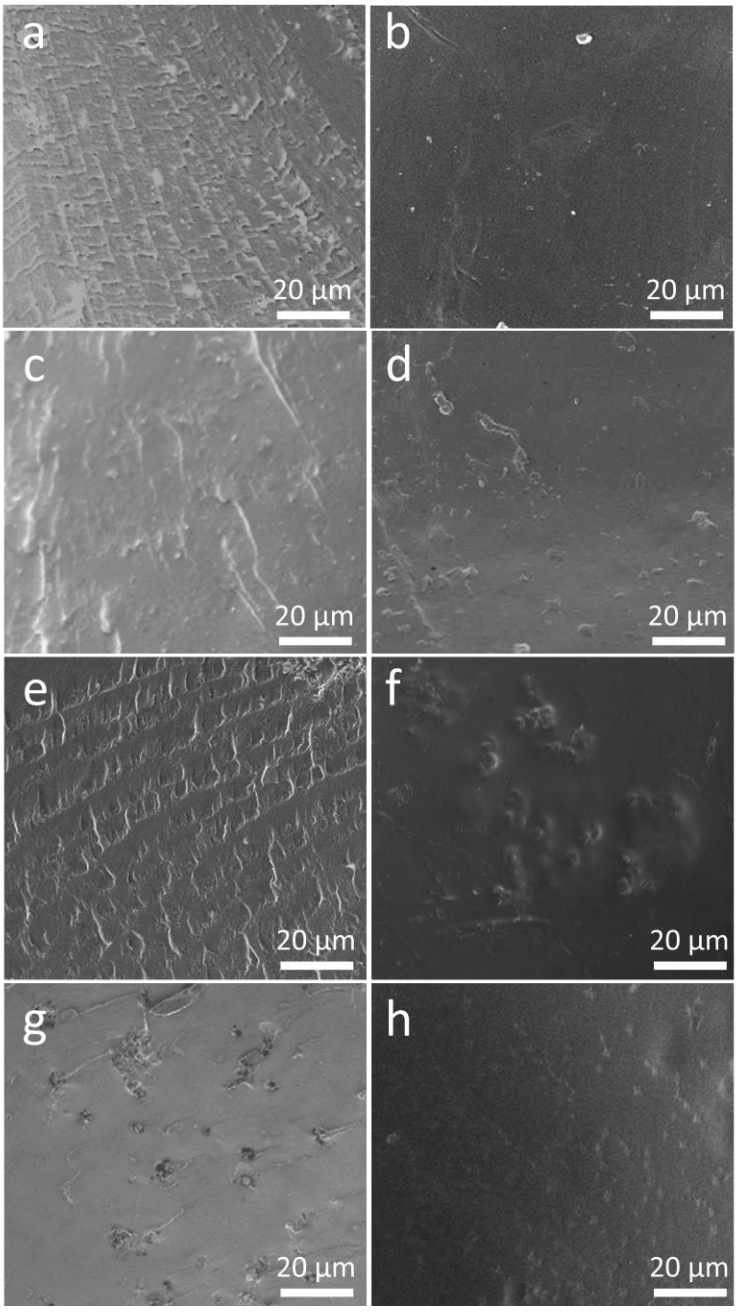

Figure 6.3 a, c, e and g are the cross section of SF film, 20% Fe_3O_4-SF, 20% BaM-SF and 20% Co-SF composite, respectively. b, d, f and h are the surface morphology of SF film, 20% Fe_3O_4-SF, 20% BaM-SF and 20% Co-SF composite, respectively.

6.3.3 Thermal Analysis

Thermal stability of the silk magnetic composite films was characterized by TGA (Figure 6.4). All three types of magnetic particles are thermally stable with no degradation for all of them up to 800 °C. All Fe_3O_4-SF composite films showed a small degradation between 209~226 °C (T_{d1}), a major degradation between 296~303 °C (T_{d2}) and a third degradation around 650 °C (T_{d3}). The residual weight of Fe_3O_4-SF samples at 800 °C was between 26.6% to 48.2%, which generally increased with Fe_3O_4 content. All BaM-SF composite films showed a small degradation between 238-251 °C (T_{d1}) and a major degradation between 301-309 °C (T_{d2}). When the BaM concentration was 10% or above, a third degradation was found around 700 °C (T_{d3}). The residual weight of BaM-SF samples at 800 °C was between 27.1% to 46.1%, and the residual weight of increased with BaM content. All Co-SF composite films showed a small degradation at 214~233 °C (T_{d1}) and a major degradation at 300~307 °C (T_{d2}). The residual weight of Co-SF samples at 800 °C is between 27.1% to 55.1%, and increased with Co content. However, no third degradation peak (T_{d3}) was observed around 600~700 °C for any of Co-SF samples. The first small degradation is mainly from the unstable part of silk proteins [282, 342, 343]. BaM-SF samples showed a higher T_{d1} than that of the other two types of composites, suggesting that BaM particles were able to best protect silk materials. The third degradation for Fe_3O_4-SF and BaM-SF samples is probably from a stable phase that formed when the Fe combined with the silk protein.

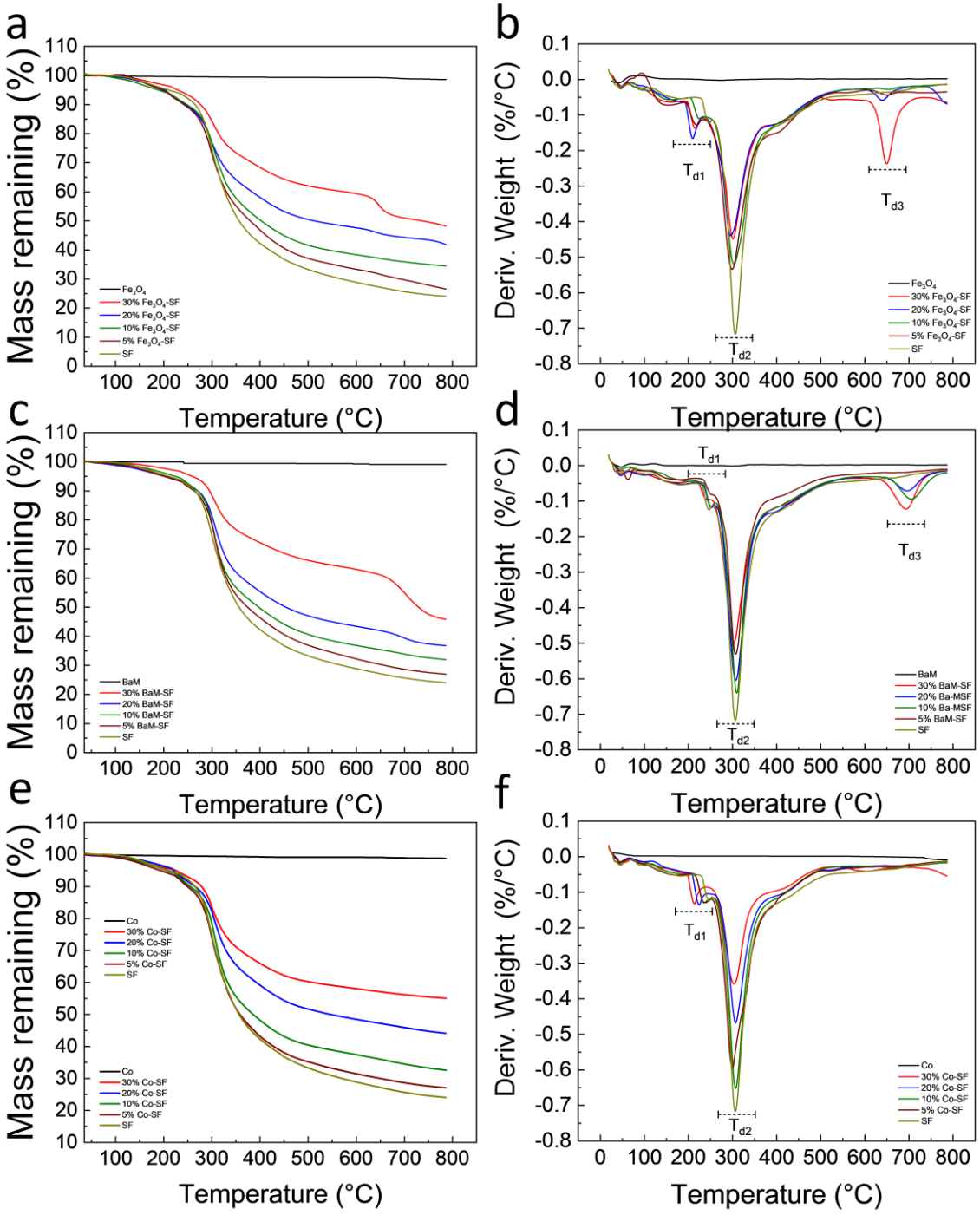

Figure 6.4 Thermogravimetric curves of a) Fe_3O_4-SF, c) BaM-SF and e) Co-SF composite films. The 1st derivative TG (DTG) curves of b) Fe_3O_4-SF, d) BaM-SF and f) Co-SF composite films.

Table 6.1

Thermal properties of Fe_3O_4-SF, BaM-SF and Co-SF composite films

	T_w (°C)	T_{d1} (°C)	T_{d2} (°C)	T_{d3} (°C)
SF	48	245	308	-
5% Fe_3O_4-SF	49	219	303	657
10% Fe_3O_4-SF	52	226	297	659
20% Fe_3O_4-SF	46	209	296	641
30% Fe_3O_4-SF	50	215	303	650
5% BaM-SF	63	250	308	-
10% BaM-SF	64	251	309	708
20% BaM-SF	60	250	306	697
30% BaM-SF	61	238	301	696
5% Co-SF	52	233	300	-
10% Co-SF	54	234	307	-
20% Co-SF	50	223	307	-
30% Co-SF	52	214	303	-

Note. Data was obtained from TGA. The weight derivative peak position was used as the degradation temperature.

Heat flow and reversing heat capacity of magnetic silk composite films are shown in Figure 7.5. Heat flow analysis shows that all three type composite films have a major degradation about 260 °C, which is from the decomposition of silk proteins. The amorphous part of the polymer has a greater mobility with increasing temperature, which is defined as the glass transition. The glass transition is gradual and reversible, and the heat capacity of the polymer changes dramatically during this transition[344]. All Fe_3O_4-SF samples showed a similar glass transition temperature at around 172 °C. The glass transition temperature of BaM-SF composite films increased from 172 °C for SF, to 192 °C for 30% BaM-SF, suggesting that the mobility of the amorphous structure in BaM-SF

composites can be tuned by the BaM particles. All Co-SF composite films showed a glass transition temperature around 180 °C.

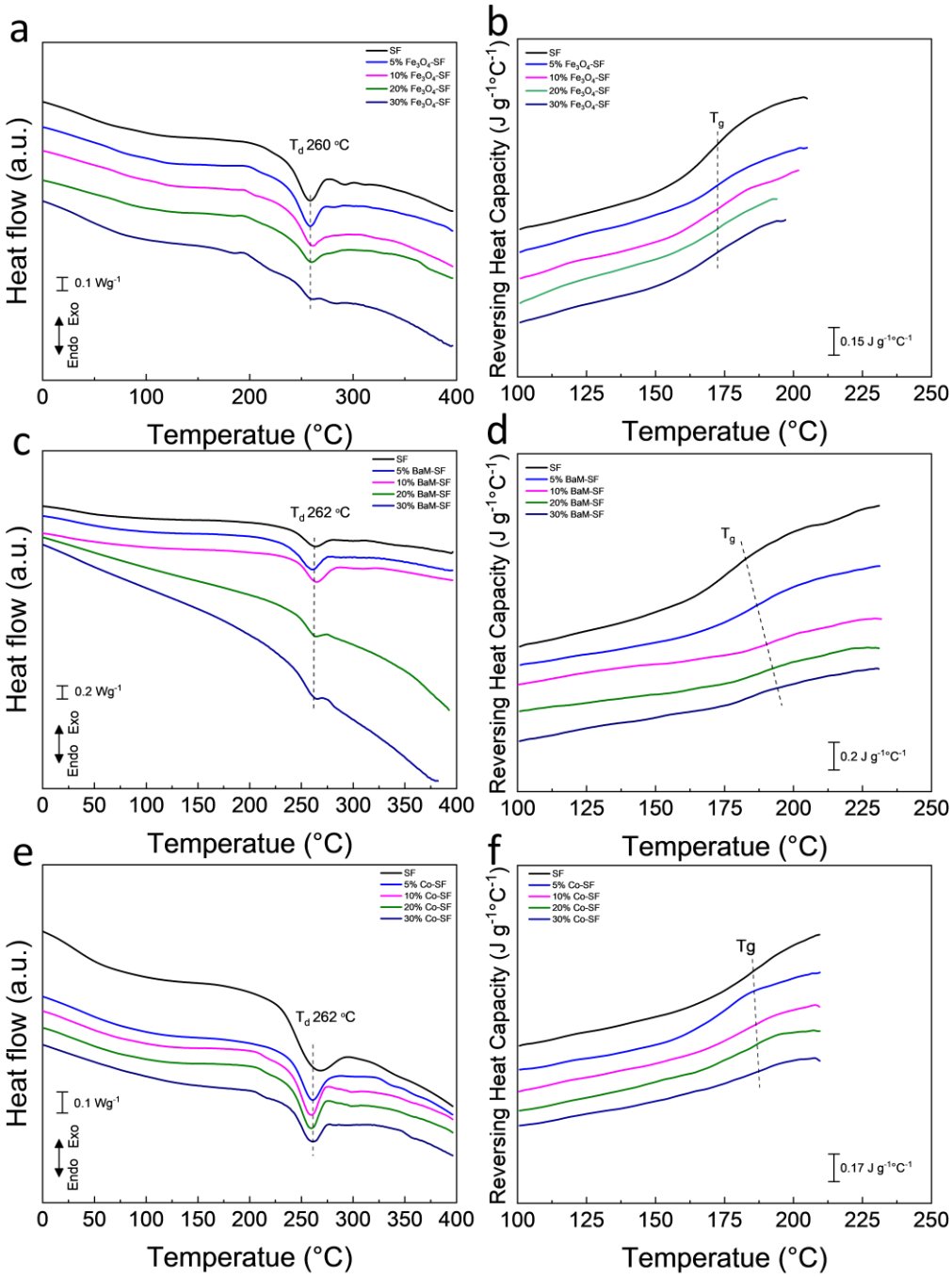

Figure 6.5 Heat flow of a) Fe_3O_4-SF, c) BaM-SF and e) Co-SF composite films. Reversing heat capacity of b) Fe_3O_4-SF, d) BaM-SF and f) Co-SF.

6.3.4 Magnetization Analysis

Magnetization of the three types of composite films showed typical ferromagnetic behavior with coercive field of about 128 Oe, 3660 Oe and 165 Oe for Fe_3O_4, BaM and Co nanoparticles, respectively (Figure 6.6a-c). The dependence of the magnetization on weight fraction of magnetic particles are shown in Figure 6.6d. The saturation magnetization M_s of Fe_3O_4, BaM and Co nanoparticles is about 61 emu/g, 68 emu/g and 156 emu/g, respectively. Since silk protein matrix has magnetic susceptibility near zero, it can be assumed that the moment of the composite films depends only on the net weight of the magnetic particles. Therefore, one would anticipate that the M_s value of the composite should be about xM_s, where x is the weight fraction of magnetic particles. All samples display a linear dependence of Ms on weight fraction; however note that neither line intercepts the origin. Presumably, all three types magnetic particles partially dissolved in the formic acid solution, saturating the solution at about 3.7 wt%, 3.4 wt % and 1.1 wt % (horizontal intercept of the graph) for Fe_3O_4, BaM and Co particles, respectively. In any case, at sufficient loading, of three types of composite films maintain a sizable magnetization for potential use in MRI imaging or targeted drug delivery.

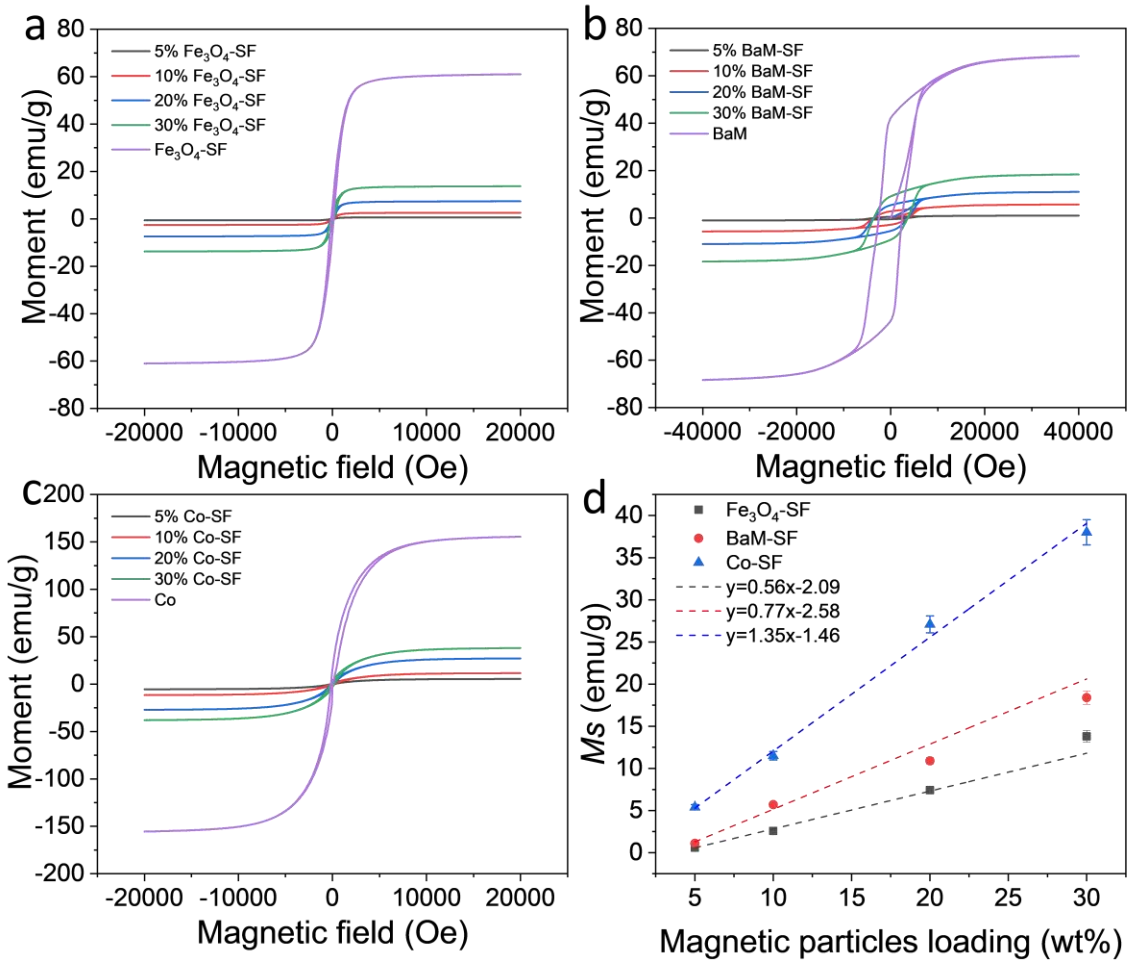

Figure 6.6 Magnetization and Hysteresis loops of a) Fe_3O_4-SF, b) BaM-SF and c) Co-SF composite films at room temperature. (d) Saturation moment of Fe_3O_4-SF, BaM-SF and Co-SF composite films as a function of the magnetic particle content.

6.3.5 Self-Assembly Mechanism

With the experimental evidence and analysis provided above, I can confirm that Fe_3O_4 and BaM particles can slightly prevent the β-sheet crystal formation, suggesting that the Fe_3O_4-SF and BaM-SF composite films have more noncrystalline structures. This is probably caused by the strong coordination bonding between Fe^{3+} ions and carboxylate

ions on silk fibroin chain [345-347]. Most β-sheet crystals usually formed during the water annealing and wet pressing process. However, when the Fe_3O_4 and BaM particles were present, the strong coordination bonding limited the mobility of silk fibroin chain, interrupted the regularly arrange chains and further prohibit the β-sheet crystal formation. On the other hand, the amount of dissolved Co is minimal as compared to that of the Fe and so the addition of Co nanoparticles has minimal effect on the secondary structure.

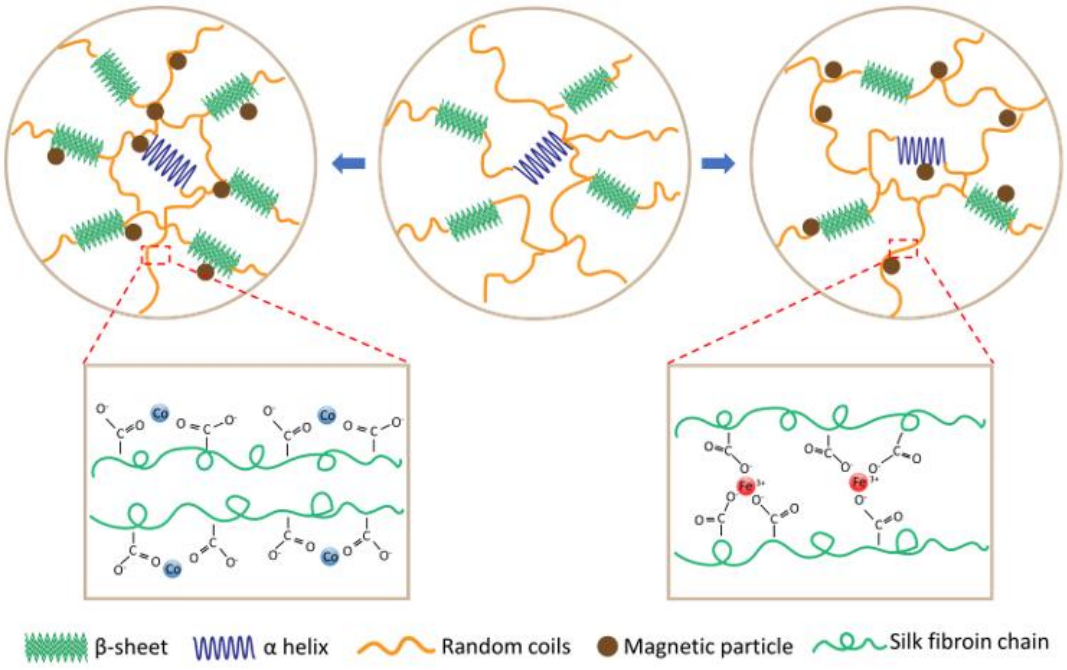

Figure 6.7 Mechanism of Fe_3O_4, BaM and Co magnetic particles on the secondary structures of silk protein.

6.4 Conclusion

In this study, effects of three commonly used biocompatible magnetic particles on silk protein secondary structures and properties were discussed. Structural analysis using FTIR indicated that Fe_3O_4 and BaM particles prohibited β-sheet crystal formation, while the addition of Co particles had minimal effect. The decrease of crystal structure is probably caused by the strong coordination bonding between Fe from Fe_3O_4/BaM and carboxylate ions on silk fibroin chains. The magnetization studies indicated that almost 4 wt% was dissolved and this likely led to the formation of the phases that coincide with the high temperature degradation (> 640 °C) that was seen in both Fe_3O_4-SF and BaM-SF composites. All three types of magnetic composite films maintained high magnetization, suggesting potential biomedical applications such as MRI imaging, tissue regeneration, magnetic hyperthermia and controlled drug delivery in the future.

Chapter 7

Magnetic Nanofibers from Silk/ BaM Composites

7.1 Introduction

Magnetic materials are beginning to play a significant role in the biomedical field. Through the use of an external magnetic field, magnetic nanoparticles (MNPs) can be influenced to perform tasks such as delivering drugs to specific sites of the body [348-350] or increasing the temperature in a specific region of the body to eliminate malignant cells [351-353]. Attaching biological labels such as antibodies to MNPs allows them to detect various biomolecules so they can be used in biosensors and in the diagnosis of certain ailments [354, 355].

Incorporating magnetic nanoparticles into biocompatible polymers provides a means to protect the magnetic material from its surrounding environment as well as shielding a living organism from the potential toxicity of the compound [356]. In tissue engineering, cells can be magnetically labeled so that a magnet can guide the cells to form desired two-dimensional and three-dimensional structures to later differentiate and form desired tissues. A magnetic polymer scaffold could be used as a more localized and noninvasive means of using the many applications of MNPs *in vitro* and *in vivo* [357]. Primarily, magnetic scaffolds could enhance tissue engineering by directing magnetically labeled cells, growth factors, and other needed material in a way that contributes to tissue development both before and after implantation into the body [358]. The use of an external magnetic field to cause physical changes in the magnetic scaffolds, like stretching or contracting [359, 360], could provide mechanical cues to cells that could also help tissue development [361]. Additionally, drugs labeled with MNPs could be led by the scaffold to

specific regions of the body, or an external magnetic field could be used to change the dimensions of the scaffold and cause the scaffold to release drugs as needed by the body [124, 361, 362].

Silk is one of the commonly natural polymer used to make protein-based biomaterials [3, 125, 295, 363]. Silk fibers mainly consist of the protein fibroin, which appears as a double-stranded fiber, and sericin, which coats the fibers and bonds them together. Silk fibroins can be easily fabricated into various structures such as films, fibers, gels, particles and scaffolds [125, 310, 338, 364-366]. Due to its predominant β-sheet crystal structure, silk fibroins are also known to have excellent mechanical stability and tunability in terms of its biodegradation rates and mechanical properties [154, 194, 270, 296]. The physical and chemical properties of silk fibroins can vary based on different amino acid sequences, artificial treatments with substances such as methanol, and composites resulting from mixing silk with various other materials [125, 367]. Recently, a water annealing method was found to induce up to 30% crystallization of β-sheets [188, 189]. That crystalline structure in the silk protein matrix can act as a crosslinker to efficiently encapsulate small inclusions such as nanoparticles or inorganic drugs in the matrix [188, 189].

In this study, biocompatible M-type barium hexaferrite ($BaFe_{12}O_{19}$ or BaM) was added into the *B. Mori* silk fibroin protein, and fibers were produced by electrospinning [289, 366, 368, 369]. The objective was to develop composites whose properties can be modified to fit the application. I have investigated the interaction between the magnetic inclusions and the protein matrix, measured their physical properties and analyzed the

magnetic field dependence of the cytotoxicity of these hybrid fibers with human embryonic kidney cell proliferation.

7.2 Materials and Methods

7.2.1 Raw Materials

Bombyx mori silk cocoons were purchased from Treenway Silks (Lakewood, CO, USA). Silk cocoons were firstly degummed by boiling in a 0.02 M $NaHCO_3$ (Sigma-Aldrich, St. Louis, MO, USA) solution for 30 min. Then the degummed fibers were rinsed three times in DI water to thoroughly remove the sericin coatings. The rinsed fibers were dried in a vacuum oven overnight. The following materials were used as purchased: M-type barium hexaferrite ($BaFe_{12}O_{19}$), Alfa Aesar (MA, USA); formic acid (ACS Grade 98%), EMD Millipore Corporation (Burlington, MA, USA); and anhydrous calcium chloride, AMRESCO Inc. (Solon, OH, USA).

7.2.2 Material Synthesis

Dried silk fibroin (SF) was dissolved in a formic acid solution with 4% w/v calcium chloride at a concentration of 0.15 g/mL. The SF solution was centrifuged to remove the undissolved parts at 5000 rpm for 10 minutes. BaM was added to the solution in various weight ratios to the silk fibroin, inculding BaM/SF= 0 (0% BaM), 1/20 (~4.8% BaM), 1/10 (~9.1% BaM), 1/4 (20% BaM), 1/2 (~33% BaM). The SF/BaM solution was shaken with a vortex mixer for 10 minutes. The thoroughly mixed BaM/SF solution was electrospun into nanofibers with an 18-kV applied voltage at room temperature and relative humidity between 45 and 65%. A syringe pump (Harvard Apparatus Model 22, Holliston, MA) was used to control the solution flow rate at 15 µml/min. Electrospun samples were collected

between two parallel metal plates lined with aluminum foil, placed at 4 cm from the needle tip (Figure 7.1). Collecting from the two parallel plates can help the solvent evaporate faster from the as-spun fibers and slightly improve the alignment of the fibers as compared to that of the pad collector[292]. In addition, free standing fiber mesh samples can be collected directly. The fibers were then dried in a vacuum oven for 24 hours.

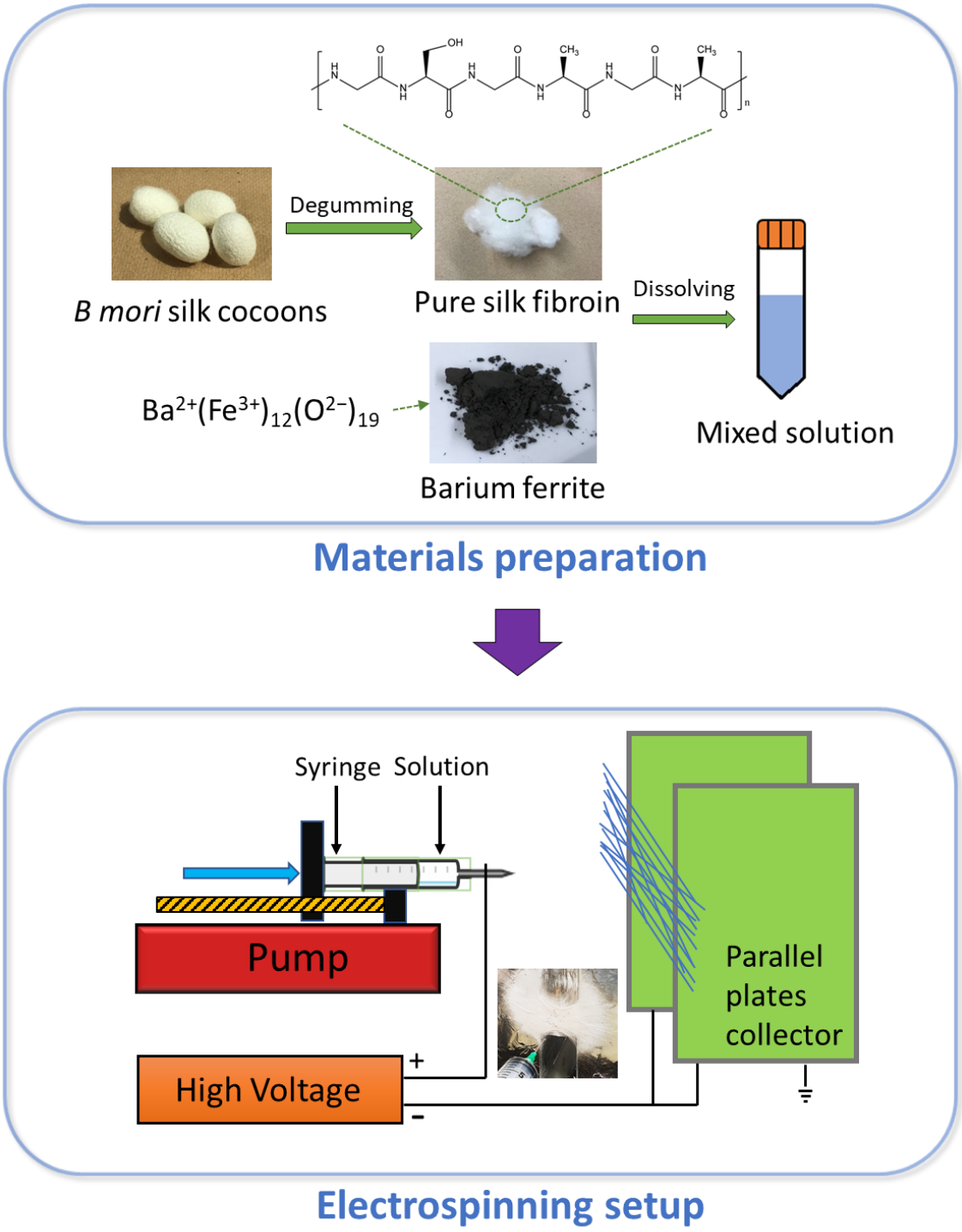

Figure 7.1 A diagram shows procedure to prepare SF/BaM solution and electrospun SF/BaM composite nanofibers.

Samples collected directly from the vacuum oven are called as-spun (AS) samples. Some as-spun samples were then annealed in DI water for 1 h and then dried in a vacuum oven for another 24 h are designated water-annealed (WA) samples. To further check the impact of stretching on the alignment of the electrospun fibers, the just annealed wet 1/20 BaM/SF sample was stretched at 110%, 150% and 200% ratio to its original length before the drying procedure. The 100% (original length) 1/20 BaM/SF sample was used as a control. Stretched electrospun fibers were immediately fixed at two ends and held in DI water for 30 min, and then dried in the vacuum oven for 24 h.

7.2.3 Surface Morphology Characterization

The electrospun fibers were imaged with a Leo 1530 VP scanning electron microscope (SEM) (Oberkochen, Germany). All samples were sputter-coated with gold before SEM imaging which was done with an accelerating voltage ranging between 10 and 20 kV.

7.2.4 Structure Characterization

A Bruker Tensor 27 Fourier-transform infrared (FTIR) spectrometer (Billerica, MA, USA) was used to investigate the structure information of the electrospun fibers. The spectrometer is equipped with a deuterated triglycine sulfate detector and a multiple reflection, horizontal MIRacle ATR attachment with a Ge crystal (Pike Tech, Madison, WI, USA). Experiments were conducted while continuously purging with nitrogen gas. The spectra were taken at a range of 4000 to 400 cm^{-1} with 64 background scans and 64 sample scans at a resolution of 4 cm^{-1}. Each sample was characterized at three different spots to ensure homogeneity, and the obtained spectra were then all normalized. Between each

measurement, the ATR crystal was cleaned with a lint-free tissue. The Fourier self-deconvolution (FSD) was conducted as reported previously [164].

7.2.5 Thermal Stability Characterization

Thermal analysis of BaM/SF electrospun fibers was conducted with simultaneous differential scanning calorimetry and thermogravimetric analysis (Q600 TA Instruments, Wilmington, DE, USA). The experiment was conducted with continuous nitrogen gas flow rate of 50 mL/min, and each specimen weighed between 5-10 mg. Measurements were made from 30 °C to 800 °C at a heating rate of 10 °C/min.

7.2.6 Mechanical Testing

Mechanical properties of samples were characterized with an EZ tensile tester (Shimadzu, Kyoto, Japan). The electrospun fiber mesh was cut into a rectangular shape with length 10 mm and width 3 mm. The average thickness of the electrospun fiber mesh was around 0.1 mm. Each end of the sample was fixed with adhesive tape which was then placed between the test clamps. Tensile tests were executed at 5 mm/min until specimen failure. The cross-sectional area of the specimen was used to calculate the stress and Young's modulus of the electrospun fiber mesh.

7.2.7 Magnetic Property Characterization

Physical property measurement system (PPMS, Quantum Design, San Diego, CA, USA) with a vibrating sample magnetometer (VSM) attachment was used to measure the magnetic properties. The experiment was performed at room temperature with magnetic fields up to 4 T. The procedure of measurements is summarized in Figure 7.2.

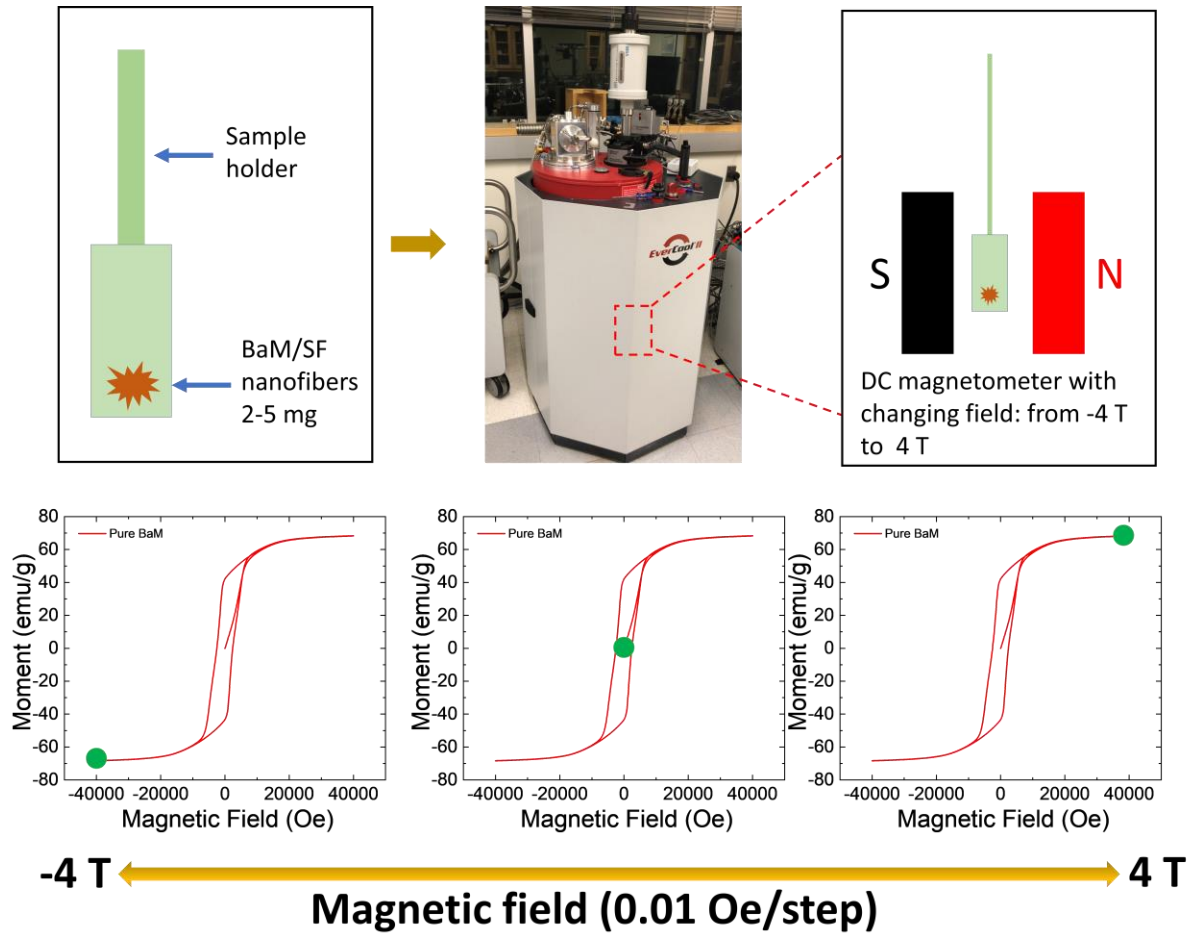

Figure 7.2 Procedure of magnetic properties measurements of BaM/SF nanofibers. The measurement is conducted at room temperature with an external magnetic field ranging from -4 T to 4 T. Magnetic field changes around 0.01 Oe between two measurements, and the measurement sensitivity of the system is less than 10^{-6} emu at a data rate of 1 Hz.

7.2.8 Biocompatibility Study

Mesh of the annealed samples (n=8 per set) were cut into the disc shapes the same size as the culture plate wells, and placed into 96-well tissue culture plates. The samples were first sterilized with UV light for 24 h before adding the cell culture medium (Dulbecco's modified Eagle's medium (HyClone, with 4.00 mM L-Glutamine and 4500 mg/L Glucose), supplemented with 10% fetal bovine serum (Life Technologies Inc.) and

100 U/mL Penicillin-Streptomycin (Thermo Fisher Scientific Inc., USA)). After 12 h, human embryonic kidney cells (HEK293) from ATCC: cr1-322 (American Type Culture Collection) were plated into the 96-well plate. Two sets of cell studies were performed: One set of experiments was performed with in a magnetic field of 1 T, and the other set was performed without an external magnetic field. Cells cultured on the pure silk fibroin fibers mesh in the plate with or without magnetic field were used as controls, respectively. After incubating the cells in an atmosphere of 95% air, 5% CO_2, at 37°C for 48 h, cell numbers were acquired with a 3-[4,5-dimethylthiazole-2-yl]-2,5-diphenyltetrazolium bromide (MTT) assay.

7.3 Results and Discussion

7.3.1 Morphology Analysis

All as-spun (AS) samples showed smooth and uniform surfaces (Fig. 7.3a, d, g and j) for BaM/SF= 0, 1/20, 1/10, 1/4; however, the AS 1/2 BaM/SF samples has a rougher surface (Fig. 7.3m) due to the high content (~12 vol%) of BaM nanoparticles in the SF matrix. The AS 0 (pure SF) sample had the largest fiber diameter with a size distribution centered around 2 μm (Fig. 7.3b), while all other AS samples showed a smaller diameter with an average diameter of 1.6 μm or less (Fig. 7.3e, h, k, n), suggesting substantial interaction between the protein and the inclusions. In comparison, electrospun water-annealed (WA) fibers (Fig. 7.3c, f, I, and o) were completely physically cross-linked by the β-sheet crystals in the silk proteins (see FTIR section), unlike the overlapping pattern of the AS samples or other electrospun synthetic polymer nanofibers [370-372]. Generally, all WA samples showed a dense mat-like pattern of

fibers embedded within a matrix. Basically, water annealing caused the fibers to be closer to each other with smaller scaffold pores although the alignment remained unchanged.

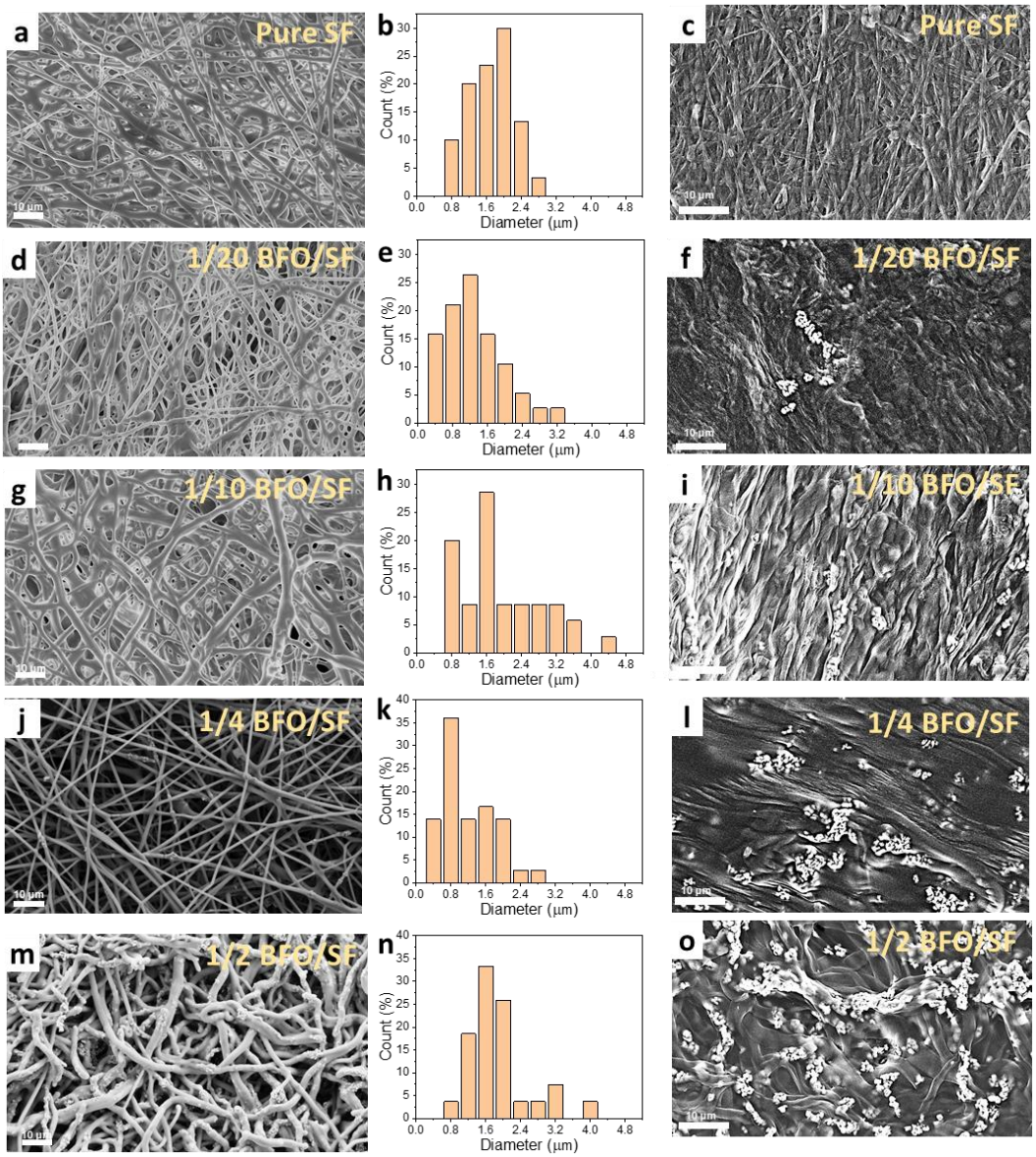

Figure 7.3 SEM images of as-spun (AS) fibers, diameter distribution of as-spun (AS) fibers and SEM images of water-annealed (WA) fibers, respectively, for BaM/SF= 0 (a-c), 1/20 (d-f), 1/10 (g-i), 1/4 (j-l), and 1/2 (m-o). The scale bar for all the images is 10 μm.

7.3.2 Structural Analysis

FTIR spectroscopy was performed to characterize effects of BaM content and water annealing treatment on the secondary structures of SF proteins. All AS samples showed a similar pattern in the amide I region with a peak centered around 1640 cm^{-1} for AS 0 (pure SF) fibers that slightly shifted to 1643 cm^{-1} for AS 1/2 BaM/SF fibers, which indicates that the structure of AS fibers was dominated by random coils. In the amide II region, AS samples showed a peak centered around 1540 cm^{-1} with a shoulder around 1514 cm^{-1}, which typically suggests a loose side-chain group in the protein matrix [175, 188, 189, 373]. In comparison, the amide I peak of the WA samples all shifted to around 1621 cm^{-1}, indicating a predominant β-sheet crystal structure. In the amide II region, the peak at 1540 cm^{-1} disappeared while the peak at 1514 cm^{-1} became sharp, suggesting a tightly packed protein matrix with side-chain groups such as tyrosines outside the protein backbones [188, 189].

More quantitative analysis of the secondary structure content was done with a Fourier self-deconvoluted curve fitting method [98, 164] (Fig. 7.4c, d, and Fig. 7.5). It shows that β-sheet content of the AS samples is around 20% and probably dominated by intra-molecular beta sheets [3, 125, 295]. The beta sheet content of the WA samples is about 35-38% with perhaps a small decrease with BaM content. It has been well established that water annealing can induce the formation of β-sheet crystalline structure in SF [189], which could play the role of crosslinkers to encapsulate the nanoparticles in the protein matrix. It was also found that random coils content of AS fibers was about 42% and decreased to about 30% after annealing.

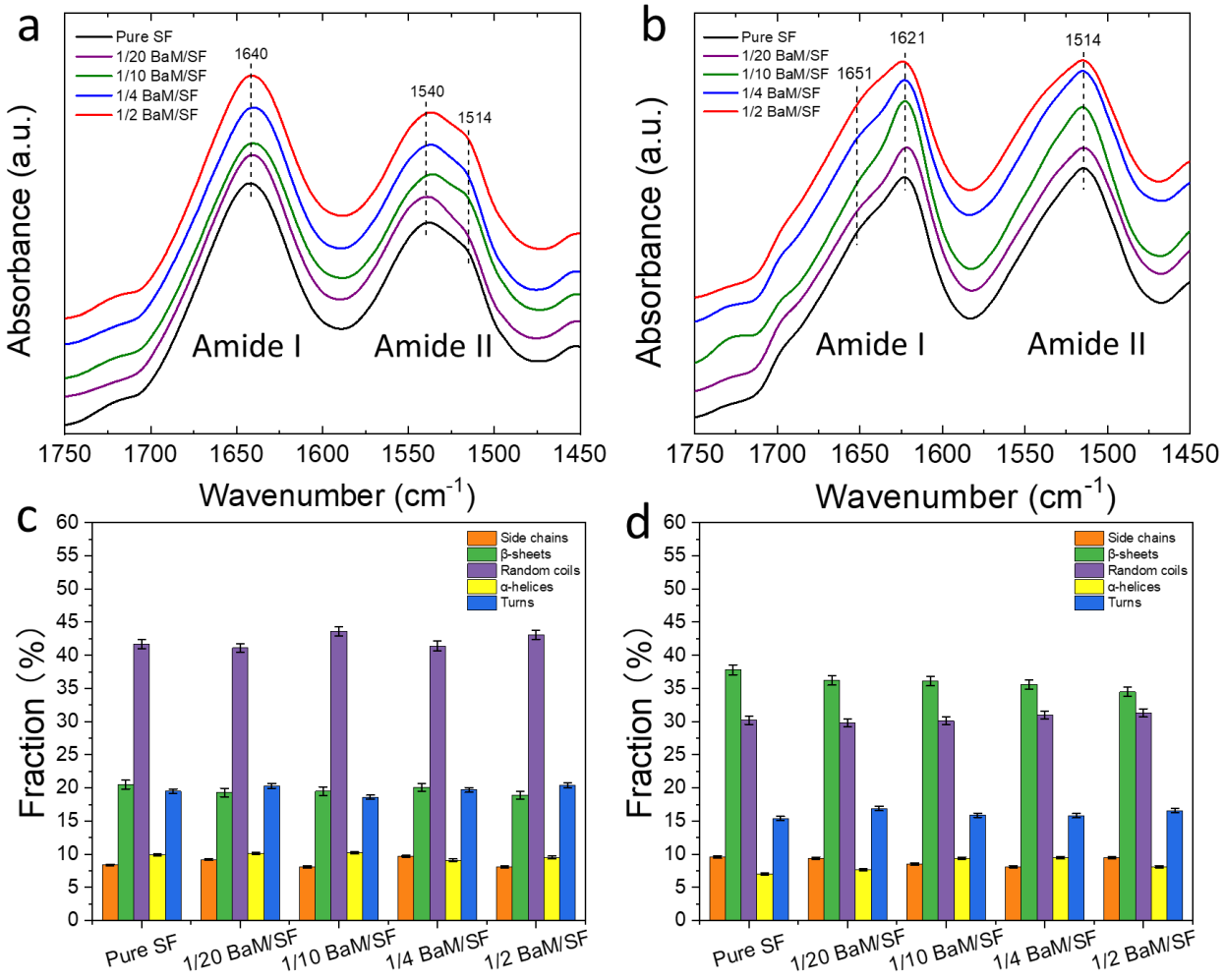

Figure 7.4 FTIR spectra of a) AS and b) WA fibers. Secondary structure contents of c) AS and d) WA fibers. Note that the secondary structure content depends strongly on processing but is effectively independent of BaM content with AS fibers containing mostly random coils and WA dominated by beta sheet crystals.

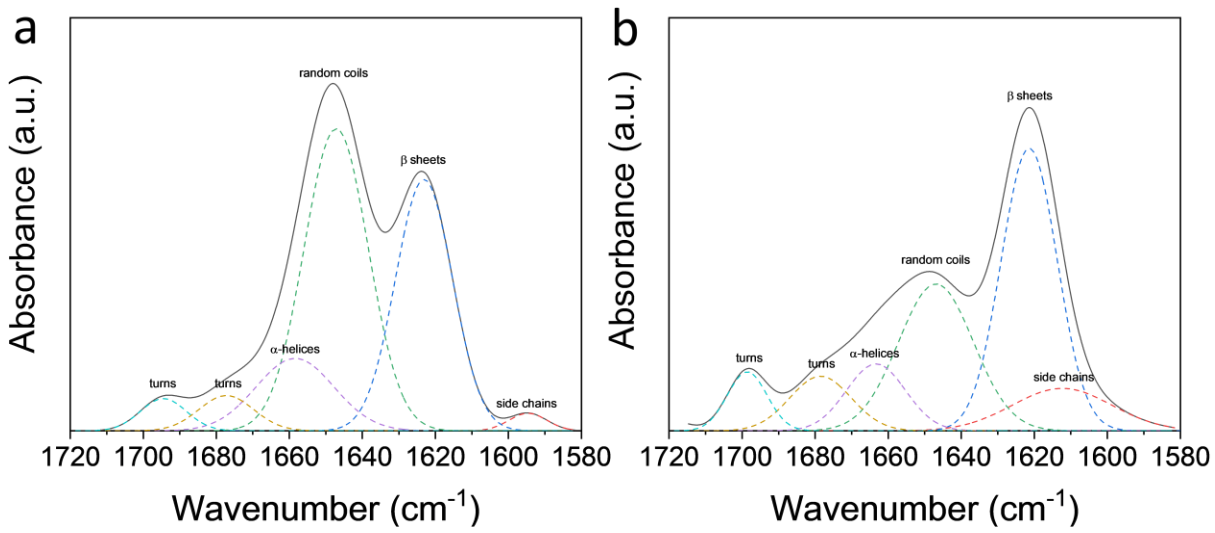

Figure 7.5 Examples of Fourier self-deconvoluted curve fitting method for (a) AS SF sample, and (b) WA SF sample.

7.3.3 Thermal Stability Analysis

Thermal stability was characterized by TGA (Fig. 7.6), and the thermal properties are summarized in Table 7.1. For the AS 0 (pure SF) sample, a 16.3% weight loss was found at 173 °C due to the evaporation of bound water in contrast to 5.9% weight loss found in the WA 0 (pure SF) sample at the same temperature. This difference is probably due to the larger content of random coils in the AS samples, which can maintain more bound water molecules in the matrix. All AS samples showed a small degradation around 220 °C (T_{d1}) and a major degradation around 310 °C (T_{d2}). In comparison, the water annealed pure SF sample only showed a significant degradation peak around 267 °C (T_{d2}), indicating that the silk proteins were tightly bounded with the BaM nanoparticles after the water annealing treatment, and thus only one major degradation from the composites was observed. For WA samples with more than 5% BaM nanoparticles, there

is an additional degradation peak (T_{d3}) near 700 °C which is absent in the AS samples. This may indicate that some parts of water-annealed composites with strong molecular interactions are so stable that decompose only at high temperatures. The residual weight of AS samples at 800 °C is between 35-38%, while the residual weight of WA samples generally increases with BaM content, which again suggest that the water annealing process improves the thermal stability of the fibers.

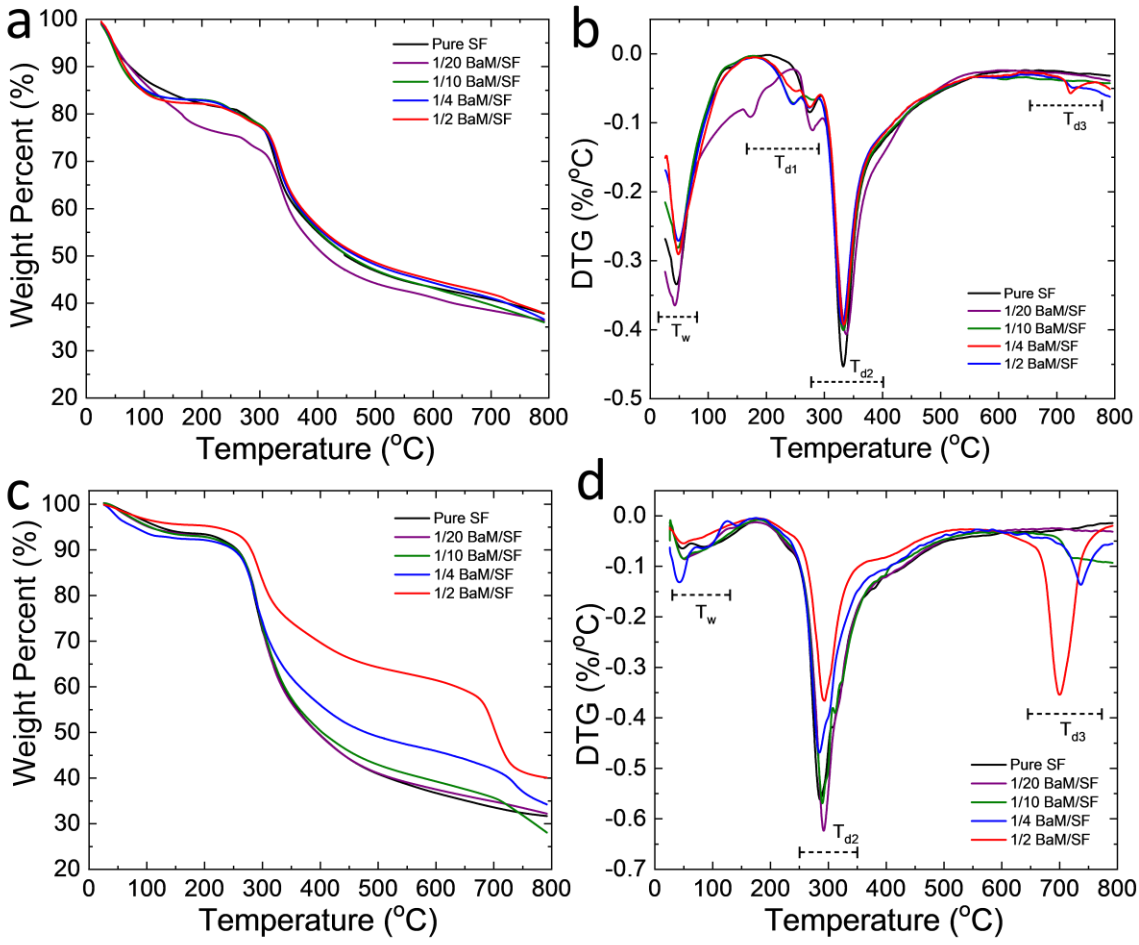

Figure 7.6 Thermogravimetric curves of a) AS and b) WA fibers. c) and d) display the 1st derivative TG (DTG) curves of AS and WA fibers, respectively.

Table 7.1

Thermal properties of AS and WA electrospun fibers

	T_w (°C)	T_{d1} (°C)	T_{d2} (°C)	T_{d3} (°C)
Pure SF	58	267	318	-
1/20 BaM/SF	47	265	311	-
1/10 BaM/SF	66	224	317	-
1/4 BaM/SF	81	223	315	-
1/2 BaM/SF	77	227	318	716
WA Pure SF	34	-	263	-
WA 1/20 BaM/SF	38	-	270	-
WA 1/10 BaM/SF	39	-	267	708
WA 1/4 BaM/SF	33	-	262	707
WA 1/2 BaM/SF	36	-	269	676

7.3.4 Mechanical Properties

Results of stress-train tensile test are shown in Figure 7.7 and are summarized in Figure 7.8. The ultimate strength of AS samples gradually decreased from the maximum for pure SF (~ 1 GPa) (Fig. 7b) while the Young's modulus of all AS samples was similar (Fig. 7.8a), both results being attributed to the weak bonding between the SF matrix and the BaM inclusions. This is in accord with the smaller diameter of the AS fibers when BaM was incorporated. On the other hand for WA composites, while the WA 0 (pure SF) sample showed the highest ultimate strength (~1 GPa) it also had lowest value for Young's modulus (1.0 GPa). As expected for composites with strong interfacial bonding, Young's modulus of the WA samples increased with BaM content. The AS samples generally showed much higher strain elongation ratio (1.5~2 times) than that of their WA

counterparts (Fig. 7.8c), which indicates that the annealed samples may lose some flexibility of the materials due to the high crystallinity. The average strain ratio of the WA samples was in the range of 45% to 55%.

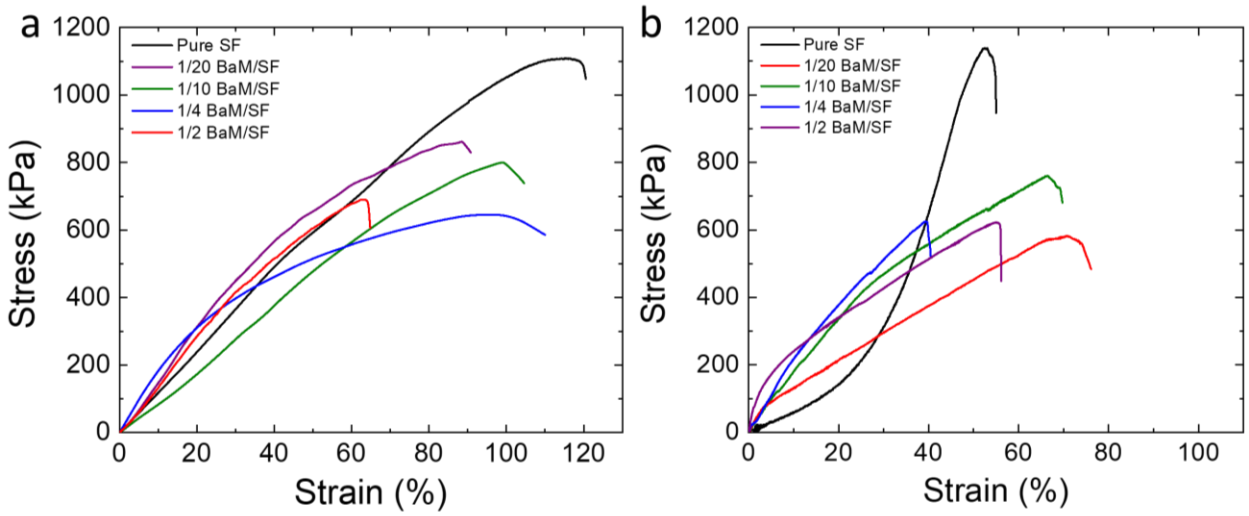

Figure 7.7 Representative stress-strain curves of (a) AS and (b) WA fibers.

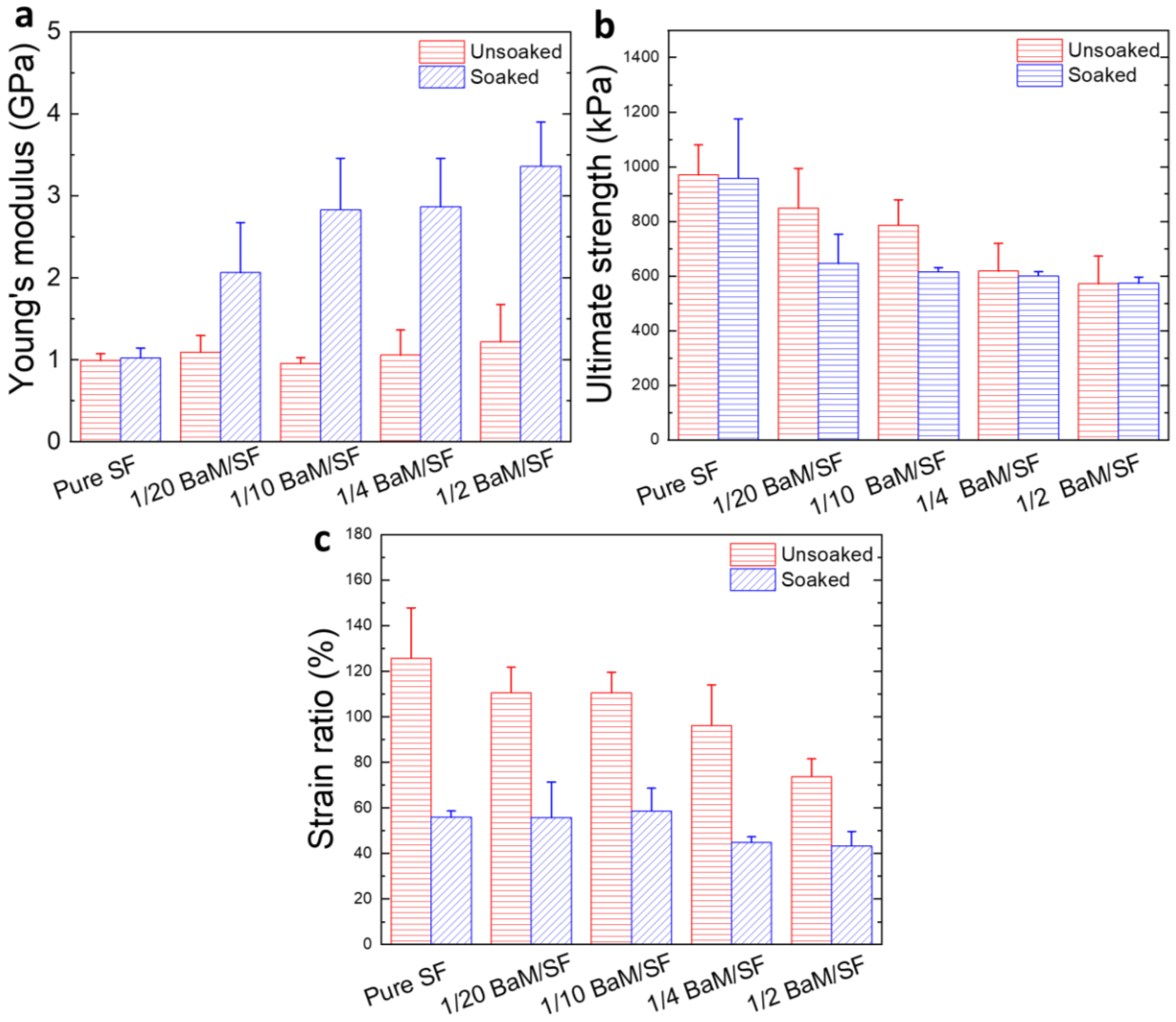

Figure 7.8 (a) Young's modulus, (b) ultimate strength, and (c) strain ratio of AS and WA fibers.

7.3.5 Post-Stretching Study

As discovered in the mechanical study, the Young's modulus of the as-spun samples is very small, and their strain ratios can be quite large. It was hypothesized that the fiber alignment could be improved by stretching the AS fibers while being annealed in water. To further investigate the effect of stretching on the electrospun fibers

alignment, AS 1/20 BaM/SF samples were stretched to different ratios, and the ends were fixed while the sample was annealed in deionized water. As the draw ratio increased, the alignment of the fiber improved (Fig. 7.9a-d) so that at an elongation of 100%, the fibers became parallel to each other (Fig. 7.9d). Natural silk fibroin consists of a large proportion of α-amino acids, glycine, alanine, and serine [374, 375], and the water molecule functions as plasticizer while the stretched fibers were annealed in DI water, giving the amorphous part of the fiber much higher mobility [189, 376, 377]. Stretching improves the alignment of the fibers while the drying procedure can fix the alignment of the fibers.

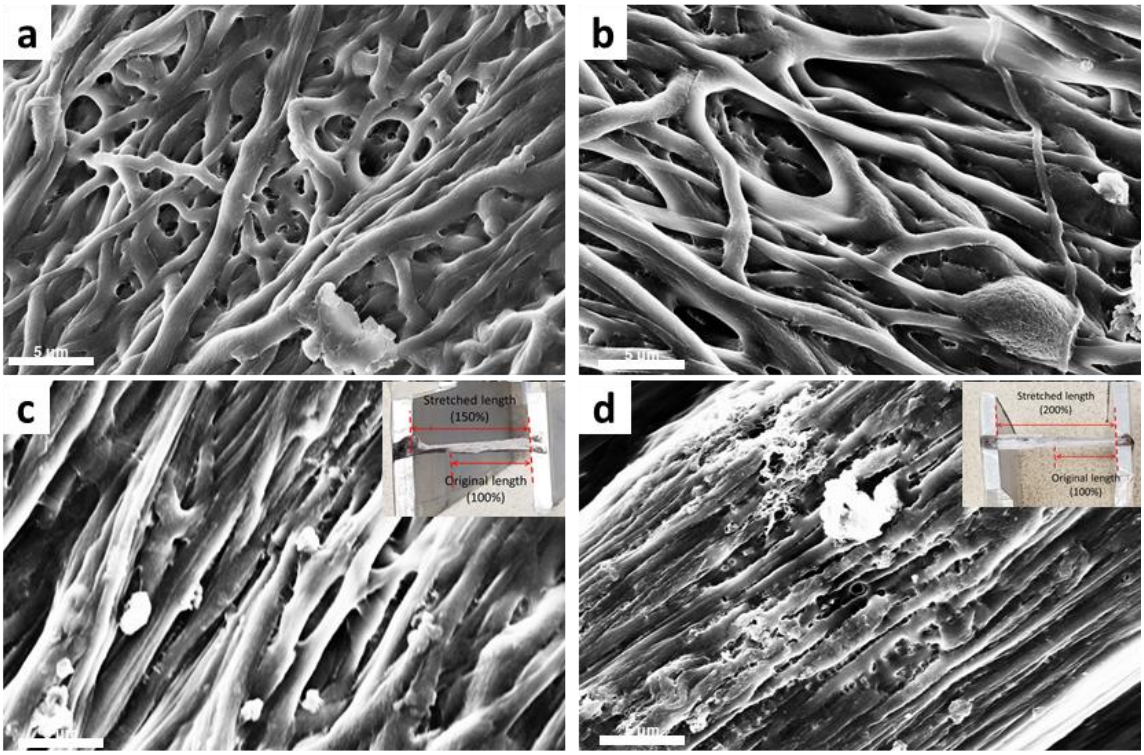

Figure 7.9 SEM images of annealed and stretched 1/20 BaM/SF nanofiber sample: (a) 100% (original fiber), (b) 110%, (c) 150%, and (d) 200% of the original length; The inset graph in 3c and 3d show the 150% and 200% stretching setup, respectively; the scale bar is 5 μm.

7.3.6 Magnetic Properties

All BaM-containing samples showed typical ferromagnetic behavior with coercive field of about 8.33 kOe (Fig. 7.10a and 7.10b). The dependence of the magnetization on weight fraction of BaM is shown in Fig. 7.10c. The saturation magnetization M_s of BaM is about 69 emu/g. Assuming that there were no changes in the magnetic properties of the BaM due to processing, the M_s value of the composite should be about 69x emu/g, where x is the weight fraction of BaM. Note that there is a linear relationship between the weight fraction and M_s except it does not go through the origin. Presumably, the BaM nanoparticles dissolved in the formic acid solution, saturating the solution at about 4 wt % (horizontal intercept of the graph) with any additional BaM nanoparticles remain unaltered. Since BaM is a hard magnet, the composites maintain a strong permanent magnetic moment for consideration in use biomedical applications such as magnetic thermotherapy and tissue engineering (Fig. 7.10d).

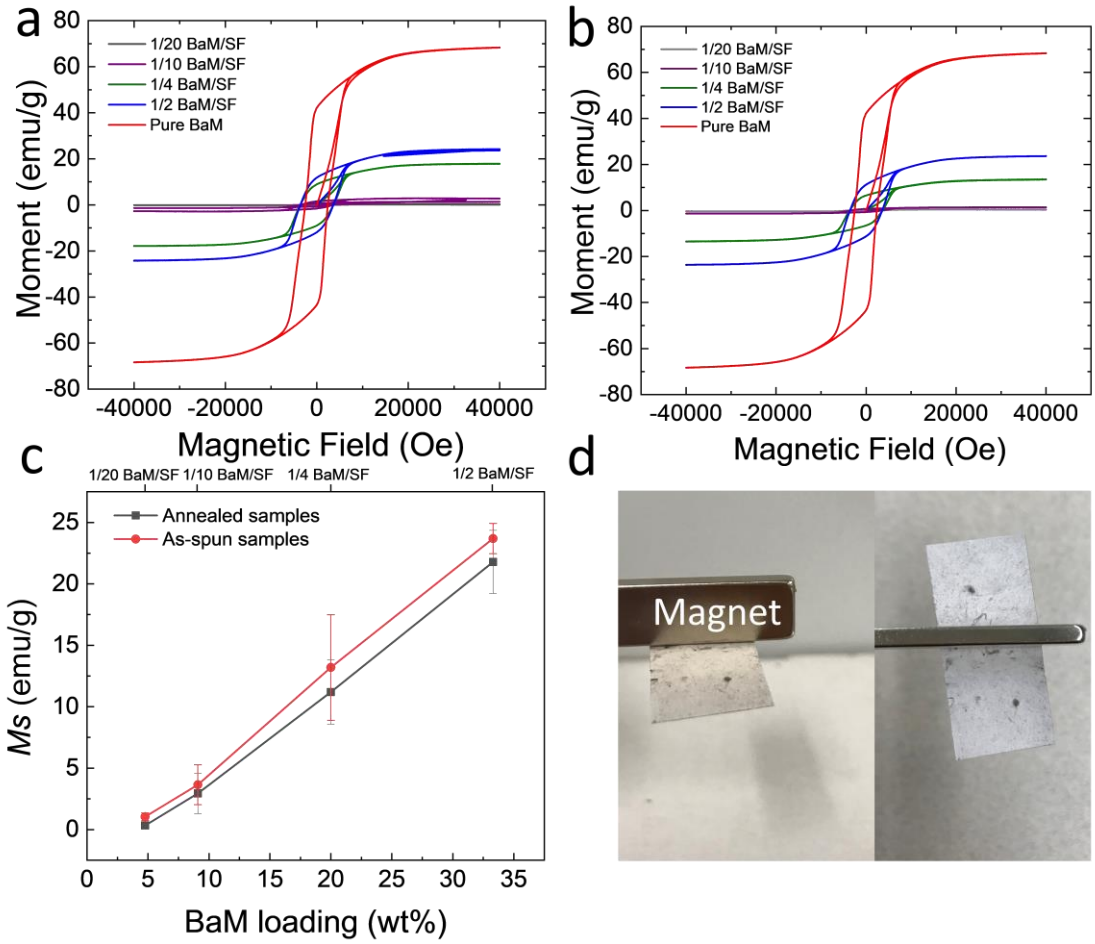

Figure 7.10 Magnetization and Hysteresis loops of (a) AS and (b) WA fiber samples at room temperature. (c) Saturation moment of AS and WA BaM/SF nanofibers as a function of the magnetic particle content. (d) Photo of a AS 1/4 BaM/SF mesh attracted to a magnet.

7.3.7 Biocompatibility Analysis

WA fiber meshes were placed into cell culture plates, seeded with human embryonic kidney cells (HEK293) for *in vitro* biocompatibility study. Since the culture medium was water-based, AS samples would be transformed to the WA samples during the multiday cell study, and so they were not tested separately. WA fibers promoted cell growth significantly (Fig. 7.11), since the porous 3D structure of the mesh provided more

space for cells to proliferate. In the absence of magnetic field, cell growth increased slightly with increasing BaM content (Fig. 7.11), indicating that the composite system is non-cytotoxic to human cells and biocompatible for various medical applications. However, when field was applied, there was enhanced cell growth in samples with BaM, and that was most significant for the WA 1/20 and WA 1/10 samples.

I propose the following mechanism for human cell proliferation in BaM/SF composites: the initial AS fibers are dominated by random coils (Fig. 7.12a), which have weak interaction with the BaM nanoparticles; after water annealing, the magnetic nanoparticles were encapsulated into the protein matrix due to the formation of beta-sheet crystals as crosslinkers (Fig. 7.12b), as both the thermal stability and mechanical strength of the fibers were enhanced; under the influence of an external magnetic field, the fiber matrix can further shrink during cell proliferation and provide cells with a smaller moving gap/distance during migration and proliferation in the scaffold matrix (Fig. 7.12c).

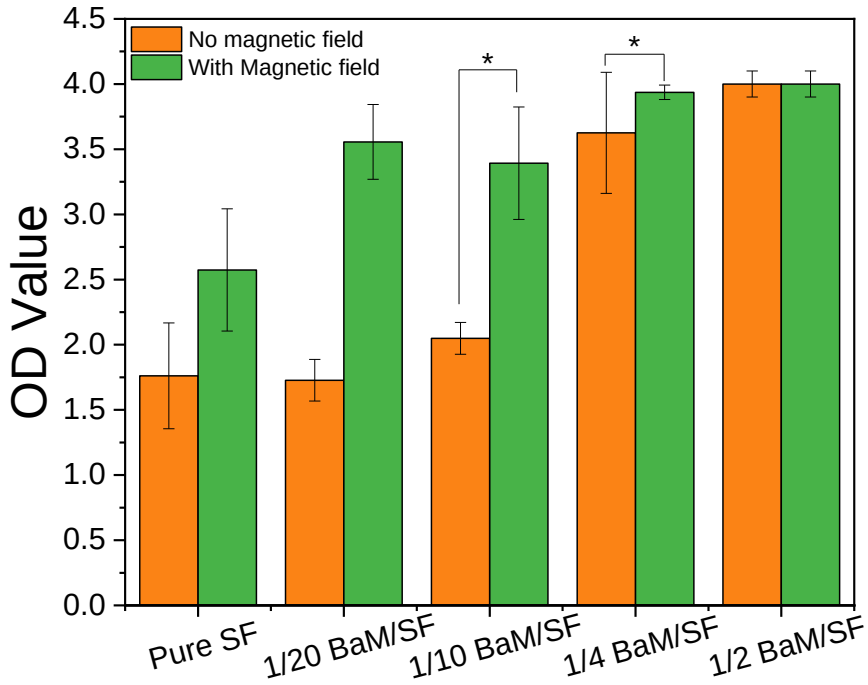

Figure 7.11 Comparison of cell viability of HEK293T cells cultured on the pure SF and BaM/SF hybrid fibers with or without an external magnetic field. The t-tests were performed between indicated groups (*: $p<0.01$).

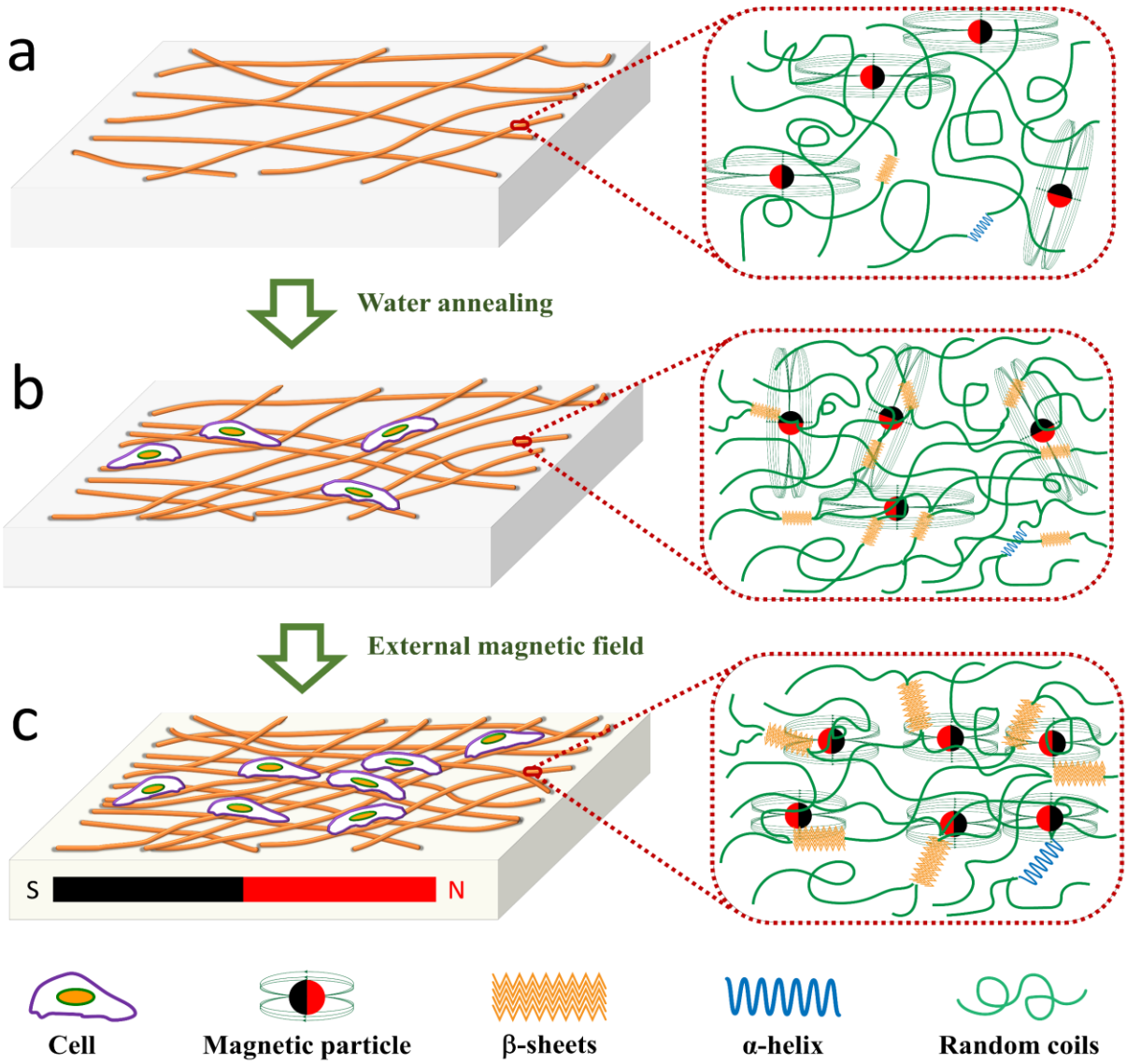

Figure 7.12 Mechanism of silk-BaM magnetic materials. (a) As-spun BaM/SF fibers are dominated by random coils; (b) after water annealing, the magnetic nanoparticles were further encapsulated into the protein matrix due to the formation of beta-sheet crystalline as crosslinkers; (c) by adding an external magnetic field, the proliferation of human cells on the annealed magnetic nanofiber matrix can be further enhanced, which may be due to the mechanical deformation of the protein scaffold under the magnetic field to help the cells migrate and interact with each other.

7.4 Conclusion

This study investigated the structure, physical properties and cytotoxicity of silk fibroin-barium hexaferrite composite fibers produced by electrospinning. Through a water-annealing method, the physical properties of the fiber materials were significantly altered due to an increase in beta sheet crystallinity. The treatment led to increased mechanical strength and thermal stability of the material. In all cases, the magnetism of the barium hexaferrite was maintained. The cytotoxicity was low and the magnetic inclusions in the fibers led to mechanical deformation during application of magnetic field which promoted the growth of human cells on the surface. Such materials provide great potential for use in a wide range of biomedical applications.

Chapter 8

Conclusion

The overall goal of this project was to develop silk protein-based composite materials with tunable heat transfer and magnetic properties. Chapter 1 reviewed the properties of protein-based materials and their applications, background information of thermal transport mechanism and measurement approaches, background information of magnets and measurement approaches. Chapter 2 presented a mechanism study on the structure and insolubility of the silk materials from five different species regenerated from a formic acid-$CaCl_2$ method. It reveals that the secondary structures of silk-FA films are different from those of their natural silk fibroin fibers, which are typically dominated by stacked intermolecular β-sheet crystals. In addition, the intramolecular β-sheet content of the silk-FA films is much higher than that regenerated from the traditional water-based method, causing silk-FA films to become insoluble in water. These results show that the intermolecular hydrogen bonds within β-sheets crystals in the silk fibers can be quickly disrupted during the dissolving process and allow a film network structure dominated by intramolecular β-sheets to form. This comparative study offers important insight into how to manipulate the secondary structures of silk-based biomaterials to tune its properties, which is important to design silk protein-based composites with tunable physical properties.

In the SF/AlN composites, the the β-sheet crystal content of the SF component decreases as the AlN content increases. AlN/SF has good thermal stability, low linear thermal expansion, and higher stiffness while maintaining flexibility. The thermal conductivity of AlN/SF is also significantly improved, which result from AlN forming networks to provide paths of low thermal resistance. This is aided by the strong hydrogen

bonding between the AlN and SF which reduced the interfacial phonon scattering. This work demonstrates that there can be significant interaction between organic and inorganic phases in composite materials, and the effects can be synergistic to create greatly enhanced materials which can be tailored for a variety of applications. The BNSF film shows enhanced thermal conductivity of up to 15 W m^{-1} K^{-1} in the in-plane direction and has sizable anisotropy. The enhanced thermal conductivity and accompanying anisotropy are attributed to the good alignment of the BN nanosheets and the strong interaction between the BN and SF matrix. The BNSF composites also have low coefficient of linear thermal expansion and are reasonably stiff yet maintain flexibility. These composites also have good electrical insulation and flame retardancy and shows promising potential as green and renewable materials for thermal management in electronic devices. For the electrospun BNSF fibers, pure SF sample showed a smooth fiber surface with uniform fiber diameter. Electrospun fibers with a high BN content (over 10%) showed rougher surface morphology and higher crosslink density. Results indicate that BN molecules can form hydrogen bonds with silk proteins and transform the α-helical structure of pure SF into random coils, which suggests that the composite material has better flexibility. Due to the high hydrophobicity of BN and the strong interaction of SF-BN, pure SF samples showed the highest bound water content and the lowest bound water evaporation temperature. The good thermal stability of BN can significantly improve the thermal stability of electrospun BNSF fibers, and a self-assembly mechanism of electrospun BNSF nanofiber materials is proposed.

Silk protein based magnetic composites in both 2D film and 1D fiber form were investigated. Structural analysis results indicated that Fe_3O_4 and BaM particles prohibited β-sheet crystal formation, while the addition of Co particles had minimal effect. The

decrease of crystal structure is probably caused by the strong coordination bonding between Fe from Fe_3O_4/BaM and carboxylate ions on silk fibroin chains. The magnetization studies indicated that almost 4 wt% was dissolved and this likely led to the formation of the phases that coincide with the high temperature degradation (> 640 °C) that was seen in both Fe_3O_4-SF and BaM-SF composites. All three types of magnetic composite films maintained high magnetization, suggesting potential biomedical applications such as MRI imaging, tissue regeneration, magnetic hyperthermia and controlled drug delivery in the future. Through a water-annealing method, physical properties of the electrospun silk fibroin-barium hexaferrite composite fibers were significantly altered due to an increase in beta sheet crystallinity. The treatment led to increased mechanical strength and thermal stability of the material. In all cases, the magnetism of the barium hexaferrite was maintained. The cytotoxicity was low and the magnetic inclusions in the fibers led to mechanical deformation during application of magnetic field which promoted the growth of human cells on the surface. Such materials provide great potential for use in a wide range of biomedical applications.

References

1. Tao, H.; Kaplan, D. L.; Omenetto, F. G., Silk materials–a road to sustainable high technology. *Advanced materials* **2012,** *24* (21), 2824-2837.

2. Wicklein, B.; Salazar-Alvarez, G., Functional hybrids based on biogenic nanofibrils and inorganic nanomaterials. *Journal of Materials Chemistry A* **2013,** *1* (18), 5469-5478.

3. Xue, Y.; Jao, D.; Hu, W.; Hu, X., Silk-silk blend materials. *Journal of Thermal Analysis and Calorimetry* **2017,** *127* (1), 915-921.

4. Rockwood, D. N.; Preda, R. C.; Yücel, T.; Wang, X.; Lovett, M. L.; Kaplan, D. L., Materials fabrication from Bombyx mori silk fibroin. *Nature protocols* **2011,** *6* (10), 1612.

5. Xia, X.-X.; Xu, Q.; Hu, X.; Qin, G.; Kaplan, D. L., Tunable self-assembly of genetically engineered silk–elastin-like protein polymers. *Biomacromolecules* **2011,** *12* (11), 3844-3850.

6. Keten, S.; Xu, Z.; Ihle, B.; Buehler, M. J., Nanoconfinement controls stiffness, strength and mechanical toughness of β-sheet crystals in silk. *Nature materials* **2010,** *9* (4), 359.

7. Li, C.; Vepari, C.; Jin, H.-J.; Kim, H. J.; Kaplan, D. L., Electrospun silk-BMP-2 scaffolds for bone tissue engineering. *Biomaterials* **2006,** *27* (16), 3115-3124.

8. Lammel, A. S.; Hu, X.; Park, S.-H.; Kaplan, D. L.; Scheibel, T. R., Controlling silk fibroin particle features for drug delivery. *Biomaterials* **2010,** *31* (16), 4583-4591.

9. Liu, H.; Fan, H.; Wang, Y.; Toh, S. L.; Goh, J. C., The interaction between a combined knitted silk scaffold and microporous silk sponge with human mesenchymal stem cells for ligament tissue engineering. *Biomaterials* **2008,** *29* (6), 662-674.

10. Marelli, B.; Brenckle, M.; Kaplan, D. L.; Omenetto, F. G., Silk fibroin as edible coating for perishable food preservation. *Scientific reports* **2016,** *6*, 25263.

11. Xing, C.; Munro, T.; White, B.; Ban, H.; Copeland, C. G.; Lewis, R. V., Thermophysical properties of the dragline silk of Nephila clavipes spider. *Polymer* **2014,** *55* (16), 4226-4231.

12. Zhang, L.; Chen, T.; Ban, H.; Liu, L., Hydrogen bonding-assisted thermal conduction in β-sheet crystals of spider silk protein. *Nanoscale* **2014,** *6* (14), 7786-7791.

13. Fuente, R.; Mendioroz, A.; Salazar, A., Revising the exceptionally high thermal diffusivity of spider silk. *Materials Letters* **2014,** *114*, 1-3.

14. Ferreira, A. M.; Gentile, P.; Chiono, V.; Ciardelli, G., Collagen for bone tissue regeneration. *Acta biomaterialia* **2012,** *8* (9), 3191-3200.

15. Balaji, S.; Kumar, R.; Sripriya, R.; Rao, U.; Mandal, A.; Kakkar, P.; Reddy, P. N.; Sehgal, P. K., Characterization of keratin–collagen 3D scaffold for biomedical applications. *Polymers for Advanced Technologies* **2012,** *23* (3), 500-507.

16. Maynes, R., *Structure and function of collagen types*. Elsevier: 2012.

17. Li, Y.; Foss, C. A.; Summerfield, D. D.; Doyle, J. J.; Torok, C. M.; Dietz, H. C.; Pomper, M. G.; Yu, S. M., Targeting collagen strands by photo-triggered triple-helix hybridization. *Proceedings of the National Academy of Sciences* **2012,** *109* (37), 14767-14772.

18. Sherman, V. R.; Yang, W.; Meyers, M. A., The materials science of collagen. *Journal of the mechanical behavior of biomedical materials* **2015,** *52*, 22-50.

19. Fujimaki, H.; Uchida, K.; Inoue, G.; Miyagi, M.; Nemoto, N.; Saku, T.; Isobe, Y.; Inage, K.; Matsushita, O.; Yagishita, S., Oriented collagen tubes combined with basic fibroblast growth factor promote peripheral nerve regeneration in a 15 mm sciatic nerve defect rat model. *Journal of Biomedical Materials Research Part A* **2017,** *105* (1), 8-14.

20. Brougham, C. M.; Levingstone, T. J.; Shen, N.; Cooney, G. M.; Jockenhoevel, S.; Flanagan, T. C.; O'brien, F. J., Freeze‐Drying as a Novel Biofabrication Method for Achieving a Controlled Microarchitecture within Large, Complex Natural Biomaterial Scaffolds. *Advanced healthcare materials* **2017,** *6* (21), 1700598.

21. Tombolato, L.; Novitskaya, E. E.; Chen, P.-Y.; Sheppard, F. A.; McKittrick, J., Microstructure, elastic properties and deformation mechanisms of horn keratin. *Acta Biomaterialia* **2010,** *6* (2), 319-330.

22. Mercer, E., The heterogeneity of the keratin fibers. *Textile Research Journal* **1953,** *23* (6), 388-397.

23. Aboushwareb, T.; Eberli, D.; Ward, C.; Broda, C.; Holcomb, J.; Atala, A.; Van Dyke, M., A keratin biomaterial gel hemostat derived from human hair: evaluation in a rabbit model of lethal liver injury. *Journal of Biomedical Materials Research Part B: Applied Biomaterials* **2009,** *90* (1), 45-54.

24. Wang, B.; Yang, W.; McKittrick, J.; Meyers, M. A., Keratin: Structure, mechanical properties, occurrence in biological organisms, and efforts at bioinspiration. *Progress in Materials Science* **2016,** *76*, 229-318.

25. Lee, H.; Noh, K.; Lee, S. C.; Kwon, I.-K.; Han, D.-W.; Lee, I.-S.; Hwang, Y.-S., Human hair keratin and its-based biomaterials for biomedical applications. *Tissue Engineering and Regenerative Medicine* **2014,** *11* (4), 255-265.

26. Li, R.; Wang, D., Preparation of regenerated wool keratin films from wool keratin–ionic liquid solutions. *Journal of Applied Polymer Science* **2013,** *127* (4), 2648-2653.

27. Edwards, A.; Jarvis, D.; Hopkins, T.; Pixley, S.; Bhattarai, N., Poly (ε - caprolactone)/keratin - based composite nanofibers for biomedical applications. *Journal of Biomedical Materials Research Part B: Applied Biomaterials* **2015,** *103* (1), 21-30.

28. Mülhaupt, R., Green Polymer Chemistry and Bio - based Plastics: Dreams and Reality. *Macromolecular Chemistry and Physics* **2013,** *214* (2), 159-174.

29. Shahil, K. M.; Balandin, A. A., Graphene–multilayer graphene nanocomposites as highly efficient thermal interface materials. *Nano letters* **2012,** *12* (2), 861-867.

30. Jin, X.; Zhang, J.; Gao, W.; Li, J.; Wang, X., Cocoon of the silkworm Antheraea pernyi as an example of a thermally insulating biological interface. *Biointerphases* **2014,** *9* (3), 031013.

31. Haxaire, K.; Marechal, Y.; Milas, M.; Rinaudo, M., Hydration of polysaccharide hyaluronan observed by IR spectrometry. I. Preliminary experiments and band assignments. *Biopolymers* **2003,** *72* (1), 10-20.

32. Toberer, E. S.; Baranowski, L. L.; Dames, C., Advances in thermal conductivity. *Annual Review of Materials Research* **2012,** *42*, 179-209.

33. Anderson, D., Thermal conductivity of polymers. *Chemical Reviews* **1966,** *66* (6), 677-690.

34. Shen, S.; Henry, A.; Tong, J.; Zheng, R.; Chen, G., Polyethylene nanofibres with very high thermal conductivities. *Nature nanotechnology* **2010,** *5* (4), 251-255.

35. Zhou, L.; Chen, X.; Shao, Z.; Huang, Y.; Knight, D. P., Effect of Metallic Ions on Silk Formation in the Mulberry Silkworm, Bombyx m ori. *The Journal of Physical Chemistry B* **2005,** *109* (35), 16937-16945.

36. Han, Z.; Fina, A., Thermal conductivity of carbon nanotubes and their polymer nanocomposites: a review. *Progress in polymer science* **2011,** *36* (7), 914-944.

37. Li, X.; Tabil, L. G.; Oguocha, I. N.; Panigrahi, S., Thermal diffusivity, thermal conductivity, and specific heat of flax fiber–HDPE biocomposites at processing temperatures. *Composites science and technology* **2008,** *68* (7-8), 1753-1758.

38. Rajkumar, G.; Srinivasan, J.; Suvitha, L., Development of novel silk/wool hybrid fibre polypropylene composites. *Iranian Polymer Journal* **2013,** *22* (4), 277-284.

39. Okabe, T.; Fujimura, T.; Okajima, J.; Aiba, S.; Maruyama, S., Non-invasive measurement of effective thermal conductivity of human skin with a guard-heated thermistor probe. *International Journal of Heat and Mass Transfer* **2018,** *126*, 625-635.

40. Tomko, J. A.; Pena-Francesch, A.; Jung, H.; Tyagi, M.; Allen, B. D.; Demirel, M. C.; Hopkins, P. E., Tunable thermal transport and reversible thermal conductivity switching in topologically networked bio-inspired materials. *Nature nanotechnology* **2018,** *13* (10), 959.

41. Willis, P. B.; Hsieh, C.-H., Space Applications of Polymeric Materials. *高分子* **2000,** *49* (2), 52-56.

42. Keller, T., Recent all - composite and hybrid fibre - reinforced polymer bridges and buildings. *Progress in Structural Engineering and Materials* **2001,** *3* (2), 132-140.

43. Fuchs, E. R.; Field, F. R.; Roth, R.; Kirchain, R. E., Strategic materials selection in the automobile body: Economic opportunities for polymer composite design. *Composites Science and Technology* **2008,** *68* (9), 1989-2002.

44. Zubkova, N., A highly effective domestic fire retardant for fireproofing fibrous textile materials. *Fibre Chemistry* **1997,** *29* (2), 126-129.

45. Wang, Y., Fiber and textile waste utilization. *Waste and biomass valorization* **2010,** *1* (1), 135-143.

46. Shahinpoor, M.; Kim, K. J., Ionic polymer–metal composites: IV. Industrial and medical applications. *Smart materials and structures* **2005,** *14* (1), 197.

47. Ashori, A., Wood–plastic composites as promising green-composites for automotive industries! *Bioresource Technology* **2008,** *99* (11), 4661-4667.

48. Polishuk, P., Plastic optical fibers branch out. *Communications Magazine, IEEE* **2006,** *44* (9), 140-148.

49. Williams, G.; Trask, R.; Bond, I., A self-healing carbon fibre reinforced polymer for aerospace applications. *Composites Part A: Applied Science and Manufacturing* **2007,** *38* (6), 1525-1532.

50. Bäcklund, T.; Österbacka, R.; Stubb, H.; Bobacka, J.; Ivaska, A., Operating principle of polymer insulator organic thin-film transistors exposed to moisture. *Journal of applied physics* **2005,** *98* (7), 074504.

51. Henry, A.; Chen, G., High thermal conductivity of single polyethylene chains using molecular dynamics simulations. *Physical review letters* **2008,** *101* (23), 235502.

52. Marconnet, A. M.; Yamamoto, N.; Panzer, M. A.; Wardle, B. L.; Goodson, K. E., Thermal conduction in aligned carbon nanotube–polymer nanocomposites with high packing density. *ACS nano* **2011,** *5* (6), 4818-4825.

53. Clarke, D. R., Materials selection guidelines for low thermal conductivity thermal barrier coatings. *Surface and Coatings Technology* **2003,** *163*, 67-74.

54. Rouison, D.; Sain, M.; Couturier, M., Resin transfer molding of natural fiber reinforced composites: cure simulation. *Composites science and technology* **2004,** *64* (5), 629-644.

55. Berber, S.; Kwon, Y.-K.; Tománek, D., Unusually high thermal conductivity of carbon nanotubes. *Physical review letters* **2000,** *84* (20), 4613.

56. Majumdar, A., Thermoelectricity in semiconductor nanostructures. *Science* **2004,** *303* (5659), 777-778.

57. Biswas, K.; He, J.; Blum, I. D.; Wu, C.-I.; Hogan, T. P.; Seidman, D. N.; Dravid, V. P.; Kanatzidis, M. G., High-performance bulk thermoelectrics with all-scale hierarchical architectures. *Nature* **2012,** *489* (7416), 414-418.

58. Boukai, A. I.; Bunimovich, Y.; Tahir-Kheli, J.; Yu, J.-K.; Goddard Iii, W. A.; Heath, J. R., Silicon nanowires as efficient thermoelectric materials. *Nature* **2008,** *451* (7175), 168-171.

59. Luckyanova, M. N.; Garg, J.; Esfarjani, K.; Jandl, A.; Bulsara, M. T.; Schmidt, A. J.; Minnich, A. J.; Chen, S.; Dresselhaus, M. S.; Ren, Z., Coherent phonon heat conduction in superlattices. *Science* **2012,** *338* (6109), 936-939.

60. Kraemer, D.; Poudel, B.; Feng, H.-P.; Caylor, J. C.; Yu, B.; Yan, X.; Ma, Y.; Wang, X.; Wang, D.; Muto, A., High-performance flat-panel solar thermoelectric generators with high thermal concentration. *Nature materials* **2011,** *10* (7), 532-538.

61. Huang, X.; Liu, G.; Wang, X., New secrets of spider silk: exceptionally high thermal conductivity and its abnormal change under stretching. *Advanced Materials* **2012,** *24* (11), 1482-1486.

62. Liu, G.; Huang, X.; Wang, Y.; Zhang, Y.-Q.; Wang, X., Thermal transport in single silkworm silks and the behavior under stretching. *Soft Matter* **2012,** *8* (38), 9792-9799.

63. Zhang, J.; Rajkhowa, R.; Li, J.; Liu, X.; Wang, X., Silkworm cocoon as natural material and structure for thermal insulation. *Materials & Design* **2013,** *49*, 842-849.

64. Chen, S.; Wu, Q.; Mishra, C.; Kang, J.; Zhang, H.; Cho, K.; Cai, W.; Balandin, A. A.; Ruoff, R. S., Thermal conductivity of isotopically modified graphene. *Nature materials* **2012,** *11* (3), 203-207.

65. Yu, J.-K.; Mitrovic, S.; Tham, D.; Varghese, J.; Heath, J. R., Reduction of thermal conductivity in phononic nanomesh structures. *Nature nanotechnology* **2010,** *5* (10), 718-721.

66. Fan, L.; Khodadadi, J., Thermal conductivity enhancement of phase change materials for thermal energy storage: a review. *Renewable and Sustainable Energy Reviews* **2011,** *15* (1), 24-46.

67. Hu, Y.; Zeng, L.; Minnich, A. J.; Dresselhaus, M. S.; Chen, G., Spectral mapping of thermal conductivity through nanoscale ballistic transport. *Nature nanotechnology* **2015**.

68. Maldovan, M., Phonon wave interference and thermal bandgap materials. *Nature materials* **2015,** *14* (7), 667-674.

69. Xu, S.; Xu, Z.; Starrett, J.; Hayashi, C.; Wang, X., Cross-plane thermal transport in micrometer-thick spider silk films. *Polymer* **2014,** *55* (7), 1845-1853.

70. Hu, M.; Yu, D.; Wei, J., Thermal conductivity determination of small polymer samples by differential scanning calorimetry. *Polymer testing* **2007,** *26* (3), 333-337.

71. Price, D. M.; Jarratt, M., Thermal conductivity of PTFE and PTFE composites. *Thermochimica Acta* **2002,** *392*, 231-236.

72. Peterlin, A., Drawing and extrusion of semi-crystalline polymers. *Colloid and polymer science* **1987,** *265* (5), 357-382.

73. Van Aerle, N.; Braam, A., A structural study on solid state drawing of solution-crystallized ultra-high molecular weight polyethylene. *Journal of materials science* **1988,** *23* (12), 4429-4436.

74. Choy, C., Thermal conductivity of polymers. *Polymer* **1977,** *18* (10), 984-1004.

75. Kanamoto, T.; Tsuruta, A.; Tanaka, K.; Takeda, M.; Porter, R. S., Super-drawing of ultrahigh molecular weight polyethylene. 1. Effect of techniques on drawing of single crystal mats. *Macromolecules* **1988,** *21* (2), 470-477.

76. Choy, C.; Wong, Y.; Yang, G.; Kanamoto, T., Elastic modulus and thermal conductivity of ultradrawn polyethylene. *Journal of Polymer Science Part B: Polymer Physics* **1999,** *37* (23), 3359-3367.

77. Terao, T.; Zhi, C.; Bando, Y.; Mitome, M.; Tang, C.; Golberg, D., Alignment of boron nitride nanotubes in polymeric composite films for thermal conductivity improvement. *The Journal of Physical Chemistry C* **2010,** *114* (10), 4340-4344.

78. Singh, V.; Bougher, T. L.; Weathers, A.; Cai, Y.; Bi, K.; Pettes, M. T.; McMenamin, S. A.; Lv, W.; Resler, D. P.; Gattuso, T. R., High thermal conductivity of chain-oriented amorphous polythiophene. *Nature nanotechnology* **2014,** *9* (5), 384-390.

79. Liu, J.; Yang, R., Length-dependent thermal conductivity of single extended polymer chains. *Physical Review B* **2012,** *86* (10), 104307.

80. Zhu, H.; Li, Y.; Fang, Z.; Xu, J.; Cao, F.; Wan, J.; Preston, C.; Yang, B.; Hu, L., Highly thermally conductive papers with percolative layered boron nitride nanosheets. *ACS nano* **2014,** *8* (4), 3606-3613.

81. Balandin, A. A.; Ghosh, S.; Bao, W.; Calizo, I.; Teweldebrhan, D.; Miao, F.; Lau, C. N., Superior thermal conductivity of single-layer graphene. *Nano letters* **2008,** *8* (3), 902-907.

82. Nan, C.-W.; Liu, G.; Lin, Y.; Li, M., Interface effect on thermal conductivity of carbon nanotube composites. *Applied Physics Letters* **2004,** *85* (16), 3549-3551.

83. Che, J.; Cagin, T.; Goddard III, W. A., Thermal conductivity of carbon nanotubes. *Nanotechnology* **2000,** *11* (2), 65.

84. Eastman, J.; Choi, S.; Li, S.; Yu, W.; Thompson, L., Anomalously increased effective thermal conductivities of ethylene glycol-based nanofluids containing copper nanoparticles. *Applied physics letters* **2001,** *78* (6), 718-720.

85. Kuang, J.; Zhang, C.; Zhou, X.; Wang, S., Synthesis of high thermal conductivity nano-scale aluminum nitride by a new carbothermal reduction method from combustion precursor. *Journal of crystal growth* **2003,** *256* (3), 288-291.

86. Ghosh, S.; Calizo, I.; Teweldebrhan, D.; Pokatilov, E.; Nika, D.; Balandin, A.; Bao, W.; Miao, F.; Lau, C., Extremely high thermal conductivity of graphene: Prospects for thermal management applications in nanoelectronic circuits. *Applied Physics Letters* **2008,** *92* (15), 151911.

87. Hu, J.; Ruan, X.; Chen, Y. P., Thermal conductivity and thermal rectification in graphene nanoribbons: a molecular dynamics study. *Nano Letters* **2009,** *9* (7), 2730-2735.

88. Ishida, H.; Rimdusit, S., Very high thermal conductivity obtained by boron nitride-filled polybenzoxazine. *Thermochimica Acta* **1998,** *320* (1), 177-186.

89. Golberg, D.; Bando, Y.; Huang, Y.; Terao, T.; Mitome, M.; Tang, C.; Zhi, C., Boron nitride nanotubes and nanosheets. *Acs Nano* **2010,** *4* (6), 2979-2993.

90. Stankovich, S.; Dikin, D. A.; Dommett, G. H.; Kohlhaas, K. M.; Zimney, E. J.; Stach, E. A.; Piner, R. D.; Nguyen, S. T.; Ruoff, R. S., Graphene-based composite materials. *Nature* **2006,** *442* (7100), 282-286.

91. Zhou, W.; Wang, C.; Ai, T.; Wu, K.; Zhao, F.; Gu, H., A novel fiber-reinforced polyethylene composite with added silicon nitride particles for enhanced thermal conductivity. *Composites Part A: Applied Science and Manufacturing* **2009,** *40* (6-7), 830-836.

92. Hung, M.-T.; Choi, O.; Ju, Y. S.; Hahn, H., Heat conduction in graphite-nanoplatelet-reinforced polymer nanocomposites. *Applied Physics Letters* **2006,** *89* (2), 023117.

93. Wang, X.; Ho, V.; Segalman, R. A.; Cahill, D. G., Thermal conductivity of high-modulus polymer fibers. *Macromolecules* **2013,** *46* (12), 4937-4943.

94. Cassignol, C.; Olivier, P.; Ricard, A., Influence of the dopant on the polypyrrole moisture content: Effects on conductivity and thermal stability. *Journal of applied polymer science* **1998,** *70* (8), 1567-1577.

95. Yano, O.; Yamaoka, H., Cryogenic properties of polymers. *Progress in Polymer Science* **1995,** *20* (4), 585-613.

96. Chen, Y.-M.; Ting, J.-M., Ultra high thermal conductivity polymer composites. *Carbon* **2002,** *40* (3), 359-362.

97. Hu, X.; Wang, X.; Rnjak, J.; Weiss, A. S.; Kaplan, D. L., Biomaterials derived from silk–tropoelastin protein systems. *Biomaterials* **2010,** *31* (32), 8121-8131.

98. Hu, X.; Lu, Q.; Sun, L.; Cebe, P.; Wang, X.; Zhang, X.; Kaplan, D. L., Biomaterials from ultrasonication-induced silk fibroin− hyaluronic acid hydrogels. *Biomacromolecules* **2010,** *11* (11), 3178-3188.

99. Bhattacharya, A.; Mahajan, R. L., Temperature dependence of thermal conductivity of biological tissues. *Physiological measurement* **2003,** *24* (3), 769-83.

100. Baxter, S., The thermal conductivity of textiles. *Proceedings of the Physical Society* **1946,** *58* (1), 105.

101. Das, S. K.; Putra, N.; Thiesen, P.; Roetzel, W., Temperature dependence of thermal conductivity enhancement for nanofluids. *Journal of Heat Transfer* **2003,** *125* (4), 567-574.

102. Ju, Y.; Goodson, K., Process-dependent thermal transport properties of silicon-dioxide films deposited using low-pressure chemical vapor deposition. *Journal of applied physics* **1999,** *85* (10), 7130-7134.

103. Morgen, M.; Ryan, E. T.; Zhao, J.-H.; Hu, C.; Cho, T.; Ho, P. S., Low dielectric constant materials for ULSI interconnects. *Annual Review of Materials Science* **2000,** *30* (1), 645-680.

104. Hu, H.; Wang, X.; Xu, X., Generalized theory of the photoacoustic effect in a multilayer material. *Journal of applied physics* **1999,** *86* (7), 3953-3958.

105. Cahill, D. G.; Pohl, R. O., Thermal conductivity of amorphous solids above the plateau. *Physical review B* **1987,** *35* (8), 4067.

106. Delan, A.; Rennau, M.; Schulz, S.; Gessner, T., Thermal conductivity of ultra low-k dielectrics. *Microelectronic engineering* **2003,** *70* (2), 280-284.

107. Rood, E. S., Thermal conductivity of some wearing materials. *Physical Review* **1921,** *18* (5), 356.

108. Cebe, P.; Hu, X.; Kaplan, D. L.; Zhuravlev, E.; Wurm, A.; Arbeiter, D.; Schick, C., Beating the heat-fast scanning melts silk beta sheet crystals. *Scientific reports* **2013,** *3*.

109. Jiang, X.; Li, Z.; Wang, J.; Gao, H.; Zhou, D.; Tang, Y.; Hu, W., Combining TMDSC measurements between chip-calorimeter and molecular simulation to study reversible melting of polymer crystals. *Thermochimica Acta* **2015,** *603*, 79-84.

110. Wang, J.; Li, Z.; Pérez, R. A.; Müller, A. J.; Zhang, B.; Grayson, S. M.; Hu, W., Comparing crystallization rates between linear and cyclic poly (epsilon-caprolactones) via fast-scan chip-calorimeter measurements. *Polymer* **2015,** *63*, 34-40.

111. Foreman, J.; Marcus, S.; Blaine, R., Thermal conductivity of polymers, glasses & ceramics by modulated DSC. *SOC OF PLASTICS ENGINEERS, BROOKFIELD, CT,(USA). 1994.* **1994**.

112. Marcus, S. M.; Blaine, R. L., Thermal conductivity of polymers, glasses and ceramics by modulated DSC. *Thermochimica Acta* **1994,** *243* (2), 231-239.

113. Chiu, J.; Fair, P., Determination of thermal conductivity by differential scanning calorimetry. *Thermochimica Acta* **1979,** *34* (2), 267-273.

114. Keating, M.; McLaren, C., Thermal conductivity of polymer melts. *Thermochimica Acta* **1990,** *166*, 69-76.

115. Sircar, A. K.; Wells, J. L., Thermal conductivity of elastomer vulcanizates by differential scanning calorimetry. *Rubber Chemistry and Technology* **1982,** *55* (1), 191-207.

116. Cahill, D. G., Thermal conductivity measurement from 30 to 750 K: the 3ω method. *Review of Scientific Instruments* **1990,** *61* (2), 802-808.

117. Koh, Y. K.; Singer, S. L.; Kim, W.; Zide, J. M.; Lu, H.; Cahill, D. G.; Majumdar, A.; Gossard, A. C., Comparison of the 3w method and time-domain thermoreflectance for measurements of the cross-plane thermal conductivity of epitaxial semiconductors. *Journal of Applied Physics* **2009,** *105* (5), 54303.

118. Guo, J.; Wang, X.; Wang, T., Thermal characterization of microscale conductive and nonconductive wires using transient electrothermal technique. *Journal of Applied Physics* **2007,** *101* (6), 063537.

119. Wang, X.; Zhong, Z.; Xu, J., Noncontact thermal characterization of multiwall carbon nanotubes. *Journal of Applied Physics* **2005,** *97* (6), 064302.

120. Wang, T.; Wang, X.; Zhang, Y.; Liu, L.; Xu, L.; Liu, Y.; Zhang, L.; Luo, Z.; Cen, K., Effect of zirconium (IV) propoxide concentration on the thermophysical properties of hybrid organic-inorganic films. *Journal of Applied Physics* **2008,** *104* (1), 013528.

121. Chen, X.; He, Y.; Zhao, Y.; Wang, X., Thermophysical properties of hydrogenated vanadium-doped magnesium porous nanostructures. *Nanotechnology* **2010,** *21* (5), 055707.

122. Balderas-López, J.; Mandelis, A., Self-normalized photothermal technique for accurate thermal diffusivity measurements in thin metal layers. *Review of scientific instruments* **2003,** *74* (12), 5219-5225.

123. Arvidson, K.; Abdallah, B.; Applegate, L.; Baldini, N.; Cenni, E.; Gomez - Barrena, E.; Granchi, D.; Kassem, M.; Konttinen, Y.; Mustafa, K., Bone regeneration and stem cells. *Journal of cellular and molecular medicine* **2011,** *15* (4), 718-746.

124. Bealer, E. J.; Kavetsky, K.; Dutko, S.; Lofland, S.; Hu, X., Protein and Polysaccharide-Based Magnetic Composite Materials for Medical Applications. *International Journal of Molecular Sciences* **2020,** *21* (1), 186.

125. Jao, D.; Xue, Y.; Medina, J.; Hu, X., Protein-based drug-delivery materials. *Materials* **2017,** *10* (5), 517.

126. Zhang, Y.-Q., Applications of natural silk protein sericin in biomaterials. *Biotechnology advances* **2002,** *20* (2), 91-100.

127. Song, F.; Tang, D.-L.; Wang, X.-L.; Wang, Y.-Z., Biodegradable soy protein isolate-based materials: a review. *Biomacromolecules* **2011,** *12* (10), 3369-3380.

128. De La Rica, R.; Matsui, H., Applications of peptide and protein-based materials in bionanotechnology. *Chemical Society Reviews* **2010,** *39* (9), 3499-3509.

129. Li, J.-h.; Hong, R.-y.; Luo, G.-h.; Zheng, Y.; Li, H.-z.; Wei, D.-g., An easy approach to encapsulating Fe3O4 nanoparticles in multiwalled carbon nanotubes. *New Carbon Materials* **2010,** *25* (3), 192-198.

130. Wang, X.; Jiang, M.; Zhou, Z.; Gou, J.; Hui, D., 3D printing of polymer matrix composites: A review and prospective. *Composites Part B: Engineering* **2017,** *110*, 442-458.

131. Ovid'ko, I., Enhanced mechanical properties of polymer-matrix nanocomposites reinforced by graphene inclusions: a review. *Reviews on Advanced Materials Science* **2013,** *34* (1), 19-25.

132. Ovid'Ko, I., Enhanced mechanical properties of polymer-matrix nanocomposites reinforced by graphene inclusions: a review. *Rev. Adv. Mater. Sci* **2013,** *34* (1), 19-25.

133. Müller, K.; Bugnicourt, E.; Latorre, M.; Jorda, M.; Echegoyen Sanz, Y.; Lagaron, J. M.; Miesbauer, O.; Bianchin, A.; Hankin, S.; Bölz, U., Review on the processing and properties of polymer nanocomposites and nanocoatings and their applications in the packaging, automotive and solar energy fields. *Nanomaterials* **2017,** *7* (4), 74.

134. DeFrates, K.; Markiewicz, T.; Gallo, P.; Rack, A.; Weyhmiller, A.; Jarmusik, B.; Hu, X., Protein polymer-based nanoparticles: fabrication and medical applications. *International journal of molecular sciences* **2018,** *19* (6).

135. Kishimoto, Y.; Morikawa, H.; Yamanaka, S.; Tamada, Y., Electrospinning of silk fibroin from all aqueous solution at low concentration. *Materials Science and Engineering: C* **2017,** *73*, 498-506.

136. Ohgo, K.; Zhao, C.; Kobayashi, M.; Asakura, T., Preparation of non-woven nanofibers of Bombyx mori silk, Samia cynthia ricini silk and recombinant hybrid silk with electrospinning method. *Polymer* **2003,** *44* (3), 841-846.

137. Saini, M.; Singh, Y.; Arora, P.; Arora, V.; Jain, K., Implant biomaterials: A comprehensive review. *World Journal of Clinical Cases: WJCC* **2015,** *3* (1), 52.

138. Chen, H.; Yuan, L.; Song, W.; Wu, Z.; Li, D., Biocompatible polymer materials: role of protein–surface interactions. *Progress in Polymer Science* **2008,** *33* (11), 1059-1087.

139. Gong, S.; Wang, H.; Sun, Q.; Xue, S.-T.; Wang, J.-Y., Mechanical properties and in vitro biocompatibility of porous zein scaffolds. *Biomaterials* **2006,** *27* (20), 3793-3799.

140. Hu, X.; Cebe, P.; Weiss, A. S.; Omenetto, F.; Kaplan, D. L., Protein-based composite materials. *Materials today* **2012,** *15* (5), 208-215.

141. Bai, L.; Zhu, L.; Min, S.; Liu, L.; Cai, Y.; Yao, J., Surface modification and properties of Bombyx mori silk fibroin films by antimicrobial peptide. *Applied Surface Science* **2008,** *254* (10), 2988-2995.

142. Vepari, C.; Kaplan, D. L., Silk as a biomaterial. *Progress in polymer science* **2007,** *32* (8-9), 991-1007.

143. Lu, Q.; Hu, X.; Wang, X.; Kluge, J. A.; Lu, S.; Cebe, P.; Kaplan, D. L., Water-insoluble silk films with silk I structure. *Acta biomaterialia* **2010,** *6* (4), 1380-1387.

144. Chao, P. H. G.; Yodmuang, S.; Wang, X.; Sun, L.; Kaplan, D. L.; Vunjak‐Novakovic, G., Silk hydrogel for cartilage tissue engineering. *Journal of biomedical materials research part B: applied biomaterials* **2010,** *95* (1), 84-90.

145. Shen, W.; Chen, X.; Chen, J.; Yin, Z.; Heng, B. C.; Chen, W.; Ouyang, H.-W., The effect of incorporation of exogenous stromal cell-derived factor-1 alpha within a knitted silk-collagen sponge scaffold on tendon regeneration. *Biomaterials* **2010,** *31* (28), 7239-7249.

146. Wang, F.; Chandler, P.; Oszust, R.; Sowell, E.; Graham, Z.; Ardito, W.; Hu, X., Thermal and structural analysis of silk–polyvinyl acetate blends. *Journal of Thermal Analysis and Calorimetry* **2017,** *127* (1), 923-929.

147. Kang, M.; Jin, H.-J., Electrically conducting electrospun silk membranes fabricated by adsorption of carbon nanotubes. *Colloid and Polymer Science* **2007,** *285* (10), 1163-1167.

148. Hronik‐Tupaj, M.; Raja, W. K.; Tang‐Schomer, M.; Omenetto, F. G.; Kaplan, D. L., Neural responses to electrical stimulation on patterned silk films. *Journal of biomedical materials research Part A* **2013,** *101* (9), 2559-2572.

149. Wang, F.; Aravind, S. J.; Wu, H.; Forys, J.; Venkataraman, V.; Ramanujachary, K.; Hu, X., Tunable green graphene-silk biomaterials: Mechanism of protein-based nanocomposites. *Materials Science and Engineering: C* **2017,** *79*, 728-739.

150. Vu, T.; Xue, Y.; Vuong, T.; Erbe, M.; Bennet, C.; Palazzo, B.; Popielski, L.; Rodriguez, N.; Hu, X., Comparative study of ultrasonication-induced and naturally self-assembled silk fibroin-wool keratin hydrogel biomaterials. *International journal of molecular sciences* **2016,** *17* (9), 1497.

151. Jin, H.-J.; Park, J.; Valluzzi, R.; Cebe, P.; Kaplan, D. L., Biomaterial films of Bombyx M ori silk Fibroin with Poly (ethylene oxide). *Biomacromolecules* **2004,** *5* (3), 711-717.

152. Jin, H.-J.; Kaplan, D. L., Mechanism of silk processing in insects and spiders. *Nature* **2003,** *424* (6952), 1057-1061.

153. Cao, Z.; Chen, X.; Yao, J.; Huang, L.; Shao, Z., The preparation of regenerated silk fibroin microspheres. *Soft Matter* **2007,** *3* (7), 910-915.

154. Zhang, F.; You, X.; Dou, H.; Liu, Z.; Zuo, B.; Zhang, X., Facile fabrication of robust silk nanofibril films via direct dissolution of silk in CaCl2–formic acid solution. *ACS applied materials & interfaces* **2015,** *7* (5), 3352-3361.

155. Pereira, R. F.; Sentanin, F.; Pawlicka, A.; Gonçalves, M. C.; Silva, M. M.; de Zea Bermudez, V., Smart windows prepared from Bombyx mori silk. *ChemElectroChem* **2016,** *3* (7), 1084-1097.

156. Lu, S.; Wang, P.; Zhang, F.; Zhou, X.; Zuo, B.; You, X.; Gao, Y.; Liu, H.; Tang, H., A novel silk fibroin nanofibrous membrane for guided bone regeneration: a study in rat calvarial defects. *American journal of translational research* **2015,** *7* (11), 2244.

157. Liu, Q.; Wang, F.; Gu, Z.; Ma, Q.; Hu, X., Exploring the structural transformation mechanism of chinese and Thailand silk fibroin fibers and formic-acid fabricated silk films. *International journal of molecular sciences* **2018,** *19* (11), 3309.

158. Wang, F.; Yu, H.-y.; Gu, Z.-G.; Si, L.; Liu, Q.-c.; Hu, X., Impact of calcium chloride concentration on structure and thermal property of Thai silk fibroin films. *Journal of Thermal Analysis and Calorimetry* **2017,** *130* (2), 851-859.

159. Yue, X.; Zhang, F.; Wu, H.; Ming, J.; Fan, Z.; Zuo, B., A novel route to prepare dry-spun silk fibers from CaCl2–formic acid solution. *Materials Letters* **2014,** *128*, 175-178.

160. Zhang, F.; Lu, Q.; Yue, X.; Zuo, B.; Qin, M.; Li, F.; Kaplan, D. L.; Zhang, X., Regeneration of high-quality silk fibroin fiber by wet spinning from CaCl2–formic acid solvent. *Acta biomaterialia* **2015,** *12*, 139-145.

161. Yang, R.; Wu, P.; Wang, X.; Liu, Z.; Zhang, C.; Shi, Y.; Zhang, F.; Zuo, B., A novel method to prepare tussah/Bombyx mori silk fibroin-based films. *RSC advances* **2018,** *8* (39), 22069-22077.

162. Leal‐Egaña, A.; Scheibel, T., Silk‐based materials for biomedical applications. *Biotechnology and applied biochemistry* **2010,** *55* (3), 155-167.

163. Wang, F.; Wolf, N.; Rocks, E.-M.; Vuong, T.; Hu, X., Comparative studies of regenerated water-based Mori, Thai, Eri, Muga and Tussah silk fibroin films. *Journal of Thermal Analysis and Calorimetry* **2015,** *122* (3), 1069-1076.

164. Hu, X.; Kaplan, D.; Cebe, P., Determining beta-sheet crystallinity in fibrous proteins by thermal analysis and infrared spectroscopy. *Macromolecules* **2006,** *39* (18), 6161-6170.

165. Hu, X.; Lu, Q.; Kaplan, D. L.; Cebe, P., Microphase separation controlled β-sheet crystallization kinetics in fibrous proteins. *Macromolecules* **2009,** *42* (6), 2079-2087.

166. Mazzi, S.; Zulker, E.; Buchicchio, J.; Anderson, B.; Hu, X., Comparative thermal analysis of Eri, Mori, Muga, and Tussar silk cocoons and fibroin fibers. *Journal of Thermal Analysis and Calorimetry* **2014,** *116* (3), 1337-1343.

167. Lu, Q.; Wang, X.; Hu, X.; Cebe, P.; Omenetto, F.; Kaplan, D. L., Stabilization and release of enzymes from silk films. *Macromolecular bioscience* **2010,** *10* (4), 359-368.

168. Goormaghtigh, E.; Cabiaux, V.; RUYSSCHAERT, J. M., Secondary structure and dosage of soluble and membrane proteins by attenuated total reflection Fourier - transform infrared spectroscopy on hydrated films. *European Journal of Biochemistry* **1990,** *193* (2), 409-420.

169. Dong, A.; Huang, P.; Caughey, W. S., Protein secondary structures in water from second-derivative amide I infrared spectra. *Biochemistry* **1990,** *29* (13), 3303-3308.

170. Mouro, C.; Jung, C.; Bondon, A.; Simonneaux, G., Comparative Fourier transform infrared studies of the secondary structure and the CO heme ligand environment in cytochrome P-450cam and cytochrome P-420cam. *Biochemistry* **1997,** *36* (26), 8125-8134.

171. Tretinnikov, O. N.; Tamada, Y., Influence of casting temperature on the near-surface structure and wettability of cast silk fibroin films. *Langmuir* **2001,** *17* (23), 7406-7413.

172. Teramoto, H.; Miyazawa, M., Molecular orientation behavior of silk sericin film as revealed by ATR infrared spectroscopy. *Biomacromolecules* **2005,** *6* (4), 2049-2057.

173. Schneider, J. P.; Pochan, D. J.; Ozbas, B.; Rajagopal, K.; Pakstis, L.; Kretsinger, J., Responsive hydrogels from the intramolecular folding and self-assembly of a designed peptide. *Journal of the American Chemical Society* **2002,** *124* (50), 15030-15037.

174. Pochan, D. J.; Schneider, J. P.; Kretsinger, J.; Ozbas, B.; Rajagopal, K.; Haines, L., Thermally reversible hydrogels via intramolecular folding and consequent self-assembly of a de novo designed peptide. *Journal of the American Chemical Society* **2003,** *125* (39), 11802-11803.

175. Chen, X.; Shao, Z.; Knight, D. P.; Vollrath, F., Conformation transition kinetics of Bombyx mori silk protein. *Proteins: Structure, Function, and Bioinformatics* **2007,** *68* (1), 223-231.

176. Du, N.; Yang, Z.; Liu, X. Y.; Li, Y.; Xu, H. Y., Structural origin of the strain - hardening of spider silk. *Advanced Functional Materials* **2011,** *21* (4), 772-778.

177. Kinahan, M. E.; Filippidi, E.; Köster, S.; Hu, X.; Evans, H. M.; Pfohl, T.; Kaplan, D. L.; Wong, J., Tunable silk: using microfluidics to fabricate silk fibers with controllable properties. *Biomacromolecules* **2011,** *12* (5), 1504-1511.

178. Wang, H.-Y.; Zhang, Y.-Q., Effect of regeneration of liquid silk fibroin on its structure and characterization. *Soft Matter* **2013,** *9* (1), 138-145.

179. Lu, S.; Li, J.; Zhang, S.; Yin, Z.; Xing, T.; Kaplan, D. L., The influence of the hydrophilic–lipophilic environment on the structure of silk fibroin protein. *Journal of Materials Chemistry B* **2015,** *3* (13), 2599-2606.

180. Zhang, F.; You, X.; Dou, H.; Liu, Z.; Zuo, B.; Zhang, X. J. A. a. m.; interfaces, Facile fabrication of robust silk nanofibril films via direct dissolution of silk in CaCl2–formic acid solution. **2015,** *7* (5), 3352-3361.

181. Kinahan, M. E.; Filippidi, E.; Köster, S.; Hu, X.; Evans, H. M.; Pfohl, T.; Kaplan, D. L.; Wong, J. J. B., Tunable silk: using microfluidics to fabricate silk fibers with controllable properties. **2011,** *12* (5), 1504-1511.

182. Wang, H.-Y.; Zhang, Y.-Q. J. S. M., Effect of regeneration of liquid silk fibroin on its structure and characterization. **2013,** *9* (1), 138-145.

183. Lu, S.; Li, J.; Zhang, S.; Yin, Z.; Xing, T.; Kaplan, D. L. J. J. o. M. C. B., The influence of the hydrophilic–lipophilic environment on the structure of silk fibroin protein. **2015,** *3* (13), 2599-2606.

184. Hu, X.; Kaplan, D.; Cebe, P. J. M., Dynamic protein− water relationships during β-sheet formation. **2008,** *41* (11), 3939-3948.

185. Fu, C.; Porter, D.; Chen, X.; Vollrath, F.; Shao, Z. J. A. F. M., Understanding the mechanical properties of Antheraea pernyi silk—from primary structure to condensed structure of the protein. **2011,** *21* (4), 729-737.

186. Andiappan, M.; Sundaramoorthy, S.; Panda, N.; Meiyazhaban, G.; Winfred, S. B.; Venkataraman, G.; Krishna, P. J. P. i. b., Electrospun eri silk fibroin scaffold coated with hydroxyapatite for bone tissue engineering applications. **2013,** *2* (1), 6.

187. Li, M.; Tao, W.; Kuga, S.; Nishiyama, Y. J. P. f. A. T., Controlling molecular conformation of regenerated wild silk fibroin by aqueous ethanol treatment. **2003,** *14* (10), 694-698.

188. Hu, X.; Kaplan, D.; Cebe, P., Dynamic protein− water relationships during β-sheet formation. *Macromolecules* **2008,** *41* (11), 3939-3948.

189. Hu, X.; Shmelev, K.; Sun, L.; Gil, E.-S.; Park, S.-H.; Cebe, P.; Kaplan, D. L., Regulation of silk material structure by temperature-controlled water vapor annealing. *Biomacromolecules* **2011,** *12* (5), 1686-1696.

190. Jin, H. J.; Park, J.; Karageorgiou, V.; Kim, U. J.; Valluzzi, R.; Cebe, P.; Kaplan, D. L., Water‐stable silk films with reduced β‐sheet content. *Advanced Functional Materials* **2005,** *15* (8), 1241-1247.

191. Fu, C.; Porter, D.; Chen, X.; Vollrath, F.; Shao, Z., Understanding the mechanical properties of Antheraea pernyi silk—from primary structure to condensed structure of the protein. *Advanced Functional Materials* **2011,** *21* (4), 729-737.

192. Andiappan, M.; Sundaramoorthy, S.; Panda, N.; Meiyazhaban, G.; Winfred, S. B.; Venkataraman, G.; Krishna, P., Electrospun eri silk fibroin scaffold coated with hydroxyapatite for bone tissue engineering applications. *Progress in biomaterials* **2013,** *2* (1), 6.

193. Li, M.; Tao, W.; Kuga, S.; Nishiyama, Y., Controlling molecular conformation of regenerated wild silk fibroin by aqueous ethanol treatment. *Polymers for Advanced Technologies* **2003,** *14* (10), 694-698.

194. Ling, S.; Qin, Z.; Li, C.; Huang, W.; Kaplan, D. L.; Buehler, M. J., Polymorphic regenerated silk fibers assembled through bioinspired spinning. *Nature communications* **2017,** *8* (1), 1-12.

195. Hu, X.; Kaplan, D.; Cebe, P., Effect of water on the thermal properties of silk fibroin. *Thermochimica Acta* **2007,** *461* (1-2), 137-144.

196. Wunderlich, B.; Jin, Y.; Boller, A., Mathematical description of differential scanning calorimetry based on periodic temperature modulation. *Thermochimica acta* **1994,** *238*, 277-293.

197. Cebe, P.; Hu, X.; Kaplan, D. L.; Zhuravlev, E.; Wurm, A.; Arbeiter, D.; Schick, C., Beating the heat-fast scanning melts silk beta sheet crystals. *Scientific reports* **2013,** *3*, 1130.

198. Wang, X.; Yucel, T.; Lu, Q.; Hu, X.; Kaplan, D. L., Silk nanospheres and microspheres from silk/pva blend films for drug delivery. *Biomaterials* **2010,** *31* (6), 1025-1035.

199. Wang, X.; Kluge, J. A.; Leisk, G. G.; Kaplan, D. L., Sonication-induced gelation of silk fibroin for cell encapsulation. *Biomaterials* **2008,** *29* (8), 1054-1064.

200. Park, S.-H.; Gil, E. S.; Shi, H.; Kim, H. J.; Lee, K.; Kaplan, D. L., Relationships between degradability of silk scaffolds and osteogenesis. *Biomaterials* **2010,** *31* (24), 6162-6172.

201. Hu, X.; Park, S.-H.; Gil, E. S.; Xia, X.-X.; Weiss, A. S.; Kaplan, D. L., The influence of elasticity and surface roughness on myogenic and osteogenic-differentiation of cells on silk-elastin biomaterials. *Biomaterials* **2011,** *32* (34), 8979-8989.

202. Bai, S.; Liu, S.; Zhang, C.; Xu, W.; Lu, Q.; Han, H.; Kaplan, D.; Zhu, H., Controllable transition of silk fibroin nanostructures: an insight into in vitro silk self-assembly process. *Acta biomaterialia* **2013,** *9* (8), 7806-7813.

203. Callone, E.; Dirè, S.; Hu, X.; Motta, A., Processing influence on molecular assembling and structural conformations in silk fibroin: elucidation by solid-state NMR. *ACS Biomaterials Science & Engineering* **2016,** *2* (5), 758-767.

204. Inoue, S.-i.; Tsuda, H.; Tanaka, T.; Kobayashi, M.; Magoshi, Y.; Magoshi, J., Nanostructure of Natural Fibrous Protein: In Vitro Nanofabric Formation of Samia c ynthia r icini Wild Silk Fibroin by Self-Assembling. *Nano Letters* **2003,** *3* (10), 1329-1332.

205. Zhou, P.; Xie, X.; Knight, D. P.; Zong, X.-H.; Deng, F.; Yao, W.-H., Effects of pH and calcium ions on the conformational transitions in silk fibroin using 2D Raman

correlation spectroscopy and 13C solid-state NMR. *Biochemistry* **2004,** *43* (35), 11302-11311.

206. Wu, Y.; Xue, Y.; Qin, S.; Liu, D.; Wang, X.; Hu, X.; Li, J.; Wang, X.; Bando, Y.; Golberg, D. J. A. a. m.; interfaces, BN Nanosheet/polymer films with highly anisotropic thermal conductivity for thermal management applications. **2017,** *9* (49), 43163-43170.

207. Hu, J.; Huang, Y.; Yao, Y.; Pan, G.; Sun, J.; Zeng, X.; Sun, R.; Xu, J.-B.; Song, B.; Wong, C.-P. J. A. a. m.; interfaces, Polymer composite with improved thermal conductivity by constructing a hierarchically ordered three-dimensional interconnected network of BN. **2017,** *9* (15), 13544-13553.

208. Barani, Z.; Mohammadzadeh, A.; Geremew, A.; Huang, C. Y.; Coleman, D.; Mangolini, L.; Kargar, F.; Balandin, A. A. J. A. F. M., Thermal Properties of the Binary‐Filler Hybrid Composites with Graphene and Copper Nanoparticles. **2019**, 1904008.

209. Wang, J.; Wu, Y.; Xue, Y.; Liu, D.; Wang, X.; Hu, X.; Bando, Y.; Lei, W. J. J. o. M. C. C., Super-compatible functional boron nitride nanosheets/polymer films with excellent mechanical properties and ultra-high thermal conductivity for thermal management. **2018,** *6* (6), 1363-1369.

210. Chang, C.; Fennimore, A.; Afanasiev, A.; Okawa, D.; Ikuno, T.; Garcia, H.; Li, D.; Majumdar, A.; Zettl, A. J. P. r. l., Isotope effect on the thermal conductivity of boron nitride nanotubes. **2006,** *97* (8), 085901.

211. Yu, J.; Huang, X.; Wu, C.; Wu, X.; Wang, G.; Jiang, P. J. P., Interfacial modification of boron nitride nanoplatelets for epoxy composites with improved thermal properties. **2012,** *53* (2), 471-480.

212. Xue, Y.; Zhou, X.; Zhan, T.; Jiang, B.; Guo, Q.; Fu, X.; Shimamura, K.; Xu, Y.; Mori, T.; Dai, P. J. A. F. M., Densely interconnected porous BN frameworks for multifunctional and isotropically thermoconductive polymer composites. **2018,** *28* (29), 1801205.

213. Fujii, M.; Zhang, X.; Takahashi, K. J. p. s. s., Measurements of thermal conductivity of individual carbon nanotubes. **2006,** *243* (13), 3385-3389.

214. Mazov, I.; Burmistrov, I.; Il'inykh, I.; Stepashkin, A.; Kuznetsov, D.; Issi, J. P. J. P. C., Anisotropic thermal conductivity of polypropylene composites filled with carbon fibers and multiwall carbon nanotubes. **2015,** *36* (11), 1951-1957.

215. Malekpour, H.; Balandin, A. A. J. J. o. R. S., Raman - based technique for measuring thermal conductivity of graphene and related materials. **2018,** *49* (1), 106-120.

216. Shtein, M.; Nadiv, R.; Buzaglo, M.; Kahil, K.; Regev, O. J. C. o. M., Thermally conductive graphene-polymer composites: size, percolation, and synergy effects. **2015,** *27* (6), 2100-2106.

217. Huxtable, S. T.; Cahill, D. G.; Shenogin, S.; Xue, L.; Ozisik, R.; Barone, P.; Usrey, M.; Strano, M. S.; Siddons, G.; Shim, M. J. N. m., Interfacial heat flow in carbon nanotube suspensions. **2003,** *2* (11), 731.

218. Huang, X.; Iizuka, T.; Jiang, P.; Ohki, Y.; Tanaka, T. J. T. J. o. P. C. C., Role of interface on the thermal conductivity of highly filled dielectric epoxy/AlN composites. **2012,** *116* (25), 13629-13639.

219. Yanagida, T.; Fujimoto, Y.; Kawaguchi, N.; Yanagida, S. J. J. o. t. C. S. o. J., Dosimeter properties of AlN. **2013,** *121* (1420), 988-991.

220. Xu, Y.; Chung, D.; Mroz, C. J. C. P. A. A. s.; manufacturing, Thermally conducting aluminum nitride polymer-matrix composites. **2001,** *32* (12), 1749-1757.

221. Kim, Y.; Ahn, C.-W.; Choi, J.-J.; Ryu, J.; Kim, J.-W.; Yoon, W.-H.; Park, D.-S.; Yoon, S.-Y.; Ma, B.; Hahn, B.-D. J. S. r., Next generation ceramic substrate fabricated at room temperature. **2017,** *7* (1), 6637.

222. Ling, S.; Kaplan, D. L.; Buehler, M. J. J. N. R. M., Nanofibrils in nature and materials engineering. **2018,** *3* (4), 18016.

223. Xue, Y.; Lofland, S.; Hu, X. J. P., Thermal conductivity of protein-based materials: A review. **2019,** *11* (3), 456.

224. Agari, Y.; Ueda, A.; Nagai, S. J. J. o. A. P. S., Thermal conductivity of a polymer composite. **1993,** *49* (9), 1625-1634.

225. Wang, X.; Wu, P. J. A. a. m.; interfaces, Preparation of highly thermally conductive polymer composite at low filler content via a self-assembly process between polystyrene microspheres and boron nitride nanosheets. **2017,** *9* (23), 19934-19944.

226. Xu, X.; Zhou, J.; Chen, J. J. A. F. M., Thermal Transport in Conductive Polymer–Based Materials. **2019**, 1904704.

227. Jiang, F.; Cui, S.; Song, N.; Shi, L.; Ding, P. J. A. a. m.; interfaces, Hydrogen bond-regulated boron nitride network structures for improved thermal conductive property of polyamide-imide composites. **2018,** *10* (19), 16812-16821.

228. Shen, H.; Guo, J.; Wang, H.; Zhao, N.; Xu, J. J. A. a. m.; interfaces, Bioinspired modification of h-BN for high thermal conductive composite films with aligned structure. **2015,** *7* (10), 5701-5708.

229. Stanton, J.; Xue, Y.; Waters, J. C.; Lewis, A.; Cowan, D.; Hu, X.; Salas-de la Cruz, D. J. C., Structure–property relationships of blended polysaccharide and protein biomaterials in ionic liquid. **2017,** *24* (4), 1775-1789.

230. Lammel, A. S.; Hu, X.; Park, S.-H.; Kaplan, D. L.; Scheibel, T. R. J. B., Controlling silk fibroin particle features for drug delivery. **2010,** *31* (16), 4583-4591.

231. Hu, X.; Kaplan, D.; Cebe, P. J. M., Determining beta-sheet crystallinity in fibrous proteins by thermal analysis and infrared spectroscopy. **2006,** *39* (18), 6161-6170.

232. Xue, Y.; Wang, F.; Torculas, M.; Lofland, S. E.; Hu, X. J. A. B. S.; Engineering, Formic Acid Regenerated Mori, Tussah, Eri, Thai and Muga Silk Materials: Mechanism of Self-assembly. **2019**.

233. Kim, H.; Kim, J.; Choi, J.; Park, Y.; Ki, C. J. P., Characterization of silk hydrogel formed with hydrolyzed silk fibroin-methacrylate via photopolymerization. **2018,** *153*, 232-240.

234. Liang, F.-C.; Huang, Y.-H.; Kuo, C.-C.; Cho, C.-J.; Rwei, S.-P.; Jia, Q.; Ding, Y.; Chen, Y.; Borsali, R. J. R.; Polymers, F., Thermally deposited silk fibroin as the gate dielectric layer in organic thin-film transistors based on conjugated polymer. **2018,** *131*, 368-377.

235. Wang, Y.; Ma, R.; Hu, K.; Kim, S.; Fang, G.; Shao, Z.; Tsukruk, V. V. J. A. a. m.; interfaces, Dramatic enhancement of graphene oxide/silk nanocomposite membranes: increasing toughness, strength, and Young's modulus via annealing of interfacial structures. **2016,** *8* (37), 24962-24973.

236. Jin, H. J.; Park, J.; Karageorgiou, V.; Kim, U. J.; Valluzzi, R.; Cebe, P.; Kaplan, D. L. J. A. F. M., Water‐stable silk films with reduced β‐sheet content. **2005,** *15* (8), 1241-1247.

237. Qi, Y.; Wang, H.; Wei, K.; Yang, Y.; Zheng, R.-Y.; Kim, I. S.; Zhang, K.-Q. J. I. j. o. m. s., A review of structure construction of silk fibroin biomaterials from single structures to multi-level structures. **2017,** *18* (3), 237.

238. Hu, X.; Shmelev, K.; Sun, L.; Gil, E.-S.; Park, S.-H.; Cebe, P.; Kaplan, D. L. J. B., Regulation of silk material structure by temperature-controlled water vapor annealing. **2011,** *12* (5), 1686-1696.

239. Liu, C.; Hu, Z.; Wu, Q.; Wang, X.; Chen, Y.; Sang, H.; Zhu, J.; Deng, S.; Xu, N. J. J. o. t. A. C. S., Vapor− solid growth and characterization of aluminum nitride nanocones. **2005,** *127* (4), 1318-1322.

240. Cebe, P.; Partlow, B. P.; Kaplan, D. L.; Wurm, A.; Zhuravlev, E.; Schick, C. J. A. b., Silk I and Silk II studied by fast scanning calorimetry. **2017,** *55*, 323-332.

241. Guo, C.; Zhang, J.; Wang, X.; Nguyen, A. T.; Liu, X. Y.; Kaplan, D. L. J. S., Comparative Study of Strain‐Dependent Structural Changes of Silkworm Silks: Insight into the Structural Origin of Strain‐Stiffening. **2017,** *13* (47), 1702266.

242. Guo, C.; Zhang, J.; Jordan, J. S.; Wang, X.; Henning, R. W.; Yarger, J. L. J. B., Structural Comparison of Various Silkworm Silks: An Insight into the Structure–Property Relationship. **2018,** *19* (3), 906-917.

243. Xue, Y.; Wang, F.; Torculas, M.; Lofland, S.; Hu, X. J. A. B. S.; Engineering, Formic Acid Regenerated Mori, Tussah, Eri, Thai, and Muga Silk Materials: Mechanism of Self-Assembly. **2019,** *5* (12), 6361-6373.

244. Ling, S.; Qi, Z.; Knight, D. P.; Shao, Z.; Chen, X. J. B., Synchrotron FTIR microspectroscopy of single natural silk fibers. **2011,** *12* (9), 3344-3349.

245. Han, T.; Clennell, M. B.; Cheng, A. C.; Pervukhina, M. J. G., Are self-consistent models capable of jointly modeling elastic velocity and electrical conductivity of reservoir sandstones? **2016,** *81* (4), D377-D382.

246. Dvorkin, J.; Berryman, J.; Nur, A. J. M. o. m., Elastic moduli of cemented sphere packs. **1999,** *31* (7), 461-469.

247. Dean, E. J. J. o. t. A. C. S., Elastic Moduli of Porous Sintered Materials as Modeled by a Variable - Aspect - Ratio Self - Consistent Oblate - Spheroidal - Inclusion Theory. **1983,** *66* (12), 847-854.

248. Watt, J. P.; Peselnick, L. J. J. o. A. P., Clarification of the Hashin - Shtrikman bounds on the effective elastic moduli of polycrystals with hexagonal, trigonal, and tetragonal symmetries. **1980,** *51* (3), 1525-1531.

249. Wall, P. J. A. o. M., A comparison of homogenization, Hashin-Shtrikman bounds and the Halpin-Tsai equations. **1997,** *42* (4), 245-257.

250. Koski, K. J.; Akhenblit, P.; McKiernan, K.; Yarger, J. L. J. N. m., Non-invasive determination of the complete elastic moduli of spider silks. **2013,** *12* (3), 262.

251. Zhang, K.; Duan, H.; Karihaloo, B. L.; Wang, J. J. P. o. t. N. A. o. S., Hierarchical, multilayered cell walls reinforced by recycled silk cocoons enhance the structural integrity of honeybee combs. **2010,** *107* (21), 9502-9506.

252. Wang, Z.; Tait, K.; Zhao, Y.; Schiferl, D.; Zha, C.; Uchida, H.; Downs, R. T. J. T. J. o. P. C. B., Size-induced reduction of transition pressure and enhancement of bulk modulus of AlN nanocrystals. **2004,** *108* (31), 11506-11508.

253. Yu, L.; Hu, X.; Kaplan, D.; Cebe, P. J. B., Dielectric relaxation spectroscopy of hydrated and dehydrated silk fibroin cast from aqueous solution. **2010,** *11* (10), 2766-2775.

254. Yazawa, K.; Malay, A. D.; Ifuku, N.; Ishii, T.; Masunaga, H.; Hikima, T.; Numata, K. J. B., Combination of amorphous silk fiber spinning and postspinning crystallization for tough regenerated silk fibers. **2018,** *19* (6), 2227-2237.

255. Yoshioka, T.; Tsubota, T.; Tashiro, K.; Jouraku, A.; Kameda, T. J. N. c., A study of the extraordinarily strong and tough silk produced by bagworms. **2019,** *10* (1), 1469.

256. Xue, Y.; Jao, D.; Hu, W.; Hu, X. J. J. o. T. A.; Calorimetry, Silk-silk blend materials. **2017,** *127* (1), 915-921.

257. DeFrates, K.; Markiewicz, T.; Callaway, K.; Xue, Y.; Stanton, J.; Salas-de la Cruz, D.; Hu, X. J. I. j. o. b. m., Structure–property relationships of Thai silk–microcrystalline cellulose biocomposite materials fabricated from ionic liquid. **2017,** *104*, 919-928.

258. He, Y. J. T. a., Heat capacity, thermal conductivity, and thermal expansion of barium titanate-based ceramics. **2004,** *419* (1-2), 135-141.

259. Gibiansky, L.; Torquato, S. J. J. o. t. M.; Solids, P. o., Thermal expansion of isotropic multiphase composites and polycrystals. **1997,** *45* (7), 1223-1252.

260. Magoshi, J.; Magoshi, Y. J. J. o. P. S. P. P. E., Physical properties and structure of silk. II. Dynamic mechanical and dielectric properties of silk fibroin. **1975,** *13* (7), 1347-1351.

261. Magoshi, J.; Magoshi, Y.; Nakamura, S.; Kasai, N.; Kakudo, M. J. J. o. P. S. P. P. E., Physical properties and structure of silk. V. Thermal behavior of silk fibroin in the random - coil conformation. **1977,** *15* (9), 1675-1683.

262. Zhi, C.; Bando, Y.; Tang, C.; Kuwahara, H.; Golberg, D. J. A. M., Large - scale fabrication of boron nitride nanosheets and their utilization in polymeric composites with improved thermal and mechanical properties. **2009,** *21* (28), 2889-2893.

263. Liu, G.; Huang, X.; Wang, Y.; Zhang, Y.-Q.; Wang, X. J. S. M., Thermal transport in single silkworm silks and the behavior under stretching. **2012,** *8* (38), 9792-9799.

264. Liu, G.; Xu, S.; Cao, T. T.; Lin, H.; Tang, X.; Zhang, Y. Q.; Wang, X. J. B., Thermally induced increase in energy transport capacity of silkworm silks. **2014,** *101* (10), 1029-1037.

265. Park, J.; Kim, D.; Lee, S.-M.; Choi, J.-u.; You, M.; So, H.-M.; Han, J.; Nah, J.; Seol, J. H. J. I. j. o. b. m., Effects of β-sheet crystals and a glycine-rich matrix on the thermal conductivity of spider dragline silk. **2017,** *96*, 384-391.

266. Zhang, L.; Bai, Z.; Ban, H.; Liu, L. J. P. C. C. P., Effects of the amino acid sequence on thermal conduction through β-sheet crystals of natural silk protein. **2015,** *17* (43), 29007-29013.

267. Gao, L.; Zhou, X. F. J. P. L. A., Differential effective medium theory for thermal conductivity in nanofluids. **2006,** *348* (3-6), 355-360.

268. Giri, A.; Niemelä, J.-P.; Tynell, T.; Gaskins, J. T.; Donovan, B. F.; Karppinen, M.; Hopkins, P. E. J. P. R. B., Heat-transport mechanisms in molecular building blocks of inorganic/organic hybrid superlattices. **2016,** *93* (11), 115310.

269. Malhotra, A.; Maldovan, M. J. J. o. A. P., Surface scattering controlled heat conduction in semiconductor thin films. **2016,** *120* (20), 204305.

270. Su, I.; Buehler, M. J., Spider silk: dynamic mechanics. *Nature materials* **2016,** *15* (10), 1054-1055.

271. Park, J.; Kim, D.; Lee, S.-M.; Choi, J.-u.; You, M.; So, H.-M.; Han, J.; Nah, J.; Seol, J. H., Effects of β-sheet crystals and a glycine-rich matrix on the thermal conductivity of spider dragline silk. *International journal of biological macromolecules* **2017,** *96*, 384-391.

272. Yuan, C.; Li, J.; Lindsay, L.; Cherns, D.; Pomeroy, J. W.; Liu, S.; Edgar, J. H.; Kuball, M., Modulating the thermal conductivity in hexagonal boron nitride via controlled boron isotope concentration. *Communications Physics* **2019,** *2* (1), 1-8.

273. Wang, C.; Guo, J.; Dong, L.; Aiyiti, A.; Xu, X.; Li, B., Superior thermal conductivity in suspended bilayer hexagonal boron nitride. *Scientific reports* **2016,** *6*, 25334.

274. Chen, K.; Song, B.; Ravichandran, N. K.; Zheng, Q.; Chen, X.; Lee, H.; Sun, H.; Li, S.; Gamage, G. A.; Tian, F., Ultrahigh thermal conductivity in isotope-enriched cubic boron nitride. *Science* **2020**.

275. Wu, Y.; Xue, Y.; Qin, S.; Liu, D.; Wang, X.; Hu, X.; Li, J.; Wang, X.; Bando, Y.; Golberg, D., BN nanosheet/polymer films with highly anisotropic thermal conductivity for thermal management applications. *ACS applied materials & interfaces* **2017,** *9* (49), 43163-43170.

276. Wang, J.; Wu, Y.; Xue, Y.; Liu, D.; Wang, X.; Hu, X.; Bando, Y.; Lei, W., Super-compatible functional boron nitride nanosheets/polymer films with excellent mechanical properties and ultra-high thermal conductivity for thermal management. *Journal of Materials Chemistry C* **2018,** *6* (6), 1363-1369.

277. Li, X.; Yan, Y.; Dong, L.; Guo, J.; Aiyiti, A.; Xu, X.; Li, B., Thermal conduction across a boron nitride and silicon oxide interface. *arXiv preprint arXiv:1703.00669* **2017**.

278. Mateti, S.; Yang, K.; Liu, X.; Huang, S.; Wang, J.; Li, L. H.; Hodgson, P.; Zhou, M.; He, J.; Chen, Y., Bulk hexagonal boron nitride with a quasi‐isotropic thermal conductivity. *Advanced Functional Materials* **2018,** *28* (28), 1707556.

279. Geim, A. K.; Grigorieva, I. V., Van der Waals heterostructures. *Nature* **2013,** *499* (7459), 419-425.

280. Wang, Y.; Xu, L.; Yang, Z.; Xie, H.; Jiang, P.; Dai, J.; Luo, W.; Yao, Y.; Hitz, E.; Yang, R., High temperature thermal management with boron nitride nanosheets. *Nanoscale* **2018,** *10* (1), 167-173.

281. Xue, Y.; Li, X.; Wang, H.; Zhao, F.; Zhang, D.; Chen, Y., Improvement in thermal conductivity of through-plane aligned boron nitride/silicone rubber composites. *Materials & Design* **2019,** *165*, 107580.

282. Xue, Y.; Lofland, S.; Hu, X., Thermal conductivity of protein-based materials: A review. *Polymers* **2019,** *11* (3), 456.

283. Chen, H.; Ginzburg, V. V.; Yang, J.; Yang, Y.; Liu, W.; Huang, Y.; Du, L.; Chen, B., Thermal conductivity of polymer-based composites: Fundamentals and applications. *Progress in Polymer Science* **2016,** *59*, 41-85.

284. Burger, N.; Laachachi, A.; Ferriol, M.; Lutz, M.; Toniazzo, V.; Ruch, D., Review of thermal conductivity in composites: mechanisms, parameters and theory. *Progress in Polymer Science* **2016,** *61*, 1-28.

285. Zeng, X.; Yao, Y.; Gong, Z.; Wang, F.; Sun, R.; Xu, J.; Wong, C. P., Ice - templated assembly strategy to construct 3D boron nitride nanosheet networks in polymer composites for thermal conductivity improvement. *Small* **2015,** *11* (46), 6205-6213.

286. Xu, X.; Zhou, J.; Chen, J., Thermal Transport in Conductive Polymer–Based Materials. *Advanced Functional Materials* **2019**, 1904704.

287. Keten, S.; Xu, Z.; Ihle, B.; Buehler, M. J., Nanoconfinement controls stiffness, strength and mechanical toughness of β-sheet crystals in silk. *Nature materials* **2010,** *9* (4), 359-367.

288. Lefevre, T.; Paquet - Mercier, F.; Rioux - Dubé, J. F.; Pézolet, M., Structure of silk by Raman spectromicroscopy: From the spinning glands to the fibers. *Biopolymers* **2012,** *97* (6), 322-336.

289. Conte, A. A.; Shirvani, K.; Hones, H.; Wildgoose, A.; Xue, Y.; Najjar, R.; Hu, X.; Xue, W.; Beachley, V. Z., Effects of post-draw processing on the structure and functional properties of electrospun PVDF-HFP nanofibers. *Polymer* **2019,** *171*, 192-200.

290. Beachley, V.; Wen, X., Polymer nanofibrous structures: Fabrication, biofunctionalization, and cell interactions. *Progress in polymer science* **2010,** *35* (7), 868-892.

291. Frenot, A.; Chronakis, I. S., Polymer nanofibers assembled by electrospinning. *Current opinion in colloid & interface science* **2003,** *8* (1), 64-75.

292. Beachley, V.; Wen, X., Effect of electrospinning parameters on the nanofiber diameter and length. *Materials Science and Engineering: C* **2009,** *29* (3), 663-668.

293. Beachley, V.; Katsanevakis, E.; Zhang, N.; Wen, X., Highly aligned polymer nanofiber structures: fabrication and applications in tissue engineering. In *Biomedical applications of polymeric nanofibers*, Springer: 2011; pp 171-212.

294. Huang, Z.-M.; Zhang, Y.-Z.; Kotaki, M.; Ramakrishna, S., A review on polymer nanofibers by electrospinning and their applications in nanocomposites. *Composites science and technology* **2003,** *63* (15), 2223-2253.

295. Xue, Y.; Wang, F.; Torculas, M.; Lofland, S.; Hu, X., Formic Acid Regenerated Mori, Tussah, Eri, Thai, and Muga Silk Materials: Mechanism of Self-Assembly. *ACS Biomaterials Science & Engineering* **2019,** *5* (12), 6361-6373.

296. Wang, F.; Wu, H.; Venkataraman, V.; Hu, X., Silk fibroin-poly (lactic acid) biocomposites: Effect of protein-synthetic polymer interactions and miscibility on material properties and biological responses. *Materials Science and Engineering: C* **2019,** *104*, 109890.

297. Tokareva, O.; Jacobsen, M.; Buehler, M.; Wong, J.; Kaplan, D. L., Structure–function–property–design interplay in biopolymers: Spider silk. *Acta biomaterialia* **2014,** *10* (4), 1612-1626.

298. Dinjaski, N.; Kaplan, D. L., Recombinant protein blends: Silk beyond natural design. *Current opinion in biotechnology* **2016,** *39*, 1-7.

299. Frandsen, J. L.; Ghandehari, H., Recombinant protein-based polymers for advanced drug delivery. *Chemical Society Reviews* **2012,** *41* (7), 2696-2706.

300. Stanton, J.; Xue, Y.; Pandher, P.; Malek, L.; Brown, T.; Hu, X.; Salas-de la Cruz, D., Impact of ionic liquid type on the structure, morphology and properties of silk-cellulose biocomposite materials. *International journal of biological macromolecules* **2018,** *108*, 333-341.

301. Guerra, V.; Wan, C.; McNally, T., Thermal conductivity of 2D nano-structured boron nitride (BN) and its composites with polymers. *Progress in Materials Science* **2019,** *100*, 170-186.

302. Zeng, X.; Sun, J.; Yao, Y.; Sun, R.; Xu, J.-B.; Wong, C.-P., A combination of boron nitride nanotubes and cellulose nanofibers for the preparation of a nanocomposite with high thermal conductivity. *ACS nano* **2017,** *11* (5), 5167-5178.

303. Kıvanç, M.; Barutca, B.; Koparal, A. T.; Göncü, Y.; Bostancı, S. H.; Ay, N., Effects of hexagonal boron nitride nanoparticles on antimicrobial and antibiofilm activities, cell viability. *Materials Science and Engineering: C* **2018,** *91*, 115-124.

304. Li, X.; Wang, X.; Zhang, J.; Hanagata, N.; Wang, X.; Weng, Q.; Ito, A.; Bando, Y.; Golberg, D., Hollow boron nitride nanospheres as boron reservoir for prostate cancer treatment. *Nature communications* **2017,** *8* (1), 1-12.

305. Li, L.; Li, J.; Shi, Y.; Du, P.; Zhang, Z.; Liu, T.; Zhang, R.; Liu, Z., On-Demand Biodegradable Boron Nitride Nanoparticles for Treating Triple Negative Breast Cancer with Boron Neutron Capture Therapy. *ACS nano* **2019,** *13* (12), 13843-13852.

306. Feng, S.; Zhang, H.; Yan, T.; Huang, D.; Zhi, C.; Nakanishi, H.; Gao, X.-D., Folate-conjugated boron nitride nanospheres for targeted delivery of anticancer drugs. *International journal of nanomedicine* **2016,** *11*, 4573.

307. Cheng, C.-C.; Muhabie, A. A.; Huang, S.-Y.; Wu, C.-Y.; Gebeyehu, B. T.; Lee, A.-W.; Lai, J.-Y.; Lee, D.-J., Dual stimuli-responsive supramolecular boron nitride with tunable physical properties for controlled drug delivery. *Nanoscale* **2019,** *11* (21), 10393-10401.

308. Permyakova, E. S.; Sukhorukova, I. V.; Antipina, L. Y.; Konopatsky, A. S.; Kovalskii, A. M.; Matveev, A. T.; Lebedev, O. I.; Golberg, D. V.; Manakhov, A. M.; Shtansky, D. V., Synthesis and characterization of folate conjugated boron nitride nanocarriers for targeted drug delivery. *The Journal of Physical Chemistry C* **2017,** *121* (50), 28096-28105.

309. Saleh, D. A.; Niskanen, J.; Xue, Y.; Golberg, D.; Winnik, F. M.; Sosnik, A., Boron nitride nanotube-based amphiphilic hybrid nanomaterials for superior encapsulation of hydrophobic cargos. *Materials today chemistry* **2017,** *6*, 45-50.

310. Callaway, K. A.; Xue, Y.; Altimari, V.; Jiang, G.; Hu, X., Comparative investigation of thermal and structural behavior in renewably sourced composite films of even-even nylons (610 and 1010) with silk fibroin. *Polymers* **2018,** *10* (9), 1029.

311. Muratov, D.; Kuznetsov, D.; Il'Inykh, I.; Burmistrov, I.; Mazov, I., Thermal conductivity of polypropylene composites filled with silane-modified hexagonal BN. *Composites Science and Technology* **2015,** *111*, 40-43.

312. Harrison, H.; Lamb, J. T.; Nowlin, K. S.; Guenthner, A. J.; Ghiassi, K. B.; Kelkar, A. D.; Alston, J. R., Quantification of hexagonal boron nitride impurities in boron nitride nanotubes via FTIR spectroscopy. *Nanoscale Advances* **2019,** *1* (5), 1693-1701.

313. Fang, C.; Zhang, M., Multifunctional magnetic nanoparticles for medical imaging applications. *Journal of materials chemistry* **2009,** *19* (35), 6258-6266.

314. Arruebo, M.; Fernández-Pacheco, R.; Ibarra, M. R.; Santamaría, J., Magnetic nanoparticles for drug delivery. *Nano today* **2007,** *2* (3), 22-32.

315. Martín, M.; Salazar, P.; Villalonga, R.; Campuzano, S.; Pingarrón, J. M.; González-Mora, J. L., Preparation of core–shell Fe 3 O 4@ poly (dopamine) magnetic nanoparticles for biosensor construction. *Journal of Materials Chemistry B* **2014,** *2* (6), 739-746.

316. Fuchikami, N., Magnetic anisotropy of magnetoplumbite BaFe12O19. *Journal of the Physical Society of Japan* **1965,** *20* (5), 760-769.

317. Anbarasu, V.; Gazzali, P. M.; Karthik, T.; Manigandan, A.; Sivakumar, K., Effect of divalent cation substitution in the magnetoplumbite structured BaFe 12 O 19 system. *Journal of Materials Science: Materials in Electronics* **2013,** *24* (3), 916-926.

318. Xu, P.; Han, X.; Zhao, H.; Liang, Z.; Wang, J., Effect of stoichiometry on the phase formation and magnetic properties of BaFe12O19 nanoparticles by reverse micelle technique. *Materials Letters* **2008,** *62* (8-9), 1305-1308.

319. Atwater, J.; Akse, J.; Jovanovic, G.; Sornchamni, T., Preparation of metallic cobalt and cobalt-barium titanate spheres as high temperature media for magnetically stabilized fluidized bed reactors. *Journal of materials science letters* **2001,** *20* (6), 487-488.

320. Lai, C. W.; Wang, Y. H.; Lai, C. H.; Yang, M. J.; Chen, C. Y.; Chou, P. T.; Chan, C. S.; Chi, Y.; Chen, Y. C.; Hsiao, J. K., Iridium‐complex‐functionalized Fe3O4/SiO2 core/shell nanoparticles: a facile three‐in‐one system in magnetic resonance imaging, luminescence imaging, and photodynamic therapy. *Small* **2008,** *4* (2), 218-224.

321. Xuan, S.; Wang, F.; Lai, J. M.; Sham, K. W.; Wang, Y.-X. J.; Lee, S.-F.; Yu, J. C.; Cheng, C. H.; Leung, K. C.-F., Synthesis of biocompatible, mesoporous Fe3O4 nano/microspheres with large surface area for magnetic resonance imaging and therapeutic applications. *ACS applied materials & interfaces* **2011,** *3* (2), 237-244.

322. Shen, J.-M.; Tang, W.-J.; Zhang, X.-L.; Chen, T.; Zhang, H.-X., A novel carboxymethyl chitosan-based folate/Fe3O4/CdTe nanoparticle for targeted drug delivery and cell imaging. *Carbohydrate polymers* **2012,** *88* (1), 239-249.

323. Xu, C.; Zheng, Y.; Gao, W.; Xu, J.; Zuo, G.; Chen, Y.; Zhao, M.; Li, J.; Song, J.; Zhang, N., Magnetic hyperthermia ablation of tumors using injectable Fe3O4/calcium phosphate cement. *ACS applied materials & interfaces* **2015,** *7* (25), 13866-13875.

324. Luo, K.-y.; Shao, Z.-z., A novel regenerated silk fibroin-based hydrogels with magnetic and catalytic activities. *Chinese Journal of Polymer Science* **2017,** *35* (4), 515-523.

325. Lamoolphak, W.; De-Eknamkul, W.; Shotipruk, A., Hydrothermal production and characterization of protein and amino acids from silk waste. *Bioresource technology* **2008,** *99* (16), 7678-7685.

326. Kawakami, M.; SHIMURA, K., Fractionation of Glycine, Alanine, and Serine Transfer Ribonucleic Acids from the Silk Gland. *The Journal of Biochemistry* **1973,** *74* (1), 33-40.

327. McGill, M.; Holland, G. P.; Kaplan, D. L., Experimental methods for characterizing the secondary structure and thermal properties of silk proteins. *Macromolecular rapid communications* **2019,** *40* (1), 1800390.

328. Choi, M.; Choi, D.; Hong, J., Multilayered controlled drug release silk fibroin nanofilm by manipulating secondary structure. *Biomacromolecules* **2018,** *19* (7), 3096-3103.

329. Liu, Q.; Wang, X.; Tan, X.; Xie, X.; Li, Y.; Zhao, P.; Xia, Q., A strategy for improving the mechanical properties of silk fiber by directly injection of ferric ions into silkworm. *Materials & Design* **2018,** *146*, 134-141.

330. Guo, Z.; Xie, W.; Gao, Q.; Wang, D.; Gao, F.; Li, S.; Zhao, L., In situ biomineralization by silkworm feeding with ion precursors for the improved mechanical properties of silk fiber. *International journal of biological macromolecules* **2018,** *109*, 21-26.

331. Cebe, P.; Partlow, B. P.; Kaplan, D. L.; Wurm, A.; Zhuravlev, E.; Schick, C., Silk I and Silk II studied by fast scanning calorimetry. *Acta biomaterialia* **2017,** *55*, 323-332.

332. Love, S. A.; Popov, E.; Rybacki, K.; Hu, X.; Salas-de la Cruz, D., Facile treatment to fine-tune cellulose crystals in cellulose-silk biocomposites through hydrogen peroxide. *International Journal of Biological Macromolecules* **2020**.

333. Crivelli, B.; Perteghella, S.; Bari, E.; Sorrenti, M.; Tripodo, G.; Chlapanidas, T.; Torre, M. L., Silk nanoparticles: From inert supports to bioactive natural carriers for drug delivery. *Soft Matter* **2018,** *14* (4), 546-557.

334. Kumar, M.; Gupta, P.; Bhattacharjee, S.; Nandi, S. K.; Mandal, B. B., Immunomodulatory injectable silk hydrogels maintaining functional islets and promoting anti-inflammatory M2 macrophage polarization. *Biomaterials* **2018,** *187*, 1-17.

335. Floren, M.; Bonani, W.; Dharmarajan, A.; Motta, A.; Migliaresi, C.; Tan, W., Human mesenchymal stem cells cultured on silk hydrogels with variable stiffness and growth factor differentiate into mature smooth muscle cell phenotype. *Acta biomaterialia* **2016,** *31*, 156-166.

336. Xiao, L.; Lu, G.; Lu, Q.; Kaplan, D. L., Direct formation of silk nanoparticles for drug delivery. *ACS Biomaterials Science & Engineering* **2016,** *2* (11), 2050-2057.

337. Dong, S.; Guo, P.; Chen, G.-y.; Jin, N.; Chen, Y., Study on the atmospheric cold plasma (ACP) treatment of zein film: Surface properties and cytocompatibility. *International journal of biological macromolecules* **2019**.

338. Torculas, M.; Medina, J.; Xue, W.; Hu, X., Protein-based bioelectronics. *ACS Biomaterials Science & Engineering* **2016,** *2* (8), 1211-1223.

339. Jia, Z.; Zhou, W.; Yan, J.; Xiong, P.; Guo, H.; Cheng, Y.; Zheng, Y., Constructing multilayer silk protein/Nanosilver biofunctionalized hierarchically structured 3D printed Ti6Al4 V scaffold for repair of infective bone defects. *ACS Biomaterials Science & Engineering* **2018,** *5* (1), 244-261.

340. Li, J.; Zhou, Y.; Chen, W.; Yuan, Z.; You, B.; Liu, Y.; Yang, S.; Li, F.; Qu, C.; Zhang, X., A novel 3D in vitro tumor model based on silk fibroin/chitosan scaffolds to mimic the tumor microenvironment. *ACS applied materials & interfaces* **2018,** *10* (43), 36641-36651.

341. Hu, X.; Lofland, S., Processes of Increasing Crystallinity Alignment of Protein Films and Products Thereof. Google Patents: 2018.

342. Guan, J.; Wang, Y.; Mortimer, B.; Holland, C.; Shao, Z.; Porter, D.; Vollrath, F., Glass transitions in native silk fibres studied by dynamic mechanical thermal analysis. *Soft Matter* **2016,** *12* (27), 5926-5936.

343. Xue, Y.; Hu, W.; Hu, X., Thermal analysis of natural fibers. In *Thermal Analysis of Textiles and Fibers*, Elsevier: 2020; pp 105-132.

344. DiBenedetto, A., Prediction of the glass transition temperature of polymers: a model based on the principle of corresponding states. *Journal of Polymer Science Part B: Polymer Physics* **1987,** *25* (9), 1949-1969.

345. Liu, Q.; Wang, X.; Tan, X.; Xie, X.; Dong, H.; Li, X.; Li, Y.; Zhao, P.; Xia, Q., Disruption of the Metal Ion Environment by EDTA for Silk Formation Affects the Mechanical Properties of Silkworm Silk. *International journal of molecular sciences* **2019,** *20* (12), 3026.

346. Zong, X.-H.; Zhou, P.; Shao, Z.-Z.; Chen, S.-M.; Chen, X.; Hu, B.-W.; Deng, F.; Yao, W.-H., Effect of pH and copper (II) on the conformation transitions of silk fibroin based on EPR, NMR, and Raman spectroscopy. *Biochemistry* **2004,** *43* (38), 11932-11941.

347. Lin, G.; Zhong, Y.; Zhong, J.; Shao, Z., Effect of Fe3+ on the Silk Fibroin Regulated Direct Growth of Nacre-like Aragonite Hybrids. *Crystal Growth & Design* **2015,** *15* (12), 5774-5780.

348. Gao, J.; Gu, H.; Xu, B., Multifunctional magnetic nanoparticles: design, synthesis, and biomedical applications. *Accounts of chemical research* **2009,** *42* (8), 1097-1107.

349. Satarkar, N. S.; Hilt, J. Z., Hydrogel nanocomposites as remote-controlled biomaterials. *Acta biomaterialia* **2008,** *4* (1), 11-16.

350. Rahimi, M.; Wadajkar, A.; Subramanian, K.; Yousef, M.; Cui, W.; Hsieh, J.-T.; Nguyen, K. T., In vitro evaluation of novel polymer-coated magnetic nanoparticles for controlled drug delivery. *Nanomedicine: Nanotechnology, Biology and Medicine* **2010,** *6* (5), 672-680.

351. Pankhurst, Q. A.; Connolly, J.; Jones, S. K.; Dobson, J., Applications of magnetic nanoparticles in biomedicine. *Journal of physics D: Applied physics* **2003,** *36* (13), R167.

352. Kobayashi, T., Cancer hyperthermia using magnetic nanoparticles. *Biotechnology journal* **2011,** *6* (11), 1342-1347.

353. Bañobre-López, M.; Teijeiro, A.; Rivas, J., Magnetic nanoparticle-based hyperthermia for cancer treatment. *Reports of Practical Oncology & Radiotherapy* **2013,** *18* (6), 397-400.

354. Corchero, J. L.; Villaverde, A., Biomedical applications of distally controlled magnetic nanoparticles. *Trends in biotechnology* **2009,** *27* (8), 468-476.

355. Haun, J. B.; Yoon, T. J.; Lee, H.; Weissleder, R., Magnetic nanoparticle biosensors. *Wiley Interdisciplinary Reviews: Nanomedicine and Nanobiotechnology* **2010,** *2* (3), 291-304.

356. Reddy, L. H.; Arias, J. L.; Nicolas, J.; Couvreur, P., Magnetic nanoparticles: design and characterization, toxicity and biocompatibility, pharmaceutical and biomedical applications. *Chemical reviews* **2012,** *112* (11), 5818-5878.

357. Gil, S.; Correia, C. R.; Mano, J. F., Magnetically Labeled Cells with Surface‐Modified Fe3O4 Spherical and Rod‐Shaped Magnetic Nanoparticles for Tissue Engineering Applications. *Advanced healthcare materials* **2015,** *4* (6), 883-891.

358. Bock, N.; Riminucci, A.; Dionigi, C.; Russo, A.; Tampieri, A.; Landi, E.; Goranov, V. A.; Marcacci, M.; Dediu, V., A novel route in bone tissue engineering: magnetic biomimetic scaffolds. *Acta Biomaterialia* **2010,** *6* (3), 786-796.

359. Tampieri, A.; Iafisco, M.; Sandri, M.; Panseri, S.; Cunha, C.; Sprio, S.; Savini, E.; Uhlarz, M.; Herrmannsdörfer, T., Magnetic bioinspired hybrid nanostructured collagen–hydroxyapatite scaffolds supporting cell proliferation and tuning regenerative process. *ACS applied materials & interfaces* **2014,** *6* (18), 15697-15707.

360. Samal, S. K.; Goranov, V.; Dash, M.; Russo, A.; Shelyakova, T.; Graziosi, P.; Lungaro, L.; Riminucci, A.; Uhlarz, M.; Bañobre-López, M., Multilayered magnetic gelatin membrane scaffolds. *ACS applied materials & interfaces* **2015,** *7* (41), 23098-23109.

361. Gil, S.; Mano, J. F., Magnetic composite biomaterials for tissue engineering. *Biomaterials Science* **2014,** *2* (6), 812-818.

362. Ulbrich, K.; Hola, K.; Subr, V.; Bakandritsos, A.; Tucek, J.; Zboril, R., Targeted drug delivery with polymers and magnetic nanoparticles: covalent and noncovalent approaches, release control, and clinical studies. *Chemical reviews* **2016,** *116* (9), 5338-5431.

363. Bealer, E. J.; Onissema-Karimu, S.; Rivera-Galletti, A.; Francis, M.; Wilkowski, J.; Salas-de la Cruz, D.; Hu, X., Protein–Polysaccharide Composite Materials: Fabrication and Applications. *Polymers* **2020,** *12* (2), 464.

364. Han, H.; Ning, H.; Liu, S.; Lu, Q.; Fan, Z.; Lu, H.; Lu, G.; Kaplan, D. L., Silk biomaterials with vascularization capacity. *Advanced functional materials* **2016,** *26* (3), 421-432.

365. Zhou, Z.; Zhang, S.; Cao, Y.; Marelli, B.; Xia, X.; Tao, T. H., Engineering the future of silk materials through advanced manufacturing. *Advanced Materials* **2018,** *30* (33), 1706983.

366. Brennan, D. A.; Conte, A. A.; Kanski, G.; Turkula, S.; Hu, X.; Kleiner, M. T.; Beachley, V., Mechanical considerations for electrospun nanofibers in tendon and ligament repair. *Advanced healthcare materials* **2018,** *7* (12), 1701277.

367. DeFrates, K.; Markiewicz, T.; Callaway, K.; Xue, Y.; Stanton, J.; Salas-de la Cruz, D.; Hu, X., Structure–property relationships of Thai silk–microcrystalline cellulose biocomposite materials fabricated from ionic liquid. *International journal of biological macromolecules* **2017,** *104*, 919-928.

368. Brennan, D. A.; Jao, D.; Siracusa, M. C.; Wilkinson, A. R.; Hu, X.; Beachley, V. Z., Concurrent collection and post-drawing of individual electrospun polymer nanofibers to enhance macromolecular alignment and mechanical properties. *Polymer* **2016,** *103*, 243-250.

369. Zhang, X.; Reagan, M. R.; Kaplan, D. L., Electrospun silk biomaterial scaffolds for regenerative medicine. *Advanced drug delivery reviews* **2009,** *61* (12), 988-1006.

370. Wang, H. B.; Mullins, M. E.; Cregg, J. M.; McCarthy, C. W.; Gilbert, R. J., Varying the diameter of aligned electrospun fibers alters neurite outgrowth and Schwann cell migration. *Acta biomaterialia* **2010,** *6* (8), 2970-2978.

371. Liang, Y.; Wu, D.; Fu, R., Carbon microfibers with hierarchical porous structure from electrospun fiber-like natural biopolymer. *Scientific reports* **2013,** *3*, 1119.

372. Croisier, F.; Duwez, A.-S.; Jérôme, C.; Léonard, A.; Van Der Werf, K.; Dijkstra, P. J.; Bennink, M. L., Mechanical testing of electrospun PCL fibers. *Acta biomaterialia* **2012,** *8* (1), 218-224.

373. Ling, S.; Qi, Z.; Knight, D. P.; Shao, Z.; Chen, X., Synchrotron FTIR microspectroscopy of single natural silk fibers. *Biomacromolecules* **2011,** *12* (9), 3344-3349.

374. Xu, Z.; Shi, L.; Yang, M.; Zhu, L., Preparation and biomedical applications of silk fibroin-nanoparticles composites with enhanced properties-A review. *Materials Science and Engineering: C* **2019,** *95*, 302-311.

375. Zheng, K.; Yu, J.; Zhang, W.; Li, X.; Fan, Y.; Kaplan, D. L., Self-assembling oxidized silk fibroin nanofibrils with controllable fractal dimensions. *Journal of Materials Chemistry B* **2018,** *6* (28), 4656-4664.

376. Lawrence, B. D.; Omenetto, F.; Chui, K.; Kaplan, D. L., Processing methods to control silk fibroin film biomaterial features. *Journal of materials science* **2008,** *43* (21), 6967-6985.

377. Wang, Y.; Ma, R.; Hu, K.; Kim, S.; Fang, G.; Shao, Z.; Tsukruk, V. V., Dramatic enhancement of graphene oxide/silk nanocomposite membranes: increasing toughness, strength, and Young's modulus via annealing of interfacial structures. *ACS applied materials & interfaces* **2016,** *8* (37), 24962-24973.